

# **HEAT TRANSFER IN NANOFUIDS OVER DIFFERENT CONFORMATIONS WITH VARIOUS EFFECTS**

By  
**PARDEEP KUMAR**  
(2019BS21D)

*Thesis submitted to Chaudhary Charan Singh Haryana  
Agricultural University in the partial fulfilment  
of the requirement for the degree of*

**DOCTOR OF PHILOSOPHY**  
**IN**  
**MATHEMATICS**



**DEPARTMENT OF MATHEMATICS & STATISTICS**  
**COLLEGE OF BASIC SCIENCES & HUMANITIES**  
**CCS HARYANA AGRICULTURAL UNIVERSITY**  
**HISAR-125 004**

**2023**

## **CERTIFICATE-I**

This is to certify that this thesis entitled, “**Heat transfer in nanofluids over different conformations with various effects**” submitted for the degree of **Doctor of Philosophy** in the subject of **Mathematics** to the Chaudhary Charan Singh Haryana Agricultural University, Hisar is bonafide research work carried out by **Mr. Pardeep Kumar** under my supervision and guidance that no part of this thesis has been submitted for any other degree. The assistance and help received during the course of investigation have been fully acknowledged.

**Dr. Hemant Poonia**

Major Advisor

Assistant Professor (Mathematics)

Department of Mathematics and Statistics

CCS Haryana Agricultural University

Hisar-125004

## **CERTIFICATE –II**

This is to certify that this thesis entitled, “**Heat transfer in nanofluids over different conformations with various effects**” submitted by **Mr. Pardeep Kumar** to the Chaudhary Charan Singh Haryana Agricultural University, Hisar in partial fulfilment of the requirements for the degree of **Doctor of Philosophy** in the subject of **Mathematics**, has been approved by the student's Advisory Committee after an oral examination on the same.

**MAJOR ADVISOR**

**EXTERNAL EXAMINER**

**HEAD OF THE DEPARTMENT**

**DEAN, POSTGRADUATE STUDIES**

### **CERTIFICATE –III**

It is certified that the thesis submitted by **Mr. Pardeep Kumar** Adm. No. **2019BS21D**, Ph.D. student of this department of **Mathematics and Statistics** has been checked and found as per specification of the format circulated by the Dean, PGS vide his Memo No. PGS/A1/09/6926-90 dated 26.8.09.

**MAJOR ADVISOR**

**PROFESSOR AND HEAD**

## *Acknowledgements*

*On the accomplishment of the present study, I would like to take this opportunity to express my deepest sense of gratitude and words of appreciation towards those, who made this thesis possible. It gives me immense pleasure to gratefully thank the Almighty God whose grace has brought me here up to. Words will not be enough to express my sincere gratitude towards my Major Advisor **Dr. Hemant Poonia**, Assistant Professor (Mathematics), Department of Mathematics and Statistics, CCS HAU, Hisar for his kind guidance, constant encouragement, valuable suggestions and softness during the course of investigation and finalizing the dimensions of manuscript. His infinite capacity for hard work, remarkable patience and affectionate behaviour will always be an illuminating light to lead me in all my pursuits in future too. In my life, he is as the lamplight in the dark phases of life. With profound indebtedness, I owe my sincere thanks and deep regards to the members of my Advisory Committee, **Dr. Vikash Siwach**, Assistant Professor (Mathematics), **Dr. Vinay Kumar**, Assistant Professor (Statistics),*

***Dr. O. P. Sheoran**, Professor (Statistics), **Dr. Ram Niwas** Assistant Professor (Computer Section), and **Dr. Anil Duhani**, Assistant Scientist, Department of Agronomy PGS nominee for the interest taken to give me the light perspective of my research and valuable guidance for my future ventures. I am highly thankful to **Dr. Manju Tonk**, Professor (Mathematics) for providing necessary and sufficient facilities and support during the course of my study. My deep sentiments of gratitude to **Dr. Liaqat Ali** Assistant Professor, Mathematics (School of Sciences, Xi'an Technological University, Xi'an, China), **Dr. Alphonsa Mathew** Professor, Mathematics (St. Thomas College, Thrissur, Kerala,) and **Sujesh Areekara**. Ph.D. scholar (St. Thomas College, Thrissur, Kerala,) who help me in hard time of research work and give their valuable time. I present my heartfelt thanks to my friends, Sombir Lamba, Sandeep Banwala, Anand Kumar, Sahil Kalra, Preeti, Phagun, Rishu Ghandi and juniors Krishan, Priya, Priyanka, Parveen for their help and co-operation.*

*While travelling on the path of life and education, hands that have pushed me forth are the actual credit holders of this assignment and other achievements to come into future. Words fail to express my deepest sense of gratitude that I owe to my loving parents **Sh. Mewa Singh** and **Mrs. Bala Devi** who struggled throughout to provide me the best of everything in life. I have no words to express my indebted feelings for my wife **Neha Banger Boora** for her selfless love, being with me in all ups and down, ever willing help, understanding & continuous inspirations and morale boosting approach always envisioned me throughout my study period to achieve this goal with commitment.*

*Last but not the least, I am thankful to all those who have helped me directly or indirectly and whose names I forgot to mention in this endeavor. Finally, I am also grateful to CCS HAU, Hisar for extending all the facilities required during the course of investigation.*

*Jan, 2023  
Hisar*

*(Pardeep Kumar)*

## CONTENTS

CHAPTERS	TITLE	PAGE(S)
I	INTRODUCTION	1-4
II	REVIEW OF LITERATURE	5-12
III	MATERIALS & METHODS	13-62
IV	RESULTS AND DISCUSSION	63-156
V	SUMMARY & CONCLUSION	157-159
VI	BIBLIOGRAPHY	i-viii

## LIST OF TABLES

Table No.	Description	Page No.
3.1	Nanofluid properties	25
3.2	Hybrid nanofluid properties	25
3.3	Thermo-physical characteristics of some base fluids and solid particles	26
4.1	Comparison of $-\theta'(0)$ for various values of $Pr$ when all other parameters are held constant	67
4.2	The Nusselt number and Skin friction for various values of $M, Qp, Rd, Bi$ while other parameters remain fixed.	67
4.3	Fluctuation in $Nu_x Re_x^{-\frac{1}{2}}$ and $Cf_x$ with different values of $Dp$ and $H$	68
4.4	A comparison of $-\theta(0)$ for different values of $Pr$	78
4.5	The variation of the Nusselt number ( $Nu_x$ ), and Sherwood number for different values of $Ec, N_T, N_B$ while other parameters remain fixed.	78
4.6	The variation of the Nusselt number ( $Nu_x$ ), skin friction coefficient ( $Cf_x$ ) and Sherwood number for different values of $M, Rd, Bi, \lambda$ while other parameters remain fixed.	78
4.7	A comparison of $-\theta(0)$ for different values of $Pr$	87
4.8	The Comparison of Nusselt number, skin friction coefficient and Sherwood number with active case and passive case for different values of $M, Pr, K, N_t, N_b$ .	87
4.9	The variation of Nusselt number for various values of $\lambda$ and remaining parameter are held fixed	101
4.10	The variation of Nusselt number, skin friction coefficient and Sherwood number for different values $M, \lambda, \Gamma, Bi, Sr$ .	101
4.11	Effective parameter levels	102
4.12	Experimental design with response	102
4.13	ANOVA table	102
4.14	Sensitivity of response $Nu_x Re_x^{-\frac{1}{2}}$ when $A = 0$	103
4.15	Comparison of $-f''(0)$ for various values of $n, We, \Gamma$ and remaining parameters are held constant	116
4.16	Comparison of $-\theta'(0)$ for various values of $Pr$ and remaining parameters are held zero	116
4.17	The variation of the Nusselt number $Nu_x Re_x^{-\frac{1}{2}}$ , skin friction coefficient $Cf_x Re_x^{-\frac{1}{2}}$ and Sherwood number $Sh_x Re_x^{-\frac{1}{2}}$ for different values of $M, \Gamma, We, \lambda_1$ ( $n < 1$ )	116

<b>4.18</b>	The variation of the Nusselt number $Nu_x Re_x^{-\frac{1}{2}}$ , skin friction coefficient $Cf_x Re_x^{-\frac{1}{2}}$ and Sherwood number $Sh_x Re_x^{-\frac{1}{2}}$ for different values of $M, \Gamma, We, \lambda_1$ ( $n > 1$ )	117
<b>4.19</b>	The variation of $Nu_x, Cf_x$ and $Sh_x$ for $\lambda, Rd, Bi, M$	128
<b>4.20</b>	The variation of $Nu_x$ and $Shx$ for $N_T, N_B, Ec$	128
<b>4.21</b>	A comparison of $-\theta(0)$ for different values of $Pr$	138
<b>4.22</b>	Comparison of physical quantities	146
<b>4.23</b>	The Comparison of Nusselt number for different values of $Rd, QT, QE, \Theta_m, Bi, \phi_1, \phi_2$ , while other parameters remain fixed.	146
<b>4.24</b>	The variation in Skin friction for different values of $M, E, \lambda, \Gamma, \phi_1, \phi_2$ while other parameters remain fixed.	147

## LIST OF FIGURES

Figure No.	Description	Pages No.
1.1	(a) Natural flow and weather, (b) Power plants	1
1.2	Classification of fluid	2
3.1	Boundary Layer Flow	15
3.2	Heat transfer Modes	18
3.3	Physical flow diagram	32
3.4	A pictorial representation of the model	35
3.5	Physical flow diagram	40
3.6	Schematic configuration with coordinate system	43
3.7	Pictorial representation of the model	48
3.8	A pictorial representation of the model	51
3.9	Physical flow diagram	56
3.10	Pictorial representation of the model	60
4.1.1	Deviation in velocity with $Dp$ at different values of $M$	68
4.1.2	Deviation in micro rotation profile with $Dp$ at different values of $M$	69
4.1.3	Deviation in temperature profile with $Dp$ at different values of $M$	69
4.1.4	Deviation in temperature profile with $Dp$ at different values of $F_w$	70
4.1.5	Deviation in temperature profile with $Dp$ at different values of $Q_p$	70
4.1.6	Deviation in velocity profile with $Dp$ at different values of $K$	71
4.1.7	Deviation in velocity profile with $Dp$ at different values of $m$	71
4.1.8	Deviation in micro rotation with $Dp$ at different values of $K$	72
4.1.9	Deviation in velocity profile with $Dp$ at different values of $n$	72
4.1.10	Deviation in temperature profile with $Dp$ at different values of $Bi$	73
4.1.11	Deviation in velocity profile with $Dp$ at different values of $W$	73
4.1.12	Deviation in micro rotation with $Dp$ at different values of $n$	74
4.1.13	Deviation in Velocity with $Dp$ at numerous different values of $F_w$	74
4.1.14	Deviation in temperature profile with $Dp$ at different values of $R_d$	75
4.1.15	Fluctuation of Nusselt number with variation of parameters $M$ and $Dp$	75
4.1.16	Fluctuation of Skin friction with variation of parameters $K$ and $Dp$	76
4.2.1	Variation in velocity profile with different values of $M$ and $\lambda$	79
4.2.2	Variation in temperature profile with different values of $M$ and $\lambda$	79
4.2.3	Variation in temperature profile with $Ec$ at different values of $\lambda$	80
4.2.4	Variation in temperature profile with $Rd$ at different values of $\lambda$	80
4.2.5	Variation in temperature profile with $Nb$ at different values of $\lambda$	81

<b>4.2.6</b>	Variation in concentration profile with $Nb$ at different values of $\lambda$	81
<b>4.2.7</b>	Variation in temperature profile with $Nt$ at different values of $\lambda$	82
<b>4.2.8</b>	Variation in concentration profile with $Nt$ at different values of $\lambda$	82
<b>4.2.9</b>	Variation in temperature profile with $Sc$ at different values of $\lambda$	83
<b>4.2.10</b>	Variation in concentration profile with $Sc$ at different values of $\lambda$	84
<b>4.2.11</b>	Variation in temperature profile with $Bi$ at different values of $\lambda$	88
<b>4.3.1</b>	Velocity at various $Fw$ and $M$ values under active and passive control	89
<b>4.3.2</b>	Variation in $G(\eta)$ with different values of $K$ and $Fw$ for both scenarios of active and passive control	90
<b>4.3.3</b>	Fluctuation in $\theta(\eta)$ with different values of $QE$ and $M$ for active and passive control cases	91
<b>4.3.4</b>	Variation in $\theta(\eta)$ at significantly different values of $\theta_m$ and $Rd$ for active and passive control cases	92
<b>4.3.5</b>	Fluctuation in $\varphi(\eta)$ at different values of $Nt$ and $Fw$ in the presence of active and passive control	93
<b>4.3.6</b>	Fluctuation in concentration profile for different values of $Kr$ and $Q_E$ for active and passive control cases	94
<b>4.3.7</b>	Variation in $\varphi(\eta)$ at significantly different values of $Bi$ and $E_A$ for active and passive control cases	95
<b>4.3.8</b>	Contour idiographic of $Nu_x$ in relation to magnetic field and thermophoretic diffusion	96
<b>4.3.9</b>	Surface idiographic of $Nu_x$ in relation to magnetic field, Biot number and thermophoretic diffusion	97
<b>4.3.10</b>	Plots of residuals for distorting stream	97
<b>4.3.11</b>	Fluctuation of skin friction along with $Nt$ for active and passive control cases.	98
<b>4.3.12</b>	Fluctuation of Nusselt number along with $m^*$ for active and passive control cases.	99
<b>4.3.13</b>	Fluctuation of Nusselt number along with parameters $Nb$ and $Bi$ in the presence of active and passive control	104
<b>4.4.1</b>	Velocity profile fluctuation against $\xi$ for values of $\lambda$ , and $\Gamma$ .	105
<b>4.4.2</b>	Velocity profile fluctuation for numerous values of $M$ and $P r$	106
<b>4.4.3</b>	Temperature distribution fluctuation against $\xi$ for $\Gamma$ and $P r$	107
<b>4.4.4</b>	Concentration profile fluctuation against $\xi$ for values of $\Gamma$ and $Ch$	108
<b>4.4.5</b>	Motile concentration profile fluctuation against $\xi$ for $\Gamma$ and $Ch$	109
<b>4.4.6</b>	Variation in skin friction against $Pe, Pr, M, Bi$	110
<b>4.4.7</b>	Variation in Nusselt number against $\phi, M, Bi$	111
<b>4.4.8</b>	Variation in Sherwood number against $Bi, M, \phi$	112
<b>4.4.9</b>	Contour plots for $Nu_x Re_x^{-\frac{1}{2}}$	112

4.4.10	Surface plots for $Nu_x Re_x^{-\frac{1}{2}}$	113
4.4.11	Residual versus Fitted value of $Nu_x Re_x^{-\frac{1}{2}}$	113
4.4.12	Bar charts depicting the sensitivity of $Nu_x Re_x^{-\frac{1}{2}}$	118
4.5.1	Variation in velocity profile with simultaneous effect of M and $\lambda_1$ for both shearing thinning and shear thickening occurrence.	119
4.5.2	Simultaneous effect of $W_e$ and $\lambda_1$ for both $n < 1$ and $n > 1$ on velocity profile	120
4.5.3	Temperature distribution fluctuation with simultaneous effect of M and $\lambda_2$ for both the shearing thinning and shear thickening instances	121
4.5.4	Temperature distribution variation with simultaneous effect of $Pr$ and $\lambda_2$ for both shearing thinning and shear thickening situations	122
4.5.5	Concentration profile fluctuation against simultaneous effect of Ch and $\lambda_3$ for both shearing thinning and the shear thickening cases.	123
4.5.6	Motile Concentration profile fluctuation with simultaneous effect of $Lb$ and $\lambda_4$ for both the shearing thinning and shear thickening situations	124
4.5.7	Variation in $Nu_x Re_x^{-\frac{1}{2}}$ and $Cf_x Re_x^{-\frac{1}{2}}$ for different values of $W_e$ and $\lambda_2$ for both dilatant and pseudo plastic fluids	125
4.5.8	Variation in $Nu_x Re_x^{-\frac{1}{2}}$ , and $Sh_x Re_x^{-\frac{1}{2}}$ for different values of $Pe, M$ and $\lambda_3$ for dilatant fluid and pseudo plastic fluid.	129
4.6.1	Velocity profiles with varying values of M with $M_1$	129
4.6.2	Velocity profiles with varying values of $\lambda_1$ with $M_1$	130
4.6.3	Variation in concentration profile with $M_1$ at different values of M	130
4.6.4	Variation in temperature profiles with $M_1$ at different values of M	131
4.6.5	Variation in temperature profiles with $M_1$ at different values of $Ec$	131
4.6.6	Variation in temperature profiles with $M_1$ at different values of Rd	132
4.6.7	Variation in temperature profiles with $M_1$ at different values of $N_B$	132
4.6.8	Variation in concentration profiles with $M_1$ at different values of $N_B$	133
4.6.9	Variation in temperature profile with $M_1$ at different values of $N_T$ .	133
4.6.10	Variation in concentration profiles with $M_1$ at different values of $N_T$	134
4.6.11	Fluctuation of temperature profiles along with variation of $\lambda_3$ and $M_1$	134
4.6.12	Fluctuation of volume fraction profiles along with variation of Sc and $M_1$	135
4.6.13	Fluctuation of temperature profiles along with variation of Bi and $M_1$	135
4.6.14	Fluctuation of temperature profiles along with variation of $\lambda_2$ and $M_1$ .	136
4.6.15	Fluctuation of $Nu_x$ along with $Nt, Nb$	136
4.6.16	Fluctuation of $Nu_x$ along with $Rd, Bi$	137
4.6.17	Sherwood number's fluctuation with variation of $Nt$ and $Nb$	139

<b>4.7.1</b>	Fluctuation of Velocity profile along with variation of $M$ .	139
<b>4.7.2</b>	Fluctuation of temperature profile along with variation of $M$ .	140
<b>4.7.3</b>	Fluctuation of concentration profile along with $M$ .	140
<b>4.7.4</b>	Fluctuation of velocity profile along with variation of $\lambda$ .	141
<b>4.7.5</b>	Fluctuation of temperature profile along with variation of $\lambda$ .	141
<b>4.7.6</b>	Variation of velocity profiles along with $Pr$ .	142
<b>4.7.7</b>	Variation of temperature profiles along with $Pr$ .	142
<b>4.7.8</b>	Temperature profiles along with variation of $Bi$ .	143
<b>4.7.9</b>	Concentration profiles along with variation of $Bi$ .	143
<b>4.7.10</b>	Fluctuation of concentration profiles along with $Sr$	147
<b>4.8.1</b>	Deviations in $F(\xi)$ with $M$	148
<b>4.8.2</b>	Deviations in $F(\xi)$ with $E$	148
<b>4.8.3</b>	Deviations in $F(\xi)$ with $\Gamma$	149
<b>4.8.4</b>	Deviations in $F(\xi)$ with $\lambda$	149
<b>4.8.5</b>	Deviations in $G(\xi)$ with $M$	150
<b>4.8.6</b>	Deviations in $G(\xi)$ with $E$	150
<b>4.8.7</b>	Deviations in $G(\xi)$ with $\Gamma$	151
<b>4.8.8</b>	Deviations in $G(\xi)$ with $\lambda$	151
<b>4.8.9</b>	Deviations in $\theta(\xi)$ with $M$	152
<b>4.8.10</b>	Deviations in $\theta(\xi)$ with $E$	152
<b>4.8.11</b>	Deviations in $\theta(\xi)$ with $\lambda$	153
<b>4.8.12</b>	Deviations in $\theta(\xi)$ with $Q_E$	153
<b>4.8.13</b>	Deviations in $\theta(\xi)$ with $Q_T$	154
<b>4.8.14</b>	Deviations in $\theta(\xi)$ with $R_d$	154
<b>4.8.15</b>	Deviations in $\theta(\xi)$ with $\theta_m$	155
<b>4.8.16</b>	Deviations in $\theta(\xi)$ with $Bi$	155
<b>4.8.17</b>	Deviations in $\psi(\xi)$ with $E_A$	156
<b>4.8.18</b>	Deviations in $\psi(\xi)$ with $K_r$	156
<b>4.8.19</b>	Deviations in $\psi(\xi)$ with $\delta$	156

<b>NOMENCLATURE</b>			
$c$	Dimensional constant	$u, v$	Velocity components ( $ms^{-1}$ )
$W_c$	Maximum cell swimming speed	$B_0$	Uniform magnetic field ( $Am^{-1}$ )
$Ec$	Eckert number	$T_\infty$	Ambient fluid temperature
$N$	Microorganism concentration	$N_0$	Reference concentration of microorganism
$C$	Fluid concentration	$C_0$	Reference nanoparticle concentration
$T$	Fluid temperature ( $K$ )	$N_\infty$	Ambient concentration of microorganisms
$N_w$	The concentration of microorganisms near the wall	$T_0$	Reference temperature
$C_w$	Nanoparticle concentration near the wall	$x, y$	Cartesian coordinates ( $m$ )
$T_w$	Wall fluid temperature	$Pe$	Bioconvection Peclet number
$Cf_x$	Local drag coefficient	$Nn_x$	Local motile density
$Lb$	Bioconvection Lewis number	$Sh_x$	Local Sherwood number
$k_r$	Reaction rate constant ( $s^{-1}$ )	$Nu_x$	Local Nusselt number
$b$	Chemotaxis constant	$E_0$	Uniform electric field
$D_B$	Chemical molecular diffusivity ( $m^2s^{-1}$ )	$D_m$	Microorganism diffusion coefficient ( $m^2s^{-1}$ )
$Kr$	Chemical reaction parameter	$C_\infty$	ambient nanoparticle concentration
$Pr$	Prandtl number	$s_1, s_2, s_3$	Stratification parameters
$E$	Electric field parameter	$M$	Magnetic field parameter
$C_p$	Specific heat	$Le$	Lewis number
<b>Greek Symbols</b>			
$\vartheta$	Kinematic viscosity ( $m^2s^{-1}$ )	$\rho$	The density of the fluid ( $kgm^{-3}$ )
$\eta$	Dimensionless variable	$\kappa$	Thermal conductivity ( $Wm^{-1}K^{-1}$ )
$\Omega$	Microorganism concentration difference parameter	$\sigma$	Electrical conductivity ( $kg^{-1} m^{-3} s^3 A^2$ )
$\phi$	Nanoparticle volume fraction	$\alpha$	Thermal diffusivity ( $m^2s^{-1}$ )
<b>Subscripts</b>			
$nf$	Nanofluid	$f$	Conventional fluid
$bf$	Base fluid	$s_1$	Frist solid particle
$s_p$	Solid particle	$s_2$	Second solid particle
$\phi_1$	volume fraction first Nanoparticle	$\phi_2$	volume fraction second Nanoparticle

#### 1.1 Fluid dynamics: An Overview

Fluid dynamics or hydrodynamics is a branch of science and applied mathematics that deals with the study of the motion of fluid in reference to its surrounding. The first pioneer work on fluid mechanics was carried out by Greek mathematician Archimedes who gave his fundamental principle known as the “Archimedes principle” to examine the concept of fluid statistics and buoyancy.

Fluid mechanics deals with the study of fluids, whether at rest or in motion. It is being utilized in numerous technological developments, for example, the designing system of canals and dams, pipe systems in chemical plants, lubricant systems, aerodynamic of automobiles, supersonic aircraft, ducting and piping utilization in water and air condition systems, and many others. The cataloging of fluid mechanics is separated into several sorts: for example, the study of fluid motion with incompressibility is said to be hydro-dynamics, the study of fluid flows in channels/pipes is named hydraulics. The study of fluid flows with the variation of density is identified as gas-dynamics, and the study of gases flow over bodies is characterized as aero-dynamics. Nevertheless, fluid mechanics plays a very important role in the advancement of science and technology. Several naturally happening wonders are governed by philosophies of fluid mechanics, like the rain cycle, the rise of groundwater to the top of plants, ocean waves, winds, etc. Some examples are given below, shown in figures 1.1 (a) and 1.1(b).



**Figure 1.1 (a) Natural flow and weather**

<https://unsplash.com>



**Figure 1.1 (b) Power plants**

<https://www.eia.gov>

It was observed that the mass and heat transfer effects on magneto hydrodynamics convective flow along with heat transference and remarkable importance in each anxiety field. Due to this reason, several scientists and technologists have been attracted to study the magnetohydrodynamic convective flow. Thus, the results of the items may have applied with inordinate exactness in particular fields.

**Fluid**

Fluid is a substance that deforms continuously under applied shear stress. A branch of fluid mechanics is fluid dynamics which describes the influence of forces on the flow of fluids. Any real fluid that moves with the solid boundary will incur shear stress on that boundary. The fluid speed at the boundary is zero when no-slip condition imposes, but a little bit above the boundary, the speed of the flow must be equal to that fluid. The area in between these spaces is called the boundary layer.

Newton (1642-1727) suggested the laws of viscosity on fluids, known as Newtonian fluids. His hypothesis has brought the theory of perfect fluid. For a Newtonian fluid, the shear stress, at a surface element parallel to a flat plate, at the  $y$  is given by:

$$\tau(y) = \mu \frac{\partial u}{\partial y} \tag{1.1}$$

where  $y$  fluid velocity above the boundary,  $u$  is the fluid velocity with the boundary, and  $\mu$  is the dynamic viscosity of the fluid. Particularly, the wall shear stress is expressed as:

$$\tau_w = \mu \frac{\partial u}{\partial y} |_{y=0} \tag{1.2}$$

those fluids that maintain a linear relation between shear stress and viscosity are called Newtonian fluids. Non-Newtonian fluids do not express flow characteristics by a single constant viscosity value.

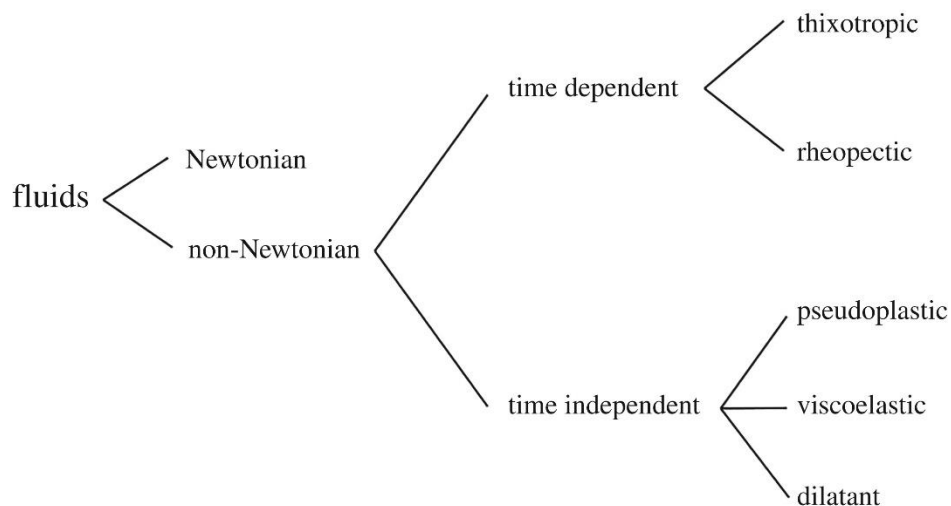


**Figure 1.2: Classification of fluid**

## **1.2 Nanofluids: An Overview**

Conventional heat transfer fluids, for instance, water, oils, ethylene glycol and their mixtures, etc., possess low thermal conductivity. Since these fluids' thermal conductivity plays a significant role in determining the heat transfer coefficient between heat transfer medium and surface of heat transfer. To overcome this problem, many researchers and scientists worked on to augment the thermal conductivity of conventional fluids. Maxwell (1873) was the first who has done remarkable work to increase the thermal conductivity of conventional fluids. Maxwell incorporated some impurities with dimensions of a millimetre into conventional fluids to increase thermal conductivity. There were many problems raised by adding these impurities, such as additional pressure drops, erosion in pipes, clogging, etc. These methods were partially failed but gave some idea to other researchers to boost thermal conductivity of base fluid.

After a century, Choi and Eastman (1995) introduced a smart fluid known as nanofluid, which refers to the colloidal suspension of submicronic solid particles known as nanoparticles (metals, amalgams, carbon nanotubes, semiconductors, etc.) with diameter 1-100 nm into regular base fluids. Choi showed experimentally that incorporating the nanoparticles into the base fluid (water, oil, ethylene glycol, etc.) enhanced the thermal conductivity as well as lead to the heat transfer enhancement.

The word “Nano” was adopted from the Greek word dwarf. Generally, nano is a unit prefix with the numerical value of “one billionth” or the reciprocal of a billion. Preparation of nanofluids is the first key step in experimental studies with nanofluids. Nanofluids are not simply liquid-solid mixtures. Some special requirements are essential e.g. even and stable suspension, durable suspension, negligible agglomeration of particles, no chemical change of the fluid, etc. Nanofluids are produced by dispersing nanometer-scale solid particles into base liquids such as water, ethylene glycol (EG), oils, etc. In the synthesis of nanofluids, the single step method and two step method are mainly two techniques used to produce nanofluids.

Due to their wide range of functions, nanofluids got tremendous interest among scientists and researchers. Nanofluids are used as a coolant in electronic devices, automobiles, heavy-duty motors and in manufacturing companies to increase the performance of machines, save energy and emission reduction. Nanofluids also have several clinical uses, for example, in cancer treatment and drug delivery. In the past few decades, nanofluids emerged as a new generation of coolant due to fast growth in nanotechnology.

## **1.3 Justification of the study**

Navier-Stokes equations are one of the well-known equations that govern many outflow phenomena. These types of equations are the simultaneous structure of PDE's (partial differential equations) that are extremely non-linear. Boundary layer equations are its easiest version, presenting a strong insight to certain outflow analysis. Depending upon the outflow

nature being viscoelastic or viscous, unsteady or steady, three-dimensional or two-dimensional, compressible or incompressible, the outflow behavior has a vast range of solution procedures and mathematical variations and nowadays, this is stimulating investigation field in computational fluid dynamics and applied mathematics.

In engineering and applied mathematics, the boundary layer technique has become a researchable topic and the most powerful approach. Heinrich Blasius analyzed the problem of *the* laminar boundary layer through a flat plate. Blasius sorted out the problem by converting PDE's (partial differential equations) into ODE's (ordinary differential equations) by choosing an independent variable; such types of variables are called the similarity variable. First time Sakiadis investigated the laminar boundary layer flow through a movable continuous surface by two integral and numerical methods. This investigation established important differences in the boundary layer behavior in a continuous movable fluid through a steady surface. A theoretical and experimental analysis of the boundary layer problem on a continuously movable surface.

The work on fluid flow through a continuous stretching/shrinking sheet has got substantial consideration due to its applications in assorted areas of industries and engineering. The stretching sheet velocity has a certain and optimistic effect on the excellence of the furnished products in the polymer and fabric industry. The stretching velocity can be linear, polynomial, exponential and hyperbolic, depending upon the nature of the problem and its industrial application. These processes involve processing polymers, manufacturing plastic sheets, paper production and concentration mechanism of metal plates and many more by Fisher (1976) and Altan *et al.* (1983).

### **Objectives of the present study**

The thermal conductivity of nanofluids gets affected by various factors such as nanoparticles volume fraction and material, shape and size of nanoparticles used, base fluid, temperature and acidity of fluid. The effect of nanoparticles interfacial layer, Brownian motion of nanoparticles and clustering of nanoparticles are also other important factors to be looked upon while talking about the thermal conductivity of nanofluids. Due to enhanced thermal properties such as thermal diffusivity, viscosity, mass diffusivity, thermal conductivity and convective heat transfer coefficients in comparison to those of base fluids, nanofluids have a wide range of applications in industrial and engineering fields.

Keeping in view the importance of high thermal conductivity and wide application of heat transfer, the study was planned with the following objectives:

- i. To study heat transfer in nanofluids over stretching sheet under the various effects
- ii. To determine heat transfer in nanofluids over a stretching cylinder with various effects
- iii. To compare the effects of heat transfer in nanofluids over conformation

## CHAPTER – II

### REVIEW OF LITERATURE

---

The geometry of the objects in which the fluid is travelling determines the properties of fluid flow entirely. Sometimes the simplest objects, such as sheets, cylinders, plates, and cones, etc., produce complicated flows. The size, direction, velocity, and fluid properties all have an impact on the objects with a specified shape for the flow field and associated forces. The study of fluid flow over submerged bodies has a wide range of practical applications, but the transmission of heat and mass through stretching sheets, stretching cylinders, Riga plate, cones, etc. serves the most important function in engineering and technology. In many engineering and research fields, fluid flow analysis over various geometries is crucial. Over the past few decades, a significant quantity of theoretical research addressing such tasks under the effect of relevant parameters was demonstrated. As a result, the bulk of publications discusses these types of research and is presented under the following headings:

- 2.1 Review on Flow past a Stretching sheet
- 2.2 Review on Flow past a Stretching Cylinder
- 2.3 Review on Flow past a Riga Plate
- 2.4 Review on Flow past a Rotating Disc

#### **2.1 Review on Flow past a Stretching sheet**

The work on fluid flow through a continuous stretching/shrinking sheet has got substantial consideration due to its applications in assorted areas of industries and engineering. The stretching sheet velocity has a certain and optimistic effect on the excellence of the furnished products in the polymer and fabric industry. The stretching velocity can be linear, polynomial, exponential and hyperbolic, depending upon the nature of the problem and its industrial applications.

Rosseland (1931) provided the Rosseland approximation for linear and non-linear radiation and characterized the flow problem under the influence of thermal radiation. Brinkman (1951) started to have a viscous dissipation effect and investigated how the heat affected capillary flow. Later, Brinkman (1952) discovered the formula for solution-suspension viscosity at a limited concentration.

Crane (1970) studied the mathematical analysis of flow over a linearly stretching sheet and presented an exact analytical solution that became a foundation for later theoretical investigations.

Gupta and Gupta (1977) added injection/suction on the surface and investigated heat and mass transfer over a linearly stretching sheet.

Elbashbeshy (2001) looked at how suction affected laminar flow across an increasing exponential stretched surface.

Azzam (2002) inspected the effect of radiation on the magnetohydrodynamic electrically conducting mixed free convection steady laminar boundary layer flow of viscous fluid through a movable semi-infinite vertical plate for a huge temperature difference.

Sajid and Hayat (2008) investigated the effect of thermal radiation on the boundary layer flow caused by an exponentially stretched sheet.

El-Aziz (2009) investigated the mixed convective flow of a micro-rotating fluid propelled by a stretched surface.

Hamad *et al.* (2011) investigated the convective flow, and heat transfer of a semi-infinite vertical stretched sheet across an incompressible viscous nanofluid in a magnetic field. The effects of relevant parameters on flow, heat transfer, Nusselt number, and the skin friction coefficient were explored.

Aziz and Khan (2012) explored the natural convection flow of nanofluid through convective boundary conditions.

Ahmad and Mustafa (2016) investigated heat transfer by using the nanoparticles Silver, copper, copper oxide, titanium oxide, and aluminum oxide.

Khan *et al.* (2016) investigated the flow and heat transmission of copper nanoparticles made of ethylene glycol and water between two parallel squeezing discs with suction/injection effects. These resulting equations were then numerically solved using the Runge-Kutta-Fehlberg (RKF) method, depending on the suction/injection parameter Hartmann number, squeezing number, and nanoparticle volume fraction.

Ahmad *et al.* (2016) discussed the exponentially expanded sheet-induced rotating flow of nanofluids. Silver (Ag), Copper (Cu), Copper oxide (CuO), Titanium oxide ( $TiO_2$ ), and Aluminum oxide were five different forms of nanoparticles that were taken into consideration. The thermal boundary layer was examined using convective boundary conditions.

Kambhatla *et al.* (2016) used the higher convected Maxwell model to simulate the MHD flow of ethylene glycol with four distinct nanoparticles. They investigated various volume fractions is the impact of the addition of Cu, Ag,  $Al_2O_3$ , and  $TiO_2$  nanoparticles on the base fluid (ethylene glycol). The influence of variable characteristics, viscoelasticity, and wall motion on Ag-ethylene glycol nanofluid was investigated using relevant non-dimensional factors and shooting techniques.

Mahanthesh *et al.* (2016) studied nonlinear radiative heat transfer in a nonlinearly stretching sheet with convective boundary conditions in a three-dimensional MHD flow of water-based nanofluid, that contain copper, aluminum oxide, and titanium dioxide. Using the shooting strategy and Runge-Kutta-Fehlberg fourth- and fifth-order method, the resulting equations were numerically solved.

Halim *et al.* (2017) considered an incompressible Williamson nanofluid's continuous stagnation point flow towards a horizontal linearly stretching/shrinking sheet with active and passive controls on the wall mass flux. The `bvp4c` package in MATLAB was used to solve the reduced system of ordinary differential equations that result from reducing the governing partial differential equations into a similarity transformation.

Hayat *et al.* (2017) investigated the impacts of heat and mass transfer in a viscous nanofluid saturating a porous medium flowing past an exponentially radiated stretched sheet in a magnetohydrodynamic (MHD) flow. It was highlighted that stratification had an impact on the local Sherwood and Nusselt numbers.

Hussain *et al.* (2017) worked on MHD tangent hyperbolic fluid flow thermophysical properties across a non-linear stretching sheet with viscous dissipation and convective boundary conditions. The homotopy analysis and shooting methods were used to solve the boundary layer ordinary differential equations.

Khan *et al.* (2018) analyzed the cross-fluid flow in two dimensions approaching the stretchable sheet with chemical reactions, nonlinear thermal radiation, and heat generation in given model.

Ali *et al.* (2019) investigated the flow of a microorganism that restricts magnetohydrodynamic (MHD) bioconvective micro-polar nanofluid. Micro-polar nanofluid boundary layer flow in 2-D laminar bioconvective flow was numerically solved. The variational finite element method was then used to solve the changed equations.

Hayat *et al.* (2019) described the three-dimensional magnetohydrodynamic flow of nano fluid by a nonlinear stretchable surface with active and passive nanoparticle controls. The flow was produced using a bidirectional nonlinear stretching surface with impact of thermophoresis and Brownian diffusion, as well as the convective condition of heat transmission, were used. When combined with a nonzero normal flux condition, a zero normal flux condition was described as an impulse that drives the particles away from the surface.

Ali *et al.* (2020) explored the impact of a magnetic dipole on the heat transfer phenomena of different nano-particles Fe (ferromagnetic) and  $\text{Fe}_3\text{O}_4$  (Ferrimagnetic) dispersed in a base fluid (60% water + 40% ethylene glycol) on micro-polar fluid flow over a stretching sheet. A magnetic dipole in the presence of the ferrites of nano-particles plays an important role in controlling the thermal and momentum boundary layers.

Bilal (2020) studied the heat and mass transfer using magneto-micropolar electrically conducting nanofluid flow over a linearly stretching sheet with convective boundary conditions, joule heating effects, and non-linear thermal radiation was included in the energy equation.

Ullah *et al.* (2021) examined the combined effects of boundary layer flow and heat transfer caused by a nonlinearly stretched sheet with a variable thickness in the presence of an electric field due to thermal radiation, chemical reaction, viscous dissipation, and ohmic heating for electrical conductivity of nanofluid.

Ramzan *et al.* (2021) explored the analytical investigation of the magnetohydrodynamic flow of an Ag, MgO water hybrid nano fluid under slip conditions across an extending surface. The effects of thermal radiation and Joule heating were presented. The resultant higher-order ordinary differential equations were solved using a powerful analytical technique known as HAM.

Areekara *et al.* (2021) determined the numerical and statistically study of the stratification effects of bioconvective electromagnetohydrodynamic flow past a stretching sheet using water-based CNT. A system of ordinary differential equations by applying similar transformations, and the `bvp5c` (MATLAB built-in function) algorithm was used to solve the problem numerically.

Wakif *et al.* (2021) explained that the heat transfer was proportionate with the Nusselt number and varied with the radius of the nanoparticles and the spacing between them and also that increase in inter-particle space can increase viscosity, and decreases the velocity.

Ali *et al.* (2021) explored the function of nanoparticle's diameter darcy forchheimer flow over a cylinder with the effect of magnetic field and thermal radiation. It was found that when nanoparticles have a large radius, the rate of friction drag coefficient declines to cause a rise in the magnetic field's inclination angle. It was also observed that a rise in temperature distribution increases the viscosity and produces inter-particle space, which drops the velocity profile.

Dawar *et al.* (2022) determined the significance of Lorentz forces on Jeffrey nanofluid flows over a convectively heated flat surface featured by multiple velocity slips and dual stretching constraint. It was found that the velocity stretching factor rises in both directions of the velocity profiles. Furthermore, this increasing impact was dominant for the velocity distribution along the y-direction as compared to the velocity field along the x-direction.

## **2.2 Review on Flow past a Stretching Cylinder**

Sulochna and Sandeep (2016) studied the behaviour of the Cu-water nanofluid's stagnation point flow and heat transfer towards horizontal and exponentially permeable stretching/shrinking cylinders in the presence of suction/injection, a heat source, and nanoparticle form. Using a similarity transformation, the governing boundary layer equations were converted to nonlinear ordinary differential equations, which were then numerically solved with the help of the `bvp4c` solver by using MATLAB software.

Azam *et al.* (2017) explored the unsteady MHD stagnation point flow of Carreau nanofluid through a contracting/expanding cylinder with the effect of nonlinear thermal radiation.

Panday and Kumar (2017) examined the impact of heat transmission on the flow of Cu-water nanofluid past a stretching cylinder. The relevant ODEs with additional boundary conditions have been solved using the shooting process, and the nonlinear numerical approach is known as RKF 4-5th.

Khan *et al.* (2017) developed a mathematical model to inspect the MHD flow of viscous fluid caused by a stretching Cylinder. These sets of equations were solved utilizing RKF technique. Effects of friction heating of Nano-particles and Ohmic heating were also observed.

Salahuddin *et al.* (2017) explained the effects of magnetic field and nanoparticles on the generalised non-Newtonian Carreau fluid flow in two dimensions across a permeable cylindrical surface with the no-slip condition in the presence of heat generation/absorption, thermal stratification, and thermal radiation.

Mishra and Panday (2018) analyzed the impact of viscous-ohmic and heat generative/absorptive on MHD flow against a stretching cylinder in the regions of suction and injection. They added silver nanoparticles into the water to improve the heat transfer rate. The system of acquired ODEs was elucidated with assisting boundary conditions by utilizing RKF technique via the shooting algorithm.

Pordanjani *et al.* (2019) used the Response Surface Methodology (RSM) to find a polynomial equation that connects the three parameters for entropy generation, the Bejan number and the Nusselt number. The sensitivity of responses to factors was assessed.

Shojaei *et al.* (2019) studied a second-grade fluid flow through a stretching cylinder using an analytical technique. The Soret and Dufour effects were also explored. Thermal radiation was used to heat the flow, and this problem was solved using the homotopy analysis method (HAM). The impact of the aforementioned physical characteristics on the velocity, temperature, and concentration profiles was examined.

Waqas *et al.* (2020) examined the bioconvection phenomena in a 3D Maxwell nanofluid flow with the help of properties of mixed convection, activation energy, motile microorganisms, and singular boundary conditions. Using MATLAB, a numerical method based on a shooting technique was used to create a `bvp4c` solver.

Khan *et al.* (2020) analyzed Arrhenius activation energy-based MHD mixed convection nanofluid, thermal radiation, heat absorption/generation, buoyancy effects, and binary chemical reactions were also involved in its flow through a porous medium.

Islam *et al.* (2020) examined the thermal effect of a mixed convection flow of spinning Maxwell nanofluid caused by a rotating and bidirectional stretching cylinder. The

impact of internal heat source/sink and Joule heating under a uniform magnetic field and convective boundary conditions were analyzed. It was observed that temperature jumps up with the rising of Eckert number, Brownian motion, and thermophoresis parameter values and jumps down with the rising of Prandtl number and heat sink values.

Rashid *et al.* (2021) worked on Ag –  $TiO_2$  /water-based nanofluid flow toward a horizontal stretching shrinking cylinder. Three distinct forms of Ag and  $TiO_2$  were used in the investigation (sphere, blade, and lamina).

Xuan *et al.* (2021) identified the sensitivity analysis with the optimal mixture ratio 40: 40: 20 ( $Al_2O_3$ : $TiO_2$ : Cu). It was found that the lowest sensitivity was observed to viscosity and the highest sensitivity to thermal conductivity.

Mallawi and Ullah (2021) explained the study of Carreau nano fluid with different parameters and geometry to analyze the heat transfer.

Jagadha *et al.* (2021) explored a mathematical representation of the MHD radiative Carreau nanofluid for laminar, steady, and incompressible flow under the influence of heat generation/absorption and radiation.

### **2.3 Review on Flow past a Riga Plate**

Gailitis (1961) initially established a gadget called a Riga plate, which was identified as an electromagnetic actuator that includes electrodes and static magnets positioned on a smooth area. The Riga plate can be utilized as a useful agent for the decrement of pressure drags and skin friction of submersible warships by averting the separation of the boundary layer.

Pantokratoras (2011) extended his work with the Riga plate. The electromagnetic actuator is either applied with uniform velocity or positioned with a constant free stream. In other words, the flow towards the Riga plate was Blasius and Sakiadis. The outcomes were obtained by solving the continuity and momentum equations with the help of numerical simulation.

Ahmad *et al.* (2016) investigated the phenomenon of steady convective flow and nanofluid heat transfer past a vertical Riga plate under a strong suction effect. They additionally considered the influence of thermophoresis and zigzag motion characteristics of nanoparticles.

Hayat *et al.* (2016) discussed the heat transfer features of nanofluid flow induced by the Riga plate by retaining the effect of heat generation/absorption and observed that the Riga plate was convectively heated with variable width. Nanofluid attributes were discussed by incorporating the Brownian motion and mechanics of thermophoresis.

Ayub *et al.* (2016) described the electrically conducting nanofluid boundary layer flow over a Riga plate. The Brownian motion and thermophoresis effects caused by the nanofluid and the Grinberg term for the wall parallel Lorentz force caused by the Riga plate

in the presence of slip effects are combined in the numerical model. The shooting method was used to present the problem's numerical solution.

Ahmad *et al.* (2017) concentrated on the flow analysis through a vertical convective Riga plate. The two-phase nanofluid model with the action of Brownian motion and thermophoresis was chosen for the study.

Ahmed *et al.* (2017) inspected the squeezing flow and heat transfer of water containing carbon nanotubes (CNT) between two Riga plates. The flow model was tackled analytically using ADM and numerical RKF procedure. The factors of dissipation and thermal radiation were also incorporated in equations.

Hayat *et al.* (2017) considered the Riga plate to discuss EMHD nanofluid flow with the effects of the chemical reaction and thermal radiation. The obtained set of PDEs was altered into a non-dimensional form of ordinary equations. The Homotopy technique was performed for computations and numerical data and compared with the exact solutions.

#### **2.4 Review on Flow past a Rotating Disc**

The rotating disc flow problem was first proposed by Von Karman and Angew (1921). To convert the governing system of partial differential equations into the system of ordinary equations, similarity transformations were introduced. Numerous scholars continued Von Karma's work on rotating disc issues while taking theoretical considerations into account.

Bödewadt *et al.* (1940) described the boundary layer approximation of rotating flow over disc.

Turkyilmazoglu (2012) investigated heat transfer and hydromagnetic flow over a stretchable rotating disc.

Rashidi *et al.* (2013) addressed the entropy generation analysis in the hydromagnetic flow of nano liquid flow over porous disc.

Turkyilmazoglu and Senel (2013) investigated flow and heat transport across a rough porous rotating disc.

Rashidi *et al.* (2014) explained the effects of hydromagnetic slip flow on entropy formation caused by a permeable rotating disc.

Hayat *et al.* (2015) found the solutions of MHD Cu-water nano liquid flow problem due to rotating disc.

Babu and Sandeep (2016) discussed on the problem of hydromagnetic nano liquid flow across a cylindrical stretching surface with slip effects.

Raju *et al.* (2016) performed a numerical analysis of hydromagnetic Cu-kerosene nanofluid passing through a cone.

Xun *et al.* (2016) performed a heat transfer analysis of an Ostwald-de liquid moving through a rotating disc with a varying thickness.

Hayat *et al.* (2017) were able to derive analytical answers for the MHD Maxwell nano liquid flow over a porous stretched surface.

Hayat *et al.* (2017) studied the numerical analyses of the MHD viscous Nano fluid flowed via spinning disc considering the slip effects.

Imtiaz *et al.* (2017) studied the characteristics of hydromagnetic slip flow around a revolving disc of varied thickness.

Hayat *et al.* (2017) employed the HAM method to study the influence of radiative flow owing to a rotating disk.

Mustafa (2017) investigated the slip effect on MHD flow of nano fluid over an RD using the Buongiorno model.

Yin *et al.* (2017) studied the flow and heat transmission of nanofluids over a rotating disc with a consistent stretching rate and included the three different types of nanoparticles  $Cu$ ,  $Al_2O_3$ , and  $CuO$  and water-based nanofluids.

Khan *et al.* (2018) described simulations of heat transport and magneto-nanofluid flow near a rotating disc. Brownian motion and thermophoresis, two novel characteristics, were applied. The energy balance equation retains the effect of heat dissipation. For the purpose of computing similarity solution, the Keller-Box method was used.

Ahmed *et al.* (2019) examined the Maxwell nanofluid rotational stagnation-point flow across a porous rotating disc that was radially stretching and shrinking. Thermophoresis and Brownian motion of the nanoparticles was monitored using an original revision of Buongiorno's nanofluid model. The governing nonlinear problem's numerical integration is implemented using the built-in numerical algorithm `bvp4c`.

Kumar and Singh (2021) studied the thermal radiation and electrical magneto hydrodynamics (EMHD) phenomena in an infinitely spinning disk's convective boundary layer flow of a nanofluid.

Usman *et al.* (2021) studied the improvement of heat and mass transmission for hybrid nanofluid flow a rotating disc with single-wall and multiwall carbon nanotubes (SWCNTs, MWCNTs) which was affected by magnetic and electric fields.

Sabu *et al.* (2021) carried out the numerical investigation of a rigid rotating disk-induced hydromagnetic alumina-water nano fluid flow. The thermo-hydrodynamic slip constraints and different nanoparticle shapes (sphere, platelet, cylinder, and brick) were considered. In order to convert the mathematically modelled equations into a system of first-order ODEs and then numerically using the generalized differential quadrature method, von Kármán's similarity transformations.

The terminology used in the study of nanofluids and their properties, similar transformations, numerical techniques such as Runge Kutta, bvp4c, bvp5c are described in this chapter. The methodological development of governing equations over different conformations such as stretching sheet, stretching cylinder, Riga plate, rotating disc, are also discussed. The physical parameters like magnetic parameter, radiation parameter, Biot number, etc. and engraining quantities are also explained in this chapter.

#### **3.1 Classification of Fluids**

The fluid was classified based on Newton's law of viscosity, the dependency of shear stress, velocity with time, and the relationship between shear stress and viscosity gradient, as follows.

##### **Newtonian Fluids:**

Newtonian fluids are all those liquids that follow Newton's law of viscosity or have the linear relationship between shear stress and gradient of velocity. Examples of Newtonian fluids are water, oil, and kerosene.

##### **Non-Newtonian Fluids:**

Non-Newtonian fluids are fluids that do not exhibit a linear relationship between the velocity gradient and the shear strain rate. Slurry, mud flow, solutions, or suspensions are a few examples.

##### **Bingham-plastic Fluids:**

A Non-Newtonian fluid type with an initial yield stress, meaning that the linear relationship between shear stress and shear rate does not pass through the origin.

##### **Dilatants:**

Dilatants fluid is an illustration of a Non-Newtonian fluid, in which viscosity increases if the shear stress is applied. Quicksand and beach sand are examples of dilatants fluid.

##### **Pseudo-plastic:**

A fluid whose viscosity declines with a rise in shear stress. It can suspend pigments or paper pulp.

##### **Rheopectic Materials:**

The Non-Newtonian fluids that exhibit a time-dependent rise in viscosity are called as Rheopectic materials. Examples are the suspensions of gypsum in water and vanadium pentoxide solution.

**Thixotropic Fluids:**

The Non-Newtonian pseudoplastic fluids viz Ink and paint exhibit time-dependent viscosity variations.

**Ideal Fluids:**

Fluids which are incompressible and have no viscosity are treated as Ideal fluids. These fluids are imaginary and would not have any impact on temperature.

**Real Fluids:**

The fluid which has viscosity are termed as real fluids. E.g. water, diesel and honey etc. The analysis of blood flow in capillaries, crude oil flow, and the comprehension of air motions during the design of various types of chemical processing equipment are just a few examples of the many obstacles that come with studying real fluids.

**3.2 Types of Fluid Flow**

The direction/dimension and speed can be used to categorise fluid flows as under.

**3.2.1 Rotational and Irrotational Flows**

Rotational flow is a fluid flow in which the fluid particles move along their path and rotate around their own alignment at the same time. Irrotational flow is a fluid flow in which the fluid particles do not rotate around their own axis.

**3.2.2 Laminar and Turbulent Flow**

Laminar flow is a type of fluid motion in which every fluid particle moves along a regular, defined path and do not cross each other. Turbulent flow is a type of fluid motion in which the paths of particles are highly irregular or do not trace out a convinced path, and the paths taken through two dissimilar particles intersect.

**3.2.3 Steady and Unsteady Flow**

The flow in which the fluid properties at a point in the system do not change over time, is called as steady flow. Mathematically it can be defined as

$$\frac{\partial P}{\partial t} = 0, \frac{\partial V}{\partial t} = 0, \frac{\partial \rho}{\partial t} = 0,$$

In unsteady flow, the velocity of the fluid particles at any point changes with respect to the time. Mathematically it can be defined as

$$\frac{\partial P}{\partial t} \neq 0, \frac{\partial V}{\partial t} \neq 0, \frac{\partial \rho}{\partial t} \neq 0,$$

**3.2.4 Uniform Flow and Non-uniform**

A flow of fluid in which every particle of fluid progresses along its path of flow with uniform velocity and cross-section of each stream pipe remains unaltered is called uniform flow. The flow in which fluid particles do not travel along its path with a constant velocity at each section of channel is known as nonuniform flow.

### 3.2.5 Compressible and Incompressible Flow

When pressure variations in the flow field are significant enough to cause a considerable change in fluid density, the flow is said to be compressible. If the density of fluid does not vary, called incompressible flow.

### 3.3 Boundary Layer Flow

Ludwig Prandtl made the initial suggestion for the boundary layer. The theory is presented when we study the two-dimensional laminar flow of a fluid with low viscosity around a solid body. It can be seen that, in contrast to an ideal flow, the fluid sticks to the surface of the body rather than sliding over it. The fluid that is in contact with the solid body will be at rest as the solid body is at rest. Moving outward along the normal, the fluid's stream velocity progressively rises until it reaches its maximum velocity at a considerable distance from the solid body.

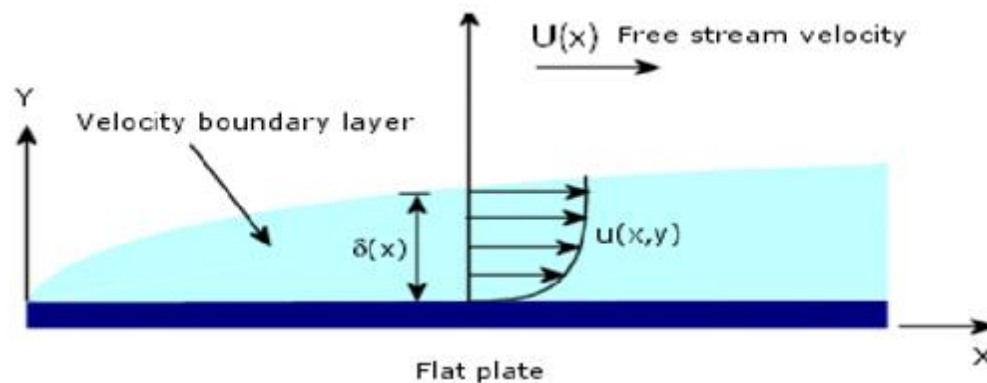


**Figure 3.1 Boundary Layer Flow**

It is presumable that within a thin layer of fluid in contact with the surface of a solid body, the velocity changes from zero at the surface to the velocity which is equivalent to the free stream velocity. The "no slip condition" is the requirement that the stream at the surface have no relative motion. As a result, we can divide the flow around a solid body into two distinct zones. The first zone is in the neighborhood of the body, where friction is quite important. It is a very thin layer. The other area is outside of this layer, where friction may be neglected. The ideal fluid theory generally influences larger-scale fluid flow, but viscosity affects flow at the boundary layer region.

#### 3.3.1 Boundary Layer Thickness

The term "boundary layer thickness" refers to the thickness of the viscous region close to the boundary layer. Viscosity slows down fluid movement close to the body's surface, extending to a point where the fluid's speed is essentially equal to that of a free stream. As fluid moves away from the surface of the body, it's velocity asymptotically tends to the free stream velocity, but in reality, it is never equal to the free stream velocity. Hence, the

thickness of the boundary layer is the distance created between the fluid and the body's surface when the local fluid velocity is almost 99% of the free stream velocity.

### **3.3.2 Suction and Injection**

Suction is defined as "the flow of liquid into a partial vacuum or region of low pressure." The difference in the pressure between the region and ambient pressure will drive matter toward the area having small pressure. One method for regulating the separation of the boundary layer is suction. It implies eliminating the boundary layer region of any fluid particles that decelerate before they separate the boundary layer. In order to reduce the drag, suction is also highly useful.

Injection is another method for retaining the boundary layer in place; it involves "supplying additional energy to the fluid particles that are being slowed in the boundary layer."

### **3.3.3 Magnetohydrodynamics**

Magnetohydrodynamics (MHD) is the study of the dynamics of electrically directed fluids in the presence of coupled magnetic and velocity effects. Magnetohydrodynamics is a combination of the word's magneto (which means magnetic region), hydro (which means liquid), and dynamics (means- movement). Hannes Alfvén received the Nobel Prize in Physics in 1970 for developing the concept of magnetohydrodynamics.

### **3.3.4 Porosity and Permeability**

According to fluid mechanics, when a fluid passes through a porous material, the amount of empty space in material is called porosity and is often denoted in percentage. The ratio of the volume of voids over the entire volume of the material, which ranges from 0 to 1, is also known as the "void fraction." It can be seen in some fluid which move through the porous medium while several masses of fluid are stored in it.

Permeability is an essential characteristic of porous medium and it measures the ease with which a fluid is transmitted through porous medium. It is measured in Darcy, which is the unit of permeability. Both the porosity and permeability are related to each other, where permeability is completely dependent on porosity, because the porosity (pores) provides path for fluid flow.

## **3.4 Heat Transfer**

Heat transfer, commonly known as heat, is the passage of thermal energy from one item to another caused by temperature differences. In other term, it is a transfer of thermal energy (heat) between two things. These things could be solids, liquids, or gases. The temperature of each body and the medium through which heat is transmitted completely influence the rate of heat transfer. Heat transfer occurs when temperature of objects is not equal and the temperature difference is transformed into an un-equilibrium state. There are

only three ways to transfer heat: conduction (through direct contact), convection (by fluid movement), and radiation (via electromagnetic waves).

### **Modes of Heat Transfer**

Heat can be transferred through three ways that are Conduction, Convection, and Radiation.

#### **Conduction**

It is a mechanism for transferring heat in which molecules vibrate at their average locations, allowing energy to pass from a high-temperature system to a low-temperature system. The law of conduction known as Fourier's law governs the rate of heat transmission in this process. The systems that allow for the flow of energy should be in close contact to one another. In solid bodies, heat conduction typically occurs if particles are arranged in a configuration that is strongly gripped by an intermolecular force of attraction. Therefore, as they absorb heat and then transfer it to the surrounding molecules through vibration, molecules merely vibrate about their average positions. Heat is moved from one location to another without any actual material movement. Generally, the heat conduction equation is,

$$\Delta Q = \rho C_p \Delta T$$

#### **Convection**

In contrast to vibration in conduction, this is one of the macroscopic methods of heat transmission. Convective heat transmission comprises both bulk motion and molecular diffusion (movement of molecules). Convection is basically the combination of conduction and advection, where convection represents bulk motion. In simpler words, it is a process in which heat is transferred through the actual motion of fluid particles. When fluids are not moving, convection's influence tends to be negligible and only conduction's impact is noticeable. Newton's law of cooling regulates the convection process. There are two different types of convection: natural convection and forced convection.

Natural convection, also known as free convection, happens when the fluid is forced into motion by Buoyancy forces that are induced due to changes in fluid density. Force convection occurs when the fluid is forced into motion by pumps or any exterior energy introduced into the system and thus the fluid flows over the solid surface. When both the natural and force convection take place simultaneously, then this process is known as mixed convection.

#### **Radiation**

All the physical matters release thermal radiations in the form of electromagnetic radiations in all the directions that move directly to the absorption point. It is temperature dependent, to 4th power and occurs without a medium. The black bodies are identified as systems that absorb total energy incidents upon it. It also emits radiation at the maximum rate

of the body of specific dimension at a certain temperature. It travels with the speed of light and the intervening medium is not essential to carry them.

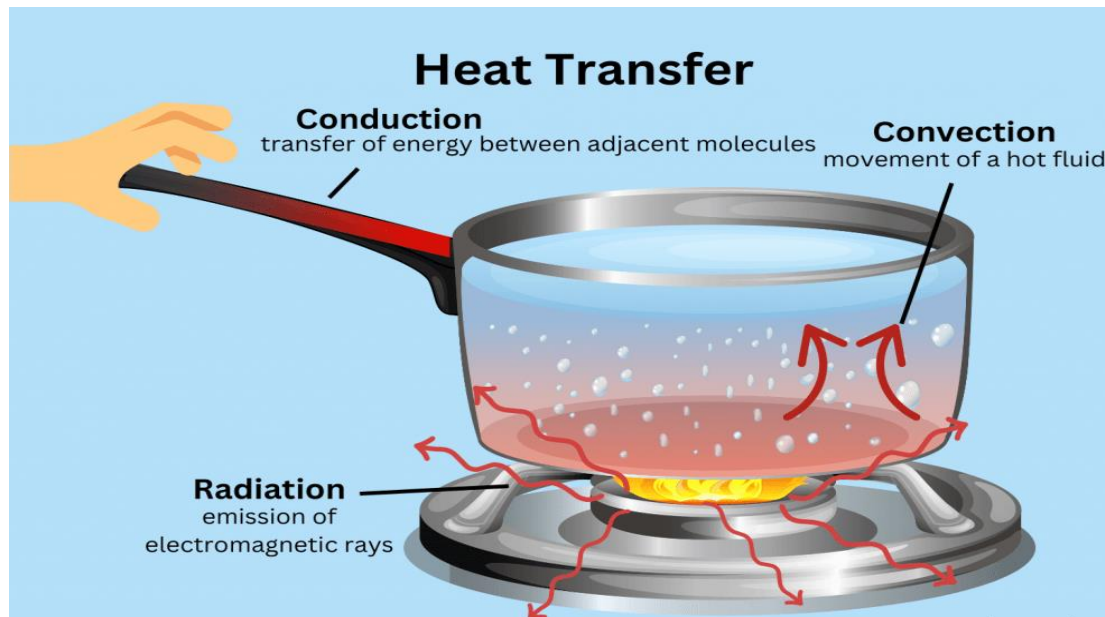


**Figure 3.2 Heat transfer Modes**

### 3.4.1 Heat Source/Sink

An object that transfers heat energy from a fluid medium with a high temperature to one with a lower temperature is referred to as a heat source. A heat sink is designed to absorb heat by expanding the contact area with the neighboring coolant, such as air. The "heat sink" is frequently referred to as a cold plate if the fluid medium is water. Energy cannot be transformed if there is no airflow surrounding the heat exchanger. For example, heat sinks (heat exchangers) are used in refrigerator and air conditioning systems. Heat source/sink can be used to cool the graphics processor or the CPU in computers.

### 3.4.2 Joule heating

Joule heating is a technique for creating extremely high temperatures in fluids using either an electric current or a magnetic field. Ohmic heating is another name for it. In general, when an electric current passes through a liquid or solid with a limited conductivity value, the medium's resistive losses cause the electric energy to be transformed to heat. When the charged particles strike the ions in the conductor, heat is produced on a microscale. Due to collision, particles are distributed and move randomly rather than aligning with the magnetic field.

### 3.4.3 Viscous Dissipation

When a viscous fluid flows, the viscosity of the fluid absorbs kinetic energy from the flow and converts it into internal energy, which causes the fluid to heat up. Viscous dissipation, generally spelled dissipation, is a largely irreversible phenomenon. Large gradients and high turbulence areas both have high dissipation rates. The quadratic function

of the 3D derivatives of the fluid velocity elements in the energy equation illustrates the rate at which mechanical energy is transformed into heat in a viscous fluid per unit volume.

### **3.5 Mass transfer**

A substance moves from one location to another at the molecular level as a result of the gradient or concentration differential. Pressure gradient, concentration, and temperature are the main forces behind mass transfer. For instance, water flowing through a pipe or smoke dispersing into the air from a chimney. Diffusion mass transfer and convective mass transfer are generally two approaches of mass transfer. Similar to conductive heat transfer diffusion is the transport of mass due to random motion of molecules in laminar flowing fluids. The hydrostatic pressure differential and concentration gradient are the fundamental causes of mass transfer by diffusion.

The molecular diffusion rate of mass is accelerated by the fluid's bulk motion. The mass transfer can take place between two moving fluids that are comparatively non-miscible, as in the vaporization of water in a kettle, or between two moving fluids and a boundary of a surface, as in the drying of textiles.

#### **3.5.1 Thermophoresis**

The Swiss physicist Soret proved in 1879 that the salt solution inside a conduit with both ends at different temperatures did not remain constant in composition. In comparison to the cold end of the conduit, he discovered that the salt solution was less concentrated close to the hot end. According to his findings, the concentration gradient formed under steady-state conditions by a temperature gradient that provided the flux of salt solution. Physically, it is defined as the movement of colloidal particles or big molecules in a solution with relation to a macroscopic temperature differential. The theoretical diffusion process (Soret effect) is the term used to describe the effect associated with this phenomenon, which typically affects liquid mixtures and some aerosol mixtures.

#### **3.5.2 Chemical reactions**

Chemical reactions are the transformation of one set of chemical substances known as reactants into another set of chemical substances known as products. Chemical reactions that start without the need for any energy are referred to as spontaneous reactions, while those need heat, light, or electricity to initiate are referred to as non-spontaneous reactions. Generally, in chemical reaction motion, electrons play an important part in the formation and deformation of the bonds (chemical).

### **3.6 Governing equation System**

#### **3.6.1 Cartesian coordinate system( $x, y, z$ )**

Navier-Stokes equations explain the motion of fluids

The Navier-Stoke momentum equation for viscous nanofluid is as under:

$$\rho \frac{DV}{Dt} = F - gradP + \mu_{nf} \nabla^2 V$$

where  $\frac{DV}{Dt}$  is convective derivative, t is time,  $\rho_{nf}$  is nanofluid density,  $\mu_{nf}$  is nanofluid dynamic viscosity,  $V = ui^{\wedge} + vj^{\wedge} + wk^{\wedge}$  the flow velocity,  $F = F_x i^{\wedge} + F_y j^{\wedge} + F_z k^{\wedge}$  is the force, pressure is assigned by P,  $\nabla^2$  is the Laplace operator.

The partial differential equations (PDEs) for 3D flow of incompressible, unsteady Newtonian fluid in the form of Cartesian co-ordinate system are as follows

### Continuity Equation

$$\left[ \begin{array}{c} \text{Net rate of mass} \\ \text{flow entering} \\ \text{volume} \\ \text{element} \\ \text{in x - direction} \end{array} \right] + \left[ \begin{array}{c} \text{Net rate of mass} \\ \text{flow entering} \\ \text{volume} \\ \text{element} \\ \text{in y - direction} \end{array} \right] + \left[ \begin{array}{c} \text{Net rate of mass} \\ \text{flow entering} \\ \text{volume} \\ \text{element} \\ \text{in z - direction} \end{array} \right] = 0$$

$$u \frac{\partial u}{\partial x} + v \frac{\partial v}{\partial y} + w \frac{\partial w}{\partial z} + \frac{\partial u}{\partial t} = 0$$

### Momentum Equation:

These equations follow Newton's 2nd law of motion, which states that the rate of change of momentum (acceleration) of an object is dependent upon two variables: the force acting upon the object and the mass of an object.

$$[mass] \left[ \begin{array}{c} \text{acceleration in} \\ \text{x, y, and z directions} \end{array} \right] + \left[ \begin{array}{c} \text{Body force(gravity, centrifugal etc.)} \\ \text{acting in x, y and z directions} \\ \text{+ surface force(pressure, viscous force, etc.)} \\ \text{acting in x, y and z direction} \end{array} \right] = 0$$

The momentum equations in x, y and z directions are described as follows:

$$\rho_{nf} \left( u \frac{\partial u}{\partial x} + v \frac{\partial u}{\partial y} + w \frac{\partial u}{\partial z} + \frac{\partial u}{\partial t} \right) = F_x - \frac{\partial P}{\partial x} + \mu_{nf} \left( \frac{\partial^2 u}{\partial x^2} + \frac{\partial^2 u}{\partial y^2} + \frac{\partial^2 u}{\partial z^2} \right)$$

$$\rho_{nf} \left( u \frac{\partial v}{\partial x} + v \frac{\partial v}{\partial y} + w \frac{\partial v}{\partial z} + \frac{\partial v}{\partial t} \right) = F_y - \frac{\partial P}{\partial y} + \mu_{nf} \left( \frac{\partial^2 v}{\partial x^2} + \frac{\partial^2 v}{\partial y^2} + \frac{\partial^2 v}{\partial z^2} \right)$$

$$\rho_{nf} \left( u \frac{\partial w}{\partial x} + v \frac{\partial w}{\partial y} + w \frac{\partial w}{\partial z} + \frac{\partial w}{\partial t} \right) = F_z - \frac{\partial P}{\partial z} + \mu_{nf} \left( \frac{\partial^2 w}{\partial x^2} + \frac{\partial^2 w}{\partial y^2} + \frac{\partial^2 w}{\partial z^2} \right)$$

### Energy Equation:

The energy equation is obtained by using the 1st law of thermodynamics, according to this law the rate of change of energy of a fluid particle is equal to the addition of rate of heat addition and rate of work done. Hence, the energy equation can be expressed as follows:

$$\left[ \begin{array}{c} \text{rate of increase} \\ \text{of energy in element} \end{array} \right] + \left[ \begin{array}{c} \text{rate of energy} \\ \text{input due} \\ \text{to conduction} \end{array} \right] + \left[ \begin{array}{c} \text{rate of energy} \\ \text{input due to} \\ \text{workdone by} \\ \text{body forces} \end{array} \right] + \left[ \begin{array}{c} \text{rate of energy} \\ \text{input due to} \\ \text{workdone by} \\ \text{surface forces} \end{array} \right]$$

$$(\rho c_p)_{nf} \left( u \frac{\partial T}{\partial x} + v \frac{\partial T}{\partial y} + w \frac{\partial T}{\partial z} + \frac{\partial T}{\partial t} \right) = \mu_{nf} \zeta + \kappa_{nf} \left( \frac{\partial^2 T}{\partial x^2} + \frac{\partial^2 T}{\partial y^2} + \frac{\partial^2 T}{\partial z^2} \right)$$

Where

$$\zeta = \left[ \left( \frac{\partial u}{\partial x} \right)^2 + \left( \frac{\partial v}{\partial y} \right)^2 + \left( \frac{\partial w}{\partial z} \right)^2 \right] + \left[ \left( \frac{\partial v}{\partial x} + \frac{\partial u}{\partial y} \right)^2 + \left( \frac{\partial w}{\partial y} + \frac{\partial v}{\partial z} \right)^2 + \left( \frac{\partial u}{\partial z} + \frac{\partial w}{\partial x} \right)^2 \right] + \frac{2}{3} \left( \frac{\partial u}{\partial x} + \frac{\partial v}{\partial y} + \frac{\partial w}{\partial z} \right)^2$$

### 3.6.2 Polar Coordinate System ( $r, \theta, z$ ):

**Continuity Equation:**

$$\frac{\partial u}{\partial r} + \frac{u}{r} + \frac{\partial w}{\partial z} + \frac{1}{r} \frac{\partial v}{\partial \theta} = 0$$

**Momentum Equation:**

$$\rho_{nf} \left( \frac{\partial u}{\partial t} + u \frac{\partial u}{\partial r} + \frac{v}{r} \frac{\partial u}{\partial \theta} + w \frac{\partial u}{\partial z} - \frac{v^2}{r} \right) = F_r - \frac{\partial P}{\partial r} + \mu_{nf} \left( \frac{\partial^2 u}{\partial r^2} - \frac{u}{r^2} + \frac{1}{r^2} \frac{\partial^2 u}{\partial \theta^2} - \frac{2}{r^2} \frac{\partial u}{\partial \theta} + \frac{\partial^2 u}{\partial z^2} + \frac{1}{r} \frac{\partial u}{\partial r} \right)$$

$$\rho_{nf} \left( \frac{\partial v}{\partial t} + u \frac{\partial v}{\partial r} + \frac{v}{r} \frac{\partial v}{\partial \theta} + w \frac{\partial v}{\partial z} + \frac{uv}{r} \right) = F_\theta - \frac{1}{r} \frac{\partial P}{\partial \theta} + \mu_{nf} \left( \frac{\partial^2 v}{\partial r^2} - \frac{v}{r^2} + \frac{1}{r^2} \frac{\partial^2 v}{\partial \theta^2} + \frac{2}{r^2} \frac{\partial v}{\partial \theta} + \frac{\partial^2 v}{\partial z^2} + \frac{1}{r} \frac{\partial v}{\partial r} \right)$$

$$\rho_{nf} \left( \frac{\partial w}{\partial t} + u \frac{\partial w}{\partial r} + \frac{v}{r} \frac{\partial w}{\partial \theta} + w \frac{\partial w}{\partial z} \right) = F_z - \frac{\partial P}{\partial z} + \mu_{nf} \left( \frac{\partial^2 w}{\partial r^2} + \frac{1}{r^2} \frac{\partial^2 w}{\partial \theta^2} + \frac{\partial^2 w}{\partial z^2} + \frac{1}{r} \frac{\partial w}{\partial r} \right)$$

**Energy Equation:**

$$\begin{aligned} (\rho c_p)_{nf} \left( \frac{\partial T}{\partial t} + u \frac{\partial T}{\partial r} + \frac{v}{r} \frac{\partial T}{\partial \theta} + w \frac{\partial T}{\partial z} - \frac{v^2}{r} \right) \\ = \kappa_{nf} \left( \frac{\partial^2 T}{\partial r^2} - \frac{u}{r^2} + \frac{1}{r^2} \frac{\partial^2 T}{\partial \theta^2} - \frac{2}{r^2} \frac{\partial v}{\partial \theta} + \frac{\partial^2 T}{\partial \theta^2} + \frac{1}{r} \frac{\partial T}{\partial r} \right) + \mu_{nf} \xi \end{aligned}$$

Where

$$\xi = \left[ \left( \frac{\partial T}{\partial r} \right)^2 + \left( \frac{\partial T}{\partial \theta} \right)^2 \right] + \left[ \left( \frac{\partial T}{\partial r} + \frac{\partial T}{\partial \theta} \right)^2 \right] + \frac{2}{3} \left( \frac{\partial T}{\partial r} + \frac{\partial T}{\partial \theta} \right)^2$$

**Mass Transfer Equation:**

$$\begin{aligned} (\rho c_p)_{nf} \left( \frac{\partial C}{\partial t} + u \frac{\partial C}{\partial r} + \frac{v}{r} \frac{\partial C}{\partial \theta} + w \frac{\partial C}{\partial z} - \frac{v^2}{r} \right) \\ = D \left( \frac{\partial^2 C}{\partial r^2} - \frac{u}{r^2} + \frac{1}{r^2} \frac{\partial^2 C}{\partial \theta^2} - \frac{2}{r^2} \frac{\partial v}{\partial \theta} + \frac{\partial^2 C}{\partial \theta^2} + \frac{1}{r} \frac{\partial C}{\partial r} \right) + D_c \end{aligned}$$

### 3.7 Non-Dimensional Parameters

A dimensionless number or parameter is a quantity without units that describes a physical phenomenon but does not change the specific phenomenon. Non-dimensional parameters are independent of the unit system and based on the physical system's

characteristic values. In the current investigation, some of the parameters illustrated below were used. The following list of parameters defines nanofluids:

### 3.7.1 Grashof number

The tendency of a particular system towards free convection is based on the Grashof number ( $Gr$ ), which is classified as the ratio of buoyancy force to viscous force. It is defined as:

$$\frac{\text{Buoyancy force}}{\text{Viscous force}} = \frac{\beta g \Delta T L}{\nu_f^2}$$

Where  $\Delta T$  is the characteristic temperature difference of the flow.

### 3.7.2 Reynolds Number

Reynolds number is the ratio of inertial forces to viscous forces. Mathematically, can be written as;

$$Re = \frac{\text{inertial forces}}{\text{viscous forces}} = \frac{U_{RL}}{\nu} = \frac{\rho U_R^2}{\mu \frac{U_R}{L}}$$

Where  $\mu$  represents the viscosity,  $L$  is reference length,  $U$  is characteristic velocity,  $\rho$  represents to density, respectively. This number is very important to solve Navier Stokes equations. Reynolds number designates whether the fluid flow is turbulent or laminar. If this number is small, the viscous forces will be greater in magnitude compared to inertial forces. So, the viscous forces will oppose any interruption that creates intensification in the flow; as a result, the flow tends to be laminar. Contrarily, when  $Re$  is large, the inertial forces will be greater in magnitude than viscous forces, so the confrontation of the flow in contradiction of distortion will be smaller, So the flow will tend to be turbulent.

### 3.7.3 Prandtl Number

Prandtl number which approximates the ratio of kinematic viscosity to thermal diffusivity of the fluid. Prandtl number can be written as;

$$Pr = \frac{\mu C_p}{K_T} = \frac{\nu}{\alpha}$$

$\alpha$  = Shows thermal diffusivity,  $\mu$  = Coefficient of kinematic viscosity,

$K_T$  = Coefficient of thermal conductivity

Prandtl number shows the effect of thermo-physical fluid properties on the transference of heat. It is consistent with the other non-dimensional numbers for defining the coefficient of heat transfer among two layers.

### 3.7.4 Skin Friction Coefficient

Skin friction is instigated by the “viscous drag in the boundary layer around the object”. The part of the boundary layer which lies in the abut of the object below the consideration is generally laminar and relatively thin also, but the flow becomes turbulent towards the tail section of the considered object. Skin friction results from the friction against the “skin” of the article that it is moving through, and it has directly link with the moistened surface, the surface area of the article that is in direct relation with the fluid. Law of viscosity

for various kinds of flow viz. straight, parallel and uniform flow as specified by Isaac Newton says that “the shear stress ( $\tau$ ) between layers of fluid is proportional to the velocity gradient  $\frac{\partial u}{\partial t}$  in the direction perpendicular to the layers”. The shear stress or viscous drag at the shell of the body or at wall is

$$C_f = \frac{\tau_w}{\rho U_0^2}$$

where  $\tau_w = \mu \left. \frac{\partial u}{\partial y} \right|_{y=0}$

### 3.7.5 Nusselt Number

The elementary mechanisms of the heat transference including convection and it can be calculated by the usage of heat transfer coefficient. In non-dimensional form this number is transmuted into a recognized parameter that is named “Nusselt number” and is represented as;

$$Nu = \frac{\text{Convective heat transfer}}{\text{Conductive heat transfer}} = \frac{hL}{K_f}$$

Here

$$h = - \frac{k \left. \frac{\partial T}{\partial y} \right|_{y=0}}{(T_w - T_\infty)}$$

where,  $L$  is the reference length and  $K$  is thermal conductivity of fluid.

### 3.7.6 Schmidt Number

Schmidt number is the ratio of diffusivity of momentum to mass molecular diffusivity, it plays a vital role in connective momentum and mass diffusivity, also it describes the mass momentum transfer, mathematically can be shown as;

$$Sc = \frac{\text{Viscous diffusion rate}}{\text{Mass diffusion rate}} = \frac{\mu}{\rho D}$$

where,  $D$  is the mass diffusivity.

### 3.7.7 Sherwood Number

The non-dimensional quantity Sherwood number is represented by “ $Sh$ ” and is defined as;

$$\frac{\text{Convective mass transfer}}{\text{mass diffusion rate}} = \frac{-h \left. \frac{\partial C}{\partial y} \right|_{y=0}}{(C_w - C_\infty)}$$

### 3.7.8 Brownian Diffusion Coefficient

The non-dimensional quantity Brownian diffusion coefficient represented by ‘ $D_B$ ’, It arises due to the constant collision within the nanoparticles and fluid molecules. It can be shown as;

$$D_B = \frac{K_B T C_C}{3\mu d_p}$$

where  $K_B$  is Boltzmann constant,  $\mu$  is the fluid viscosity,  $C_C$  Correction factor

### 3.7.9 Thermophoresis Diffusion Coefficient

The non-dimensional quantity Thermophoresis diffusion coefficient represented by ' $D_T$ ', It arises due to the effect of temperature gradient. It can be defined as;

$$D_T = -\frac{vT}{3\mu \Delta T}$$

where  $v$  is Thermophoresis velocity,  $\mu$  is the fluid viscosity.

### 3.7.10 Eckert Number

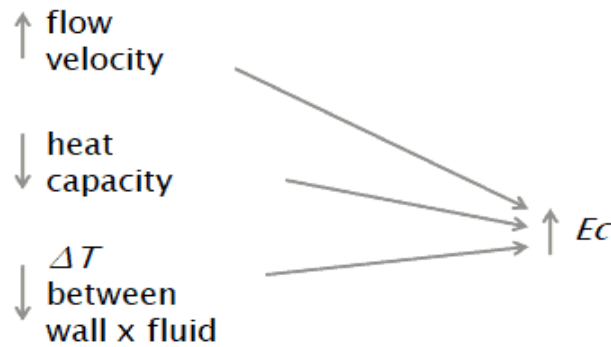
Eckert number is the ratio of advective mass transfer to the heat dissipation potential and it is named after Ernst R.G. Eckert. Mathematically expressed are;

$$Ec = \frac{\text{Advective mass transfer}}{\text{Heat dissipation}} = \frac{u^2}{C_p \Delta T}$$

$C_p$  = Capacity of specific heat transfer at fixed pressure

$\Delta T$  = Temperature difference between wall and local temperatures

$u$  = is the velocity of fluid



### 3.7.11 Biot number

The Biot number ( $Bi$ ), it is the ratio of the heat transfer resistances inside of and the surface of body.

$$Bi = \frac{hl}{k}$$

where  $h$  is coefficient of heat transfer,  $L$  is characteristic length and  $k$  is the thermal conductivity.

## 3.8 Materials for Nanoparticles and Base Fluids

### 3.8.1 Nanoparticles Materials:

- Oxide ceramics -  $Al_2O_3$ ,  $CuO$ ,  $TiO_2$
- Metal carbides -  $SiC$
- Nitrides -  $SiN$ ,  $AlN$
- Metals –  $Cu$ ,  $Al$ ,  $Ag$ ,  $Au$
- Nonmetals – Black lead,  $CNT$ , Graphite, carbon nanotubes
- Layers –  $Al + Al_2O_3$ ,  $Cu + C$

- Functionalized nanoparticles

### 3.8.2 Base Fluids:

- Water, Ethylene and coolants, Oil and lubricants, Bio-fluids,
- Kerosene oil, Glycerol, Ethylene-or tri-ethylene-glycol, Polymer solutions

**Table 3.1 Nanofluid properties**

Dynamic Viscosity	$\mu_{nf} = \mu_f(1 - \phi)^{-2.5}$
Density	$\rho_{nf} = (1 - \phi)\rho_f + \phi\rho_s$
Specific Heat Capacity	$(\rho C_p)_{nf} = (1 - \phi)(\rho C_p)_f + \phi(\rho C_p)_s$
Thermal Conductivity	$\frac{\kappa_{nf}}{\kappa_{bf}} = \frac{\kappa_s + (n - 1)\kappa_f - \phi(n - 1)(\kappa_f - \kappa_s)}{\kappa_s + (n - 1)\kappa_f + 2\phi(\kappa_{bf} - \kappa_s)}$
Kinematics Viscosity	$\nu_{nf} = \frac{\mu_{nf}}{\rho_{nf}}$
Thermal Diffusivity	$\alpha_{nf} = \frac{\kappa_{nf}}{(\rho C_p)_{nf}}$
Heat Capacitances Ratio	$\tau = \frac{(\rho C_p)_s}{(\rho C_p)_f}$
Thermal Expansion Coefficient	$(\rho\beta)_{nf} = (1 - \phi)\rho_f\beta_f + \phi\rho_s\beta_s$
Electrical Conductivity	$\sigma_{nf} = 1 + \frac{3\phi\left(\frac{\sigma_s}{\sigma_f} - 1\right)}{2 + \frac{\sigma_s}{\sigma_f} - \frac{\sigma_s}{\sigma_f}\phi + \phi}$
Empirical Shape Factor	$n = \frac{3}{\Psi}, \Psi = 1$ for spherical particles

**Table 3.2 Hybrid nanofluid properties**

Dynamic Viscosity	$\frac{\mu_{hnf}}{\mu_f} = \frac{1}{(1 - \phi_1)^{2.5}(1 - \phi_2)^{2.5}}$
Density	$\frac{\rho_{hnf}}{\rho_f} = (1 - \phi_2) \left( (1 - \phi_1) + \phi_1 \frac{\rho_{s1}}{\rho_f} \right) + \phi_2 \frac{\rho_{s2}}{\rho_f}$
Specific Heat Capacity	$\frac{(\rho C)_{hnf}}{(\rho C)_f} = (1 - \phi_2) \left( 1 - \phi_1 + \phi_1 \frac{(\rho C)_{s1}}{(\rho C)_f} \right) + \phi_2 \frac{(\rho C)_{s2}}{(\rho C)_f}$
Thermal Conductivity	$\frac{k_{hnf}}{k_f} = \frac{k_{hnf}}{k_{nf}} * \frac{k_{nf}}{k_f}$
	$\frac{k_{hnf}}{k_{nf}} = \frac{k_{s2} + 2k_{nf} - 2\phi_2(k_{nf} - k_{s2})}{k_{s2} + 2k_{nf} + \phi_2(k_{nf} - k_{s2})}$
	$\frac{k_{nf}}{k_f} = \frac{k_{s1} + 2k_f - 2\phi_1(k_f - k_{s1})}{k_{s1} + 2k_f + \phi_1(k_f - k_{s1})}$
Thermal Diffusivity	$\alpha_{nf} = \frac{\kappa_{hnf}}{(\rho C_p)_{hnf}}$
Thermal Expansion Coefficient	$\frac{(\rho\beta)_{hnf}}{(\rho\beta)_f} = (1 - \phi_2) \left( 1 - \phi_1 + \phi_1 \frac{(\rho\beta)_{s1}}{(\rho\beta)_f} \right) + \phi_2 \frac{(\rho\beta)_{s2}}{(\rho\beta)_f}$
Electrical Conductivity	$\frac{\sigma_{hnf}}{\sigma_f} = 1 + \frac{3 \left( \frac{\phi_1\sigma_{s1} + \phi_2\sigma_{s2}}{\sigma_f} - (\phi_1 + \phi_2) \right)}{2 + \left( \frac{\phi_1\sigma_{s1} + \phi_2\sigma_{s2}}{(\phi_1 + \phi_2)\sigma_f} \right) - \left( \frac{\phi_1\sigma_{s1} + \phi_2\sigma_{s2}}{\sigma_f} - (\phi_1 + \phi_2) \right)}$

**Table 3.3 Thermo-physical characteristics of some base fluids and solid particles**

Base Fluids	Density ( $\rho$ )	Thermal Conductivity ( $\kappa$ )	Specific heat ( $C_p$ )	Thermal exponential coefficient ( $\beta$ )	Electrical conductivity $\sigma$
Oil (Engine oil)	896	0.145	1830	$7 \times 10^7$	-
Water( $H_2O$ )	997.1	0.613	4179	$2.1 \times 10^{-4}$	0.05
Ethylene glycol( $C_2H_6O_2$ )	1110	0.253	2470	$57 \times 10^7$	-
Solid Particle	Density ( $\rho$ )	Thermal Conductivity ( $\kappa$ )	Specific heat ( $C_p$ )	Thermal exponential coefficient ( $\beta$ )	Electrical conductivity $\sigma$
Copper (Cu)	8933	401	385	$1.67 \times 10^{-5}$	$5.96 \times 10^7$
Silver (Ag)	10500	429	235	$1.89 \times 10^{-5}$	$6.7 \times 10^7$
$Fe_3O_4$	5180	9.7	670	$2.5 \times 10^7$	$2.5 \times 10^4$
$TiO_2$	4250	8.9538	686.2	$03.69 \times 10^7$	$10^{-10}$
$Al_2O_3$	3970.0	40	765.0	$0.85 * 10^{-5}$	$03.67 \times 10^7$

### 3.9 Similarity Transformation

In fluid dynamics, it is exceedingly challenging to solve the collection of non-linear partial differential equations associated to momentum, energy, concentration equations, and equation of state using an analytical approach. A special kind of transformation technique called similarity transformation is applied to solve this problem. Scaling and translation are some kind of transformations, which generate nontrivial solutions in majority of cases. These transformations are some of the most effective tools in producing similarity transformations. These are introduced to convert the original set of PDEs into a simplified set of ODEs. Similarity transformations are the processes that allow a collection of PDEs with  $k-1$  independent variables to be changed into a configuration with  $k$  independent variables. In the “free parameter method” it is presumed that the occurrence of dependent variable in governing PDEs can be written as a product of two functions. In this product, first function is a function of independent variable except first. The second function is considered as depend on single parameter  $\eta$ , where, the variable  $\eta$  is attained from a transformation of the variables including independent variables but not happening in the first function. The detail of this scheme was given by Hansen (1964). The second method, which is performing the similarity analysis and includes the classical separation of variables method, was given by Abbott and Kline (1960). This procedure is concerned with evaluating similarity transformation and considers boundary conditions.

### 3.10 Numerical Methods

#### 3.10.1 Runge-Kutta Method

The Runge-Kutta (RK) method is an important family of explicit and implicit iteration methods used to solve ordinary differential equations with initial conditions.

$$\frac{dy}{dx} = f(x, y), y(x_0) = y_0$$

These techniques are one-step procedures that demand the use of a first order derivative. The acquired results' accuracy is parred with the higher-order Taylor's formula. The extrapolation equation related to all variations of RK techniques can be expressed in the following general form:

$$y_{k+1} = y_k + \text{slope} \times \text{size of interval} \\ y_k + h\delta$$

Here  $\delta$  indicates the weighted averages of slopes at several points in the interval  $h$ . Generally,  $\delta$  can be calculated utilizing slopes at  $s$  points in the interval  $(x_k, x_{k+1})$ , such as:

$$\delta = \sum_{i=1}^p k_i \delta_i$$

where  $k_i$ , represents the weights of slope at different points.

The other members of RK methods are of the second order as well as of the fourth order. For the initial value problem, the fourth-order RK formula can be written as follows:

$$y_{k+1} = y_k + \frac{h}{6}(k_1 + 2k_2 + 2k_3 + k_4)$$

Each value of  $k_i$  requires the use of the following four values, such as:

$$k_1 = h f(x_k, y_k) \\ k_2 = h f\left(x_k + \frac{h}{2}, y_k + \frac{k_1}{2}\right) \\ k_3 = h f\left(x_k + \frac{h}{2}, y_k + \frac{k_2}{2}\right) \\ k_4 = h f(x_k + h, y_k + k_3)$$

The German mathematician Erwin Fehlberg developed a method to acquire numerical solution of the ODEs known as Runge-Kutta-Fehlberg scheme (RKF45) with the order of fourth-fifth. In this method, the 4th order RK method with five stages is applied along with 5th order RK method with six stages that uses all of the points of the first one.

It possesses an inbuilt procedure to determine whether the appropriate step size  $h$  is being used. Two dissimilar estimations for the solution are made and compared at each step. If two calculated results show close agreement and are repeated to get acceptance for the desired accuracy then the approximation is accepted, else then step sizes are reduced. If calculated outcomes agree to more significant digits than required, step size is increased.

Each step needs the use of the following six values, such as:

$$k_1 = h f(x_k, y_k) \\ k_2 = h f\left(x_k + \frac{h}{4}, y_k + \frac{k_1}{4}\right)$$

$$\begin{aligned}
k_3 &= h f \left( x_k + \frac{3h}{8}, y_k + \frac{3}{32}k_1 + \frac{9k_2}{32} \right) \\
k_4 &= h f \left( x_k + \frac{12}{13}h, y_k + \frac{1932}{2197}k_1 + \frac{7200k_2}{2197} + \frac{7296}{2197}k_3 \right) \\
k_5 &= h f \left( x_k + h, y_k - \frac{439}{216}k_1 - 8k_2 + \frac{3680}{513}k_3 - \frac{845}{4104}k_4 \right) \\
k_5 &= h f \left( x_k + h, y_k - \frac{8}{27}k_1 - 2k_2 + \frac{3554}{2565}k_3 + \frac{1859}{4104}k_4 - \frac{11}{40}k_5 \right)
\end{aligned}$$

Then an approximation to the solution of initial value problem (IVP) is made via RK method of 4th-order with four function values  $k_1, k_3, k_4$  and  $k_5$ , such as:

$$y_{k+1} = y_k - \frac{25}{216}k_1 + \frac{1408}{2565}k_3 + \frac{2197}{4104}k_4 - \frac{1}{5}k_5$$

and an improved value for the solution is established using Runge-Kutta method of 5 th-order with five function values  $k_1, k_3, k_4$  and  $k_5$ , such as:

$$y_{k+1} = y_k + \frac{16}{135}k_1 + \frac{6656}{12825}k_3 + \frac{28561}{56430}k_4 - \frac{9}{50}k_5 + \frac{2}{55}k_6$$

The step size (rh) know as optimal step size can be achieved by multiplying the scalar r with step size h. The scalar r can be written as:

$$\begin{aligned}
r &= \left( \frac{Tol h}{2|z_{k+1} - y_{k+1}|} \right)^{\frac{1}{4}} \\
&\approx 0.84 \left( \frac{Tol h}{2|z_{k+1} - y_{k+1}|} \right)^{\frac{1}{4}}
\end{aligned}$$

where Tol is specified error control tolerance. The RKF scheme provides lesser error over RK methods of fourth or fifth order.

### 3.10.2 Bvp4c and Bvp5c solver

A platform for solving BVPs is provided by MATLAB, and it consists of the bvp4c and bvp5c adaptive mesh solvers, which are based on residual control. These programmes were created by Kierzenka and Shampine (2001) to solve BVPs for ordinary differential equations, and they can be used to resolve a sizable class of two-point boundary value problems of the form

$$\begin{aligned}
y'(x) &= f(y, y(x), p) \\
g(x_L, x_R, y(x_L), y(x_R), p) &= 0
\end{aligned}$$

When p is a vector of unknowable parameters, f is a continuous function, and the Lipschitz function in y. Except for the difference in the two solvers' interpretations of error tolerances, the bvp5c function can be used precisely as bvp4c. An adaptive mesh solver modifies the mesh points at each iteration throughout the iterative process, distributing them to the most critical areas. In addition to giving flexibility over the grid resolution, this can be helpful in terms of computational and storage costs. The bvp4c framework's fundamental idea

is residual in charge of mesh selection and error control (Gokhan 2011; Hale 2008). The code `bvp4c` can solve explicit nonlinear systems of order one with nonlinear boundary conditions and unknown parameters. The basic solution method is based on polynomial collocation with four Lobatto points for `bvp4c`, and five Lobatto points for `bvp5c`. The order of the method is fixed to four or five. The quantity to be estimated and controlled is residual for `bvp4c`, and residual and error in the case of `bvp5c`. The initial guess's effectiveness can also significantly impact how quickly or slowly the solution completes the problem. When making incorrect assumptions about the mesh and solution, particularly for the nonlinear BVP, the MATLAB `bvp4c` and `bvp5c` solvers adopt an unusual approach to error control. If any guess values for the length range are successful, the remaining length may be increased using continuation, which takes advantage of the fact that the answer found for one input will act as the first guess for the next value tried.

As an adaptive mesh solver based on residual control, the MATLAB BVP solver of `bvp4c` is introduced. A uniform mesh approach would describe a uniform grid of data points  $x_i$  along the range  $[x_i, x_{i+1}]$  and solve in accordance. An adaptive mesh solver is an alternate method. At each stage of the iterative process, the adaptive solver will modify the mesh points, distributing them where they are most needed, having control over the grid resolution and reduced computation. The solutions are derived from an initial guess, and based on the parameter values, an appropriate initial guess must be chosen.

The solver's syntax `soll = bvp4c (@OdeBVP, @OdeBC, solinit) @ OdeBVP`, into which system of ordinary differential equations are taken. The boundary conditions of given model or problem are then programmed into the `@OdeBC` function handle. The mesh points and initial approximation of the solution are coded using `solinit`, explained by Shampine *et al.* (2003).

### 3.10.3 Shooting Method

The shooting method reduces the boundary value problem (BVP) to an initial value problem (IVP) by assuming initial values. The boundary values calculated have to be matched with the real boundary values. They were using trial and error or some scientific approach, one attempt to get as close to the boundary value as possible. The essential step of this method is to choose the appropriate finite value for far-field boundary conditions. RK techniques are employed to solve the IVP. Unless the calculated solutions agree with known boundary conditions, the initial conditions are regulated and the problem is solved again under the same procedure. The procedure is repeated until the guessed initial conditions yield a solution that agrees with known boundary conditions under some particular tolerance. This technique consists of converting the BVP into an IVP, so fine initial values for the missing initial conditions are involved. The exactness of guesses is chosen based on how strongly the solution satisfies final boundary conditions. The initial value problem is solved by applying the RK

method and the initial conditions are adjusted. The procedure is repeated within specified tolerance until the supposed initial condition yields a solution with known boundary conditions.

### 3.11 Computational Software Environment

The computational software is required to solve these types of sets of ODEs. The mathematical computing tools which provide the numerical computing environment can be used. MATLAB has a separate suite for ODEs solvers, which are worked on 2- in-1 built-in functions of ODEs, namely, ODE23, ODE45, Bvp4c and Bvp5c. Minitab software is used to plot surface and contour plots and construct ANOVA Tables.

The methodological development related to the objectives of this study is discussed in the following sections.

### 3.12 The numerical simulation of nanoparticle size and thermal radiation with the magnetic field effect based on tangent hyperbolic nanofluid flow over a stretching sheet

When there is the inclusion of thermal radiation, a heat source, and a convective boundary, magnetohydrodynamic (MHD) micropolar, tangent hyperbolic flow for water-based  $Al_2O_3$  nanofluid over a stretching sheet, this work intends to investigate the significance of a nano particle's radius. The mathematically described ordinary differential system is created by transforming a set of partial differential equations via similarity transformations. The bvp4c approach is used to solve the problem numerically (MATLAB built-in function). The velocity profiles, temperature distribution, micro-rotation distribution, and the local skin friction factor, along with the heat transfer rate, have been displayed with several physical parameters. Graphs and tables have then been used to demonstrate the consequences of these physical parameters. The impact of influential parameters on physical quantities is illustrated using three-dimensional graphs.

#### 3.12.1 Model Description

In the graphical illustration in Figure (3.3) referencing the cartesian coordinates, the intended flow is created by movement in a vertically positioned sheet at  $y = 0$ , and fluid is occupied along  $y > 0$  in the system  $OXY$ . We analyze two-dimensional (2D) tangent hyperbolic nanofluid flow through a wall that coincides with the incompressible micropolar-based nanofluid's plane  $y = 0$ . And  $u$  represents the velocity profile component in the  $x$ , and  $v$  denotes the velocity profile component in the  $y$  directions, and  $T$  represents the fluid temperature. The Tewari and Das models (2007) for nanoparticles and thermal radiation and heat effects are all considered. The sheet is stretching with the linear velocity  $U_w = ax$ , where  $a$  is constant while keeping the origin stationary.

A uniformly magnetic field is subjected in the direction transverse to the stretching surface and is regarded a heated fluid with the  $k_{nf} \frac{\partial T}{\partial y} = -h_f(T_f - T)$  wall, and the fluid is a

water-based  $Al_2O_3$  nanofluid and the material parameter  $\gamma_{nf} = \left(\mu_{nf}j + \frac{k}{2}j\right)$  denotes the spin gradient viscosity. The nanofluid flow is predicted to be laminar and incompressible. The above assumptions and boundary layer approximations are used to develop a simplified version of the governing equations for boundary layer flow.

$$\frac{\partial u}{\partial x} + \frac{\partial v}{\partial y} = 0 \quad (3.12.1)$$

$$u \frac{\partial u}{\partial x} + v \frac{\partial v}{\partial y} = v_{nf} (1 - n) \frac{\partial^2 u}{\partial y^2} + \sqrt{2}n\Gamma v_{nf} \left(\frac{\partial u}{\partial y}\right) \frac{\partial^2 u}{\partial y^2} + \frac{\kappa}{\rho_{nf}} \frac{\partial N}{\partial y} - \sigma_{nf} \frac{B_0^2 u}{\rho_{nf}} \quad (3.12.2)$$

$$v \frac{\partial N}{\partial y} + u \frac{\partial N}{\partial x} = \frac{\gamma_{nf}}{(\rho_{nf})j} \frac{\partial^2 N}{\partial y^2} - \frac{\kappa}{(\rho_{nf})j} \left(\frac{\partial N}{\partial y} + 2N\right) \quad (3.12.3)$$

$$(\rho c_p)_{nf} \left(v \frac{\partial T}{\partial y} + u \frac{\partial T}{\partial x}\right) = \kappa_{nf} \frac{\partial^2 T}{\partial y^2} - \frac{\partial q_r}{\partial y} + Q_n(T - T_\infty) \quad (3.12.4)$$

Here,  $\kappa, j, \rho$ , and  $N$  are used to indicate the vortex viscosity, microinertia, fluid density, and angular velocity (microrotation vector). And  $\kappa_{nf}$  represents the effective thermal conductivity of the nanofluid. The following are the boundary conditions for the problem described above:

$$u = U_w = ax, v = v_w, N = -m^* \frac{\partial u}{\partial y}, \quad \frac{-k_{nf}}{h_f} \frac{\partial T}{\partial y} = (T_f - T) \text{ at } y = 0 \quad (3.12.5)$$

$$u \rightarrow 0, N \rightarrow 0, T \rightarrow T_\infty, \text{ at } y \rightarrow \infty \quad (3.12.6)$$

where  $T_f$  denotes the temperature on the wall and  $T_\infty$  signifies the ambient temperature. The boundary constant parameter  $m^*$  has a value of  $0 \leq m^* \leq 1$ . When  $m^* = 0$  and the micro elements are unable to rotate,  $N = 0$  occurs at the surface; the antisymmetric portion of the stress tensor vanishes at  $m^* = 0.5$ , and turbulent boundary layer flows occur at  $m^* = 1$ . Also,  $B_0, \mu_{nf}, \rho_{nf}$  are the magnetic field parameters, dynamic viscosity, and the density of the nanofluid, respectively.

The Rosseland (1931) approximation is expressed in terms of radiative heat flux as follows:  $q_r = \frac{4\alpha^*}{3K_1} \frac{\partial T^4}{\partial y}$ , The Roseland mean absorption coefficient is  $K_1$ , while the Stefan Boltzman constant is  $\alpha^*$ . When minimal temperature variations in the flow are explored, the Taylor series is used. After ignoring the higher-order term Brewster (1992), we get

$$q_r = \frac{4\alpha^*}{3K_1} \frac{\partial T^4}{\partial y} = \frac{16\alpha^* T_\infty^3}{3K_1} \frac{\partial T}{\partial y} \quad (3.12.7)$$

The consistent characteristics are retained except for density changes that create a thermal buoyancy force. Table (3.1) summarizes the thermophysical characteristics of  $Al_2O_3$  and water. And these values are extracted from (Ali *et al.* 2021; Aziz *et al.* 2020; Dawar *et al.* 2022)

Usually, the stream function  $\psi$  is defined as  $u = \frac{\partial\psi}{\partial y}$  and  $\frac{\partial\psi}{\partial x} = -v$  which satisfies to equation (3.12.11) and converts the set of equations (3.12.2) to (3.12.6) into ordinary differential equations; the similarity transforms listed below as Ramzan *et al.* (2016).

$$\eta = y \sqrt{\frac{a}{\nu_f}}, \quad \Psi = \sqrt{a\nu_f} f_1(\eta)x, \quad u = ax f_1'(\eta), v = -\sqrt{a\nu_f} f_1(\eta), \quad \theta = \frac{T-T_\infty}{T_f-T_\infty}, \beta = \frac{N}{ax} \sqrt{\frac{a}{\nu_f}}$$

$\psi$  and  $\eta$  represent the stream function and dimensionless parameter, respectively.

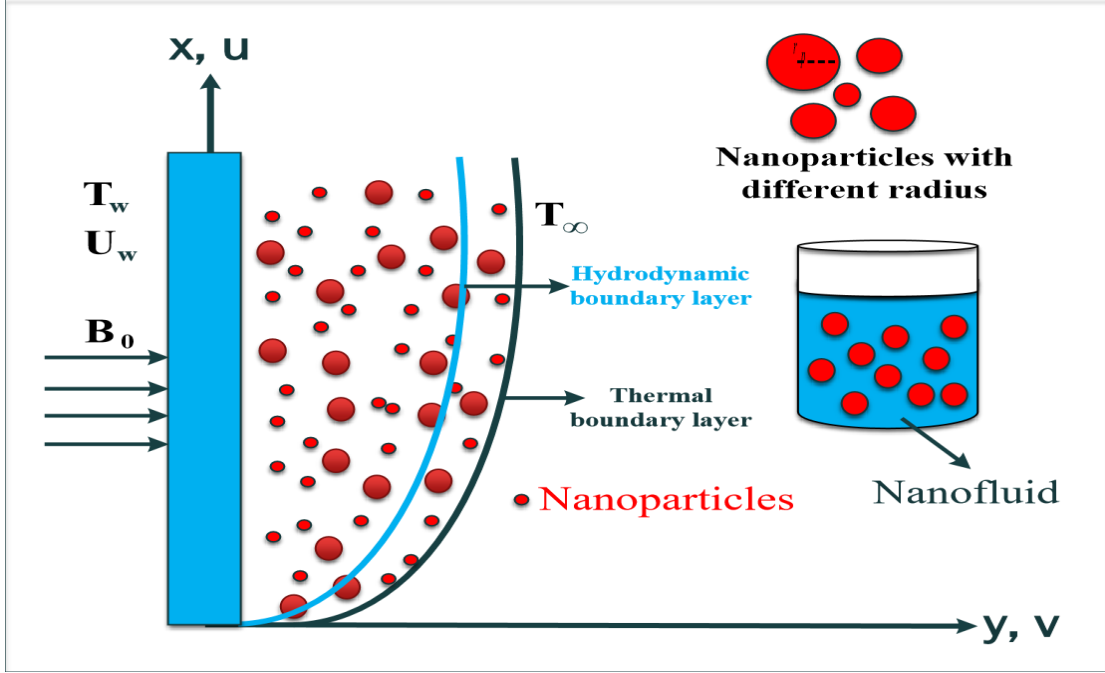


Figure 3.3 Physical flow diagram

$$\frac{B_1}{B_2}(n-1)\frac{\partial^3 f}{\partial \eta^3} - n\frac{B_1}{B_2}W\frac{\partial^2 f}{\partial \eta^2}\frac{\partial f}{\partial \eta} - K\frac{B_5}{B_2}\frac{\partial \beta}{\partial \eta} + M\frac{B_4}{B_2}\frac{\partial f}{\partial \eta} - f\frac{\partial^2 f}{\partial \eta^2} + \frac{\partial f^2}{\partial \eta^2} = 0 \quad (3.12.8)$$

$$\frac{1}{Pr}(B_5 + R_d)\frac{\partial^2 \theta}{\partial \eta^2} + Q_p\theta + B_3 f_1 \frac{\partial \theta}{\partial \eta} = 0 \quad (3.12.9)$$

$$\frac{B_1}{B_2}\left(1 + \frac{K}{2}\right)\frac{\partial^2 \beta}{\partial \eta^2} + f\frac{\partial \beta}{\partial \eta} - \frac{\partial f}{\partial \eta}\beta - K\frac{B_5}{B_2}\left(\frac{\partial f^2}{\partial \eta^2} + 2\beta\right) = 0 \quad (3.12.10)$$

and boundaries

$$f = 0, \frac{\partial f}{\partial \eta} = 1, \beta = -m^* \frac{\partial^2 f}{\partial \eta^2}, \quad B_4 \frac{\partial \theta}{\partial \eta} + Bi\theta(\eta) = (-Bi) \text{ at } \eta = 0 \quad (3.12.11)$$

$$\frac{\partial f}{\partial \eta} \rightarrow 0, \beta \rightarrow 0, \theta \rightarrow 0, \text{ at } \eta \rightarrow \infty$$

According to Graham (1981) and Gosukonda *et al.* (2015) the nanofluid's and base fluid's dynamic viscosities have the following relationship:

$$B_1 = \frac{\mu_{nf}}{\mu_{bf}} = 1 + \frac{5}{2}\varphi + 4.5 \left[ \frac{1}{\left(\frac{H}{D_p}\left(\frac{H}{D_p} + 2\right)\left(\frac{H}{D_p} + 1\right)\right)^2} \right]$$

The term  $D_p$  for the nanoparticle radius and  $H$  for the inter-particle spacing was used.

The characteristics of effective nanofluids are determined by

$$B_2 = \varphi \rho_s + \rho_f(1-\varphi) \quad B_3 = \varphi \frac{(\rho c_p)_s}{(\rho c_p)_f} + (\rho c_p)_f(1-\varphi),$$

$$B_4 = \frac{2k_f + k_s - 2\varphi(k_f - k_s)}{2k_f + k_s + \varphi(k_f - k_s)}, \quad B_5 = 1 + 3 \frac{(\frac{\sigma_s}{\sigma_f} - 1)\varphi}{(\frac{\sigma_s}{\sigma_f} + 2) - (\frac{\sigma_s}{\sigma_f} - 1)\varphi},$$

Where the involving parameters are defined as  $B_5$  is electrical conductivity ( $\sigma_{nf}$ ) taken from the Maxwell Garnett model (1904). The thermal conductivity of fluid can be determined by Maxwell Garnett's (MG model) self-consistent approximation model, effective density, specific heat, and thermal conductivity of nanofluid by Tiwari and Das (2007) Here,  $F_w$  is the suction parameter, magnetic field parameter  $M$ , Prandtl number  $Pr$ , Weissenberg number  $W$ , heat source parameter  $Q_p$ , Biot number  $B_i$ , and radiation parameter  $R_d$ , material parameter  $K$ .

$$F_w = -\frac{v_w}{\sqrt{av}}, \quad M = \frac{\sigma_f B_0^2}{a\rho_f}, \quad W = \Gamma x \sqrt{\frac{2a^3}{v_f}}, \quad Pr = \frac{v_f}{\alpha}$$

$$R_d = \frac{4\alpha^* T^3}{3K_1 k_f}, \quad Bi = \frac{h_f}{k_f} \sqrt{\frac{v_f}{a}}, \quad Q_p = \frac{Q_h}{a(\rho c_p)_f}, \quad K = \frac{k_f}{v_f}$$

### 3.12.2 Engineering Quantities

The skin friction coefficient  $C_{f_x}$  and Nusselt number  $Nu_x$  are defined as

$$C_{f_x} = \frac{\tau_w}{\rho_f (U_w)^2} = \frac{\mu_{nf} \frac{\partial u}{\partial x} |_{y=0}}{\rho_f (U_w)^2}, \quad Nu_x = \frac{x q_w}{k_f (T_f - T_\infty)} = \frac{-x k_{nf} \frac{\partial T}{\partial y} |_{y=0}}{k_f (T_f - T_\infty)}$$

Where  $q_w, \tau_w$  are heat flux, and shear stress respectively. The dimensionless Nusselt number  $Nu_x$  and friction drag coefficient  $C_{f_x}$  are described as,

$$\frac{1}{2} \sqrt{Re^x} C_{f_x} = \frac{B_1}{B_2} (1-n) \frac{\partial^2 f_1(0)}{\partial \eta^2} + \frac{B_1 n}{B_2} W \frac{\partial^2 f_1(0)}{\partial \eta^2}, \quad \frac{Nu_x}{\sqrt{Re^x}} = -(B_5 + R_d) \frac{\partial \theta(0)}{\partial \eta}$$

where  $\sqrt{Re^x} = \frac{\sqrt{ax}}{\sqrt{v_f}}$  is Reynold number.

### 3.12.3 Method of Solution and Validation

The bvp4c solver, which is a MATLAB built-in function, solves the equations and boundary conditions numerically. The solutions are derived from an initial guess, and based on the parameter values, an appropriate initial guess must be chosen. The first step is to reduce the partial governing equations to a series of first-order ordinary differential equations. As a result, the set of equations (3.12.8–3.12.11) is written as follows:

$$f_1 = y_1, \quad f_1' = y_2, \quad f_1'' = y_3$$

$$f_1''' = \frac{1}{B_1 [n(1 - W y_3) - 1]} [B_5 K y_7 - B_4 M y_2 + B_2 (y_1 y_3 - y_2^2)]$$

$$\theta = y_4, \theta' = y_5, \theta'' = \frac{-P_r}{[B_5 + R_d]} [Q_p y_4 + B_3 y_2 + B_2 y_1 y_5]$$

$$\beta = y_6, \beta' = y_7, \beta'' = \frac{2}{B_1 [(2 + K)]} [B_2 y_6 y_2 - B_2 y_1 y_7 + K B_5 (y_3 + 2y_6^2)]$$

The boundary conditions as

$$y_1^a = F_w, y_2^a = 1, B_5 y_5^a - B_i y_4^a + B_i = 0$$

$$y_2^r = 0, y_4^r = 0, y_6^a + m^* y_3^a = 0, y_6^r = 0$$

### 3.13 Magnetohydrodynamic boundary layer flow of nanofluid over an exponential stretching sheet with thermal radiation and Slip effect on boundary condition

This research investigates the magnetohydrodynamic flow of an ethylene glycol-based nanofluid containing Copper nanoparticles over an exponentially stretching sheet. Brownian diffusion parameter, thermophoretic parameter, thermal radiation parameter, and Joule effect are studied for their impact on fluid flow, concentration, and heat transfer profiles with convective boundary conditions, whereas Navier slips effect has been considered simultaneously. The fundamental partial differential equations are converted into non-dimensional ODE's using proper similarity transformations and numerically solved using bvp4c in MATLAB. The graphs explore at the effects of pertinent parameters on the profiles of mass, heat, and velocity transfers. In two and three-dimensional graphs and tables, the influence of several physical quantities were illustrated.

#### 3.13.1 Physical Model and Mathematical Formulation

The two-dimensional, incompressible flow of water-based Copper nanofluid over an exponentially stretching sheet has been considered. An exponentially stretching sheet is visualized in Figure (3.4) by the  $x$  coordinate running to flow direction and the  $y$  co-ordinate perpendicular to flow direction. Furthermore, fluid flow is subjected to the magnetic field  $B_0$  in a normal direction. Additionally, the effects of additional factors such as Joule heating, thermal radiation, thermophoresis, and Brownian motion was analyzed. The linear velocity  $U_w = e^{\frac{x}{L}}$  in  $x$  direction and convective condition at the wall is  $-\kappa_{nf} \frac{\partial T}{\partial y} = h_f (T_f - T)$ , where  $h_f = h e^{\frac{x}{L}}$  is the convective heat transfer coefficient. In accordance with the model equations provided by Tiwari and Das (2007), the fundamental continuity, momentum, energy, and concentration equations are as follows:

$$\frac{\partial u}{\partial x} + \frac{\partial v}{\partial y} = 0 \quad (3.13.1)$$

$$u \frac{\partial(u)}{\partial x} + v \frac{\partial(u)}{\partial y} = \nu_{nf} \frac{\partial^2 u}{\partial y^2} - \frac{\sigma_{nf}}{\rho_{nf}} B_0^2 u \quad (3.13.2)$$

$$u \frac{\partial(T)}{\partial x} + v \frac{\partial(T)}{\partial y} = \frac{\kappa_{nf}}{(\rho C_p)_{nf}} \frac{\partial^2 T}{\partial y^2} + \frac{\sigma_{nf} B_0^2 u^2}{(\rho C_p)_{nf}} - \frac{1}{(\rho C_p)_{nf}} \frac{\partial q_r}{\partial y} \quad (3.13.3)$$

$$\begin{aligned}
& + \frac{\tau}{(\rho C_p)_{nf}} \left[ D_B \left( \frac{\partial T}{\partial y} \frac{\partial C}{\partial y} \right) + \frac{D_T}{T_\infty} \left( \frac{\partial T}{\partial y} \right)^2 \right] \\
u \frac{\partial(C)}{\partial x} + v \frac{\partial(C)}{\partial y} & = D_B \frac{\partial^2 C}{\partial y^2} + \frac{D_T}{T_\infty} \left( \frac{\partial^2 T}{\partial y^2} \right)
\end{aligned} \tag{3.13.4}$$

In addition,  $T$  represents the fluid temperature,  $(u, v)$  shows a component of velocity, thermophoretic diffusion coefficient, is represented by  $D_T$  respectively.  $\alpha_1$  denotes the diameter of the magnets positioned in the interval separating the electrodes.

Here the boundary condition we have for the problem above:

$$u = \exp\left(\frac{x}{L}\right) + Nv_f U_w, v = 0, -\kappa_{nf} \frac{\partial T}{\partial y} = h_f(-T + T_f), C = C_w \text{ at } y = 0 \tag{3.13.5}$$

$$u \rightarrow 0, T \rightarrow T_\infty, C \rightarrow C_\infty \text{ at } y \rightarrow \infty \tag{3.13.6}$$

where  $T_f$  denotes the wall temperature. Also  $N, B_0, \mu_{nf}, \rho_{nf}, h_f$  are the slip velocity factor, magnetic field parameter, viscosity, density and the convective heat transfer coefficient respectively.

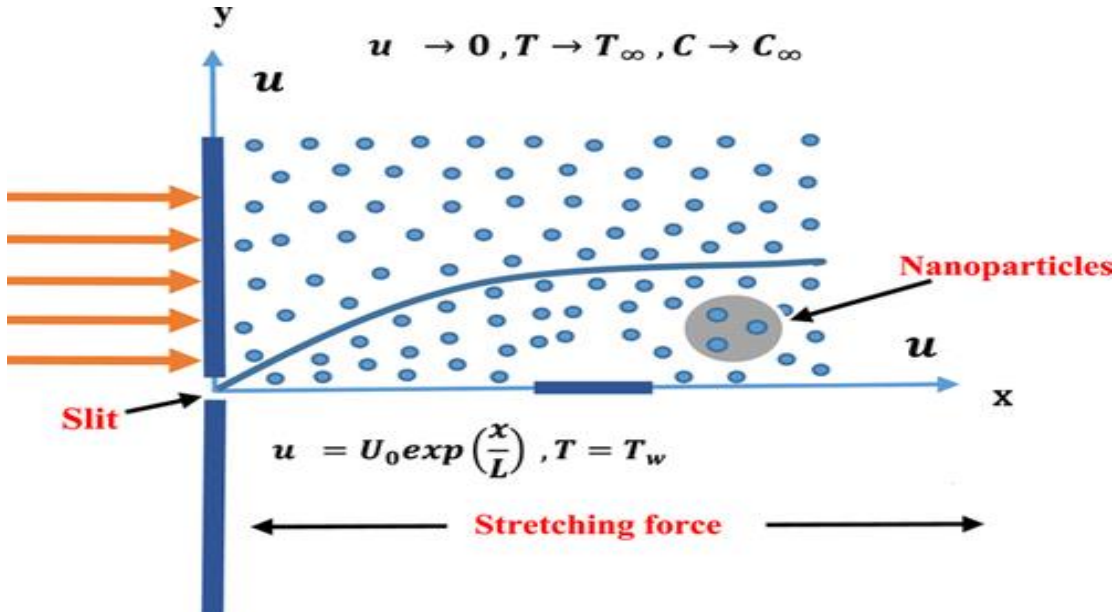


**Figure 3.4 A pictorial representation of the model**

When expressing the radiative heat flux, the Rosseland (1931) approximation was used as follows  $q_r = \frac{4\alpha^*}{3K_1} \frac{\partial T^4}{\partial y}$ . Where,  $K_1$  is Roseland's mean absorption co-efficient and  $\alpha^*$  is the Boltzmann constant. Assuming minimal temperature variations in the flow, we get using Taylor series, neglecting the higher-order variables, and assuming small temperature fluctuations in the flow Datti *et al.* (2004).

$$q_r = \frac{4\alpha^* \partial T^4}{3K_1 \partial y} = -\frac{16\alpha^* T_\infty^3 \partial T}{3K_1 \partial y}$$

The properties of Copper nanoparticle and base fluid water are showcased in Table (3.3). The similarity techniques used to transform governing equations (3.13.1) to (3.13.4) are listed below Hayat *et al.* (2017).

$$u = U_0 e^{\frac{x}{L}} f'(\eta), \quad (T_f - T_\infty) \theta = (T - T_\infty), \quad y \sqrt{\frac{U_0}{2Lv_f}} e^{\frac{zx}{L}} = \eta$$

$$\Psi(C_f - C_\infty) = (C - C_\infty), \quad v = y \sqrt{\frac{U_0 v_f}{2L}} e^{\frac{x}{L}} (f(\eta) + \eta f'(\eta))$$

Using the similarity techniques listed above, the governing equations are converted to ODEs as follows:

$$\frac{B_1 \partial^3 f}{B_2 \partial \xi^3} - \frac{\partial f^2}{\partial \xi^2} + f \frac{\partial^2 f}{\partial \xi^2} - \frac{M \partial f}{B_2 \partial \xi} = 0 \quad (3.13.7)$$

$$\frac{1}{B_3 Pr} (B_4 + R_d) \frac{\partial^2 \theta}{\partial \xi^2} + \frac{ME_C}{B_3} \left( \frac{\partial f}{\partial \xi} \right)^2 + N_B \frac{\partial \theta}{\partial \xi} \frac{\partial \Psi}{\partial \xi} + N_T \left( \frac{\partial \theta}{\partial \xi} \right)^2 + f \frac{\partial \theta}{\partial \xi} = 0 \quad (3.13.8)$$

$$\frac{\partial^2 \Psi}{\partial \xi^2} - S_C f \frac{\partial \Psi}{\partial \xi} - \frac{N_T \partial^2 \theta}{N_B \partial \xi^2} = 0 \quad (3.13.9)$$

And the boundary conditions are;

$$f = 0, \quad f' = 1 + \lambda f'', \quad A_4 \theta' - B_i = -B_i, \quad \Psi = 1 \text{ at } \eta = 0$$

$$f' \rightarrow 0, \quad \theta \rightarrow 0, \quad \Psi \rightarrow 0 \text{ at } \eta \rightarrow \infty \quad (3.13.10)$$

$$B_1 = (1 - \phi)^{-5}, \quad B_2 = \phi \rho_s - \rho_f (\phi - 1),$$

$$B_3 = \phi \frac{(\rho c_p)_s}{(\rho c_p)_f} + (1 - \phi), \quad B_4 = \frac{2k_f + k_s - 2(\phi k_f - \phi k_s)}{2k_f + k_s + (\phi k_f - \phi k_s)}$$

Here,  $\mu_f$  refers to the dynamic viscosity of the base fluid,  $\phi$  refers to the volume fraction of solids,  $\rho_f$  and  $\rho_s$  refer to the densities. There are  $\kappa_f$  and  $\kappa_s$  thermal conductivities,  $(\rho c_p)_f$  and  $(\rho c_p)_s$  thermal conductivities based on the heat conduction capacity of the base fluid and nanoparticles. The effective thermal conductivity of fluid using Maxwell Garnett's model by adjusting the magnetic field, Prandtl number  $Pr$ , Biot number  $Bi$ , and thermophoretic variable  $N_T$ , Schmidt number  $S_C$ , Eckert number  $E_C$ , brownian diffusion  $N_B$ , slip effect  $\lambda$  and radiation parameter  $R_d$ .

$$M = \frac{\sigma_{nf} B_0^2}{\rho_{nf} a}, \quad E_C = \frac{U_w^2}{(T_f - T_\infty)(c_p)_f}, \quad Pr = \frac{(\mu c_p)_f}{\kappa_{nf}},$$

$$R_d = \frac{16\alpha^* T^3}{3K_1 \kappa_{nf}}, \quad N_B = \frac{\tau^*(\zeta_w - \zeta_\infty)D_B}{v_f}, \quad N_T = \frac{\tau^*(T_w - T_\infty)D_T}{v_f T_\infty},$$

$$S_c = \frac{v_{nf}}{D_B}, \quad \lambda = N_0 \sqrt{\frac{(U_0 v_f)}{2L}}, \quad B_i = \frac{h_f}{\kappa_{nf}} \sqrt{\frac{v_f}{a}},$$

### 3.13.2 Method of Solution and Validation

Mathematical equations and boundary conditions are solved numerically using the `bvp4c` solver in MATLAB. In this approach, Runge–Kutta formula is used to achieve numerical solutions. In order to satisfy the boundary layer thickness requirement, the appropriate initial guess as well as the parameter values must be determined (Kierzenka and Shampine (2008), Kandasamy *et al.* (2016)). Below are three reduced sets of first-order ordinary differential equations (3.13.7-3.13.10):

$$\begin{aligned} f &= y_1, f' = y_2, f'' = y_3, \\ f''' &= \frac{1}{B_1} [B_2(2(y_2)^2 - y_1 y_3) + M y_2] \\ \theta &= y_4, \theta' = y_5, \\ \theta'' &= \frac{-P_r}{[B_4 + R_d]} [M E_C y_2^2 + A_3(N_B y_7 y_5 + N_T (y_5)^2 + y_1 y_5)] \\ \varphi &= y_6, \varphi' = y_7, \\ \varphi'' &= - \left[ S_C y_7 y_1 + \frac{N_T}{N_B} \frac{-P_r}{[B_4 + R_d]} \{M E_C y_2^2 + B_3(N_B y_7 y_5 + N_T (y_5)^2 + y_1 y_5)\} \right] \end{aligned}$$

As boundary conditions are

$$\begin{aligned} y_1(0) &= 0, y_2(0) = 1 + \lambda y_3, B_4 y_5(0) + B_i y_4(0) + B_i, y_6 = 1, \\ y_2(\infty) &\rightarrow 0, y_4(\infty) \rightarrow 0, y_6(\infty) \rightarrow 0 \end{aligned}$$

### 3.13.3 Physical Quantities

The local skin friction coefficient, the local Nusselt-number, and the local Sherwood number are defined as

$$Sh_x = \left[ \frac{x q_p}{D_m (C_f - C_\infty)} \right]_{y=0}, \quad Nu_x = \left[ \frac{x q_w}{\kappa_f (T_f - T_\infty)} \right]_{y=0}, \quad Cf_x = \left[ \frac{\tau_w}{U_w \rho_f} \right]_{u,y=0}$$

Where  $\tau_w, q_w, q_p$  are shear stress, heat flux, and the mass flux at the surface respectively.

The above quantities  $Cf_x, Nu_x,$  and  $Sh_x$  can be written in non-dimensional as:

$$\sqrt{Re_x} Cf_x = \frac{\partial f^2(0)}{\partial \xi^2}, \quad \frac{Nu_x}{\sqrt{Re_x}} = -(B_4 + R_d) \frac{\partial \theta(0)}{\partial \xi}, \quad \frac{Sh_x}{\sqrt{Re_x}} = -\frac{\partial \Psi(0)}{\partial \xi}$$

## 3.14 The dynamics of active and passive controls over the measurement of thermal conductivity of nanofluids subject to magnetic field and thermal radiation through the stretching surface

This extensive study enhances heat transformation while accounting for the magnetohydrodynamic (MHD) nanofluid flow with the impact of non-linear thermal radiation and an irregular heat source over the stretching sheet. The impact of Arrhenius activation energy with active and passive controls of nanoparticles, thermophoresis and Brownian

diffusion has elaborated. The system of partial differential equations is first represented mathematically and converted into the system of ordinary differential equations using similarity transformations. A well-known Runge Kutta method with a shooting technique is implemented for numerical analysis. The influence of various parameters is displayed through tables numerically, graphical impact, and surface plots on heat and mass transfer, micro-rotation distribution, and the Nusselt number.

### 3.14.1 Model Description

Consider the two-dimensional flow of a water-based nanofluid containing nanoparticles ( $Ag$ ) over a nonlinear stretching surface under situations of zero and nonzero mass flux of nanoparticles. A non-uniform magnetic field of strength  $B_0$  is applied to the stretching sheet in the  $y$ -direction. It adopts a nanofluid model responsive to thermophoresis and Brownian motion. Referencing the cartesian coordinate, the graphical representation is shown in Figure (3.5). The stretching velocity is  $U_w = ax^n$ , where  $a$  is constant, and  $n > 0$  as the constants. Additionally, the impacts of magnetic parameters, activation energy, and nonlinear thermal radiation are taken into consideration. It is anticipated that the nanofluid flow will be laminar and incompressible. The governing equations for boundary layer flow are developed using the aforementioned presumptions and boundary layer approximations as,

$$\frac{\partial u}{\partial x} + \frac{\partial v}{\partial y} = 0 \quad (3.14.1)$$

$$u \frac{\partial u}{\partial x} + v \frac{\partial v}{\partial y} = (\mu_{nf} + \kappa) \frac{\partial^2 u}{\partial y^2} - \frac{\sigma_{nf}}{\rho_{nf}} (B_0^2 u) + \frac{\kappa_{nf}}{\sigma_{nf}} \frac{\partial N}{\partial y} \quad (3.14.2)$$

$$v \frac{\partial N}{\partial y} + u \frac{\partial N}{\partial x} = \frac{\gamma_{nf}}{(\rho_{nf})_j} \frac{\partial^2 N}{\partial y^2} - \frac{\kappa_{nf}}{(\rho_{nf})_j} \left( \frac{\partial N}{\partial y} + 2N \right) \quad (3.14.3)$$

$$\begin{aligned} (\rho C_p)_{nf} \left( u \frac{\partial T}{\partial x} + v \frac{\partial T}{\partial y} \right) = & k_{nf} \left( \frac{\partial^2 T}{\partial y^2} \right) + (\rho C_p)_p \left\{ D_B \left( \frac{\partial T}{\partial y} \frac{\partial C}{\partial y} \right) + \frac{D_T}{T_\infty} \left[ \left( \frac{\partial T}{\partial y} \right)^2 \right] \right\} \\ & - Q_e^* (T_w - T_\infty) e^{-m \sqrt{\frac{\alpha}{\nu_f}} x^{\left(\frac{n-1}{2}\right)} y} + \frac{\partial}{\partial z} \left( \frac{16\sigma^*}{3k^*} T^3 \frac{\partial T}{\partial y} \right), \end{aligned} \quad (3.14.4)$$

$$u \frac{\partial C}{\partial x} + v \frac{\partial C}{\partial y} = D_B \frac{\partial^2 C}{\partial y^2} - k_r^2 (C - C_\infty) \left( \frac{T}{T_\infty} \right)^m e^{-\frac{E_a}{K^* T}} \quad (3.14.5)$$

In addition,  $u$  represents the velocity profile component in the  $x$ ,  $v$  denotes the velocity profile component in the  $y$  directions, and  $T$  represents the fluid temperature. Also, the material parameter  $\gamma_{nf} = (\mu_{nf} j + \frac{k}{2} j)$  denotes the spin gradient viscosity. Furthermore,  $\kappa, j, \rho$ , and  $N$  are used to indicate viscosity vortex, micro inertia, fluid density,

and angular velocity (micro-rotation vector). The following are the boundary conditions for the problem described above:

$$u = U_w = ax^n, v = v_w, N = -m_1^* \frac{\partial u}{\partial y}, \quad -\frac{\kappa_{nf}}{h_f} \frac{\partial T}{\partial y} = (T_f - T), \quad (3.14.6)$$

$$D_B \left( \frac{\partial C}{\partial y} \right) + \frac{D_T}{T_\infty} \left( \frac{\partial T}{\partial y} \right) = 0 \text{ for passive control,} \\ C = C_w \text{ for active control} \quad \text{at } y = 0$$

$$u \rightarrow 0, \quad N \rightarrow 0, \quad T \rightarrow T_\infty, \quad C \rightarrow C_\infty \quad \text{at } y \rightarrow \infty \quad (3.14.7)$$

where  $T_f$  denotes the temperature on the wall and  $T_\infty$  signifies the ambient temperature. The boundary constant parameter  $m_1^*$  has a value of  $0 \leq m_1^* \leq 1$ . When  $m_1^* = 0$  and the micro elements are unable to rotate,  $N = 0$  occurs at the surface; the antisymmetric portion of the stress tensor vanishes at  $m_1^* = 0.5$ , and turbulent boundary layer flows occur at  $m_1^* = 1$ . Also  $B_0, \mu_{nf}, \rho_{nf}$  are the magnetic field parameters, dynamic viscosity, and the density of the based fluid, respectively. The consistent characteristics are retained with the exception of density changes that create a thermal buoyancy force. Table 3.3 summarizes the thermophysical characteristics of nanofluid and water.

The efficient nanofluids have features that are determined by

$$\frac{\mu_{nf}}{\mu_f} = \frac{1}{(1 - \phi_1)^{2.5}} = A_1, \quad \frac{\rho_{nf}}{\rho_f} = \left( (1 - \phi_1) + \phi_1 \frac{\rho_s}{\rho_f} \right) = A_2$$

$$\frac{\sigma_{nf}}{\sigma_f} = 1 + \frac{3 \left( \frac{\phi_1 \sigma_s}{\sigma_f} - (\phi_1) \right)}{2 + \left( \frac{\phi_1 \sigma_s}{(\phi_1) \sigma_f} \right) - \left( \frac{\phi_1 \sigma_s}{\sigma_f} - (\phi_1) \right)} = A_3$$

$$\frac{k_{nf}}{k_f} = \frac{k_s + 2k_f - 2\phi_1(k_f - k_s)}{k_s + 2k_f + \phi_1(k_f - k_s)} = A_4,$$

$$\frac{(\rho C)_{nf}}{(\rho C)_f} = \left( 1 - \phi_1 + \phi_1 \frac{(\rho C)_s}{(\rho C)_f} \right) = A_5$$

Here,  $\phi$  represents the volume fraction of solids, and  $\mu_f$  stands for the base fluid's dynamic viscosity. The base fluid and nanoparticles have densities of  $\rho_f$  and  $\rho_s$ , thermal conductivities of  $\kappa_f$  and  $\kappa_s$ , electrical conductivities of  $\sigma_f$  and  $\sigma_s$ , and heat capacitances of  $(\rho c_p)_f$  and  $(\rho c_p)_s$ , respectively.

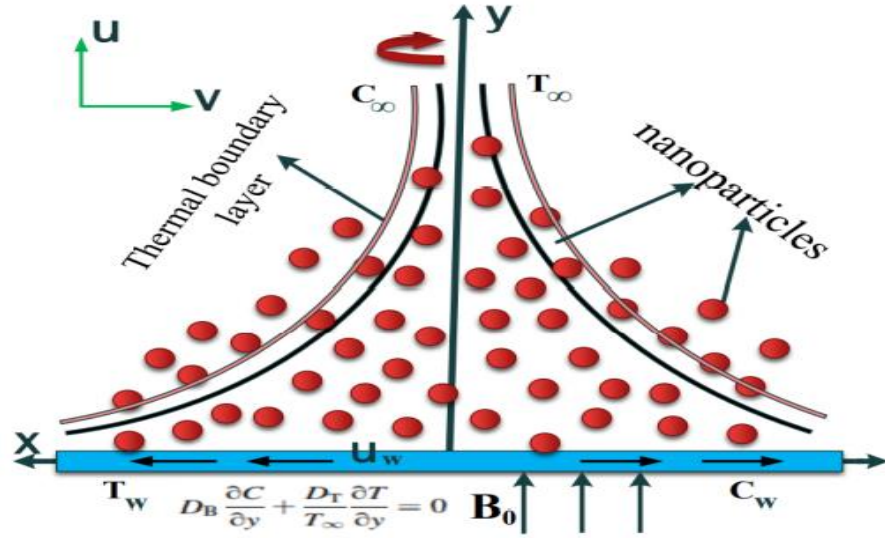


Figure 3.5 Physical flow diagram

The similarity transforms described below are used to transform the equations (3.14.2) to (3.14.5) in the set of ordinary differential equations (Abo-Dahab *et al.* 2021; Ahmad *et al.* 2021; Halim *et al.* 2017) as,

$$u = ax^n f'(\eta); \quad v = -ax^{\frac{n-1}{2}} \sqrt{\frac{\bar{v}}{a}} \left[ \left( \frac{n+1}{2} \right) f(\eta) + \left( \frac{n-1}{2} \right) \eta f'(\eta) \right]$$

$$\eta = \sqrt{\frac{\bar{a}}{v}} x^{\left( \frac{n-1}{2} \right)} y; \quad \theta(\eta) = \frac{T - T_\infty}{T_w - T_\infty},$$

$$\phi(\eta) = \frac{c - c_\infty}{c_w - c_\infty} \quad \text{for active case}$$

$$\phi(\eta) = \frac{c - c_\infty}{c_\infty} \quad \text{for passive case}$$

The dimensionless coordinate and the stream function are denoted by the symbols  $\eta$  and  $\psi$ . The resulting system of equations is attained as,

$$\frac{A_1 + K}{A_2} f''' - \frac{A_3}{A_2} M f' + \left( \frac{n+1}{2} \right) f f'' - n f'^2 + \frac{K}{A_2} G' = 0 \quad (3.14.8.)$$

$$\left( 1 + \frac{K}{2} \right) \frac{A_1}{A_2} G'' - (2G + f'') \left( \frac{K}{A_2} \right) + \left( \frac{n+1}{2} f G' - \frac{(3n-1)}{2} f' G' \right) = 0 \quad (3.14.9)$$

$$\left( \frac{A_4}{A_5} \right) \frac{1}{P_r} \theta'' + \left( \frac{4R_d}{3A_5 P_r} \right) [(\theta_M - 1)\theta + 1]^3 \theta'' + \left( \frac{4R_d}{A_5 P_r} \right) [(\theta_M - 1)\theta + 1]^2 (\theta_M - 1) (\theta')^2$$

$$+ \left( \frac{N_b}{A_5} \right) \theta' \Psi' + \left( \frac{N_t}{A_5} \right) \theta'^2 + \left( \frac{Q_E}{A_5} \right) e^{-m\eta} + \left( \frac{n+1}{2} \right) f \theta' - n f' \theta = 0 \quad (3.14.10)$$

$$\Psi'' + \frac{S_c(n+1)}{2} f \Psi' + \frac{N_t}{N_b} \theta'' - K_r S_c \Psi (1 + \delta \theta)^n \varrho \left( -\frac{E_a}{1 + \delta \theta} \right) = 0 \quad (3.14.11)$$

And the transformed boundary conditions are as,

$$f(0) = f_w, f'(0) = 1, \theta'(0) - B_i(1 - \theta(0)); G = -m_1^* f'';$$

$$N_b \Psi'(0) + N_t \theta'(0); \text{ for passive control,}$$

$$\Psi(0) = 1; \text{ for active control,}$$

$$f' \rightarrow 0, \theta(0) \rightarrow 0, \Psi(\infty) \rightarrow 0; G \rightarrow 0 \text{ as } \eta \rightarrow \infty$$

Where the involving parameters magnetic field parameter (M), Prandtl number ( $Pr$ ), Biot number (Bi), and radiation parameter (Rd), material parameter (K).

### 3.14.2 Method of Solution and Validation

The system of governing equations (3.14.8-3.14.11) are solved numerically by using RK method with shooting technique. The mathematical solution of the equation by Runge-Kutta method (for solutions) in MATLAB with the Newton-Raphson method (Kiusalaas 2005; Kalaivanan *et al.* 2020).

We do this by first assuming that;

$$\begin{aligned} f &= y_1, f' = y_2, f'' = y_3, G = y_4, G' = y_5, \theta = y_6, \theta' = y_7, \Psi = y_8, \Psi' = y_9, \\ y_2' &= y_3 \\ y_3' &= \left(\frac{A_2}{A_1}\right) \left[ \eta y_2^2 - \left(\frac{n+1}{2}\right) (y_3 y_1) \right] + \frac{A_3}{A_1} M y_2 - \left(\frac{K}{A_1}\right) y_4 \\ y_4' &= y_5 \\ y_5' &= \left(\frac{2}{K+2}\right) \left[ \left(\frac{K}{A_1}\right) (2y_4 + y_3) - \left(\frac{A_2}{A_1}\right) \left(\frac{n+1}{2}\right) (y_5 y_1) - \frac{(3n-1)}{2} y_2 y_4 \right]; \\ y_6' &= y_7 \\ y_7' &= \frac{Pr}{\left[ \left(A_4 + \frac{4}{3} R_d\right) (Q_M - 1) y_6 + 1 \right]^3} \left[ A_5 \eta y_2 y_6 - A_5 \left(\frac{n+1}{2}\right) y_1 y_7 - N_b y_7 y_9 - N_t (y_7)^2 \right. \\ &\quad \left. - Q_E e^{-mx} - \frac{4R_d}{Pr} (\theta_M - 1) (y_7)^2 \right] \\ y_9' &= -S_c \left[ \left(\frac{n+1}{2}\right) y_1 y_9 - \frac{N_t}{N_b} \theta'' + K_r (1 + \delta y_6^n) y_8 e^{-\frac{E_a}{(1+\delta y_6)}} \right]; \end{aligned}$$

Subject to the boundary conditions as,

For active case

$$\begin{aligned} y_1^a &= F_w; y_2^a = 1; y_4^a = m^* y_2^a, A_4 y_7^a = B_i (y_6^a - 1), y_8^a = 1; \\ y_2^b &= 0; y_4^b = 0; y_6^b = 0; y_8^b = 0 \end{aligned}$$

For active case

$$\begin{aligned} y_1^a &= F_w; y_2^a = 1; y_4^a = m^* y_2^a, A_4 y_7^a = B_i (y_6^a - 1), N_b y_9^a + N_t y_7^a, \\ y_2^b &= 0, y_4^b = 0, y_6^b = 0, y_8^b = 0 \end{aligned}$$

Where  $y_3(0) = \Delta_1, y_5(0) = \Delta_2, y_7(0) = \Delta_3, y_9(0) = \Delta_4$  are calculated with an appropriate initial guess using the Newton Raphson technique.

### 3.14.3 Engineering Quantities

The skin friction coefficient  $C_{f_x}$  and Nusselt number  $Nu_x$  are defined as

$$C_{f_x} = \frac{\tau_w}{\rho_f (U_w)^2} = \frac{\mu_{nf} \frac{\partial u}{\partial x} |_{y=0}}{\rho_f (U_w)^2}, Nu_x = \frac{x q_w}{k_f (T_f - T_\infty)} = \frac{-x k_{nf} \frac{\partial T}{\partial y} |_{y=0}}{k_f (T_f - T_\infty)}$$

Where  $q_w, \tau_w$  are heat flux, and shear stress respectively. The dimensionless Nusselt number  $Nu_x$ , Sherwood number  $Sh_x$ , and friction drag coefficient  $Cf_x$  are described as,

$$\frac{1}{2}\sqrt{Re^x}Cf_x = (A_1 + (1 + m^*)K)\frac{\partial^2 F(0)}{\partial \eta^2},$$

$$Nu_x Re_x^{-\frac{1}{2}} = -\left\{A_4 + \left(\frac{4R_d}{3}\right)[(\theta_m - 1) + 1]^3\right\}\frac{\partial \theta(0)}{\partial \eta}$$

$$Sh_x Re_x^{-\frac{1}{2}} = \frac{\partial C(0)}{\partial \eta}$$

where  $\sqrt{Re^x} = \frac{\sqrt{ax}}{\sqrt{\nu_f}}$  is Reynold number.

### 3.15 Heat transfer analysis of thermally convective nanofluid flow over the stretching cylinder with the impact of heat flux model

This study focused on sensitivity analysis of two-dimensional incompressible magnetohydrodynamic hybrid nanofluid Cu – Ag/water and  $TiO_2$  – Ag/water flow across a stretching cylinder containing microorganisms with impacts of chemical reaction, mixed convection, heat source, and convective boundary condition. The response surface methodology technique and the sensitivity analysis has used to examine the effects of nanoparticle volume fraction, Biot number, and magnetic parameter on the rate of heat transfer statistically. A set of equations is formed from the governing partial differential equations by implementing suitable similarity transformations. A well-known method Runge Kutta with shooting has used. The influence of various parameters has been displayed through tables, graphs, and surface plots on heat transfer, mass transfer, and local Nusselt number.

#### 3.15.1 Physical Pattern and Interpretation

The motion across the cylinder depicted in Figure (3.6) induces the proposed flow. Heat and mass transfer are analyzed using a 2D mathematical model in this section. Hybrid nanofluid flow with microorganisms in the presence of chemically reactive species towards a cylinder with radius  $R$  with free stream velocity  $U$  was considered. The impacts of chemical reaction, mixed convection parameter, and the heat source are included in this paper to broaden the scope of the research. Let free stream velocity  $u_w = \frac{ax}{l}$  flow over the cylinder, where  $a$  is a positive constant. The  $x$ -axis along the cylinder's surface and  $r$  in the axial direction are both taken into consideration by the coordination system. Convective heating from a hot fluid causes the surface temperature, which is indicated by  $T$ , and thermal efficiency, which is indicated by  $h_f$ . Under the boundary stacking and Oberbeck-Boussinesq approximations, the viscous effects of dissipation are ignored. The heated fluid along the wall is characterized as  $-k_{nf} \frac{\partial T}{\partial r} = h_f(T - T_\infty)$ . The thermo-physical characteristics of nanoparticles are shown in Table 3.1. The aggregation of tiny particles is disregarded since the nanofluid mixture is assumed to be a stable substance. The Cattaneo Christov heat flux

prototype and the Tiwari and Das (2007) model have both been considered. Based on these assumptions, we can derive the following governing equations:

$$\frac{\partial(ru)}{\partial x} + \frac{\partial(rv)}{\partial r} = 0 \quad (3.15.1)$$

$$u \frac{\partial u}{\partial x} + v \frac{\partial u}{\partial r} = \frac{\mu_{hnf}}{\rho_{hnf}} \left( \frac{\partial^2 u}{\partial r^2} + \frac{1}{r} \frac{\partial u}{\partial r} \right) - \frac{\sigma B_0^2 u}{\sigma_{hnf}} + \left[ \frac{(\rho\beta)_{hnf}}{\rho_{hnf}} g(T - T_\infty) \right] \quad (3.15.2)$$

$$(\rho C_p)_{hnf} \left( u \frac{\partial T}{\partial x} + v \frac{\partial T}{\partial r} \right) = -(\rho C_p)_{hnf} \delta T_\delta + \kappa_{hnf} \left( \frac{\partial^2 T}{\partial r^2} + \frac{1}{r} \frac{\partial T}{\partial r} \right) \quad (3.15.3)$$

$$u \frac{\partial C}{\partial x} + v \frac{\partial C}{\partial r} + K_c(C - C_\infty) = D_m \left( \frac{\partial^2 C}{\partial r^2} + \frac{1}{r} \frac{\partial C}{\partial r} \right) + \frac{D_m \kappa_t}{T_m} \left( \frac{\partial^2 T}{\partial r^2} + \frac{1}{r} \frac{\partial T}{\partial r} \right) \quad (3.15.4)$$

$$u \frac{\partial N}{\partial x} + v \frac{\partial N}{\partial r} + K_c(N - N_\infty) = -\frac{bW_c}{C_w - C_\infty} \left[ \frac{\partial}{\partial r} \left( N \frac{\partial C}{\partial r} \right) \right] + D_n \left( \frac{\partial^2 N}{\partial r^2} + \frac{1}{r} \frac{\partial N}{\partial r} \right) \quad (3.15.5)$$

$$\text{where } T_\delta = u^2 \frac{\partial^2 T}{\partial x^2} + \left( u \frac{\partial u}{\partial x} + v \frac{\partial u}{\partial r} \right) \frac{\partial T}{\partial x} + \left( v \frac{\partial v}{\partial r} + u \frac{\partial v}{\partial x} \right) \frac{\partial T}{\partial r} + 2uv \frac{\partial^2 T}{\partial x \partial r} + v^2 \frac{\partial^2 T}{\partial r^2}$$

According to the problem's geometry, the boundary conditions can be divided into the proceeding classes:

$$u = U_w = 0, v = 0, \kappa_{nf} \frac{\partial T}{\partial r} = -h_{nf} \{T_w - T\}, \quad C = C_w, \quad N = N_w \quad \text{at } r = R \quad (3.15.6)$$

$$u \rightarrow u_w = \frac{ax}{l}, \quad T \rightarrow T_\infty, \quad C \rightarrow C_\infty, \quad N \rightarrow N_\infty \quad \text{at } r \rightarrow \infty \quad (3.15.7)$$

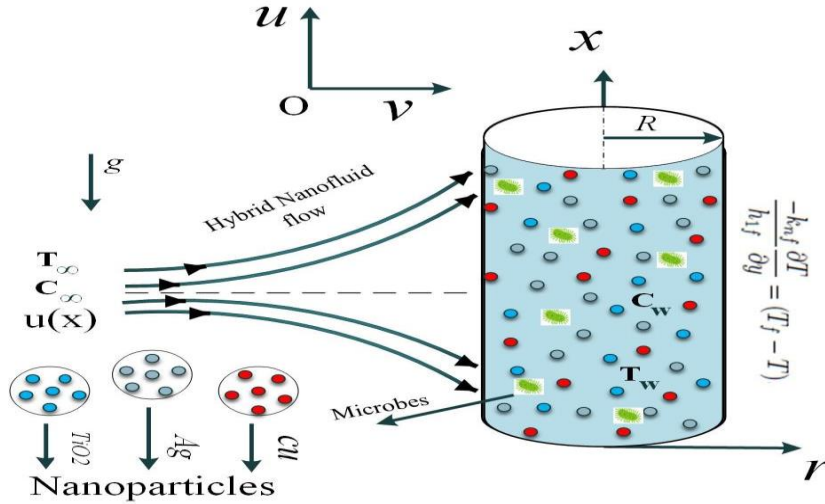


**Figure 3.6 Schematic configuration with coordinate system**

A velocity component is represented by  $u$  and  $v$  along directions  $x$  and  $r$ , respectively, thermal relaxation ( $\delta$ ), chemical reaction parameter ( $K_r$ ), and magnetic field intensity ( $B_0$ ). Microorganism's maximum swimming speed in hybrid nanofluid ( $W_c$ ), and their diffusivity ( $D_n$ ). Except for density changes that create a thermal buoyancy force retain

consistent characteristics. In Table 2, the subscript  $f_s$  is represent fluid. In order to reduce the complexity of the elaborated problem, the following nondimensional variables must be included:

$$\psi(x, r) = R\sqrt{u_w v_f x} f(\xi), \quad \xi = \frac{r^2 - R^2}{2R} \left( \frac{u_w}{v_f x} \right)^{\frac{1}{2}}, \quad u = \frac{1}{r} \frac{\partial \psi}{\partial r}, \quad v = -\frac{1}{r} \frac{\partial \psi}{\partial x},$$

$$\theta(\xi) = \frac{T - T_\infty}{T_w - T_\infty}, \quad \Phi(\xi) = \frac{C - C_\infty}{C_w - C_\infty}, \quad \zeta(\xi) = \frac{N - N_\infty}{N_w - N_\infty}, \quad u_w = \frac{ax}{l}$$

Here the stream functions  $\Psi$  and  $\xi$  are dimensionless. Usually, equation (3.15.1) is satisfied by demarcating this  $\Psi$  stream function. Following this, the non-linear partial differential equations (3.15.2)–(3.15.5) are transformed as:

$$(2\xi\Gamma + 1)f_1''' + 2\Gamma f_1'' + \frac{B_3}{B_1} \lambda \theta + \frac{B_2}{B_1} [1 + f_1 f_1'' - (f_1')^2] - \frac{M}{B_1} f_1' = 0 \quad (3.15.8)$$

$$[(2\xi\Gamma + 1)\theta'' + 2\Gamma\theta'] + \frac{B_5}{B_4} Pr [f_1' \theta] - \frac{B_5}{B_4} Pr \theta_t [f_1^2 \theta'' + f_1 f_1' \theta'] = 0 \quad (3.15.9)$$

$$(1 + 2\xi\Gamma)\Phi'' + (Le f_1 + 2\Gamma)\Phi' + Sr[(2\xi\Gamma + 1)\theta'' + 2\Gamma\theta'] - Le C_h \Phi = 0 \quad (3.15.10)$$

$$(1 + 2\xi\Gamma)\zeta'' - Pe[(1 + 2\xi\Gamma)\zeta\Phi'' + \Gamma(\zeta + \omega)\Phi' + \omega(1 + 2\xi\Gamma)\Phi'' + (1 + 2\xi\Gamma)\Phi'\zeta'] - Lb C_h \zeta + (Lb f_1 + 2\Gamma)\zeta' = 0 \quad (3.15.11)$$

Moreover, the modified boundary conditions are as follows;

$$f_1(\xi) = 0, \quad f_1'(\xi) = 0, \quad \theta'(\xi) = -Bi\{1 - \theta(0)\}, \quad \Phi(\xi) = 1, \quad \zeta(\xi) = 1 \quad \text{at } \xi = 0 \quad (3.15.12)$$

$$f_1'(\xi) \rightarrow 1, \quad \theta(\xi) \rightarrow 0, \quad \Phi(\xi) \rightarrow 0, \quad \zeta(\xi) \rightarrow 0 \quad \text{at } \xi \rightarrow \infty$$

The thermos-physical factors are explained such as; Elsaid and Abdel-wahed (2021).

$$B_1 = \mu_{hnf} = \frac{\mu_f}{(1 - \phi_1)^{\frac{5}{2}}(1 - \phi_2)^{\frac{5}{2}}},$$

$$B_2 = \frac{\rho_{hnf}}{\rho_f} = \{(1 - \phi_1)\} + \frac{\rho_{s1}}{\rho_f} \phi_1 (1 - \phi_2) + \frac{\rho_{s2}}{\rho_f} \phi_2$$

$$B_3 = \frac{(\rho\beta)_{hnf}}{(\rho\beta)_f} = \left( (1 - \phi_1) + \frac{(\beta\rho)_{s1}}{(\beta\rho)_f} \phi_1 \right) (1 - \phi_2) + \frac{(\beta\rho)_{s2}}{(\beta\rho)_f} \phi_2$$

$$B_4 = \frac{\kappa_{hnf}}{\kappa_f} = \frac{\kappa_{s2} + 2\kappa_{bf} - 2(\kappa_{bf} - \kappa_{s2})\phi_2}{\kappa_{s2} + 2\kappa_{bf} + (\kappa_{bf} - \kappa_{s2})\phi_2},$$

$$B_5 = \frac{(\rho C_p)_{hnf}}{(\rho C_p)_f} = \left( (1 - \phi_1) + \frac{(\rho C_p)_{s1}}{(\rho C_p)_f} \phi_1 \right) (1 - \phi_2) + \frac{(\rho C_p)_{s2}}{(\rho C_p)_f} \phi_2$$

### 3.15.2 Physical Quantities

The various involving parameters in equations (3.15.8) to (3.15.12) are also described, as are the numerous participating parameters are Prandtl number ( $P_r$ ), Magnetic parameter ( $M$ ), traditional Lewis number ( $Le$ ), chemical reaction parameter ( $C_h$ ), Péclet number ( $P_e$ ), Biot number ( $B_i$ ), Lewis number ( $L_b$ ), mixed convection parameter ( $\lambda$ ), Grashof number ( $G_r$ ), Reynolds number, ( $S_r$ ) Soret number, microorganisms difference parameter ( $w$ ), thermally stratified variable ( $\theta_t$ ) and the curvature parameter ( $\Gamma$ )

$$\begin{aligned}\theta_t &= \frac{a\delta}{l}, & M &= \frac{\sigma_f B_0^2 l}{\rho_f a}, & S_r &= \frac{\kappa_t (T_w - T_\infty)}{T_m (C_w - C_\infty)}, & C_h &= \frac{K_c l}{a} \\ Le &= \frac{\mu_f}{\rho_f D_m}, & \lambda &= \frac{G_r}{R_E}, & G_r &= \frac{\beta_f g (T_w - T_\infty) l^3}{\nu_f^2}, & P_r &= \frac{\mu_f}{\rho_f \alpha_f} \\ \Gamma &= \frac{1}{R} \sqrt{\frac{\mu_f l}{\rho_f a}}, & P_e &= \frac{b W_c}{D_m}, & \omega &= \frac{N_\infty}{N_w - N_\infty}, & L_b &= \frac{\mu_f}{\rho_f D_m}, \\ B_i &= \frac{R h_{nf}}{(\kappa_{nf}) r} \sqrt{\frac{l \nu_f}{a}}, & \alpha_f &= \frac{\kappa_f}{(\rho c)_f}, & R_e &= \frac{U - w l}{\nu_f}\end{aligned}$$

### 3.15.3 Engineering Quantities

The requisite aspects of engineering concerns skin friction coefficient  $\{C_{f_x} Re_x^{-\frac{1}{2}}\}$ , local Sherwood number  $\{Sh_x Re_x^{-\frac{1}{2}}\}$ , local Nusselt number  $\{Nu_x Re_x^{-\frac{1}{2}}\}$ , and local density of the motile microorganism  $\{N_{n_x}\}$  the following specific interest includes:

$$\begin{aligned}C_{f_x} &= \frac{2\mu_{nf}}{\rho_f U_w^2} \left( \frac{\partial u}{\partial r} \right)_{r=R}, & Nu_x &= \frac{x \kappa_{nf}}{\kappa_f (T_w - T_\infty)} \left( \frac{\partial T}{\partial r} \right)_{r=R} \\ Sh_x &= \frac{-x D_m}{D_m (C_w - C_\infty)} \left( \frac{\partial C}{\partial r} \right)_{r=R}, & N_{n_x} &= \frac{-x D_n}{D_n (N_w - N_\infty)} \left( \frac{\partial N}{\partial r} \right)_{r=R}\end{aligned}$$

Utilizing the above similarity transformations (7), can be calculated as:

$$C_{f_x} = \sqrt{Re_x} C_f = 2B_1 \frac{d^2 f_1(0)}{d\xi^2}, \quad \frac{Nu_x}{\sqrt{Re_x}} = -B_4 \{\theta'(0)\}, \quad \frac{Sh_x}{\sqrt{Re_x}} = -\Phi'(0), \quad \frac{N_{n_x}}{\sqrt{Re_x}} = \zeta'(0)$$

where,  $Re_x = \frac{x u_w}{\nu_f}$  is the local Reynold's number.

### 3.15.3 Execution of Methodology

The system of ODE's is numerically solved by the RK technique. In which estimates the mathematical solutions numerically using an adaptive Runge-Kutta method (for solutions) in MATLAB and for shooting we implemented the Newton-Raphson method Kiusalaas (2005). We do this by first assuming

$$\begin{aligned}f_1 &= \Pi_1, & f_1' &= \Pi_2, & f_1'' &= \Pi_3 \\ \theta &= \Pi_4, & \theta' &= \Pi_5, & \Phi &= \Pi_6, & \Phi' &= \Pi_7, \\ \zeta &= \Pi_8, & \zeta' &= \Pi_9 \\ \Pi_1' &= \Pi_2,\end{aligned}$$

$$\begin{aligned}
\Pi'_2 &= \Pi_3, \\
\Pi'_3 &= -\frac{1}{(1+2\Gamma\xi)} \left[ 2\Gamma\Pi_3 + \frac{B_2}{B_1} (1 + \Pi_1\Pi_3 - \Pi_2^2) + \frac{B_3}{B_1} \lambda\Pi_4 - \frac{M}{B_1} \Pi_2 \right] \\
\Pi'_4 &= \Pi_5 \\
\Pi'_5 &= \frac{1}{(B_5 P_r \theta_t \Pi_1^2 - B_4 (1 + 2\xi\Gamma))} [2B_4 \Gamma\Pi_5 + B_5 (P_r) (\Pi_1\Pi_5) - B_5 P_r \theta_t \Pi_1 \Pi_2 \Pi_5] \\
\Pi'_6 &= \Pi_7 \\
\Pi'_7 &= -\frac{1}{(1+2\Gamma\xi)} [(2\Gamma + Le\Pi_1)\Pi_7 + S_r(1+2\Gamma\xi)(\Pi'_5) + 2\Gamma\Pi_5] - LeC_h\Pi_6 \\
\Pi'_8 &= \Pi_9 \\
\Pi'_9 &= -\frac{1}{(1+2\Gamma\xi)} [(2\Gamma + L_b\Pi_1)\Pi_9 - Pe(\Gamma(\Pi_8 + w)\Pi_7 \\
&\quad + ((1+2\Gamma\xi)\Pi_8 + w(1+2\Gamma\xi)\Pi'_7 + (1+2\Gamma\xi)\Pi_7\Pi_9) - L_bCh\Pi_8]
\end{aligned}$$

with

$$\begin{aligned}
\Pi_1(0) = 0, \Pi_2(0) = 1, \Pi_3(0) = \Delta_1, \Pi_4(0) = \Delta_2, \Pi_5(0) = Bi(1 + \Pi_4(0)), \Pi_6(0) = 1, \\
\Pi_7(0) = \Delta_3, \Pi_8(0) = 1, \Pi_9(0) = \Delta_4
\end{aligned}$$

where  $\Delta_1, \Delta_2, \Delta_3, \Delta_4$  are calculated with an appropriate initial guess using the Newton Raphson technique.

### 3.15.4 RESPONSE SURFACE METHODOLOGY

The collaborative effect of pertinent parameters (independent variables) on the physical quantity of choice (response or dependent variable) is statistically analyzed with the aid of response surface methodology (RSM). RSM uses the central composite design (CCD) based data to estimate the model for the dependent variable (Sabu *et al.* (2021)). In this problem, the heat transport of  $Cu - Ag/H_2O$  hybrid nanoliquid denoted as  $Nu_x Re_x^{-1/2}$  is chosen as the dependent variable and Biot number ( $0.1 \leq Bi \leq 0.9$ ), magnetic parameter ( $0.1 \leq M \leq 0.9$ ) and nanoparticle volume fraction of  $Ag$  ( $0.01 \leq \phi_2 \leq 0.09$ ) are chosen as the independent variables. Table 4.10 depicts the effective parameters and their levels. The general model for the response variable including the linear, quadratic, and interactive terms is given by:

$$Response = z_1 A + z_2 B + z_3 C + z_4 AB + z_5 BC + z_6 AC + z_7 A^2 + z_8 B^2 + z_9 C^2 + z_{10} \quad (3.15.13)$$

where  $z_i$  ( $i = 1$  to  $10$ ) represent the regression coefficients. The experimental design and the response for the 20 runs according to CCD are given in Table 4.11.

The fitted quadratic model for  $Nu_x Re_x^{-1/2}$  in uncoded form is given by:

$$\begin{aligned}
Nu_x Re_x^{-1/2} = 0.01382 + 1.48870 Bi + 0.00330 M + 0.26100 \phi_2 - 0.64660 Bi^2 \\
- 0.03060 Bi M + 2.04200 Bi \phi_2
\end{aligned} \quad (3.15.14)$$

### 3.15.5 SENSITIVITY ANALYSIS

The statistical mechanism that analyses the nature and magnitude of dependency exhibited by the independent variables on the dependent variable is known as sensitivity analysis (Mathew *et al.* (2021)). The quadratic model for  $Nu_x Re_x^{-1/2}$  in uncoded form after neglecting the insignificant terms is given by:

$$Nu_x Re_x^{-1/2} = 0.65668 + 0.37151 A - 0.00528 B + 0.05512 C - 0.10346 A^2 - 0.00490 AB + 0.03266 AC \quad (3.15.15)$$

Then the sensitivity functions are:

$$\frac{\partial \left( Nu_x Re_x^{-1/2} \right)}{\partial A} = 0.37151 - 0.20692 A - 0.00490 B + 0.03266 C \quad (3.15.16)$$

$$\frac{\partial \left( Nu_x Re_x^{-1/2} \right)}{\partial B} = -0.00528 - 0.00490 A \quad (3.15.17)$$

$$\frac{\partial \left( Nu_x Re_x^{-1/2} \right)}{\partial C} = 0.05512 + 0.03266 A \quad (3.15.18)$$

### 3.16 Chemically reactive species effect on MHD Carreau nanofluid flow over the stretching cylinder with the impact of multiple slip and motile microorganisms

This study focused on the analysis of two-dimensional incompressible magnetohydrodynamic Carreau nanofluid flow across a stretching cylinder containing microorganisms with impacts of chemical reaction, heat source, and multiple slip boundary conditions. A set of equations is formed from the governing partial differential equations by implementing suitable similarity transformations. An effective numerical solver, the *bvp5c* package, is used for numerical computations. The influence of various parameters has been displayed through tables, graphs, and surface plots on heat transfer, mass transfer, and local Nusselt number for both the shearing thinning ( $n < 1$ ) and the shear thickening ( $n > 1$ ) instances. Motile concentration profiles decrease with  $Lb$  and motile microorganism density slips parameter. Weissenberg number demonstrates a different nature depending on the type of fluid; Skin friction, the velocity profile and the Nusselt number are dropped when  $n < 1$  and enhanced when  $n > 1$ . The two and three-dimensional graphs show the simultaneous effect of involving parameters on physical quantities

#### 3.16.1 Physical Pattern and Interpretation

Heat and mass transfer are analyzed using a 2D mathematical model in this section, Carreau nanofluid flow with microorganisms in the presence of chemically reactive species towards a cylinder with radius  $R$  with free stream velocity  $U_\infty$  was consider. The impacts of chemical reaction, the heat source and multi-slip are included in this paper to broaden the scope of the research. Let free stream velocity  $u_w = \frac{ax}{l}$  flow over the cylinder, where  $a$  is a positive constant. The motion across the cylinder depicted in Figure 1 induces the proposed

flow. The  $x$ -axis along the cylinder's surface and  $r$  in the axial direction are both taken into consideration by the coordination system. Along the  $r$  direction, a consistent magnetic field (of intensity  $B_0$ ) is applied. The temperature and concentration at the stretching cylinder are denoted by  $T_w$  and  $C_w$ , also the ambient values are represented by  $T_\infty$  and  $C_\infty$  when  $r$  approaching to infinity. Based on these assumptions, we can derive the following governing equations:

$$\frac{\partial(ru)}{\partial x} + \frac{\partial(rv)}{\partial r} = 0 \quad (3.16.1)$$

$$u \frac{\partial u}{\partial x} + v \frac{\partial u}{\partial r} = \nu_f \frac{\partial^2 u}{\partial r^2} \left( 1 + \left( \tau_c \frac{\partial u}{\partial r} \right)^2 \right)^{\frac{n-1}{2}} + \frac{\nu_f}{r} \frac{\partial u}{\partial r} \left( 1 + \left( \tau_c \frac{\partial u}{\partial r} \right)^2 \right)^{\frac{n-1}{2}} + (n-1) \nu_f \left( \tau_c \frac{\partial u}{\partial r} \right)^2 \frac{\partial^2 u}{\partial r^2} \left( 1 + \left( \tau_c \frac{\partial u}{\partial r} \right)^2 \right)^{\frac{n-3}{2}} - \frac{\sigma B_0^2 u}{\rho_f} \quad (3.16.2)$$

$$(\rho C_p)_f \left( u \frac{\partial T}{\partial x} + v \frac{\partial T}{\partial r} \right) = \kappa_f \left( \frac{\partial^2 T}{\partial r^2} + \frac{1}{r} \frac{\partial T}{\partial r} \right) + \frac{q_t}{(\rho C_p)_f} (T - T_\infty) \quad (3.16.3)$$

$$u \frac{\partial C}{\partial x} + v \frac{\partial C}{\partial r} + K_c(C - C_\infty) = D_m \left( \frac{\partial^2 C}{\partial r^2} + \frac{1}{r} \frac{\partial C}{\partial r} \right) + \frac{D_m \kappa_t}{T_m} \left( \frac{\partial^2 T}{\partial r^2} + \frac{1}{r} \frac{\partial T}{\partial r} \right) \quad (3.16.4)$$

$$u \frac{\partial N}{\partial x} + v \frac{\partial N}{\partial r} + K_c(N - N_\infty) = -\frac{bW_c}{C_w - C_\infty} \left[ \frac{\partial}{\partial r} \left( N \frac{\partial C}{\partial r} \right) \right] + D_n \left( \frac{\partial^2 N}{\partial r^2} + \frac{1}{r} \frac{\partial N}{\partial r} \right) \quad (3.16.5)$$

According to the problem's geometry, the boundary conditions can be divided into the proceeding classes:

$$u = U_w = \frac{ax}{l} + K_1 \frac{\partial u}{\partial r} \left( 1 + \left( \tau_c \frac{\partial u}{\partial r} \right)^2 \right)^{\frac{n-1}{2}}, v = 0, \quad K_2 \frac{\partial T}{\partial r} = \{T - T_w\}, \quad (3.16.6)$$

$$C = C_w + K_3 \frac{\partial C}{\partial r} N = N_w + K_4 \frac{\partial N}{\partial r} \text{ at } r = R$$

$$u \rightarrow 0, \quad T \rightarrow T_\infty, \quad C \rightarrow C_\infty, \quad N \rightarrow N_\infty \text{ at } r \rightarrow \infty \quad (3.16.7)$$

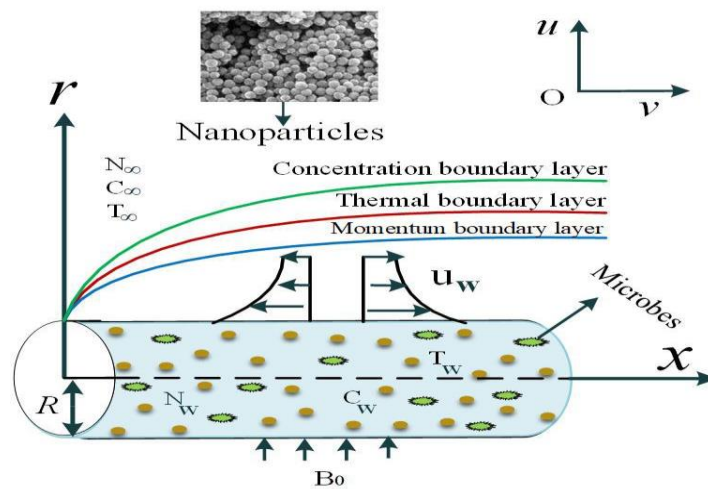


Figure 3.7 Pictorial representation of the model

A velocity component is represented by  $u$  and  $v$  along directions  $x$  and  $r$ , respectively, thermal relaxation ( $\delta$ ), chemical reaction parameter ( $K_r$ ), and magnetic field intensity ( $B_o$ ). Microorganism's maximum swimming speed in hybrid nanofluid ( $W_c$ ), and their diffusivity ( $D_n$ ). In order to reduce the complexity of the elaborated problem, the following nondimensional variables must be included:

$$\psi(x, r) = R\sqrt{u_w v_f x} f(\zeta), \quad \zeta = \frac{r^2 - R^2}{2R} \left( \frac{u_w}{v_f x} \right)^{\frac{1}{2}}, \quad u = \frac{1}{r} \frac{\partial \psi}{\partial r}, \quad v = -\frac{1}{r} \frac{\partial \psi}{\partial x},$$

$$\theta(\zeta) = \frac{T - T_\infty}{T_w - T_\infty}, \quad \varphi(\zeta) = \frac{C - C_\infty}{C_w - C_\infty}, \quad \chi(\zeta) = \frac{N - N_\infty}{N_w - N_\infty}, \quad u_w = \frac{ax}{l}$$

Here the stream functions  $\Psi$  and  $\zeta$  are dimensionless. Usually, equation (3.16.1) is satisfied by demarcating this  $\Psi$  stream function. Following this, the non-linear partial differential equations (3.16.2)- (3.16.5) are transformed as:

$$(2\zeta\Gamma + 1)(1 + W_e^2 f''^2)^{\left(\frac{n-1}{2}\right)} f'''' + (n-1)W_e^2(2\Gamma + 1)(1 + W_e^2 f''^2)^{\left(\frac{n-3}{2}\right)} f''^2 f'''' - MF' + ff'' + (n-1)W_e^2(\Gamma)(1 + W_e^2 f''^2)^{\left(\frac{n-3}{2}\right)} f''^3 - f'^2 = 0 \quad (3.16.8)$$

$$[(2\zeta\Gamma + 1)\theta'' + 2\Gamma\theta'] + Pr[f'\theta + Q_t\theta] = 0 \quad (3.16.9)$$

$$(1 + 2\zeta\Gamma)\varphi'' + (Le f + 2\Gamma)\varphi' + Sr[(2\zeta\Gamma + 1)\theta'' + 2\Gamma\theta'] - Le C_h \varphi = 0 \quad (3.16.10)$$

$$(1 + 2\zeta\Gamma)\chi'' - Pe[(1 + 2\zeta\Gamma)\chi\varphi'' + \Gamma(\chi + \omega)\varphi' + \omega(1 + 2\zeta\Gamma)\varphi'' + (1 + 2\zeta\Gamma)\varphi' \chi'] + (Lb f + 2\Gamma)\chi' - Lb C_h \chi = 0 \quad (3.16.11)$$

Moreover, the modified boundary conditions are as follows;

$$f(\zeta) = 0, \quad f'(\zeta) = 1 + \lambda_1 f''(1 + W_e^2 f''^2)^{\left(\frac{n-1}{2}\right)}, \quad \theta(\zeta) = 1 + \lambda_2 \theta', \quad (3.16.12)$$

$$\chi(\zeta) = 1 + \lambda_3 \varphi', \quad \chi(\zeta) = 1 + \lambda_4 \chi(\zeta)', \quad \zeta = 0$$

$$f'(\zeta) \rightarrow 1, \theta(\zeta) \rightarrow 0, \quad \varphi(\zeta) \rightarrow 0, \quad \chi(\zeta) \rightarrow 0 \quad \text{at } \zeta \rightarrow \infty$$

### 3.16.2 Physical Quantities

The various involving parameters in equations (3.16.8) to (3.16.11) are also described, as are the numerous participating parameters are Prandtl number ( $Pr$ ), Magnetic parameter ( $M$ ), traditional Lewis number ( $Le$ ), chemical reaction parameter ( $C_h$ ), Péclet number ( $Pe$ ), Biot number ( $B_i$ ), Lewis number ( $L_b$ ), mixed convection parameter ( $\lambda$ ), Grashof number ( $Gr$ ), Reynolds number, ( $S_r$ ) Soret number, microorganisms difference parameter ( $w$ ), thermally stratified variable ( $\theta_t$ ) and the curvature parameter ( $\Gamma$ )

$$M = \frac{\sigma_f B_0^2 l}{\rho_f a}, \quad Q_t = \frac{qT}{(\rho C_p)_f}, \quad Sr = \frac{\kappa_t(T_w - T_\infty)}{T_m(C_w - C_\infty)}, \quad C_h = \frac{K_c l}{a}$$

$$(W_e)^2 = \frac{\tau_c a^3 x^2 r^2}{v_f l^3 R^2}, \quad Le = \frac{\mu_f}{\rho_f D_m}, \quad Pr = \frac{\mu_f}{\rho_f \alpha_f}, \quad \alpha_f = \frac{\kappa_f}{(\rho c)_f},$$

$$\Gamma = \frac{1}{R} \sqrt{\frac{\mu_f l}{\rho_f a}}, \quad Pe = \frac{bW_c}{D_m}, \quad \omega = \frac{N_\infty}{N_w - N_\infty}, \quad Lb = \frac{\mu_f}{\rho_f D_m},$$

### 3.16.3 Engineering Quantities

The requisite aspects of engineering concerns skin friction coefficient  $\{C_{fx}Re_x^{-\frac{1}{2}}\}$ , local Sherwood number  $\{Sh_xRe_x^{-\frac{1}{2}}\}$ , local Nusselt number  $\{Nu_xRe_x^{-\frac{1}{2}}\}$ , and local density of the motile microorganism  $\{N_{nx}\}$  the following specific interest includes:

$$C_{fx} = \frac{2\mu_f}{\rho_f U_w^2} (\tau_{rx}), \quad Nu_x = \frac{x\kappa_{nf}}{\kappa_f(T_w - T_\infty)} \left( \frac{\partial T}{\partial r} \right)_{r=R}$$

$$Sh_x = \frac{-xD_m}{D_m(C_w - C_\infty)} \left( \frac{\partial C}{\partial r} \right)_{r=R}, \quad N_{nx} = \frac{-xD_n}{D_n(N_w - N_\infty)} \left( \frac{\partial N}{\partial r} \right)_{r=R}$$

$$\text{where } \tau_{rx} = \left( \mu_f \frac{\partial u}{\partial r} \left( 1 + \left( \tau_c \frac{\partial u}{\partial r} \right)^2 \right)^{\frac{n-1}{2}} \right)_{r=R}$$

Utilizing the above similarity transformations (7), can be calculated as:

$$C_{fx} = \sqrt{Re_x} C_f = f''(0)(1 + W_e^2(f''(0))^2), \quad \frac{Nu_x}{\sqrt{Re_x}} = \{\theta'(0)\}, \quad \frac{Sh_x}{\sqrt{Re_x}} = -\phi'(0), \quad \frac{N_{nx}}{\sqrt{Re_x}} = \chi'(0)$$

where  $Re_x = \frac{xu_w}{\nu_f}$  is the local Reynold's number.

### 3.16.4 Execution of Methodology

First assuming:

$$f = \Pi_1, \quad f' = \Pi_2, f'' = \Pi_3$$

$$\theta = \Pi_4, \theta' = \Pi_5, \quad \phi = \Pi_6, \phi' = \Pi_7,$$

$$x = \Pi_8, x' = \Pi_9$$

$$\Pi'_1 = \Pi_2,$$

$$\Pi'_2 = \Pi_3,$$

$$\Pi'_3 = \frac{(-1) \left( M\Pi_2 + \Pi_1\Pi_3 + (n-1)W_e^2(\Gamma)(1 + W_e^2\Pi_3^2)^{\frac{(n-3)}{2}}\Pi_3^2 - \Pi_2^2 \right)}{(1 + 2\Gamma\zeta)(1 + W_e^2\Pi_3^2)^{\frac{(n-1)}{2}} + (n-1)W_e^2(\Gamma)(1 + W_e^2\Pi_3^2)^{\frac{(n-3)}{2}}\Pi_3^2}$$

$$\Pi'_4 = \Pi_5$$

$$\Pi'_5 = \frac{-1}{(1 + 2\zeta\Gamma)} [(P_r)(\Pi_1\Pi_5) - P_r Q_t \Pi_5 + 2\Gamma\Pi_5]$$

$$\Pi'_6 = \Pi_7$$

$$\Pi'_7 = -\frac{1}{(1 + 2\Gamma\zeta)} [(2\Gamma + Le\Pi_1)\Pi_7 + S_r(1 + 2\Gamma\zeta)(\Pi'_5) + 2\Gamma\Pi_5] - LeC_h\Pi_6$$

$$\Pi'_8 = \Pi_9$$

$$\Pi'_9 = -\frac{1}{(1 + 2\Gamma\zeta)} [(2\Gamma + L_b\Pi_1)\Pi_9 - Pe(\Gamma(\Pi_8 + w)\Pi_7 + ((1 + 2\Gamma\zeta)\Pi_8 + w(1 + 2\Gamma\zeta)\Pi'_7 + (1 + 2\Gamma\zeta)\Pi_7\Pi_9) - L_bCh\Pi_8]$$

With

$$\begin{aligned} \Pi_1(0) = 0, \quad \Pi_2(0) = 1 + \lambda_1 \Pi_3 (1 + W_e^2 \Pi_3^2)^{\frac{(n-1)}{2}}, \\ \Pi_4(0) = 1 + \lambda_2 \Pi_5, \quad \Pi_6(0) = 1 + \lambda_3 \Pi_7, \quad \Pi_8(0) = 1 + \lambda_4 \Pi_9, \\ \Pi_2 = 0, \Pi_4 = 0, \Pi_6 = 0, \Pi_8 = 0 \end{aligned}$$

The reduced set of ODEs are numerically resolved utilizing the finite-difference based bvp5c algorithm. The infinity condition was rescaled to 10.

### 3.17 To compare the effects of heat transfer through copper nanofluid with convective boundary effect via heated Riga plate

This study investigates the heat and mass transfer of magnetohydrodynamic nanofluids via the Riga plate subjected to convective boundary conditions, including the thermal radiation parameter. Utilizing variable thermal conductivity and mixed convection effects, the heat transfer process is investigated. The peculiarity of the flow model enables us to investigate the importance of thermophoresis and Brownian motion to the kinetics of Newtonian fluids. The governing partial differential equations are converted into non-dimensional ordinary differential equations using proper similarity transformations and numerically solved using bvp4c in MATLAB. The influence of several physical quantities is illustrated and displayed through graphs and tables.

#### 3.17.1 Physical Model and Mathematical Formulation

Considered the two-dimensional, incompressible flow of ethylene-glycol-based Copper nanofluid over a vertical infinite Riga plate is considered. The Riga plate is visualized in Figure (3.8) by the  $x$  coordinate running to the flow direction and the  $y$  coordinate perpendicular to the flow direction. Furthermore, fluid flow is subjected to the magnetic field  $B_0$  in a normal direction. Additionally, the effects of additional factors such as Joule heating, thermal radiation, thermophoresis, and Brownian motion have been analyzed. The linear velocity  $U_w = e^{\frac{x}{L}}$  in  $y$  direction and convective condition at the wall is  $-k_{nf} \frac{\partial T}{\partial y} = h_f(T_f - T)$ , where  $h_f$  is the convective heat transfer coefficient.

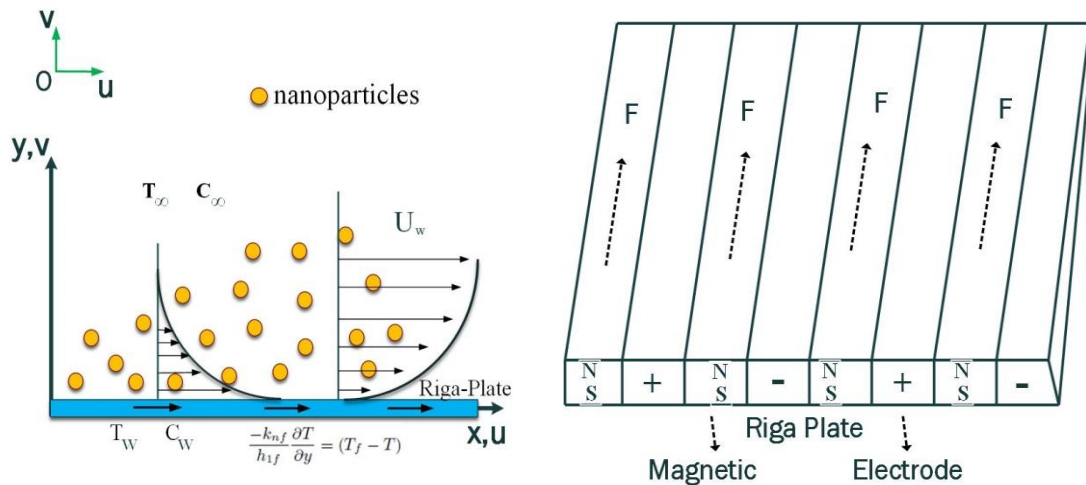


Figure 3.8 A pictorial representation of the model

In accordance with the model equations provided by Tiwari and Das (2007), the fundamental continuity, momentum, energy, and concentration equations are as follows:

$$\frac{\partial u}{\partial x} + \frac{\partial v}{\partial y} = 0 \quad (3.17.1)$$

$$u \frac{\partial(u)}{\partial x} + v \frac{\partial(u)}{\partial y} = v_{nf} \frac{\partial^2 u}{\partial y^2} - \frac{\sigma_{nf}}{\rho_{nf}} B_0^2 u + g \frac{\beta}{\rho_{nf}} \{(T - T_\infty) + (C - C_\infty)\} + \frac{M_0 J_1}{8\pi} \exp\left(-\frac{\pi}{\alpha_1} y\right) \quad (3.17.2)$$

$$u \frac{\partial(T)}{\partial x} + v \frac{\partial(T)}{\partial y} = \frac{\kappa_{nf}}{(\rho C_p)_{nf}} + \frac{\partial^2 T}{\partial y^2} \frac{1}{(\rho C_p)_{nf}} \frac{\partial}{\partial y} \left( \kappa(T) \frac{\partial T}{\partial y} \right) + \left( \frac{\mu + \kappa}{\rho C_p} \right)_{nf} \left( \frac{\partial u}{\partial y} \right)^2 \quad (3.17.3)$$

$$+ \frac{\sigma_{nf} B_0^2 u^2}{(\rho C_p)_{nf}} + - \frac{1}{(\rho C_p)_{nf}} \frac{\partial q_r}{\partial y} + \frac{\tau}{(\rho C_p)_{nf}} \left[ D_B \left( \frac{\partial T}{\partial y} \frac{\partial \zeta}{\partial y} \right) + \frac{D_T}{T_\infty} \left( \frac{\partial T}{\partial y} \right)^2 \right] \\ u \frac{\partial(C)}{\partial x} + v \frac{\partial(C)}{\partial y} = D_B \frac{\partial^2 C}{\partial y^2} + \frac{D_T}{T_\infty} \left( \frac{\partial^2 T}{\partial y^2} \right) \quad (3.17.4)$$

In addition,  $T$  represents the fluid temperature,  $(u, v)$  shows component of velocity, thermophoretic diffusion coefficient, is represented by  $D_T$  respectively.  $\alpha_1$  denotes the diameter of the magnets positioned in the interval separating the electrodes.

Here is the boundary condition we have for the problem above:

$$u = U_w, v = 0, -\kappa_{nf} \frac{\partial T}{\partial y} = h_f (-T + T_f), C = C_w \text{ at } y = 0 \quad (3.17.5)$$

$$u \rightarrow 0, T \rightarrow T_\infty, C \rightarrow C_\infty \text{ at } y \rightarrow \infty \quad (3.17.6)$$

where  $T_f$  denotes the wall temperature. Also  $B_0$ ,  $\mu_{nf}$ ,  $\rho_{nf}$ ,  $h_f$  are magnetic field parameter, viscosity, density and the convective heat transfer coefficient, respectively. When expressing the radiative heat flux, the Rosseland approximation is used as follows  $q_r = \frac{4\alpha^* \partial T^4}{3K_1 \partial y}$ . Where  $K_1$  is the Roseland's mean absorption co-efficient and  $\alpha^*$  is the Boltzman constant. Assuming minimal temperature variations in the flow, we use Taylor series, neglecting the higher-order variables, and assuming small temperature fluctuations in the flow Datti *et al.* (2004).

$$q_r = \frac{4\alpha^* \partial T^4}{3K_1 \partial y} = -\frac{16\alpha^* T_\infty^3 \partial T}{3K_1 \partial y}$$

Where the empirical constants  $\delta, K(T)$  variable thermal/heat conductivity, and  $k$  coefficient of heat conductivity are far from the exponential plate displayed as  $K(T) = k(1 - \delta(T - T_\infty))$ . The properties of Copper nanoparticle and base fluid ethylene glycol are showcased in Table 3.1, and these values are extracted from Kambhatla *et al.* (2019).

The similarity techniques used to transform governing equations (3.17.1) to (3.17.4) are listed below:

$$u = U_0 e^{\frac{x}{L}} f'(\eta), \quad (T_f - T_\infty) \theta = (T - T_\infty), \quad y \sqrt{\frac{U_0}{2L\nu_f}} e^{\frac{2x}{L}} = \eta$$

$$\varphi(C_f - C_\infty) = (C - C_\infty), \quad v = y \sqrt{\frac{U_0 \nu_f}{2L}} e^{\frac{x}{L}} (f(\eta) + \eta f'(\eta))$$

Using the similarity techniques listed above, the governing equations are converted to ODEs as follows:

$$\frac{A_1}{A_2} \frac{\partial^3 f}{\partial \eta^3} - \frac{\partial f^2}{\partial \eta^2} + f \frac{\partial^2 f}{\partial \eta^2} - \frac{M}{A_2} \frac{\partial f}{\partial \eta} \lambda_1 \varphi + \lambda_2 \theta + M_1 e^{(-\eta \lambda_3)} = 0 \quad (3.17.7)$$

$$\begin{aligned} \frac{1}{A_3 Pr} (A_4 + R_d) \frac{\partial^2 \theta}{\partial \eta^2} + \frac{1}{A_3 Pr} (\epsilon \theta'^2 + \epsilon \theta \theta'') + \frac{ME_C}{A_3} \left( \frac{\partial f}{\partial \eta} \right)^2 + N_B \frac{\partial \theta}{\partial \eta} \frac{\partial \varphi}{\partial \eta} \\ + N_T \left( \frac{\partial \theta}{\partial \eta} \right)^2 + E_C \left( \frac{A_4}{A_3} + 1 \right) \frac{\partial^2 f}{\partial \eta^2} + f \frac{\partial \theta}{\partial \eta} = 0 \end{aligned} \quad (3.17.8)$$

$$\frac{\partial^2 \varphi}{\partial \eta^2} - S_c f \frac{\partial \varphi}{\partial \eta} - \frac{N_T}{N_B} \frac{\partial^2 \theta}{\partial \eta^2} = 0 \quad (3.17.9)$$

And the boundary conditions are;

$$f = 0, f' = 1, \quad A_4 \theta' - Bi = -Bi, \quad \varphi = 1 \text{ at } \eta = 0 \quad (3.17.10)$$

$$f' \rightarrow 0, \quad \theta \rightarrow 0, \quad \varphi \rightarrow 0 \text{ at } \eta \rightarrow \infty$$

$$A_1 = \sqrt{(1 - \phi)^{-5}}, \quad A_2 = \phi \rho_s - \rho_f (\phi - 1),$$

$$A_3 = \phi \frac{(\rho c_p)_s}{(\rho c_p)_f} + (1 - \phi), \quad A_4 = \frac{2k_f + k_s - 2(\phi k_f - \phi k_s)}{2k_f + k_s + (\phi k_f - \phi k_s)}$$

Here,  $\mu_f$  refers to the dynamic viscosity of the base fluid,  $\phi$  refers to the volume fraction of solids,  $\rho_f$  and  $\rho_s$  refer to the densities. There are  $\kappa_f$  and  $\kappa_s$  thermal conductivities,  $(\rho c_p)_f$  and  $(\rho c_p)_s$  thermal conductivities based on the heat conduction capacity of the base fluid and nanoparticles. The effective thermal conductivity of fluid using Maxwell Garnett's model by adjusting the magnetic field, Prandtl number  $Pr$ , Biot number  $Bi$ , and thermophoretic variable  $N_T$ , Schmidt number  $S_c$ , Eckert number  $E_C$ , Hartmann number  $M_1$ , thermal conductivity parameter  $\epsilon$ , brownian diffusion  $N_B$ , and radiation parameter  $R_d$ . And

$$M_1 = \frac{\sigma_{nf} B_0^2}{\rho_{nf} a}, \quad E_C = \frac{U_w^2}{(T_f - T_\infty)(c_p)_f}, \quad Pr = \frac{(\mu c_p)_f}{\kappa_{nf}},$$

$$R_d = \frac{16\alpha^* T^3}{3K_1 \kappa_{nf}}, \quad N_B = \frac{\tau^*(\zeta_w - \zeta_\infty) D_B}{\nu_f}, \quad N_T = \frac{\tau^*(T_w - T_\infty) D_T}{\nu_f T_\infty},$$

$$Bi = \frac{h_f}{\kappa_{nf}} \sqrt{\frac{\nu_f}{a}}, \quad \lambda_1 = g\beta(C_f - C_\infty) \frac{e^{\frac{x}{L}}}{U_w^2},$$

$$S_C = \frac{v_{nf}}{D_B}, \quad \lambda_2 = \frac{eL^3}{U_w^2}, \quad \lambda_3 = \pi/\alpha_1 \sqrt{\frac{U_0}{v_f}}, \quad M_1 = \frac{4eL M_0 J_1}{24u_w^2 \pi}$$

### 3.17.2 Physical Quantities

The local skin friction coefficient, the local Nusselt-number, and the local Sherwood number are defined as

$$Sh_x = \left[ \frac{xq_p}{D_m(C_f - C_\infty)} \right]_{y=0}, \quad Nu_x = \left[ \frac{xq_w}{\kappa_f(T_f - T_\infty)} \right]_{y=0}, \quad Cf_x = \left[ \frac{\tau_w}{U_w \rho_f} \frac{\partial u}{\partial y} \right]_{u,y=0}$$

Where  $\tau_w, q_w, q_p$  are shear stress, heat flux, and the mass flux at the surface respectively.

The above quantities  $Cf_x, Nu_x$ , and  $Sh_x$  can be written in non-dimensional as:

$$\frac{1}{2} \sqrt{Re_x} Cf_x = \frac{\partial f^2(0)}{\partial \eta^2}, \quad \frac{Nu_x}{\sqrt{Re_x}} = -(A_4 + R_d) \frac{\partial \theta(0)}{\partial \eta}, \quad \frac{Sh_x}{\sqrt{Re_x}} = -\frac{\partial \varphi(0)}{\partial \eta}$$

### 3.17.3 Method of Solution and Validation

Mathematical equations and boundary conditions are solved numerically using the `bvp4c` solver in MATLAB. This approach uses the Lobatto IIIa implicit Runge–Kutta formula to achieve numerical solutions. Below are three reduced sets of first-order ordinary differential equations (3.17.9-3.17.11):

$$f = y_1, \quad f' = y_2, \quad f'' = y_3,$$

$$f''' = \frac{1}{A_1} [A_2(2(y_2)^2 - y_1 y_3) + M y_2 + \lambda_1 y(5) + \lambda_2 y(6) + M_1 e^{(-\lambda_3 \eta)}]$$

$$\theta = y_4, \quad \theta' = y_5,$$

$$\theta'' = \frac{-P_r}{[A_4 + R_d + \epsilon y(4)]} \left[ ME_C y_2^2 + A_3(N_B y_7 y_5 + N_T (y_5)^2 + y_1 y_5) + \epsilon \frac{1}{P_r} (y(2))^2 + E_C (A_3 + A_4) (y(3))^2 \right]$$

$$\varphi = y_6, \quad \varphi' = y_7,$$

$$\varphi'' = - \left[ S_C y_7 y_1 + \frac{N_T}{N_B} \frac{-P_r}{[A_4 + R_d + \epsilon y(4)]} \left\{ ME_C y_2^2 + A_3(N_B y_7 y_5 + N_T (y_5)^2 + y_1 y_5) + \epsilon \frac{1}{P_r} (y(2))^2 + E_C (A_3 + A_4) (y(3))^2 \right\} \right]$$

As boundary conditions are

$$y_1(0) = 0, y_2(0) = 1, A_4 y_5(0) + B_i y_4(0) + B_i, y_6 = 1,$$

$$y_2(\infty) \rightarrow 0, y_4(\infty) \rightarrow 0, y_6(\infty) \rightarrow 0$$

### 3.18 To compare the effects of heat transfer analysis of thermally convective nanofluid flow over the stretching cylinder and stretching sheet.

This study focused on sensitivity analysis of two-dimensional incompressible magnetohydrodynamic nanofluid Cu – water flows across a stretching cylinder containing

microorganisms with impacts of chemical reaction, mixed convection, heat source, and convective boundary condition. The response surface methodology technique and the sensitivity analysis has used to examine the effects of nanoparticle volume fraction, Biot number, and magnetic parameter on the rate of heat transfer statistically. A set of equations is formed from the governing partial differential equations by implementing suitable similarity transformations. A well-known method Runge Kutta with shooting has used. The influence of various parameters has been displayed through tables, graphs, and surface plots on heat transfer, mass transfer, and local Nusselt number.

### 3.18.1 Physical Pattern and Interpretation

The motion across the cylinder depicted in Figure (3.7) induces the proposed flow. Heat and mass transfer are analyzed using a 2D mathematical model in this section, nanofluid flow with microorganisms in the presence of chemically reactive species towards a cylinder with radius  $R$  with free stream velocity  $U$  has been consider. The impacts of chemical reaction, mixed convection parameter, the heat source is included in this paper to broaden the scope of the research. Let free stream velocity  $u_w = \frac{ax}{l}$  flow over the cylinder, where  $a$  is a positive constant. The  $x$ -axis along the cylinder's surface and  $r$  in the axial direction are both taken into consideration by the coordination system. Convective heating from a hot fluid causes the surface temperature, which is indicated by  $T$ , and thermal efficiency, which is indicated by  $h_f$ . Under the boundary stacking and Oberbeck-Boussinesq approximations, the viscous effects of dissipation are ignored. The heated fluid along the wall is characterized as  $-k_{nf} \frac{\partial T}{\partial r} = h_f(T - T_\infty)$ . The thermo-physical characteristics of nanoparticles are shown in Table 3.1. The aggregation of tiny particles is disregarded since the nanofluid mixture is assumed to be a stable substance. The Cattaneo Christov heat flux prototype and the Tiwari and Das (2007) model have both been considered. Based on these assumptions, we can derive the following governing equations:

$$\frac{\partial(ru)}{\partial x} + \frac{\partial(rv)}{\partial r} = 0 \quad (3.18.1)$$

$$u \frac{\partial u}{\partial x} + v \frac{\partial u}{\partial r} = \frac{\mu_{nf}}{\rho_{nf}} \left( \frac{\partial^2 u}{\partial r^2} + \frac{1}{r} \frac{\partial u}{\partial r} \right) - \frac{\sigma B_0^2 u}{\sigma_{nf}} + \left[ \frac{(\rho\beta)_{nf}}{\rho_{nf}} g(T - T_\infty) \right] \quad (3.18.2)$$

$$(\rho C_p)_{nf} \left( u \frac{\partial T}{\partial x} + v \frac{\partial T}{\partial r} \right) = -(\rho C_p)_{nf} \delta T_\delta + \kappa_{nf} \left( \frac{\partial^2 T}{\partial r^2} + \frac{1}{r} \frac{\partial T}{\partial r} \right) \quad (3.18.3)$$

$$u \frac{\partial C}{\partial x} + v \frac{\partial C}{\partial r} + K_c(C - C_\infty) = D_m \left( \frac{\partial^2 C}{\partial r^2} + \frac{1}{r} \frac{\partial C}{\partial r} \right) + \frac{D_m \kappa_t}{T_m} \left( \frac{\partial^2 T}{\partial r^2} + \frac{1}{r} \frac{\partial T}{\partial r} \right) \quad (3.18.4)$$

$$\text{where } T_\delta = u^2 \frac{\partial^2 T}{\partial x^2} + \left( u \frac{\partial u}{\partial x} + v \frac{\partial u}{\partial r} \right) \frac{\partial T}{\partial x} + \left( v \frac{\partial v}{\partial r} + u \frac{\partial v}{\partial x} \right) \frac{\partial T}{\partial r} + 2uv \frac{\partial^2 T}{\partial x \partial r} + v^2 \frac{\partial^2 T}{\partial r^2}$$

According to the problem's geometry, the boundary conditions can be divided into the proceeding classes:

$$\begin{aligned} u = U_w = 0, v = 0, \kappa_{nf} \frac{\partial T}{\partial r} = -h_{nf} \{T_w - T\}, \quad C = C_w, \text{ at } r = R \\ u \rightarrow u_w = \frac{ax}{l}, \quad T \rightarrow T_\infty, \quad C \rightarrow C_\infty \quad \text{at } r \rightarrow \infty \end{aligned} \quad (3.18.5)$$

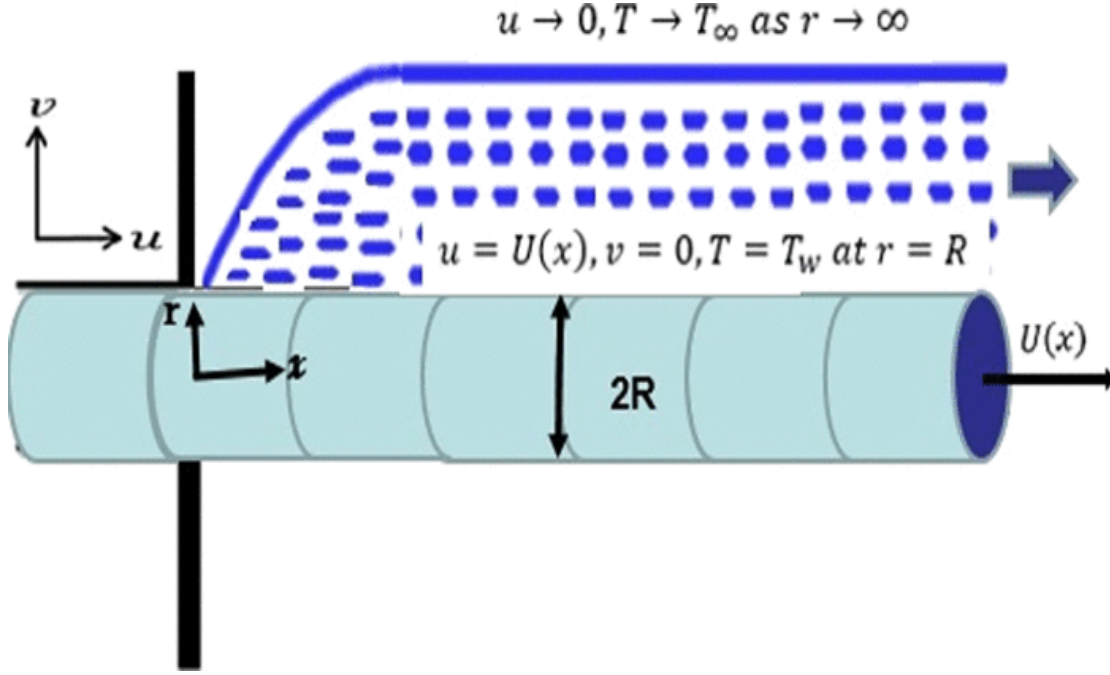


**Figure 3.9 Schematic configuration with coordinate system**

A velocity component is represented by  $u$  and  $v$  along directions  $x$  and  $r$ , respectively, thermal relaxation ( $\delta$ ), chemical reaction parameter ( $K_r$ ), and magnetic field intensity ( $B_0$ ). Except for density changes that create a thermal buoyancy force retains consistent characteristics. In Table 3.2, the subscript  $f_s$  is represent fluid. In order to reduce the complexity of the elaborated problem, the following nondimensional variables must be included:

$$\begin{aligned} \psi(x, r) = R\sqrt{u_w v_f x} f(\xi), \quad \xi = \frac{r^2 - R^2}{2R} \left( \frac{u_w}{v_f x} \right)^{\frac{1}{2}}, \quad u = \frac{1}{r} \frac{\partial \psi}{\partial r}, \quad v = -\frac{1}{r} \frac{\partial \psi}{\partial x}, \\ \theta(\xi) = \frac{T - T_\infty}{T_w - T_\infty}, \quad \Phi(\xi) = \frac{C - C_\infty}{C_w - C_\infty}, \quad u_w = \frac{ax}{l} \end{aligned}$$

Here the stream functions  $\Psi$  and  $\xi$  are dimensionless. Usually, equation (3.18.1) is satisfied by demarcating this  $\Psi$  stream function. Following this, the non-linear partial differential equations (3.18.2)–(3.18.4) are transformed as:

$$(2\xi\Gamma + 1)f_1''' + 2\Gamma f_1'' + \frac{B_3}{B_1} \lambda \theta + \frac{B_2}{B_1} [1 + f_1 f_1'' - (f_1')^2] - \frac{M}{B_1} f_1' = 0 \quad (3.18.6)$$

$$[(2\xi\Gamma + 1)\theta'' + 2\Gamma\theta'] + \frac{B_5}{B_4} P_r [f' \theta] - \frac{B_5}{B_4} P_r \theta_t [f_1^2 \theta'' + f_1 f_1' \theta'] = 0 \quad (3.18.7)$$

$$(1 + 2\xi\Gamma)\Phi'' + (Le f_1 + 2\Gamma)\Phi' + Sr[(2\xi\Gamma + 1)\theta'' + 2\Gamma\theta'] - Le C_h \Phi = 0 \quad (3.18.8)$$

Moreover, the modified boundary conditions are as follows;

$$f_1(\xi) = 0, \quad f_1'(\xi) = 0, \quad \theta'(\xi) = -Bi\{1 - \theta(0)\}, \quad \Phi(\xi) = 1 \quad \text{at } \xi = 0 \quad (3.18.9)$$

$$f_1'(\xi) \rightarrow 1, \theta(\xi) \rightarrow 0, \quad \Phi(\xi) \rightarrow 0, \quad \text{at } \xi \rightarrow \infty$$

The thermos-physical factors are explained such as; Elsaid and Abdel-wahed (2021).

$$B_1 = \mu_{nf} = \frac{\mu_f}{(1 - \phi)^{\frac{5}{2}}},$$

$$B_2 = \frac{\rho_{nf}}{\rho_f} = \{(1 - \phi)\} + \frac{\rho_{s_1}}{\rho_f} \phi$$

$$B_3 = \frac{(\rho\beta)_{nf}}{(\rho\beta)_f} = \left( (1 - \phi) + \frac{(\beta\rho)_s}{(\beta\rho)_f} \phi \right)$$

$$B_4 = \frac{\kappa_{nf}}{\kappa_f} = \frac{\kappa_s + 2\kappa_f - 2(\kappa_f - \kappa_s)\phi}{\kappa_s + 2\kappa_f + (\kappa_f - \kappa_s)\phi},$$

$$B_5 = \frac{(\rho C_p)_{nf}}{(\rho C_p)_f} = \left( (1 - \phi) + \frac{(\rho C_p)_s}{(\rho C_p)_f} \phi \right)$$

### 3.18.2 Physical Quantities

The various involving parameters in equations (3.18.6) to (3.18.9) are also described, as are the numerous participating parameters are Prandtl number ( $Pr$ ), Magnetic parameter ( $M$ ), traditional Lewis number ( $Le$ ), chemical reaction parameter ( $C_h$ ), Biot number ( $B_i$ ), mixed convection parameter ( $\lambda$ ), Grashof number ( $G_r$ ), Reynolds number, ( $S_r$ ) Soret number, and the curvature parameter ( $\Gamma$ )

$$\theta_t = \frac{\alpha\delta}{l}, \quad M = \frac{\sigma_f B_0^2 l}{\rho_f a}, \quad Sr = \frac{\kappa_t(T_w - T_\infty)}{T_m(C_w - C_\infty)}, \quad C_h = \frac{K_c l}{a}$$

$$Le = \frac{\mu_f}{\rho_f D_m}, \quad \lambda = \frac{G_r}{Re}, \quad G_r = \frac{\beta_f g(T_w - T_\infty) l^3}{\nu_f^2}, \quad Pr = \frac{\mu_f}{\rho_f \alpha_f}$$

$$\Gamma = \frac{1}{R} \sqrt{\frac{\mu_f l}{\rho_f a}}, \quad Bi = \frac{R h_{nf}}{(\kappa_{nf}) r} \sqrt{\frac{l \nu_f}{a}}, \quad \alpha_f = \frac{\kappa_f}{(\rho c)_f}, \quad Re = \frac{U - wl}{\nu_f}$$

### 3.18.3 Engineering Quantities

The requisite aspects of engineering concerns skin friction coefficient  $\{C_{fx} Re_x^{-\frac{1}{2}}\}$ , local Sherwood number  $\{Sh_x Re_x^{-\frac{1}{2}}\}$ , local Nusselt number  $\{Nu_x Re_x^{-\frac{1}{2}}\}$ , and local density of the motile microorganism  $\{Nn_x\}$  the following specific interest includes:

$$C_{fx} = \frac{2\mu_{nf}}{\rho_f U_w^2} \left( \frac{\partial u}{\partial r} \right)_{r=R}, \quad Nu_x = \frac{x \kappa_{nf}}{\kappa_f (T_w - T_\infty)} \left( \frac{\partial T}{\partial r} \right)_{r=R}$$

$$Sh_x = \frac{-x D_m}{D_m (C_w - C_\infty)} \left( \frac{\partial C}{\partial r} \right)_{r=R}$$

Utilizing the above similarity transformations, can be calculated as:

$$C_{fx} = \sqrt{Re_x} C_f = 2B_1 \frac{d^2 f_1(0)}{d\xi^2}, \frac{Nu_x}{\sqrt{Re_x}} = -B_4 \{\theta'(0)\}, \frac{Sh_x}{\sqrt{Re_x}} = -\Phi'(0)$$

Where,  $Re_x = \frac{xu_w}{\nu_f}$  is the local Reynold's number.

### 3.18.4 Execution of Methodology

The system of ODE's is numerically solved by the RK technique. In which estimates the mathematical solutions numerically using an adaptive Runge-Kutta method (for solutions) in MATLAB and for shooting we implemented the Newton-Raphson method Kiusalaas (2005). We do this by first assuming

$$\begin{aligned} f_1 &= \Pi_1, & f_1' &= \Pi_2, & f_1'' &= \Pi_3 \\ \theta &= \Pi_4, & \theta' &= \Pi_5, & \Phi &= \Pi_6, & \Phi' &= \Pi_7, \\ \zeta &= \Pi_8, & \zeta' &= \Pi_9 \\ \Pi_1' &= \Pi_2, \\ \Pi_2' &= \Pi_3, \\ \Pi_3' &= -\frac{1}{(1+2\Gamma\xi)} \left[ 2\Gamma\Pi_3 + \frac{B_2}{B_1} (1 + \Pi_1\Pi_3 - \Pi_2^2) + \frac{B_3}{B_1} \lambda\Pi_4 - \frac{M}{B_1} \Pi_2 \right] \\ \Pi_4' &= \Pi_5 \\ \Pi_5' &= \frac{1}{(B_5 P_r \theta_t \Pi_1^2 - B_4(1+2\xi\Gamma))} [2B_4 \Gamma\Pi_5 + B_5(P_r)(\Pi_1\Pi_5) - B_5 P_r \theta_t \Pi_1 \Pi_2 \Pi_5] \\ \Pi_6' &= \Pi_7 \\ \Pi_7' &= -\frac{1}{(1+2\Gamma\xi)} [(2\Gamma + Le\Pi_1)\Pi_7 + S_r(1+2\Gamma\xi)(\Pi_5') + 2\Gamma\Pi_5] - LeC_h\Pi_6 \end{aligned}$$

with

$$\Pi_1(0) = 0, \Pi_2(0) = 1, \Pi_3(0) = \Delta_1, \Pi_4(0) = \Delta_2, \Pi_5(0) = Bi(1 + \Pi_4(0)), \Pi_6(0) = 1, \Pi_7(0) = \Delta_3$$

where  $\Delta_1, \Delta_2, \Delta_3$ , are calculated with an appropriate initial guess using the Newton Raphson technique.

### 3.19 Significance of irregular heat source and Arrhenius energy on electro magneto hydro dynamic hybrid nanofluid flow over a rotating stretchable disk with nonlinear radiation

This extensive study enhances heat transformation while accounting for the electro-magnetohydrodynamic (EMHD) hybrid nanofluid flow in the presence of non-linear thermal radiation and irregular heat source over a rotating disk considering the Arrhenius activation energy and the modified Buongiorno model. The convective and zero-mass flux boundary constraints on the flow of water-based  $Cu - Fe_3O_4$  hybrid nanofluid is also accounted. The system of partial differential equations is first represented mathematically and then converted into a system of ordinary differential equations using adequate transformations. The ordinary differential equations are then numerically solved using the bvp5c (MATLAB built-in function) algorithm. In graphs, fluid velocity, temperature, concentration profiles, and

quantities of practical interest are described, including skin friction coefficient and Nusselt number. The magnitude of the influence of significant parameters on local skin friction and local Nusselt number are demonstrated using linear regression slope.

### 3.19.1 Formulation of the problem

A steady hydromagnetic incompressible and axisymmetric water-based  $Cu - Fe_3O_4$  hybrid nano-liquid flow due to a circular rigid disk has been considered. The disk rotates with an angular velocity  $\Omega$  about  $z - axis$  and is placed at  $z = 0$ , which is illustrated in Figure (3.10). The fluid velocity components  $(u, v, w)$  are in directions determined by their respective cylindrical coordinates  $(r, \varphi, z)$ . The pressure, temperature and concentration of the ambient nanofluid are maintained at  $p_\infty$ ,  $T_\infty$ , and  $C_\infty$ , respectively. Additionally, Arrhenius activation energy is taken into consideration along with magnetic and electric fields normal to the disk and is regarded a heated fluid with the  $-k_{hnf} \left( \frac{\partial T}{\partial z} \right) = h_f(T_f - T)$  wall. A two-phase modified Buongiorno hybrid nano fluid model assumes zero mass flux at the boundary, resulting the governing equations for hybrid nanofluids in laminar and incompressible boundary layers can be formulated (Kumar and Singh 2021; Reddy *et al.* 2021; Raju *et al.* 2016; Ghadikolaei *et al.* 2017) as:

$$\frac{\partial u}{\partial r} + \frac{u}{r} + \frac{\partial w}{\partial z} = 0 \quad (3.17.1)$$

$$\rho_{hnf} \left( u \frac{\partial u}{\partial r} - \frac{v^2}{r} + w \frac{\partial u}{\partial z} \right) = -\frac{\partial p}{\partial r} + \left( \frac{\partial^2 u}{\partial r^2} + \frac{1}{r} \frac{\partial u}{\partial r} - \frac{u}{r^2} + \frac{\partial^2 u}{\partial z^2} \right) + \sigma_{hnf} (E_0 B_0 - B_0^2 u), \quad (3.17.2)$$

$$\rho_{hnf} \left( u \frac{\partial v}{\partial r} + \frac{uv}{r} + w \frac{\partial v}{\partial z} \right) = \mu_{hnf} \left( \frac{\partial^2 v}{\partial r^2} + \frac{1}{r} \frac{\partial v}{\partial r} - \frac{v}{r^2} + \frac{\partial^2 v}{\partial z^2} \right) + \sigma_{hnf} (E_0 B_0 - B_0^2 v), \quad (3.17.3)$$

$$\rho_{hnf} \left( u \frac{\partial w}{\partial r} + w \frac{\partial w}{\partial z} \right) = -\frac{\partial p}{\partial z} + \mu_{hnf} \left( \frac{\partial^2 w}{\partial r^2} + \frac{1}{r} \frac{\partial w}{\partial r} + \frac{\partial^2 w}{\partial z^2} \right), \quad (3.17.4)$$

$$(\rho C_p)_{hnf} \left( u \frac{\partial T}{\partial r} + w \frac{\partial T}{\partial z} \right) = k_{hnf} \left( \frac{\partial^2 T}{\partial r^2} + \frac{1}{r} \frac{\partial T}{\partial r} + \frac{\partial^2 T}{\partial z^2} \right) + (\rho C_p)_p \left\{ D_B \left( \frac{\partial T}{\partial z} \frac{\partial C}{\partial z} + \frac{\partial T}{\partial r} \frac{\partial C}{\partial r} \right) + \right. \quad (3.17.5)$$

$$\left. \frac{D_T}{T_\infty} \left[ \left( \frac{\partial T}{\partial z} \right)^2 + \left( \frac{\partial T}{\partial r} \right)^2 \right] \right\} + Q_t (T - T_\infty) + Q_e (T_f - T_\infty) e^{-mz} \sqrt{\frac{\Omega}{\nu_f}} + \frac{\partial}{\partial z} \left( \frac{16\sigma^*}{3k^*} T^3 \frac{\partial T}{\partial z} \right),$$

$$u \frac{\partial C}{\partial r} + w \frac{\partial C}{\partial z} = D_B \left( \frac{\partial^2 C}{\partial z^2} + \frac{1}{r} \frac{\partial C}{\partial r} + \frac{\partial^2 C}{\partial r^2} \right) + \frac{D_T}{T_\infty} \left( \frac{\partial^2 T}{\partial r^2} + \frac{1}{r} \frac{\partial T}{\partial r} + \frac{\partial^2 T}{\partial z^2} \right) - k_r^2 (C - C_\infty) \left( \frac{T}{T_\infty} \right)^n e^{-\frac{E_a}{K^* T}}. \quad (3.17.6)$$

subject to the boundary conditions

$$\left. \begin{aligned} u &= sr + \alpha_1 \left( \frac{\partial u}{\partial z} \right), v = \Omega r + \alpha_1 \left( \frac{\partial v}{\partial z} \right), w = 0, \\ -k_{hnf} \left( \frac{\partial T}{\partial z} \right) &= h_f (T_f - T), D_B \left( \frac{\partial C}{\partial z} \right) + \frac{D_T}{T_\infty} \left( \frac{\partial T}{\partial z} \right) = 0 \end{aligned} \right\} \text{when } z = 0 \quad (3.17.8)$$

$$u \rightarrow 0, v \rightarrow 0, T \rightarrow T_\infty, C \rightarrow C_\infty \quad \text{as } z \rightarrow \infty$$

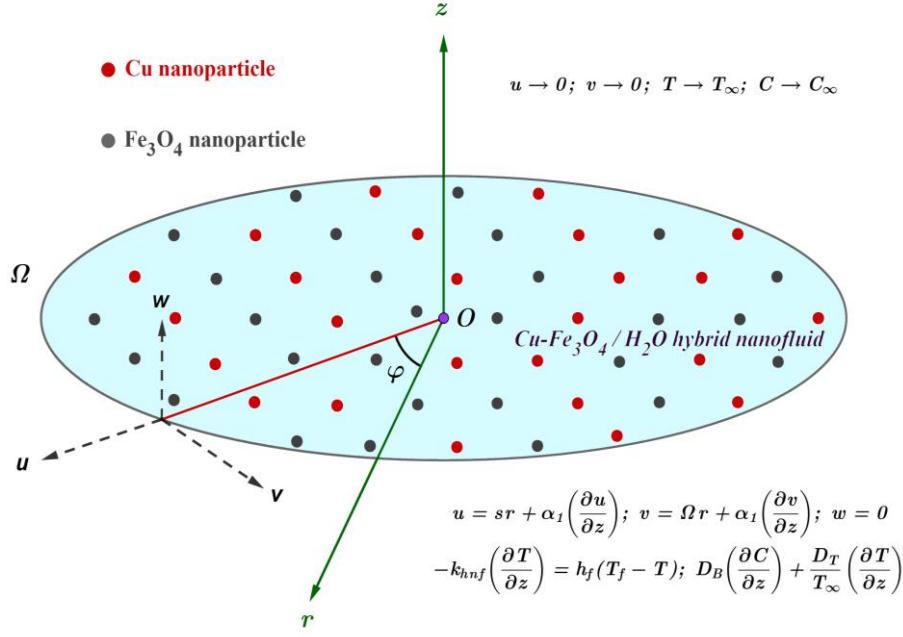


**Figure 3.10 Pictorial representation of the model**

The following acronyms stand for the following terms:  $D_T$  stands for the thermophoretic diffusion coefficient,  $(\rho C_p)_p$  denotes the effective heat capacity of the particle,  $Q_e$  stand for the exponential space-dependent heat source coefficient,  $k_r$  stands for reaction rate,  $h_f$  coefficient of heat transfer,  $E_a$  stands for activation energy,  $m$  the exponential index,  $n$  the fitted rate constant and is the  $k_r^2 (C - C_\infty) \left(\frac{T}{T_\infty}\right)^n e^{-\frac{E_a}{K^* T}}$  Arrhenius function,  $D_B$  stands for Brownian diffusion coefficient,  $Q_t$  thermal dependent linear heat source coefficient. Table 1 summarizes the thermophysical characteristics of  $Cu$ ,  $Fe_3O_4$  and water

Introducing the following similarity transformations Raju *et al.* (2021):

$$\xi = z \sqrt{\frac{\Omega}{\vartheta_f}}, u = r \Omega F(\xi), v = r \Omega G(\xi), w = \sqrt{\vartheta_f \Omega} H(\xi),$$

$$p = p_\infty - 2\Omega\mu_f P(\xi), T = T_\infty + (T_f - T_\infty) \theta(\xi), C = C_\infty + C_\infty \psi(\xi)$$

into (1) – (5), the governing equations reduce to:

$$H' + 2F = 0 \quad (3.19.9)$$

$$\frac{A_1}{A_2} F'' - HF' + (G)^2 - F^2 - \frac{A_3}{A_2} (M(E - F)) = 0 \quad (3.19.10)$$

$$\frac{A_1}{A_2} G'' - HG' - 2GF - \frac{A_3}{A_2} (M(E - G)) = 0 \quad (3.19.11)$$

$$\left(\frac{A_4}{A_5 Pr}\right) \theta'' + \left(\frac{4R_d}{3A_5 Pr}\right) [(\theta_m - 1) + 1]^3 \theta'' + \left(\frac{4R_d}{3A_5 Pr}\right) [(\theta_m - 1) + 1]^2 (\theta')^2 + \frac{N_t}{A_5} (\theta')^2 + \frac{N_b}{A_5} \psi' \theta' - H\theta' + \left(\frac{Q_e}{A_5}\right) e^{(-M\xi)} = 0 \quad (3.19.12)$$

$$\psi'' + S_c H \psi' - \left(\frac{N_t}{N_b}\right) \theta'' - Kr S_c (1 + \delta\theta)^n e^{\left(\frac{-E_A}{(1+\delta\theta)}\right)} \psi = 0 \quad (3.19.13)$$

With

$$\begin{aligned} F(0) &= \lambda + \Gamma F'(0), G(0) = 1 + \Gamma G'(0), H = 0, \\ A_4 \theta(0)' &= -B_i(\theta(0) - 1), \psi'(0) + \left(\frac{N_t}{N_b}\right) \theta'(0) = 0 \\ F(\infty) &\rightarrow 0, G(\infty) \rightarrow 0, \theta(\infty) \rightarrow 0, \psi(\infty) \rightarrow 0 \end{aligned} \quad (3.19.14)$$

where the dimensionless parameters are:

$$\begin{aligned} M &= \frac{\sigma_f B_0^2}{\Omega \rho_f}, E = \frac{E_0}{B_0 \Omega r}, Pr = \frac{(\mu C_p)_f}{\kappa_f} = \frac{\vartheta_f}{\alpha_f}, Kr = \frac{k_r^2}{\Omega}, N_t = \frac{\tau D_t (T_f - T_\infty)}{(v)_f T_\infty}, \\ R_d &= \frac{4(T_\infty)^3 \sigma^*}{\kappa^* k_f}, Q_E = \frac{Q_e}{(\Omega \rho C_p)_f}, \tau = \frac{(\rho C_p)_p}{(\rho C_p)_f}, E_A = \frac{E_A}{(k)_f T_\infty}, \\ S_c &= \frac{\vartheta_f}{D_B}, \theta_m = \frac{T_f}{T_\infty}, N_b = \frac{\tau D_B C_\infty}{(v)_f}, \theta_m = \frac{T_f}{T_\infty} - 1, \lambda = \frac{s}{\Omega}, B_i = \frac{h_f}{k_f} \sqrt{\frac{\nu_f}{\Omega}}, \end{aligned}$$

Physical quantities in the non-dimensional form are given by:

$$\begin{aligned} \frac{\mu_{hnf}}{\mu_f} &= \frac{1}{(1 - \phi_1)^{2.5} (1 - \phi_2)^{2.5}} = A_1, \frac{\rho_{hnf}}{\rho_f} = (1 - \phi_2) \left( (1 - \phi_1) + \phi_1 \frac{\rho_{s_1}}{\rho_f} \right) + \phi_2 \frac{\rho_{s_2}}{\rho_f} = A_2 \\ \frac{\sigma_{hnf}}{\sigma_f} &= 1 + \frac{3 \left( \frac{\phi_1 \sigma_{s_1} + \phi_2 \sigma_{s_2}}{\sigma_f} - (\phi_1 + \phi_2) \right)}{2 + \left( \frac{\phi_1 \sigma_{s_1} + \phi_2 \sigma_{s_2}}{(\phi_1 + \phi_2) \sigma_f} \right) - \left( \frac{\phi_1 \sigma_{s_1} + \phi_2 \sigma_{s_2}}{\sigma_f} - (\phi_1 + \phi_2) \right)} = A_3 \\ \frac{k_{hnf}}{k_f} &= \frac{k_{hnf}}{k_{nf}} * \frac{k_{nf}}{k_f} = A_4, \text{ where } \frac{k_{hnf}}{k_{nf}} = \frac{k_{s_2} + 2k_{nf} - 2\phi_2(k_{nf} - k_{s_2})}{k_{s_2} + 2k_{nf} + \phi_2(k_{nf} - k_{s_2})}, \\ \frac{k_{nf}}{k_f} &= \frac{k_{s_1} + 2k_f - 2\phi_1(k_f - k_{s_1})}{k_{s_1} + 2k_f + \phi_1(k_f - k_{s_1})}, \frac{(\rho C)_{hnf}}{(\rho C)_f} = (1 - \phi_2) \left( 1 - \phi_1 + \phi_1 \frac{(\rho C)_{s_1}}{(\rho C)_f} \right) + \phi_2 \frac{(\rho C)_{s_2}}{(\rho C)_f} = A_5 \end{aligned}$$

### 3.19.2 Engineering Quantities

The skin friction coefficient ( $Cf_x$ ) quantifying the drag rate and the Nusselt number (Nu) quantifying the heat transfer rate are defined as:

$$\begin{aligned} Cf_x &= \sqrt{\frac{\tau_r^2 + \tau_\varphi^2}{\rho_f (\Omega r)^2}} \quad \text{As } \tau_r = \mu_{hnf} \left. \frac{\partial u}{\partial z} \right|_{z=0}, \tau_\varphi = \mu_{hnf} \left. \frac{\partial v}{\partial z} \right|_{z=0} \\ Nu_x &= \frac{x q_\omega}{\kappa_f (T_W - T_0)} = \frac{-x \kappa_{nf} \left. \frac{\partial T}{\partial z} \right|_{z=0}}{\kappa_f (T_W - T_0)} + q_r|_{z=0} \end{aligned}$$

the engineering quantities reduces to:

$$\begin{aligned} Cf_x Re_x^{1/2} &= A_1 \sqrt{F'(0) + G'(0)} \\ Nu_x Re_x^{-\frac{1}{2}} &= - \left\{ A_4 + \left( \frac{4R_d}{3} \right) [(\theta_m - 1) + 1]^3 \right\} \theta'(0) \end{aligned}$$

Where,  $Re_x = \frac{\Omega r^2}{\vartheta_f}$  is the local Reynold's number.

### 3.19.3 Numerical Procedure and Validation

Initially assume:

$$F = \Pi_1, \quad F' = \Pi_2, \quad G = \Pi_3, \quad G' = \Pi_4, \quad H = \Pi_5, \\ \theta = \Pi_6, \quad \theta' = \Pi_7, \quad \psi = \Pi_8, \quad \psi' = \Pi_9$$

Accordingly, the system of first-order ODEs is given by:

$$\begin{aligned} \Pi'_1 &= \Pi_2, & \Pi'_2 &= \frac{A_2}{A_1} ((\Pi_1)^2 - (\Pi_3)^2 + \Pi_4 \Pi_5) - \frac{A_3}{A_1} (M(E - \Pi_1)) \\ \Pi'_3 &= \Pi_4, & \Pi'_4 &= \frac{A_2}{A_1} (2\Pi_1 \Pi_3 + \Pi_4 \Pi_5) - \frac{A_3}{A_1} (M(E - \Pi_3)) \\ \Pi'_6 &= \Pi_7, & \Pi'_7 &= \left( \frac{P_r}{\left( A_1 + \left( \frac{4R_d}{3} \right) [(\theta_m - 1)\Pi_6 + 1]^3 \right)} \right) [A_5 \Pi_5 \Pi_7 - N_t (\Pi_7)^2 - N_b \Pi_7 \Pi_9 - Q_E e^{(-M\xi)}] + \\ & & & \left( \frac{P_r}{\left( A_1 + \left( \frac{4R_d}{3} \right) [(\theta_m - 1)\Pi_6 + 1]^3 \right)} \right) \left[ -Q_t \Pi_7 - \left( \frac{4R_d}{3} \right) [(\theta_m - 1)\Pi_6 + 1]^2 (\theta_m - 1) (\Pi_7)^2 \right] \\ \Pi'_8 &= \Pi_9, & \Pi'_9 &= S_c \Pi_5 \Pi_9 - \left( \frac{N_t}{N_b} \right) \Pi'_7 - Kr S_c (1 + \delta \Pi_6)^n e^{\left( \frac{-E_A}{(1 + \Pi_6 \delta)} \right)} \end{aligned}$$

subject to the boundary conditions

$$\begin{aligned} \Pi_1(0) &= \lambda + \Gamma \Pi_2(0), \Pi_3(0) = 1 + \Gamma \Pi_4(0), \Pi_5(0) = 0, \\ A_4 \Pi_7(0) &= B_i (\Pi_6(0) - 1), \Pi_9(0) + \left( \frac{N_t}{N_b} \right) \Pi_7(0) = 0 \\ \Pi_1(\infty) &\rightarrow 0, \Pi_2(\infty) \rightarrow 0, \Pi_6(\infty) \rightarrow 0, \Pi_8(\infty) \rightarrow 0 \end{aligned}$$

The reduced set of ODEs are numerically resolved utilizing the finite-difference based `bvp5c` algorithm. The infinity condition was rescaled to 4. The Prandtl number, Brownian motion parameter, Schmidt number, and thermophoresis parameter have been fixed at 6.2, 0.04, 2.62, and 0.04, respectively. The accuracy of the numerical procedure is validated through restrictive comparison with the works of Sabu *et al.* (2021), Turkyilmazoglu (2014) and Khan *et al.* (2018). The value of thermo-physical characteristics of some base fluids and solid particles in Table 3.3 extract from (Ghadikolaei *et al.* 2017; Khan *et al.* 2016; Jamshed and Aziz 2018; Nandi *et al.* 2022; Raju *et al.* 2016; Reddy *et al.* 2021).

### RESULTS AND DISCUSSION

---

The governing equations with boundary conditions have been numerically solved using a standard software package with computational techniques. The impact of several developing parameters on the flow field, temperature and concentration distributions, skin friction coefficient, Nusselt number and Sherwood number have been shown via graphs and tables.

In section 4.1, the consequences of various influential parameters magnetic field parameter ( $M$ ), Weissenberg number ( $W$ ), heat source parameter ( $Q_p$ ) Biot number ( $B_i$ ), suction/blowing parameter ( $F_w$ ), material parameter ( $K$ ), the inter-particle spacing  $H$  and the radiation parameter ( $R_d$ ), the nanoparticle's radius ( $D_p$ ), on velocity  $f(\eta)$ , micro-rotation  $\beta(\eta)$ , and the temperature  $\theta(\eta)$  profiles are illustrated in Figures. To authenticate the accuracy of code, the results of temperature gradient ( $\theta'(0)$ ) are compared with the results those obtained by previous work for different estimations of Prandtl number  $Pr$  in the absence of above-mentioned parameters. The results are found in superior agreement and confirm that the outcomes are novel and authentic. The impact of influential parameters on physical quantities is illustrated using three-dimensional graphs.

In the next section, 4.2, the influence of the MHD flow of an ethylene glycol-based nanofluid containing copper nanoparticles through an exponential stretching sheet has been studied. The impact of parameters such as the magnetic field, Prandtl number  $Pr$ , Biot number  $Bi$ , and thermophoretic variable  $N_T$ , Schmidt number  $S_c$ , Eckert number  $E_c$ , Brownian diffusion  $N_B$ , slip effect  $\lambda$  and radiation parameter  $R_d$  on velocity  $f'(\xi)$ , concentration ( $\psi(\xi)$ ), and temperature ( $\theta(\xi)$ ) profiles are illustrated with Figures. The code was verified as accurate for various values of  $Pr$  as shown in Table 4.1. The variation of the Nusselt number, skin friction coefficient and Sherwood number for different values of parameters have been also described in tables.

The section 4.3 includes the results on enhancement of heat transformation while accounting for the magnetohydrodynamic (MHD) nanofluid flow with the impact of non-linear thermal radiation and an irregular heat source over the stretching sheet. The impact of Arrhenius activation energy with active and passive controls of nanoparticles, thermophoresis and Brownian diffusion has been elaborated. The effects of involving parameters on the profiles of radial velocity, micro rotation velocity  $G(\eta)$ , nanofluid concentration  $\phi(\eta)$ , and nanofluid temperature  $\theta(\eta)$  are shown in Figures. The Comparison of Nusselt number, skin friction coefficient and Sherwood number with active case and passive case for different values of parameters are shown in table.

In section 4.4, the physical parameters of the significant like curvature parameter ( $\Gamma$ ), Prandtl number ( $Pr$ ), impact of chemical parameter  $C_h$ , the mixed convection parameter ( $\lambda$ ), impact on momentum profile  $f_1(\xi)$ , thermal distribution  $\theta(\xi)$ , nanoparticle concentration profile  $\Phi(\xi)$ , motile concentration profile  $\zeta_1(\xi)$  with local drag coefficients discussed using graphs and tables. The response surface methodology technique and sensitivity analysis have been used to examine the effects of nanoparticle volume fraction.

Section 4.5 focuses on analysis of two-dimensional incompressible magnetohydrodynamic Carreau nanofluid flow across a stretching cylinder containing microorganisms with impacts of chemical reaction, heat source, and multiple slip boundary conditions.

Section 4.6 describes flow field, temperature and concentration distributions under the effect of relevant parameters, such as magnetic field, Prandtl number  $Pr$ , Biot number  $Bi$ , and thermophoretic variable  $N_T$ , Schmidt number  $S_c$ , Eckert number  $E_c$ , Hartmann number  $M_1$ , thermal conductivity parameter  $\epsilon$ , brownian diffusion  $N_B$ , and radiation parameter  $R_d$  on nanofluid flow over Riga plate. The numerical values of surface drag force and temperature gradient for different parameters are shown with the help of table.

In section 4.7, the physical parameters like Prandtl number ( $Pr$ ), chemical reaction parameter  $C_h$ , the mixed convection parameter ( $\lambda$ ), curvature parameter ( $\Gamma$ ), impact on momentum profile  $F(\xi)$ , thermal distribution  $\theta(\xi)$ , Biot number ( $bi$ ), nanoparticle concentration profile  $\Phi(\xi)$ , with local drag coefficient are clarified using graphs and tables.

The section 4.8 describes the electro-magnetohydrodynamic (EMHD) hybrid nanofluid flow in the presence of non-linear thermal radiation and irregular heat source over a rotating disk considering the Arrhenius activation energy and the modified Buongiorno model. The consequence of various influential parameters on radial velocity ( $F(\xi)$ ), azimuthal velocity ( $G(\xi)$ ), nanofluid concentration ( $\psi(\xi)$ ) and nanofluid temperature ( $\theta(\xi)$ ) profiles and quantities of practical interest are described and illustrated through Figures.

#### **4.1 The numerical simulation of nanoparticle size and thermal radiation with the magnetic field effect based on tangent hyperbolic nanofluid flow over a stretching sheet**

The consequences of various influential parameters on velocity  $f(\eta)$ , micro-rotation  $\beta(\eta)$ , and the temperature  $\theta(\eta)$  profiles with magnetic field parameter  $M = 0.01$ ,  $Pr = 6.2$ ,  $W = 1$ , heat source parameter  $Q_p = 0.1$ ,  $\phi = 0.1$ , Biot number  $B_i = 0.5$ , the nanoparticle's radius  $D_p = 1.5$ ,  $Fw = 0.5$ ,  $K = 0.2$ ,  $n = 0.1$  and the inter-particle spacing  $H = 1$  and radiation parameter  $R_d = 0.5$  respectively were obtained and illustrated in Figures.

The magnitude of the distribution of velocity raised as the radius of the  $Al_2O_3$  nanoparticle and shown in the Figures 4.1.1 – 4.1.4, since the radius of nanoparticles has an impact on the interphase and nanoparticles. The relative viscosity of these nanofluids decreased with an increase in particle size which meant that the current transport phenomenon's velocity grew as the radius of  $Al_2O_3$  increases.

The velocity declined with a higher value of magnetic strength (M) as illustrated in Figure (4.1.1). Since Lorentz force is a resistive form of force that retards the flow of an electrically conducting fluid when a magnetic field is normal to it. This resistive force regulates nanofluids and reduces the velocity profile.

Figure (4.1.2-4.1.3) indicates that temperature and micro-rotation distribution were reduced by a rise in the radius of  $Al_2O_3$  nanoparticles. The temperature and micro-rotation distribution were enhanced with a higher value of the magnetic parameter. Since the introduction of Lorentz, drag has improved frictional heating between the fluid layers and releases energy in the form of heat, which thickens the thermal boundary layer.

In Figure (4.1.4), the thermal boundary layer gets reduced with an increase in the radius of nanoparticles  $Al_2O_3$  under the influence of  $F_w$ . Since the addition of nanoparticles enhances the temperature due to the extraordinary property, the base fluid temperature gets raised.

In figure (4.1.5), the thermal boundary layer was observed significantly increasing property of fluid layers with an increase in the value of  $Q_p$ , but reduced by an increase in the nanoparticle's radius. Figure (4.1.6) shows the connection between the material parameter and the velocity profile. It was noticed that the velocity profile was found to have a declining function of  $K$  whereas the magnitude of the velocity profile enhanced with the radius ( $D_p = 0.5, 1.5, 2.5, 3.5, 4.5$ ) of the nanoparticle. Physically, higher  $K$  values correspond to lower viscosity and a weaker rotation of the particle moment in the fluid. The material parameters allow the material to be changed without restructuring. As a result, the fluid moves at a high-velocity at near to the wall and velocity of fluid declines as fluid moves away from wall.

Figure (4.1.7-4.1.8) illustrates the impact of various parameters on the velocity profile. With a larger radius of  $Al_2O_3$  nanoparticles, the velocity profile improved. When  $m$  is increased, the concentration of the micro-element is reduced, which causes a decline in the velocity profile. The declination in micro-rotation distribution with an increase in the radius of nanoparticles when  $K = 0$  was observed. Micro-rotation distribution was detected with greater properties of fluid layers when  $K = 0.5$ . Since the fluid viscosity reduces with the increase of material parameters, which causes an enhancement in the flow of microrotation distribution.

The impact of the power-law index  $n$  on the velocity profile with concerning variation in the radius of  $Al_2O_3$  nanoparticles was shown in Figure (4.1.9). With increasing radius  $D_p$ , the strength of the velocity profile enhanced. The associated velocity layer thickness reduced as the power-law index raised. Physically fluid behavior approaches from lower to higher shear for greater values of  $n$ , resulting an increase in viscosity.

In Figure (4.1.10), the thermal boundary layer was observed to be a significantly increasing property of fluid layers with  $Bi = 0.5$  and  $Bi = 1.0$  but reduced by an increase in the radius of nanoparticles. Physically, a larger  $Bi$  correlates with more convective heating at the sheet, which raises the temperature gradient. The thermal effect can permeate deeper into the quiescent fluid with a bigger temperature differential. It's also worth noting that as the Biot number on the right side of the stretching sheet rises, the fluid temperature rises, lowering the thermal resistance of the sheet and enhancing convective heat transfer.

Figure (4.1.11) reveals the effect of the Weissenberg number  $W$  on the velocity field. It describes how the velocity layer thickness diminishes as  $W$  grows. When  $W = 2$ , the velocity profile has a slightly decreasing property of fluid layers, whereas it gets bigger as the radius of  $Al_2O_3$  nanoparticles increased. Physically, the fluid's relaxation time and a specified process time ratio determine the Weissenberg number. As the Weissenberg number rises, the relaxation time increases, causing an increase in resistance to fluid motion and, as a result, a reduction in the velocity field.

Figure (4.1.12) depicts that micro-rotation distribution in the absence of power index parameter  $n$  decreased with the increase in nanoparticle's radius. For power index  $n = 0.2$ , the layers increased to the earlier observation.

Figure (4.1.13) shows the deviation in velocity with  $D_p$  at numerous different values of  $F_w$ . In figure (4.1.14), the thermal boundary layer was observed to be a significantly increasing property of fluid layers with  $Rd = 0$  and  $Rd = 0.5$  but reduced by an increase in the radius of nanoparticles.

Figure (4.1.15) displays the effect of involving parameters  $(K, m^*, Rd, Bi)$  on the Nusselt number in conjunction with the effect of  $M, D_p$ . The Nusselt number was amplified by both the radiation parameter  $Rd$  and the Biot number  $(Bi)$ . The Nusselt number attenuated with material parameter and micro-element concentration  $m^*$ , whereas the local skin friction gets moderated with an effect of  $(K, m^*, F_w)$  is displayed in figures (4.1.16).

Table 4.1 gives a comparison of the current work with previously published works, validates the results and shows that the developed code was found accurate.

Table (4.2-4.3) elucidates the variation of pertinent parameters on heat transfer and drag coefficient. Firstly, Table 4.2 depicts the validation of our results under the implication of two different methods with the variation in values of  $M, Q_p, Rd, and Bi$  parameters. While

Table 4.3 shows the fluctuation in Nusselt number and skin friction number with the fluctuating values of nanoparticle's radius ( $D_p$ ) and inter-particle spacing ( $H$ ).

**Table 4.1: Comparison of  $-\theta'(0)$  for various values of  $Pr$  when all other parameters are held constant at 0.1**

$Pr$	Gorla and Sidawi (1994)	Khan and Pop (2010)	Hamad (2011)	Present Result
0.07	0.0656	0.0663	0.0656	0.066265
0.20	0.1691	0.1691	0.16909	0.169089
0.70	0.5349	0.4539	0.45391	0.453916
2.0	0.9114	0.9113	0.91136	0.911358
7.0	1.8905	1.8954	1.89540	1.895406
20.0	3.3539	3.3539	3.35390	3.353926
70.0	6.4622	6.4622	6.46220	6.462363

**Table 4.2: Fluctuation in  $Nu_x Re_x^{-\frac{1}{2}}$  and  $Cf_x \sqrt{Re_x}$  with different values of  $D_p$  and  $H$**

$D_p$	$H$	$Nu_x Re_x^{-\frac{1}{2}}$	$Cf_x \sqrt{Re_x}$
0.5	0.5	0.126253	-1.194712
1.5	-	0.128345	-1.940865
2.5	-	0.128877	-2.619126
3.5	-	0.129118	-3.190518
4.5	-	0.129250	-3.687111
0.5	01	0.125246	-1.081733
1.5	-	0.127126	-1.366168
2.5	-	0.128084	-1.751991
3.5	-	0.128534	-2.122199
4.5	-	0.128793	-2.460924

**Table 4.3: The Nusselt number and Skin friction for various values of  $M, Q_p, R_d, Bi$  while other parameters remain fixed**

$M$	$Q_p$	$R_d$	$Bi$	$Nu_x(Re_x)^{-\frac{1}{2}}$	$Cf_x\sqrt{Re_x}$
0	0.1	0.5	0.1	0.131126	-1.125957
0.1	-	-	-	0.131075	-1.179792
0.3	-	-	-	0.130978	-1.280456
0.5	-	-	-	0.130886	-1.373535
0.2	0.1	0.5	0.1	0.130285	-1.057739
-	0.3	-	-	0.127756	-1.057740
-	0.5	-	-	0.124954	-1.057740
-	0.6	-	-	0.117391	-1.057740
0.2	0.1	0.1	0.1	0.102991	-1.057740
-	-	0.3	-	0.117056	-1.057740
-	-	0.5	-	0.130285	-1.057740
-	-	0.7	-	0.144904	-1.057740
0.2	0.1	0.5	0.1	0.131027	-1.057740
-	-	-	0.01	0.013724	-1.057740
-	-	-	0.02	0.027304	-1.057740
-	-	-	0.05	0.067204	-1.057740

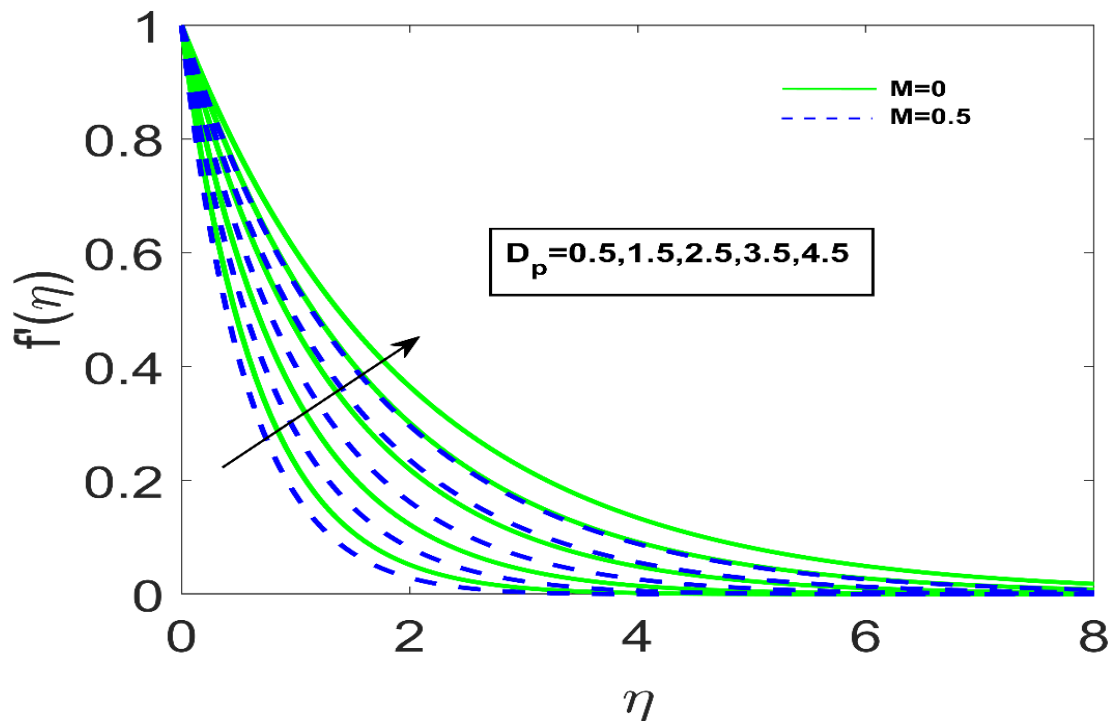


**Figure 4.1.1 Deviation in velocity with  $D_p$  at different values of  $M$**

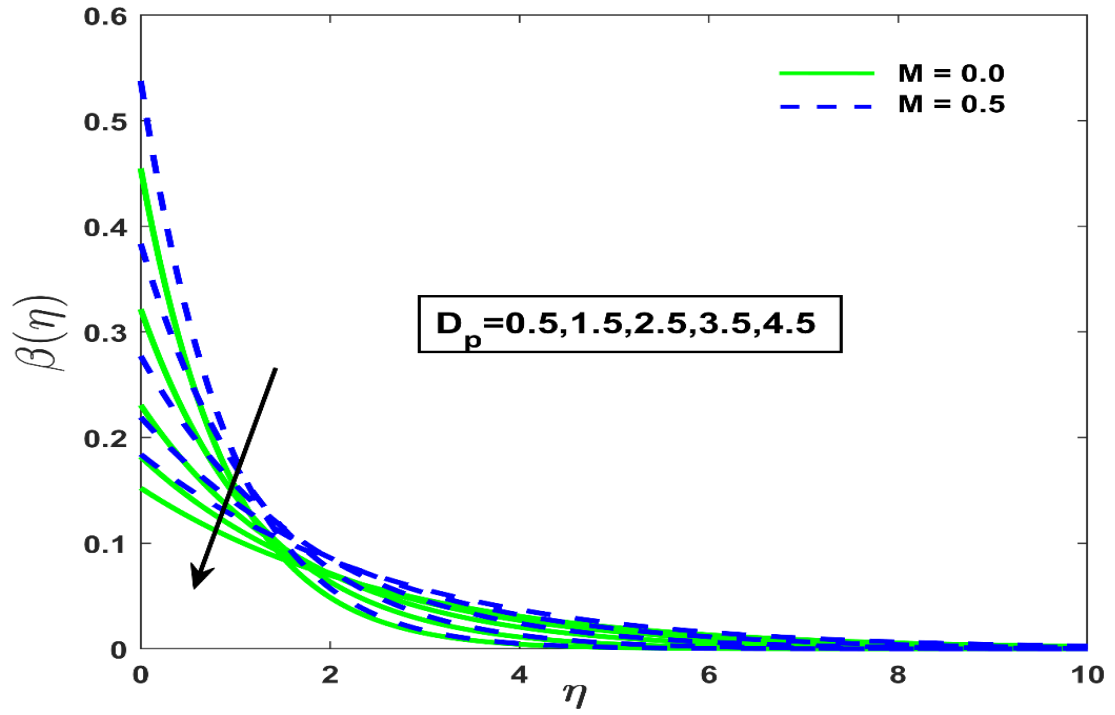


Figure 4.1.2 Deviation in micro rotation profile with  $D_p$  at different values of  $M$

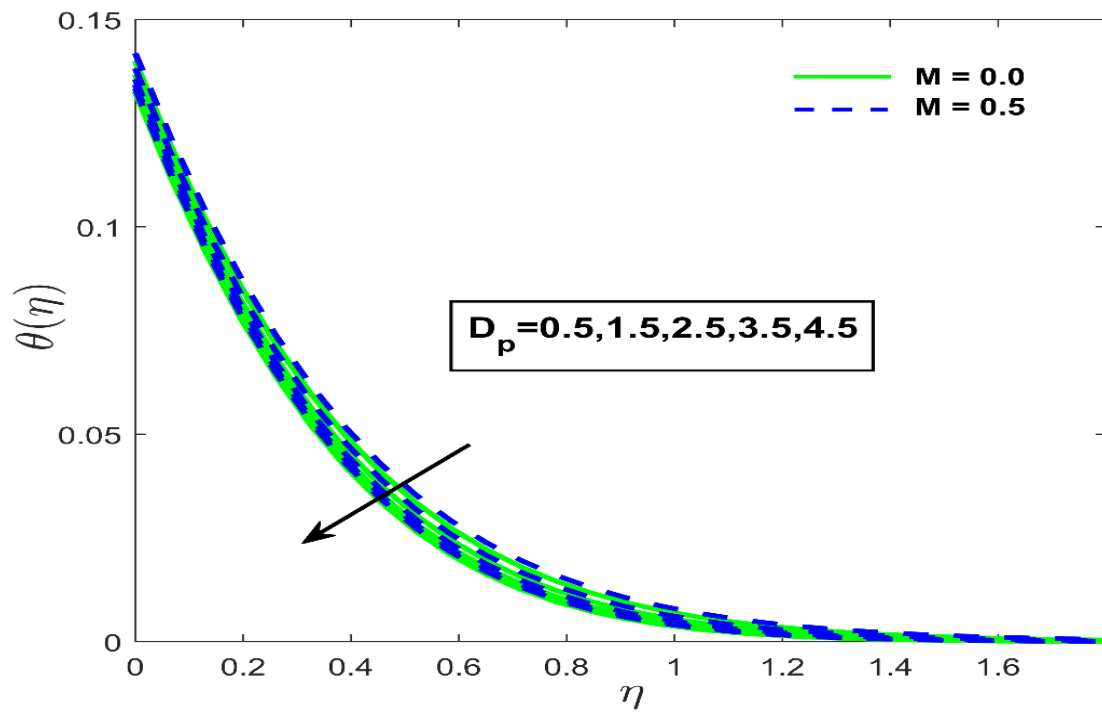


Figure 4.1.3 Deviation in temperature profile with  $D_p$  at different values of  $M$

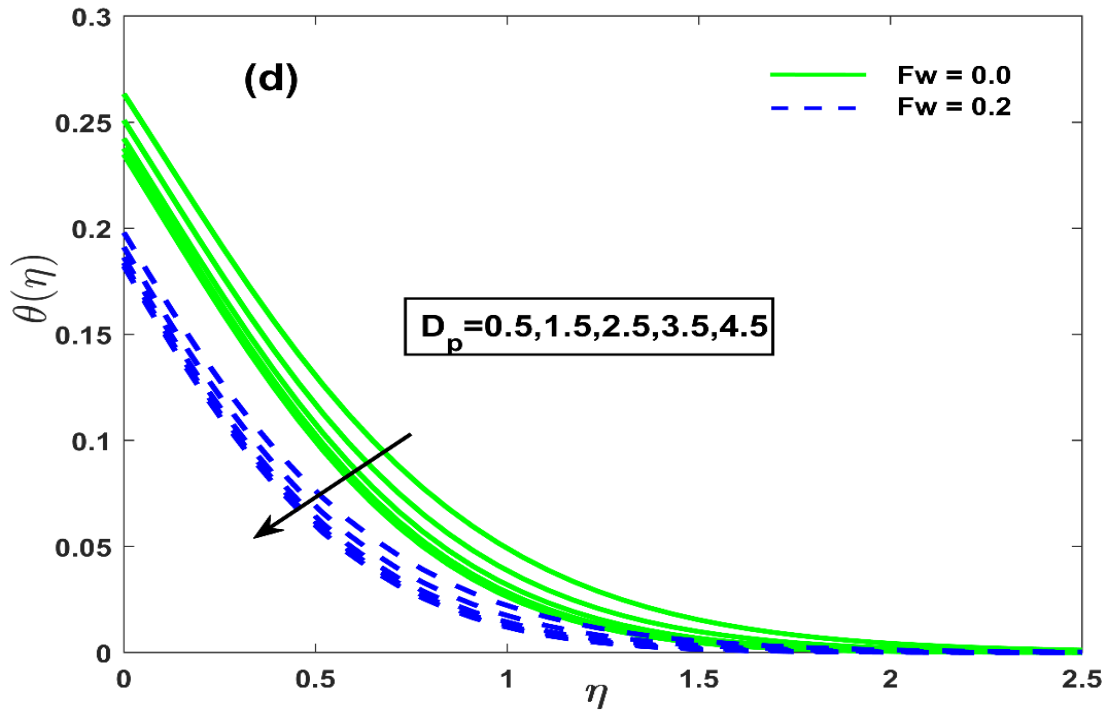


Figure 4.1.4 Deviation in temperature profile with  $D_p$  at different values of  $F_w$

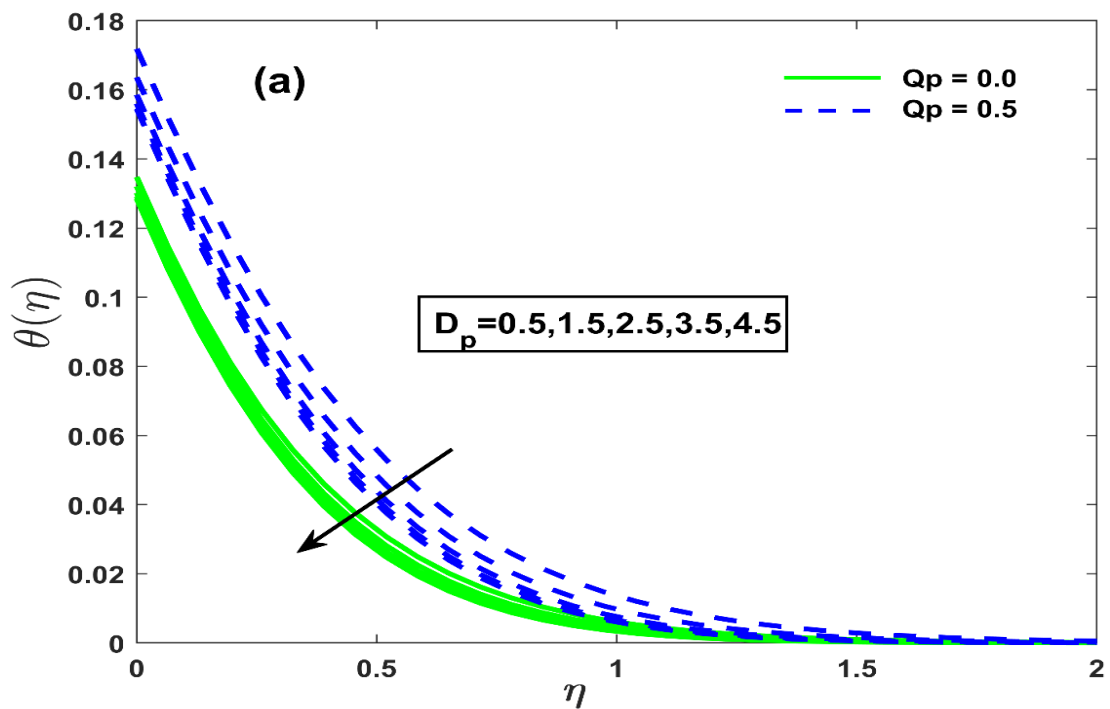


Figure 4.1.5 Deviation in temperature profile with  $D_p$  at different values of  $Q_p$

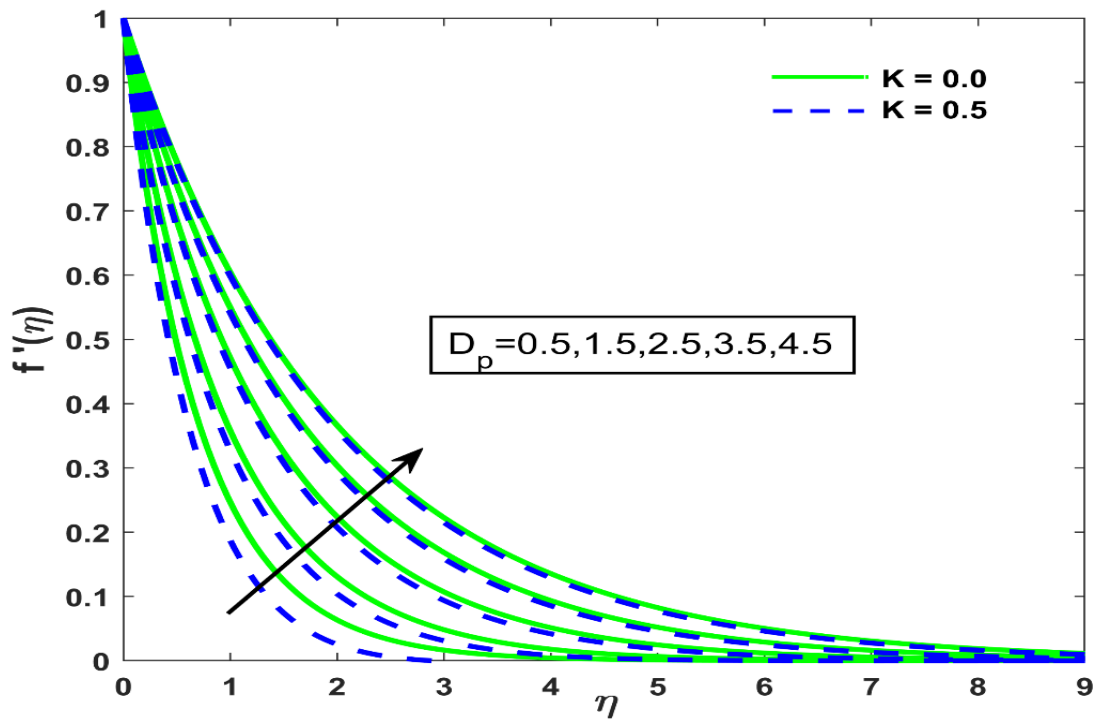


Figure 4.1.6 Deviation in velocity profile with  $D_p$  at different values of  $K$

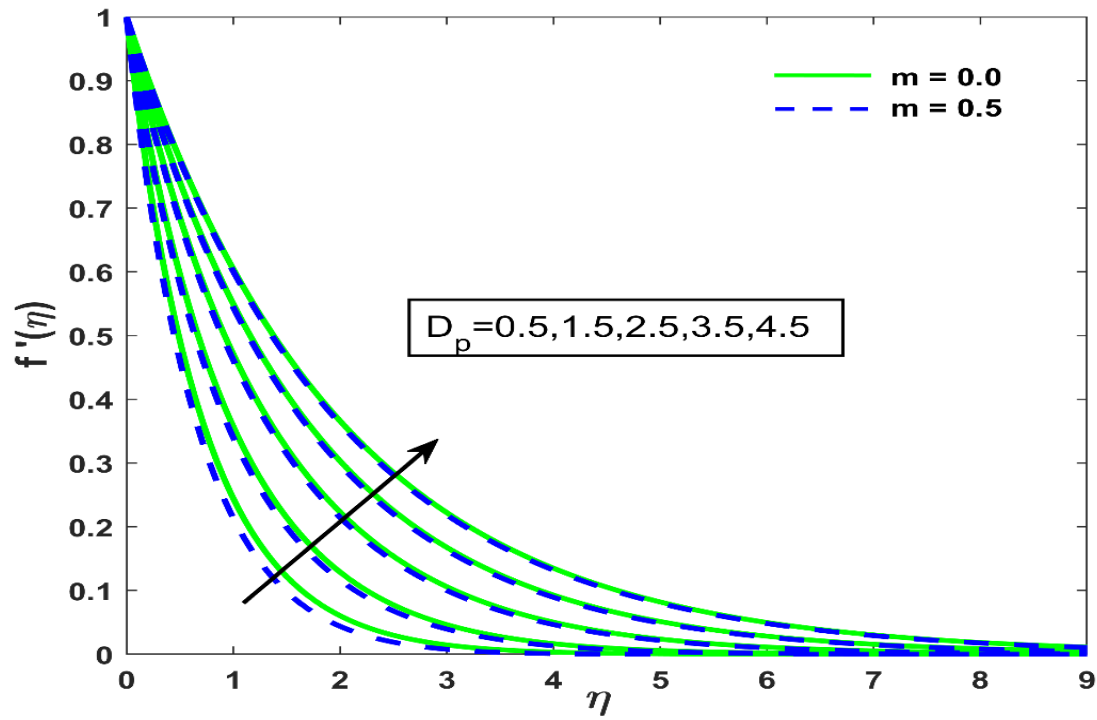


Figure 4.1.7 Deviation in velocity profile with  $D_p$  at numerous different values of  $m$

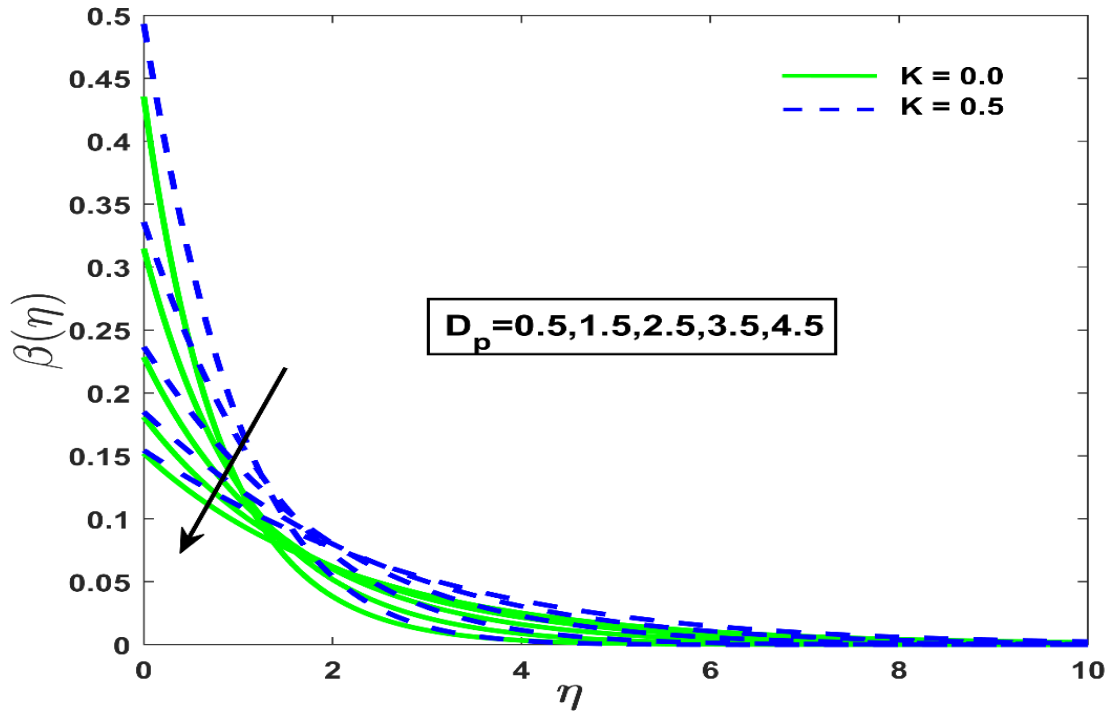


Figure 4.1.8 Deviation in micro rotation with  $D_p$  at numerous different values of  $K$

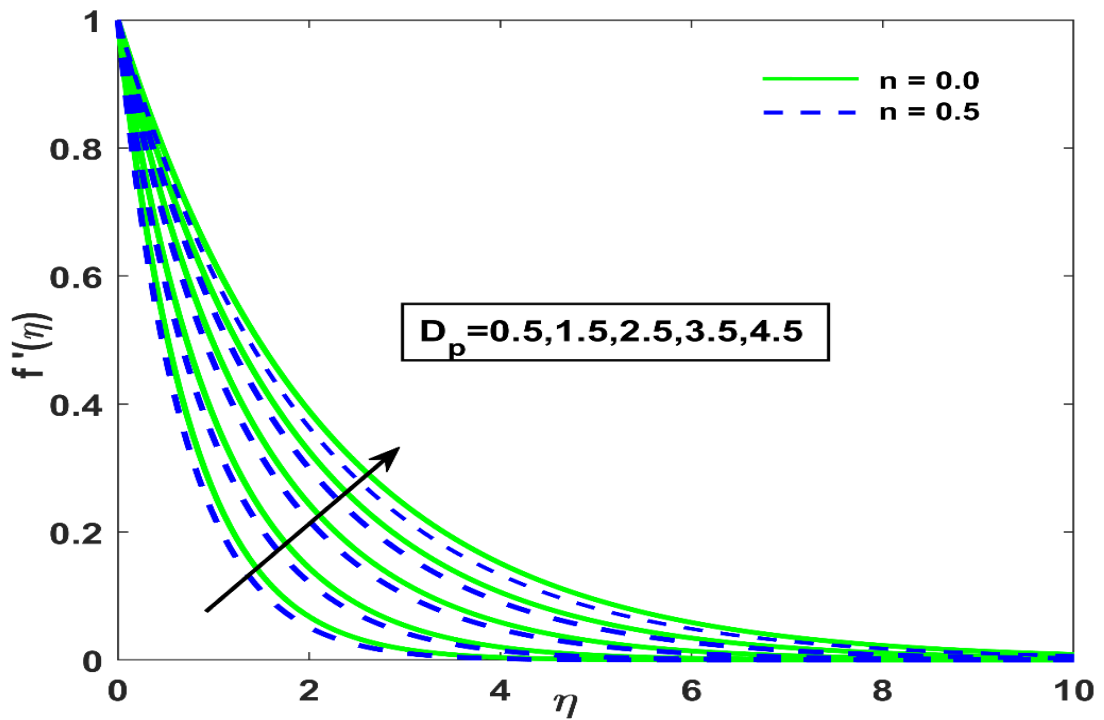


Figure 4.1.9 Deviation in velocity profile with  $D_p$  at numerous different values of  $n$

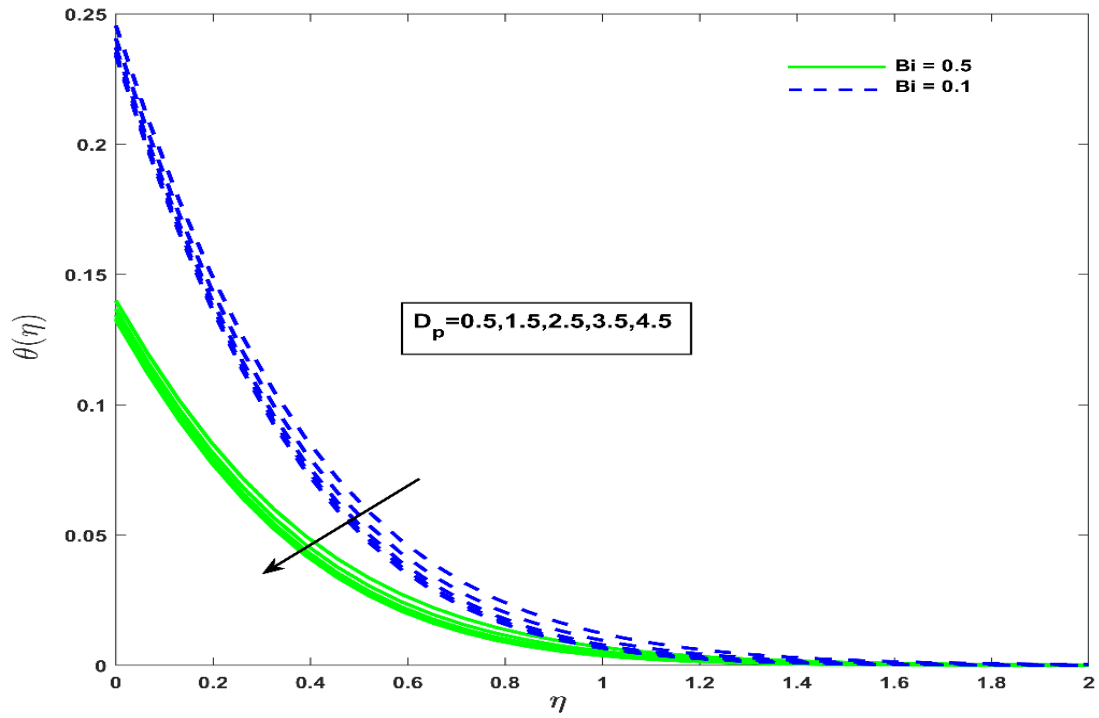


Figure 4.1.10 Deviation in temperature profile with  $D_p$  at different values of  $B_i$

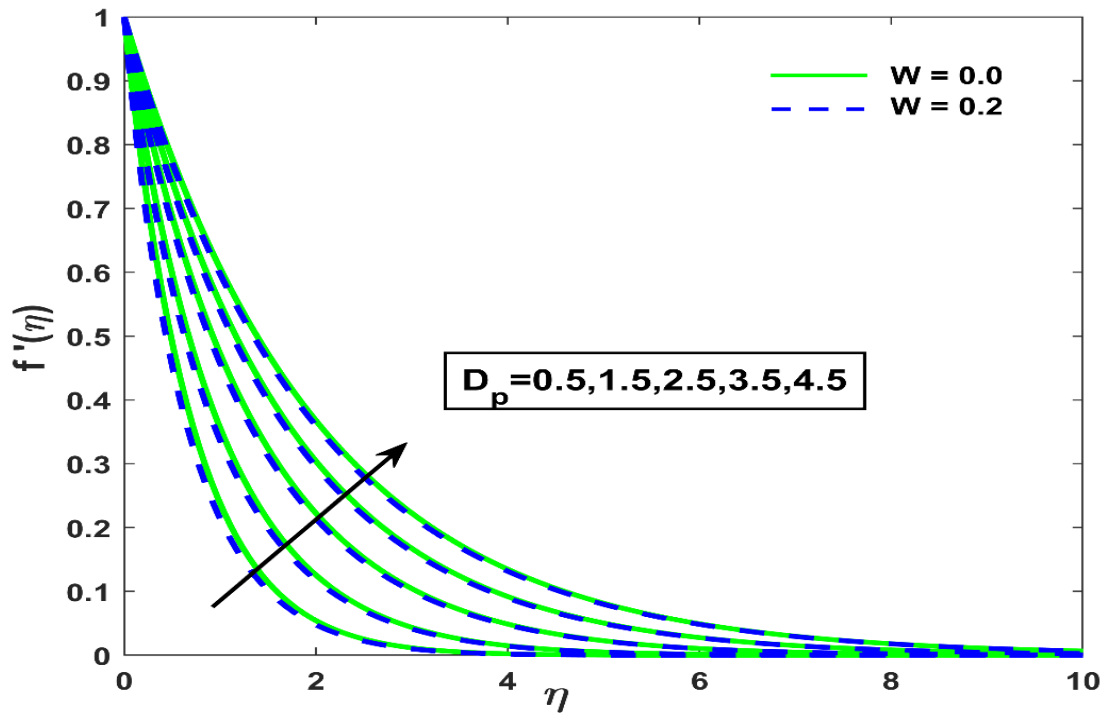


Figure 4.1.11 Deviation in velocity profile with  $D_p$  at different values of  $W$

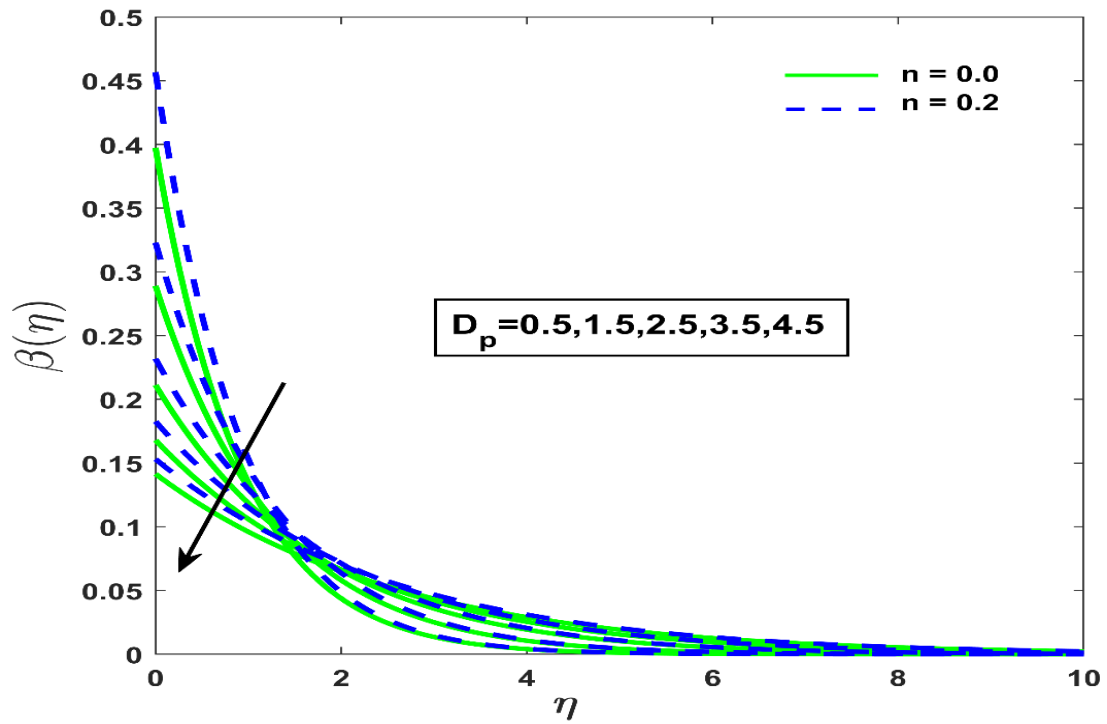


Figure 4.1.12 Deviation in micro rotation with  $D_p$  at numerous different values of  $n$

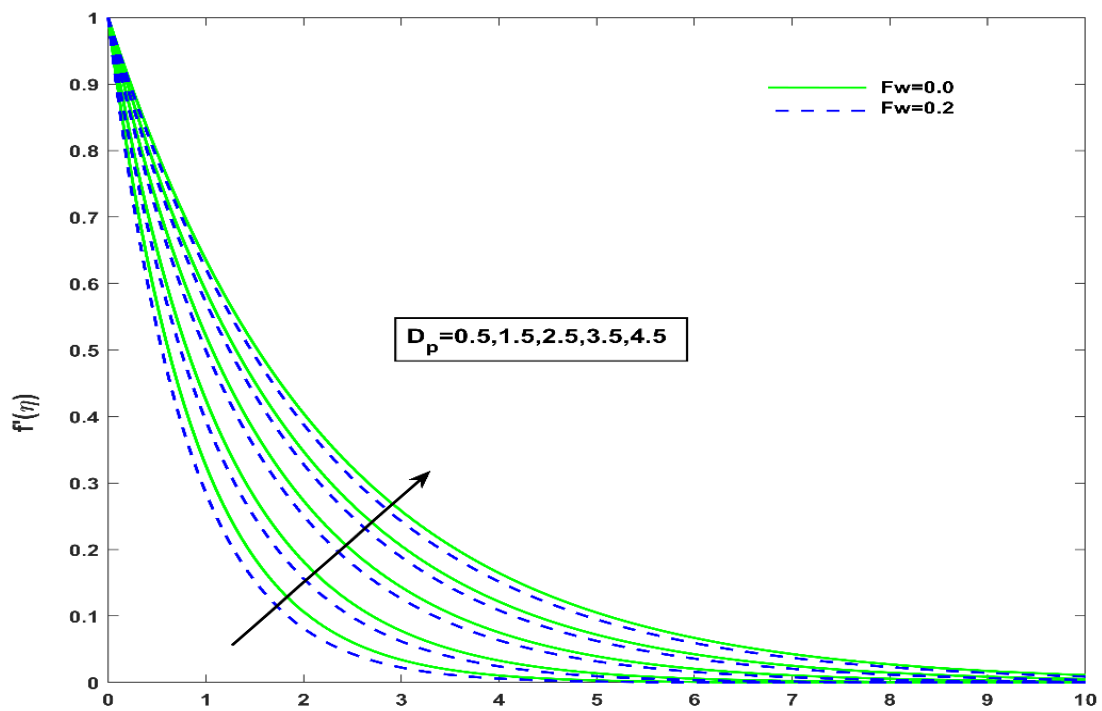


Figure 4.1.13 Deviation in Velocity with  $D_p$  at numerous different values of  $F_w$

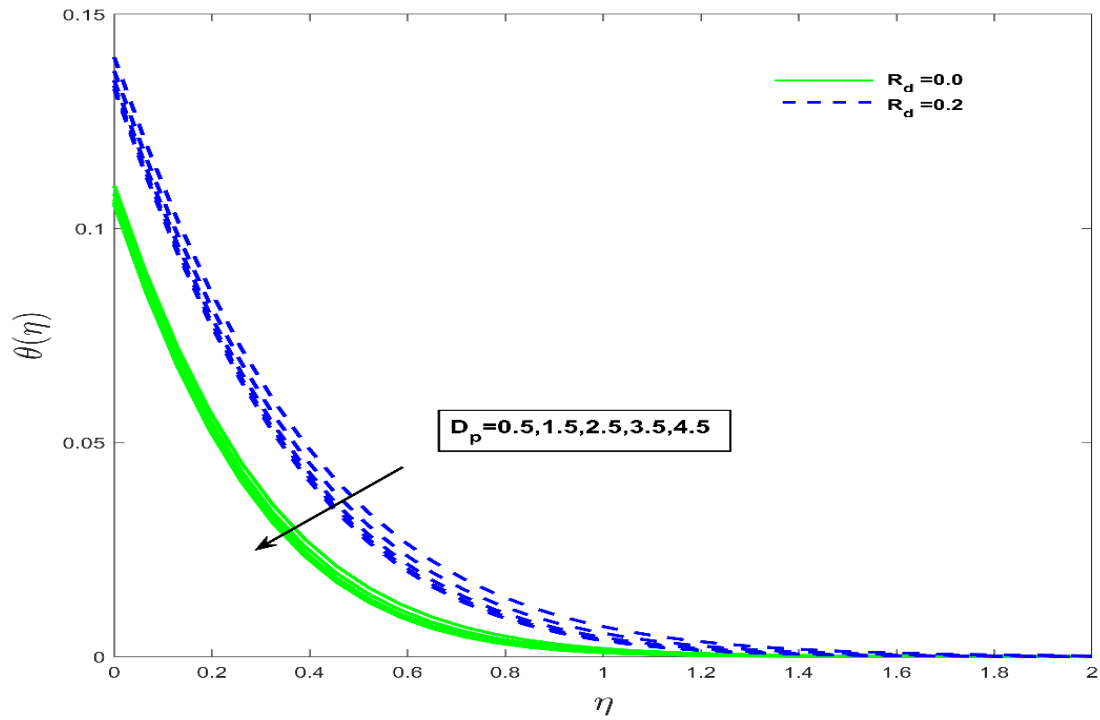


Figure 4.1.14 Deviation in temperature profile with  $D_p$  at different values of  $R_d$

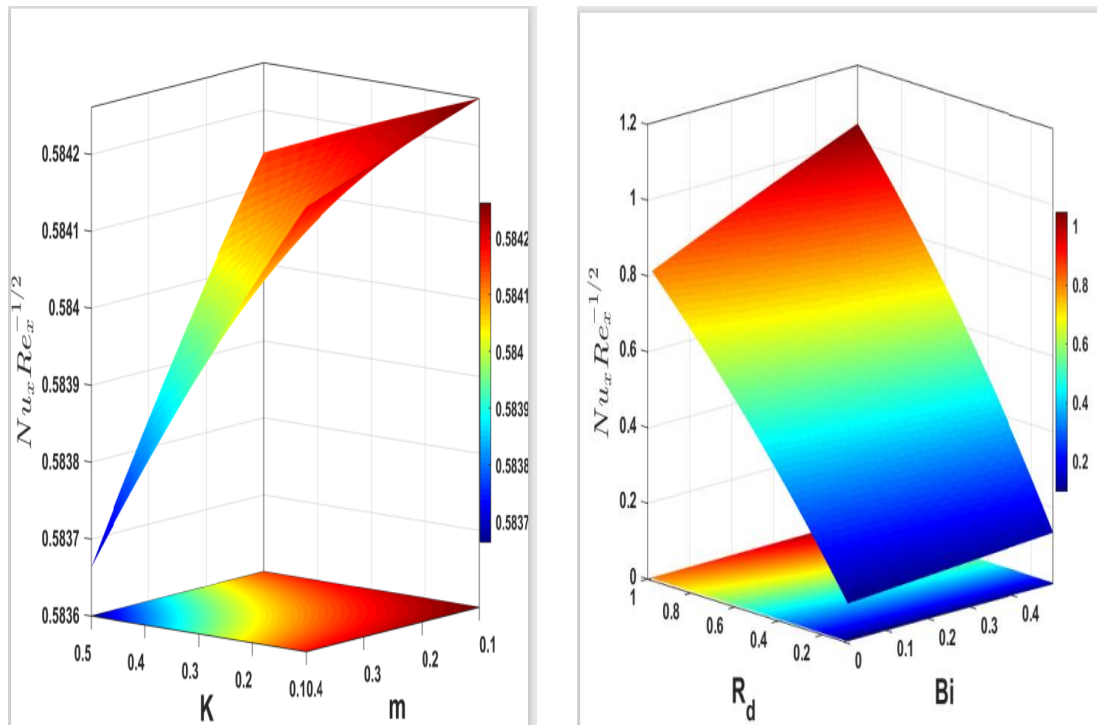
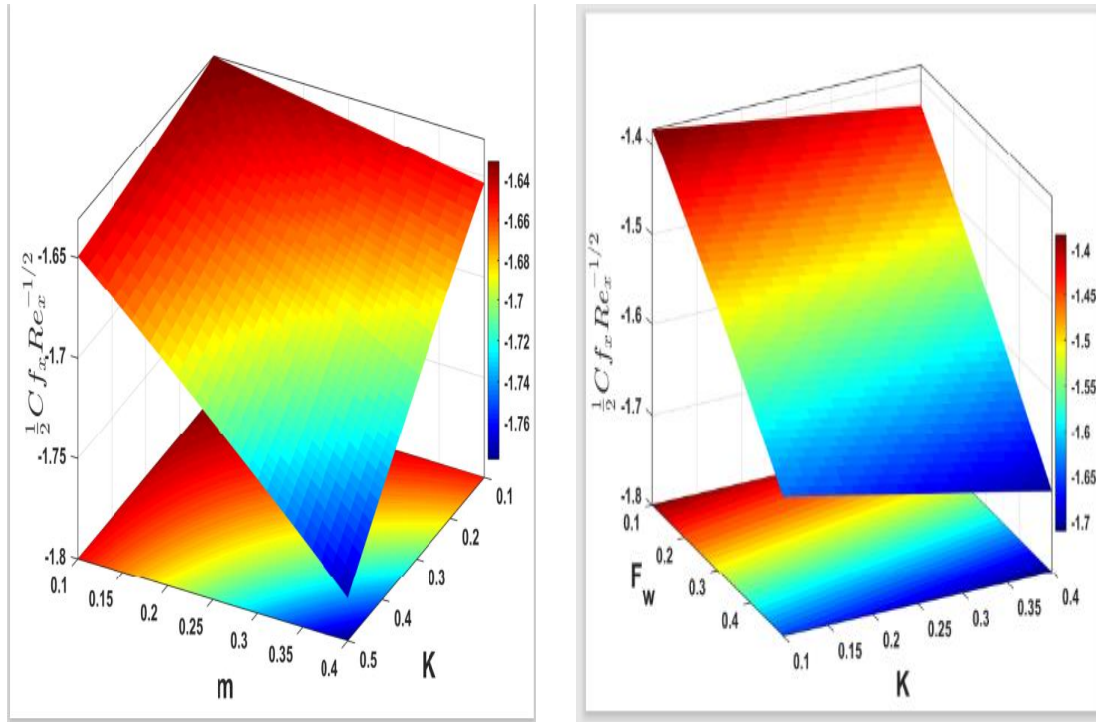


Figure 4.1.15 Fluctuation of Nusselt number with variation of parameters  $M$  and  $D_p$



**Figure 4.1.16 Fluctuation of Skin friction with variation of parameters  $K$  and  $Dp$**

#### **4.2 Magnetohydrodynamic boundary layer flow of nanofluid over an exponential stretching sheet with thermal radiation and Slip effect on boundary condition**

The consequences of various influential parameters on velocity  $f'(\xi)$ , concentration  $(\psi(\xi))$ , and temperature  $(\theta(\xi))$  profiles with magnetic field parameter  $M = 0.01$ , Prandtl number  $Pr = 6.2$ , thermophoretic variable  $Nt = 0.1$ , Biot number  $Bi = 0.1$ , Schmidt number  $Sc = 0.4$ , Eckert number  $Ec = 0.3$ , Brownian diffusion  $NB = 0.3$ , slip effect  $\lambda = 0.5$  and radiation parameter  $Rd = 0.5$  were illustrated in Figures. We have verified both the accuracy of the code and the validation of the present problem by comparing the new work to earlier released work.

Figures (4.2.1 – 4.2.2) depicts that as  $M$  increased, the velocity profile reduced, while the temperature profile increased in the presence and absence of slip effect  $\lambda$ . Since the magnetic field creates an opposing/resistive force known as the Lorentz force, which reduces fluid velocity and thins the flow boundary layer, it was observed that when slip parameter  $\lambda$  increased, the velocity profile decreased, eventually reaching zero at the boundary layer's edges.

Figure (4.2.3) illustrates the effect of the Eckert number  $Ec$  and slip parameter temperature profile. It was found that temperature profile became thicker as both parameters raised. This result is manifested from reality, because the presence of Eckert number in nanofluid increases the intensity of thermal energy production, resulting in better temperature distributions. The energy caused by frictional heat from the flow is converted into internal energy inside the fluid.

Also, an inverse relationship exists for slip parameter between surface slipperiness and fluid temperature.

The temperature distribution broadened as the thermal radiation parameter  $Rd$  was raised as illustrated in figure (4.2.4). Physically when the radiation parameter  $Rd$  is increased, the fluid discharges heat energy from the flow area, which boosts the temperature of the nanofluid. These particle releases heat and cools down the system.

Figure (4.2.4) shows the effect of Brownian diffusion  $N_b$  on a temperature field with simultaneous effect of slip parameter. The thermal field raised with increment in Brownian diffusion parameter. Since Brownian motion is the disordered movement of suspended particles in a liquid produced by collisions. The unsystematic movement of suspended nanoparticles increases as the system's internal energy rises for greater values of Brownian diffusion.

Figure (4.2.6) explains the behavior of  $N_b$  with concentration layer. As the value for Brownian diffusion parameter was increased the concentration profile decreased.

Figure (4.2.7 – 4.2.8) elucidates the relationship between the temperature and concentration profiles with disruptions in thermophoretic parameter  $Nt$ . Both the profiles appeared to be higher due to the larger thermophoretic parameter. Physically the thermophoretic parameter boost the convection process in the current flow analysis, causing material elements to migrate from a heated to a cold surface. Kinetic energy is created when elements are transferred from one surface to another, and the temperature field rises as a result.

The simultaneous impact of Schmidt number  $Sc$  and velocity slip  $\lambda$  parameters on the thermal layer and concentration profile is depicted in figures (4.2.9 – 4.2.10). The temperature profile enhanced with increase in  $Sc$  whereas opposite behavior was observed in case of concentration profile. As a matter of fact, rise in the Schmidt number increases the momentum diffusivity. Whereas, it dilutes the fluid's molecular diffusivity, which decreases the concentration boundary layer.

With increasing Biot number  $Bi$ , the thermal boundary layer was observed to be significant growing feature of fluid layers as shown in figure (4.2.11). Table 4.4 shows the validation of coding for given problem.

Table (4.5 – 4.6) elucidates the variation of pertinent parameters on heat transfer, drag coefficient and mass transfer. Further, a decreasing effect on the local Nusselt number with an increase in  $Ec$ ,  $N_b$  and magnetic field was observed, but the local Sherwood number raised with these parameters while both physical quantities had shown same effect with rise in  $Nt$ . The Nusselt number was reinforced with increase in  $\lambda$ , radiation  $Rd$ , Biot number  $Bi$ . Also, local skin friction coefficient and velocity profiles decreased with increase in slip parameters  $\lambda$ .

**Table 4.4: Comparison of  $-\theta'(0)$  for various values of  $Pr$**

$Pr$	Khan and Pop (2010)	Hamad (2011)	Present Result
0.07	0.0663	0.0656	0.066261
0.20	0.1691	0.16909	0.169080
0.70	0.4539	0.45391	0.453990
2.0	0.9113	0.91136	0.911375
7.0	1.8954	1.89540	1.895411
20.0	3.3539	3.35390	3.353960
70.0	6.4622	6.46220	6.462308

**Table 4.5 The variation of the Nusselt number ( $Nu_x$ ), and Sherwood number for different values of  $E_c, N_T, N_B$  while other parameters remain fixed**

$E_c$	$N_t$	$N_b$	$Nu_x Re_x^{-\frac{1}{2}}$	$Sh_x Re_x^{-\frac{1}{2}}$
0.1	0.2	0.3	0.269495	0.017084
0.3	-	-	0.247896	0.030569
0.5	-	-	0.225844	0.044336
0.2	0.2	0.3	0.258750	0.023793
-	0.3	-	0.258424	-0.026446
-	0.5	-	0.257734	-0.126245
-	0.7	-	0.256986	-0.225046
0.2	0.2	0.1	0.264615	-0.189596
-	-	0.4	0.254912	0.050892
-	-	0.6	0.244483	0.078847
-	-	0.7	0.237306	0.087354

**Table 4.6 The variation of the Nusselt number ( $Nu_x$ ), skin friction coefficient ( $Cf_x$ ) and Sherwood number for different values of  $M, Rd, Bi, \lambda$**

$M$	$\lambda$	$R_d$	$Bi$	$Nu_x Re_x^{-\frac{1}{2}}$	$\frac{-1}{2} Cf_x Re_x^{-\frac{1}{2}}$	$Sh_x Re_x^{-\frac{1}{2}}$
<b>0</b>	0.2	0.5	0.2	0.281470	0.979396	-0.038852
<b>0.1</b>	-	-	-	0.271511	1.001847	-0.034269
<b>0.5</b>	-	-	-	0.235195	1.083861	-0.017071
<b>0.7</b>	-	-	-	0.218747	1.121052	-0.009132
<b>0.2</b>	0.2	0.5	0.2	0.261939	1.023443	-0.029795
-	0.4	-	-	0.264232	0.810002	-0.043344
-	0.7	-	-	0.266164	0.623996	-0.056729
-	1.0	-	-	0.267249	0.510861	-0.065875
<b>0.2</b>	0.2	0.1	0.2	0.195584	1.023443	-0.028931
-	-	0.3	-	0.228775	1.023443	-0.029435
-	-	0.5	-	0.261939	1.023443	-0.029795
-	-	0.7	-	0.2950721	1.023443	-0.030055
<b>0.2</b>	0.2	0.5	0.05	0.067253	1.023443	0.089807
-	-	-	0.1	0.133310	1.023443	0.049222
-	-	-	0.3	0.386078	1.023443	-0.106043
-	-	-	0.5	0.621619	1.023443	-0.250682

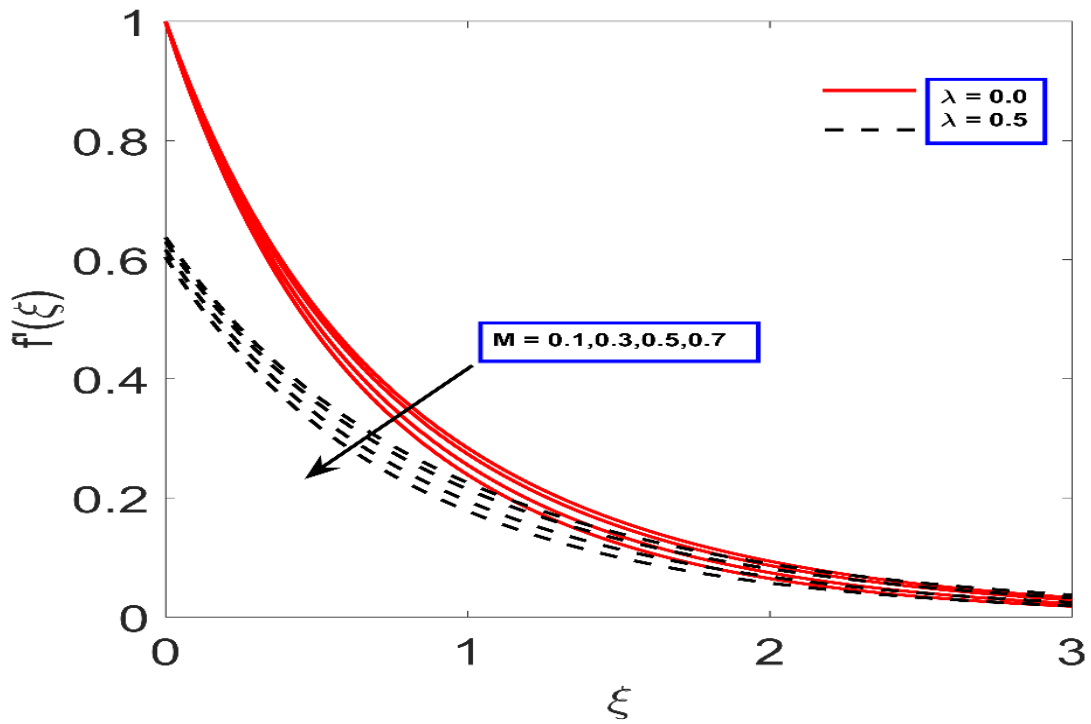


Figure 4.2.1 Variation in velocity profile with different values of  $M$  and  $\lambda$

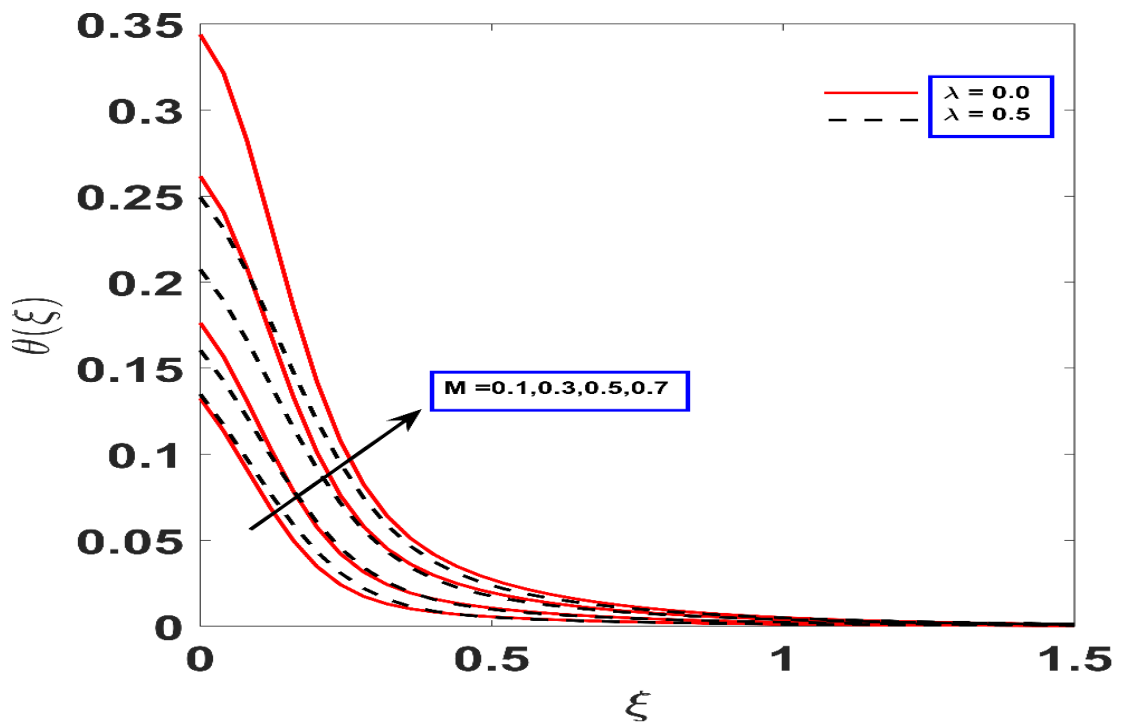


Figure 4.2.2 Variation in temperature profile with different values of  $M$  and  $\lambda$

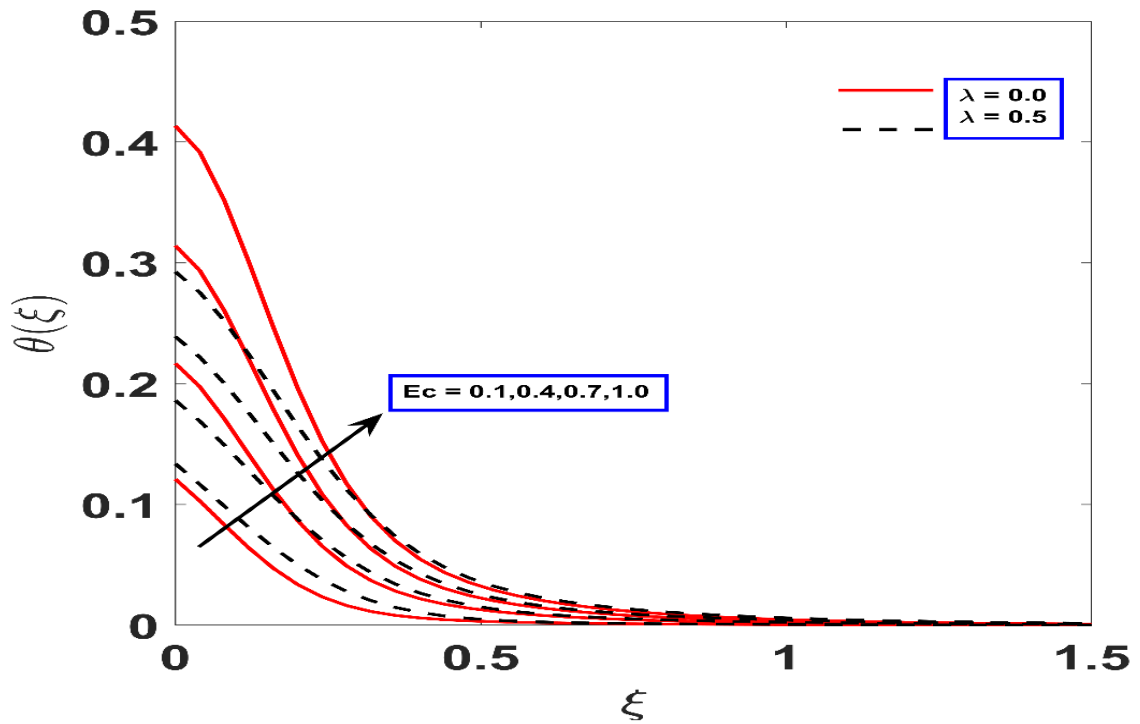


Figure 4.2.3 Variation in temperature profile with  $Ec$  at different values of  $\lambda$

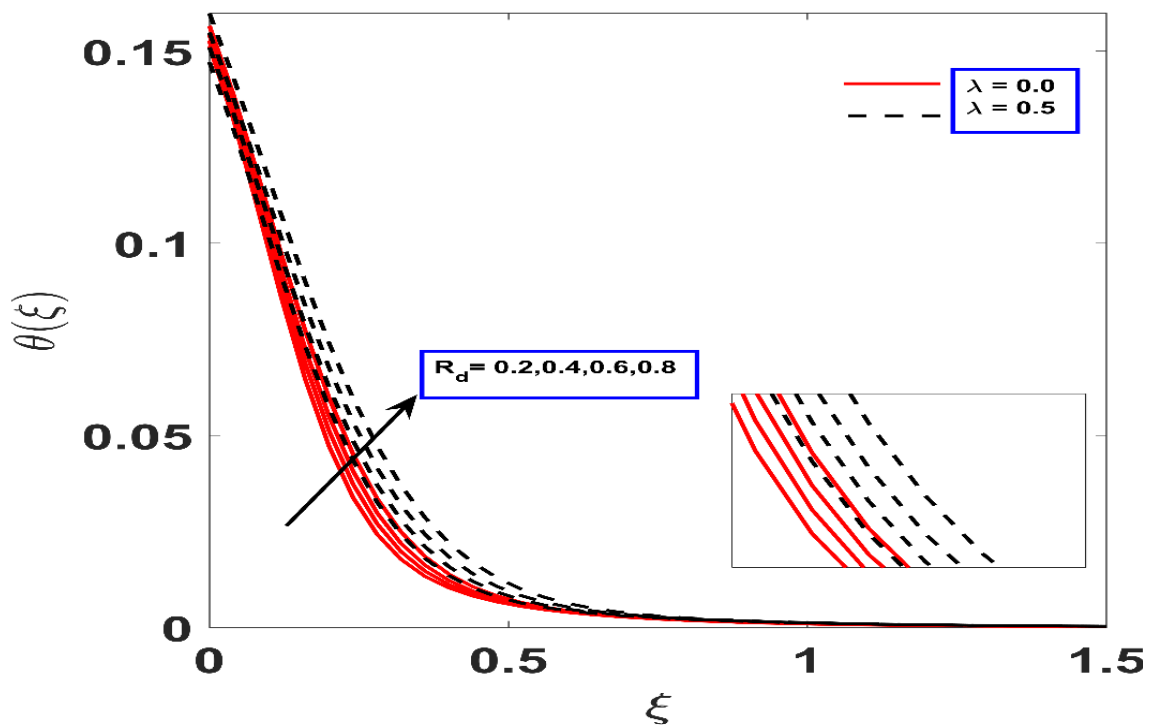


Figure 4.2.4 Variation in temperature profile with  $R_d$  at different values of  $\lambda$

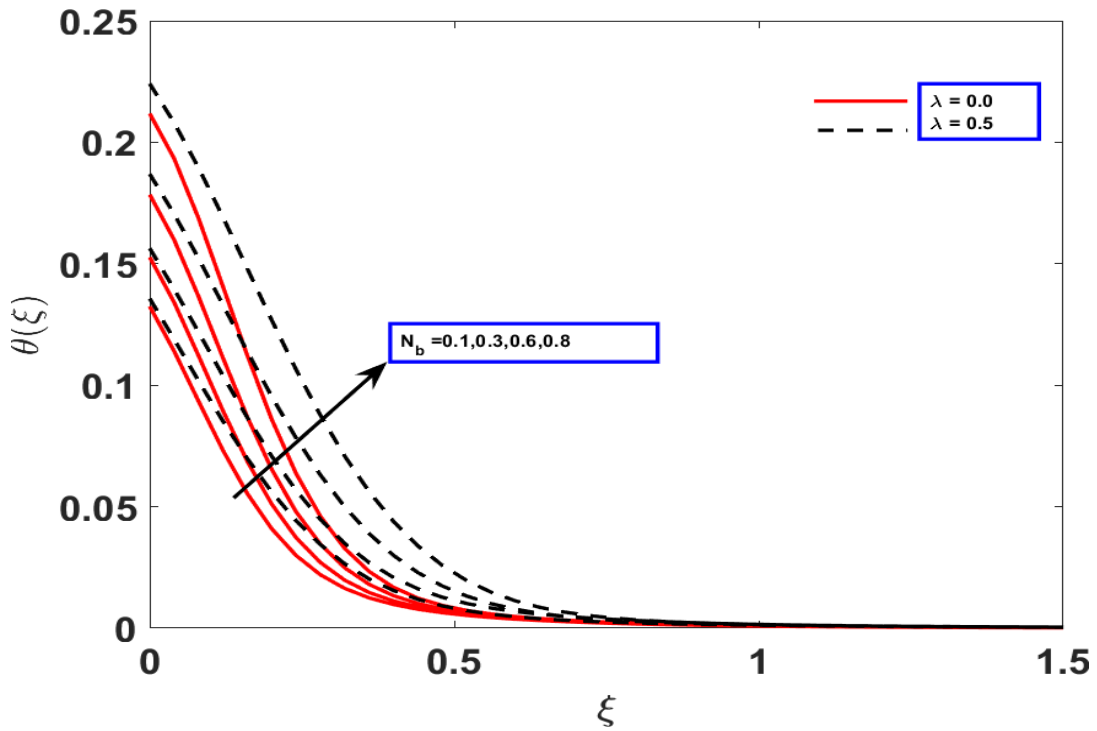


Figure 4.2.5 Variation in temperature profile with  $N_b$  at different values of  $\lambda$

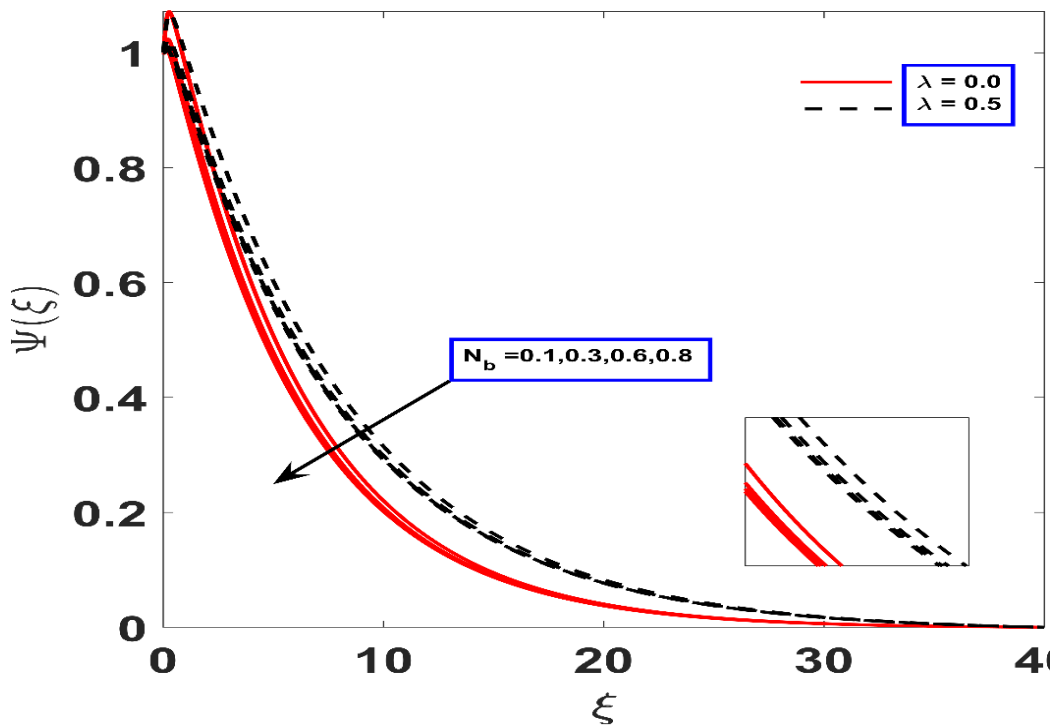


Figure 4.2.6 Variation in concentration profile with  $N_b$  at different values of  $\lambda$

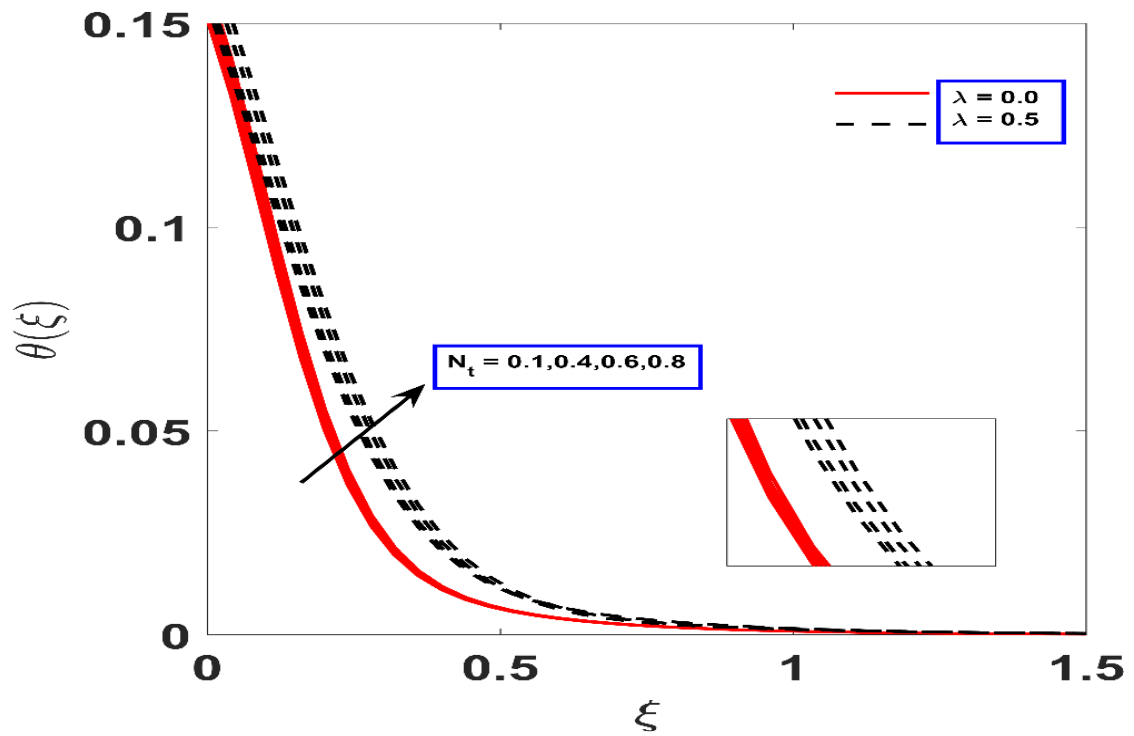


Figure 4.2.7 Variation in temperature profile with  $N_t$  at different values of  $\lambda$

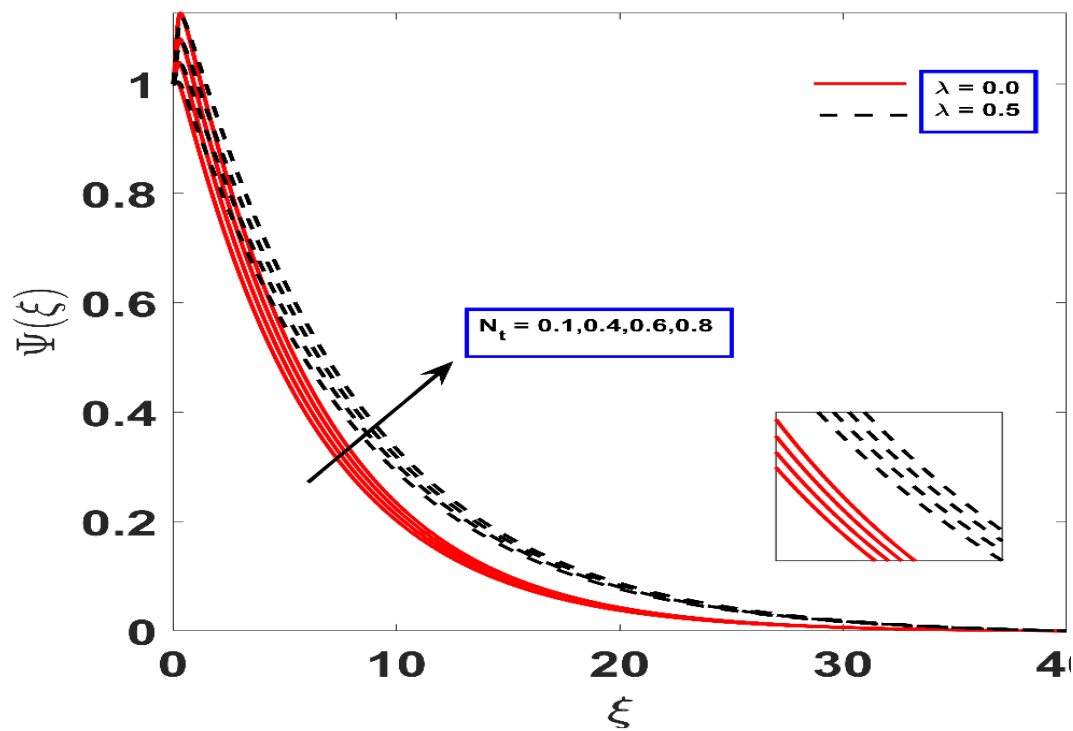


Figure 4.2.8 Variation in concentration profile with  $Nt$  at different values of  $\lambda$

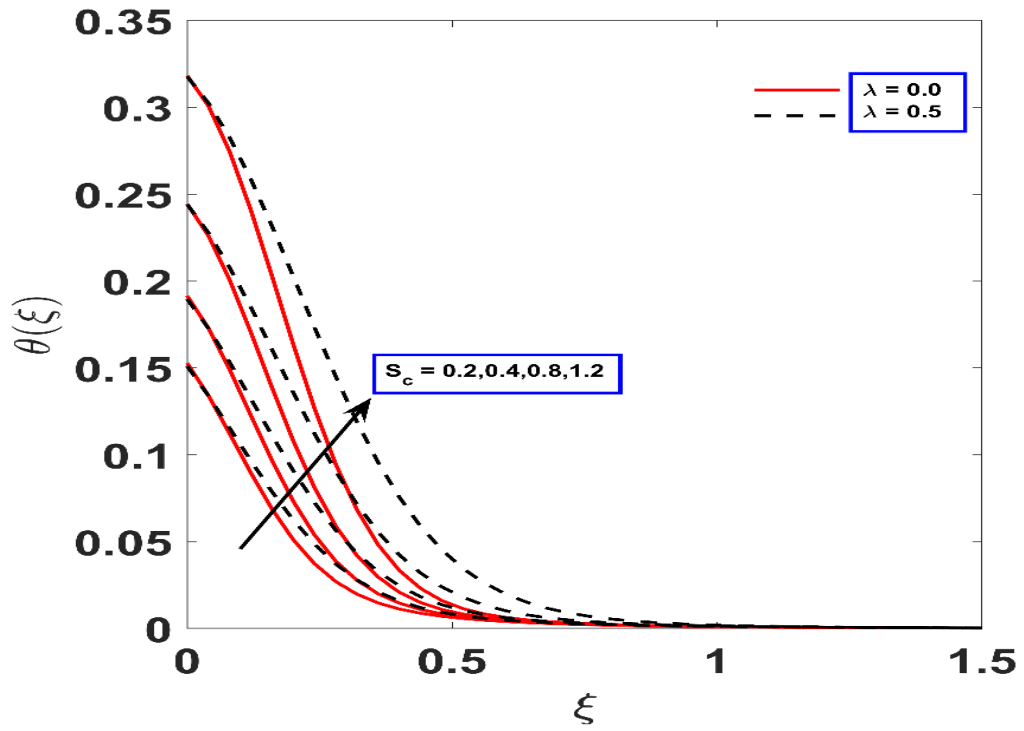


Figure 4.2.9 Variation in temperature profile with  $Sc$  at different values of  $\lambda$ .

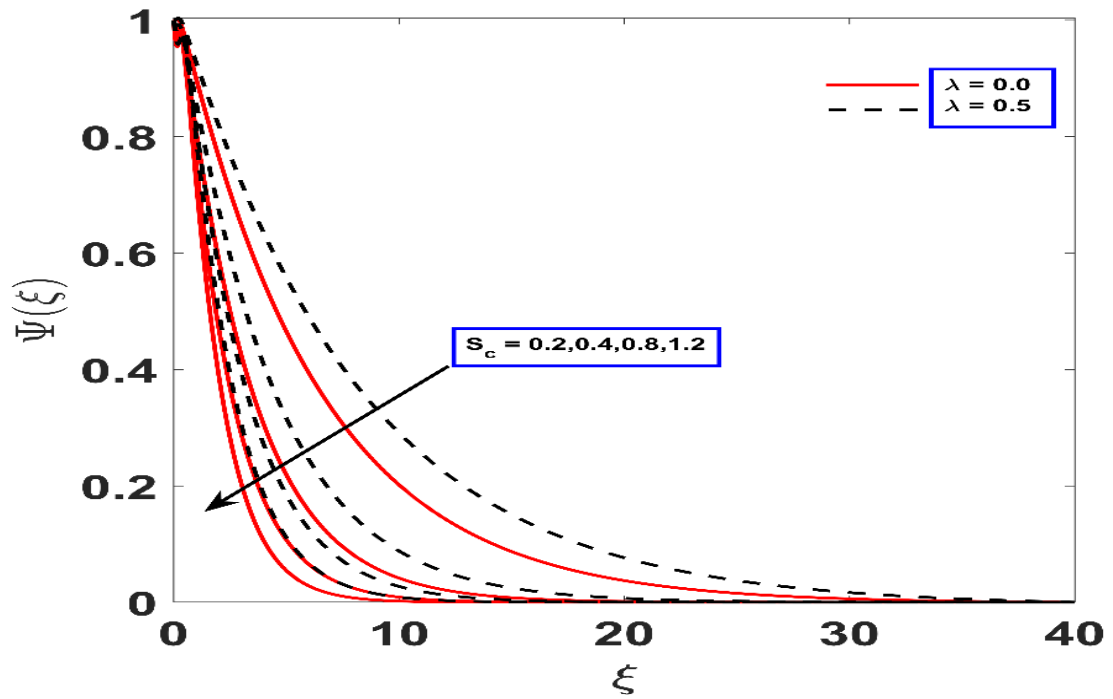


Figure 4.2.10 Variation in concentration profile with  $Sc$  at different values of  $\lambda$ .

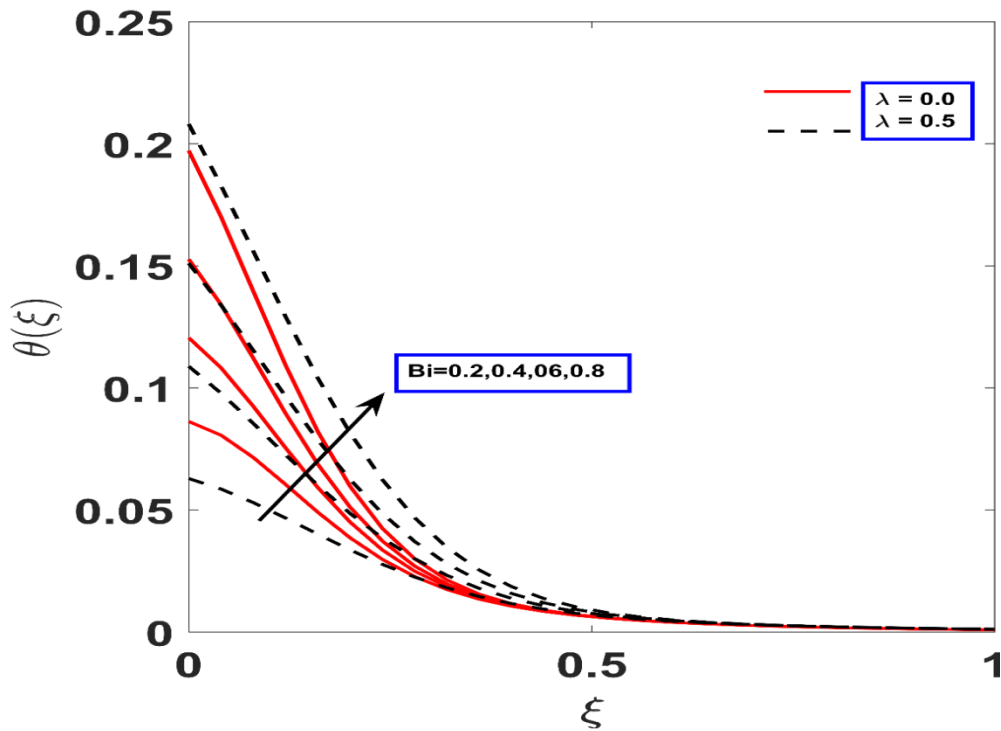


Figure 4.2.11 Variation in temperature profile with Bi at different values of  $\lambda$

#### 4.3 The dynamics of active and passive controls over the measurement of thermal conductivity of nanofluids subject to magnetic field and thermal radiation through the stretching surface

The effects of different influencing parameters on the profiles of radial velocity  $f'(\eta)$ , micro rotation velocity  $G(\eta)$ , nanofluid concentration  $\phi(\eta)$ , and nanofluid temperature  $\theta(\eta)$  are shown in Figures (4.3.1(a-b)-4.3.6 (a-b)).

Figure (4.3.1 (a)) illustrates the impact of the suction/injection parameter ( $F_w$ ) on velocity profiles in the presence of active and passive control cases. It demonstrated that the velocity profile was reduced as the suction/injection parameter values were raised. The result indicates that fluid layers adhere to the wall with stronger forces as suction prevails. As a consequence, boundary layer thickness decreases in both active and passive control cases.

Figure (4.3.1 (b)) illustrates how the magnetic parameter affects velocity in both active and passive controls. Velocity profile declined with rise in the magnetic parameter. Physically, magnetic parameters are connected to the Lorentz force, which resists fluid flow.

The impact of the micropolar parameter  $K$  and suction/injection parameter ( $F_w$ ) upon microrotation velocity profile  $G(\eta)$  is depicted in Figure (4.3.2 (a)) and Figure (4.3.2 (b)), respectively for active and passive control. The microrotation velocity profile increased with the micropolar parameter  $K$ . The fluid motion experiences more resistance in the linear direction of motion due to greater values of  $K$ , but the rotational motion is supported in this process. As a

result, greater values of the micropolar parameter cause thickness in the profile of  $G(\eta)$ . Whereas the microrotation profile reduced as the suction/injection parameter ( $F_w$ ) value increases.

Figure 4.3.3 (a-b) clarified the effect of exponentially space-dependent heat source  $Q_E$  and magnetic parameter ( $M$ ) on temperature profile  $\theta(\eta)$  for active and passive control cases. Increasing  $Q_E$  values represent an improvement in the profiles of the thermal boundary layer and their corresponding thickness. Also, the temperature distribution shows increasing properties of fluid layers with magnetic parameter ( $M$ ). Physically, Lorentz drag increases frictional heat transfer between fluid layers and releases energy. This causes the growth of the thermal boundary layer. According to Figure 4.3.4 (a-b), the temperature ratio parameter  $\theta_m$  and radiation parameter  $R_d$  have an identical impact on temperature profiles. It is obvious that an increase in the temperature ratio parameter  $\theta_m$  results in a greater wall temperature than the ambient fluid temperature. So, improvement in thermal conductivity results in better temperature profiles.

The variations in the temperature profile with respect to the radiation parameter ( $R_d$ ) are shown in Figure 4.3.4(b) in the presence of active and passive control. It is claimed that a rise in the ( $R_d$ ) parameter leads to the temperature profile. Physically, the radiation parameter compares conduction heat transfer with thermal radiation heat transfer. An increase in the radiation parameter causes the temperature to rise. Furthermore, there is a positive relationship between the radiation parameter and the temperature gradient near the surface of the plate.

In Figure 4.3.5 (a), the impact of the thermophoresis parameter  $N_t$  on the concentration profile  $\phi$  is illustrated for active case control and passive case control. In both cases as the thermophoresis parameter was raised, the nanoparticle concentration profile was enhanced. The existence of thermophoresis force causes the boundary layer thickness for the nanoparticle concentration profile to increase due to shifting of more heated fluid away from the surface.

Figure 4.3.5 (b) demonstrates the impact of the suction/injection parameter  $F_w$  for active and passive control cases on the concentration profile  $\phi$ . A decline in the concentration profile was observed when  $F_w$  was increased in the active control case. We observed interesting phenomena in the passive control case, the concentration seemed to be increased when the suction/injection parameter was increased.

The concentration profile  $\phi$  significantly decreased for active and passive control cases, as we kept increasing the chemical reaction parameter  $K_r$  as displayed in figure 4.3.6 (a). It denotes an inverse relationship between  $K_r$  and  $\phi$ . Which manifests that positive values of  $K_r$  indicate destructive chemical reactions, which represents a healthier rate of consumption of species. Therefore, the concentration profile decreases in both cases.

The effect of exponentially space-dependent heat source parameter  $Q_E$  for active and passive control cases on concentration profile  $\phi$  is clarified in figure (4.3.6 (b)). The profiles of the  $\phi$

became thicker in both active control and passive control cases, with improvement in exponentially space-dependent heat source parameter values.

Figure (4.3.7 (a)) shows variation in fluid concentration profile  $\phi$  with greater variations in the Biot number  $Bi$  for active and passive control cases. The increment in Biot number, will increase the concentration profile  $\phi$ . Figure (4.3.7 (b)) depicts the relationship between the activation energy parameter  $E_A$  and concentration profile for active and passive control cases. It was demonstrated that the concentration profile raised (for the major portion of  $\eta$ ) as  $E_A$  increased. Physically, the activation energy parameter gives atoms or molecules more energy to interact with one another, so it generates chemical process, which increases concentration profile  $\phi$  for both active and passive control cases.

Figure (4.3.8) demonstrates the two-dimensional contour map of the relationship based on the magnetic field and thermophoretic diffusion of nanoparticles for active and passive control cases for the Nusselt number. The disaster value rises as the red color spirals downward, and the loss value drops as the dark blue becomes denser in passive case but for active case the impact of involving parameters are opposite.

The residue profiles for the straining stream are portrayed in Figure (4.3.9). This statistic illustrates the percentages of residue on ordinary probability, residue via fitted value on against the snaps, residue frequencies on the spectrum, and residue through assessment ordering on vs. ordered. A surface plotting is a three-dimensional dataset's visualization. Rather of illustrating the particular data values, it displays the structural interaction across two autonomous parameters.

Figure (4.3.10) shows the surface plotting of Nusselt number in relation to magnetic field, Biot number and thermophoretic diffusion. In this study, we found that, in the presence of both active and passive controls of nanoparticles, the local Sherwood number has greater values for varying Brownian motion parameter  $Nb$  while a reverse trend is shown for thermophoresis parameter  $N_t$ . Also, the Nusselt number decreases with  $M$ ,  $N_t$  and  $Nb$  but is enhanced with  $P$   $r$ , and skin friction increased with  $K$  for both active and passive control cases.

For active and passive control cases on the skin friction  $Cf_x$  increased as we kept increasing the  $K$  and  $N_t$  as displayed in Figure (4.3.11 (a-b)). The relative lines of active and passive control cases in  $Cf_x$  overlap. The effect of  $N_t$  on Nusselt number  $Nu_x$  had a significant difference in the case of active and passive controls. So  $Nu_x$  decreased with increase in  $N_t$  and  $m^*$  for both cases. Variation in Nusselt number in combination with  $Nb$ ,  $Rd$  and  $Bi$  parameters in the presence of active and passive control is shown in figures (4.3.12 (a-b)) respectively. We have seen that the passive case dominates the active control case.

The numerical technique (Runge Kutta) is validated through previously published studies, and it was found to have an excellent agreement with Table 4.7. The Comparison of Nusselt

number ( $Nu_x$ ), skin friction coefficient ( $Cf_x$ ) and Sherwood number with active case and the passive case for different values of  $M, Pr, K, N_t, N_b$  is visualized in Table 4.8.

**Table 4.7 A comparison of  $-\theta(0)$  for different values of  $Pr$**

$Pr$	Khan <i>et al.</i> (2014)	Acharya <i>et al.</i> (2016)	Das <i>et al.</i> (2015)	Present result
1	0.40135	0.40145361	0.401452	0.40146012
10	0.46903	0.46931620	0.469315	0.46931623
100	0.49260	0.49252822	0.492529	0.49252820

**Table 4.8 The Comparison of Nusselt number, skin friction coefficient and Sherwood number with active case and passive case for different values of  $M, Pr, K, N_t, N_b$ .**

$M$	$Pr$	$K$	$N_t$	$N_b$	Active case		
					$Nu_x$	$Cf_x$	$Sh_x$
0.5	-	-	-	-	0.479182	0.100683	1.464142
1.0	-	-	-	-	0.476777	0.092393	1.449661
2.0	-	-	-	-	0.472597	0.411437	1.429607
-	2	-	-	-	0.424080	0.100683	1.566991
-	4	-	-	-	0.459188	0.100683	1.503650
-	6	-	-	-	0.474405	0.100683	1.473902
-	10	-	-	-	0.488424	0.100683	1.444536
-	-	0.1	-	-	0.479039	0.048280	1.463187
-	-	0.3	-	-	0.479076	0.072725	1.463434
-	-	0.5	-	-	0.479182	0.100683	1.464142
-	-	-	0.4	-	0.475504	0.100683	1.105362
-	-	-	0.7	-	0.471422	0.100683	0.780026
-	-	-	1.0	-	0.466884	0.100683	0.491530
-	-	-	-	0.2	0.469049	0.100683	1.543643
-	-	-	-	0.5	0.431265	0.100683	1.617698
-	-	-	-	0.8	0.384891	0.100683	1.666076
-	-	-	-	1.2	0.320565	0.100683	1.722339
$M$	$Pr$	$K$	$N_t$	$N_b$	Passive case		
					$Nu_x$	$Cf_x$	$Sh_x$
0.5	-	-	-	-	0.488631	0.100683	-0.245445
1.0	-	-	-	-	0.486531	0.092393	-0.243936
2.0	-	-	-	-	0.482903	0.411437	-0.241341
-	2	-	-	-	0.430753	0.100683	-0.205817
-	4	-	-	-	0.467589	0.100683	-0.230570
-	6	-	-	-	0.483586	0.100683	-0.241828
-	10	-	-	-	0.498462	0.100683	-0.252587
-	-	0.1	-	-	0.488504	0.048280	-0.245354
-	-	0.3	-	-	0.488537	0.072725	-0.245377
-	-	0.5	-	-	0.488631	0.100683	-0.245445
-	-	0.7	-	-	0.488759	0.130497	-0.245537
-	-	-	0.4	-	0.487448	0.100683	-0.978378
-	-	-	0.7	-	0.486206	0.100683	-1.705921
-	-	-	1.0	-	0.484902	0.100683	-2.427686
-	-	-	-	0.2	0.488631	0.100683	-0.122722
-	-	-	-	0.5	0.488631	0.100683	-0.049089
-	-	-	-	0.8	0.488631	0.100683	-0.030680
-	-	-	-	1.2	0.488631	0.100683	-0.020453

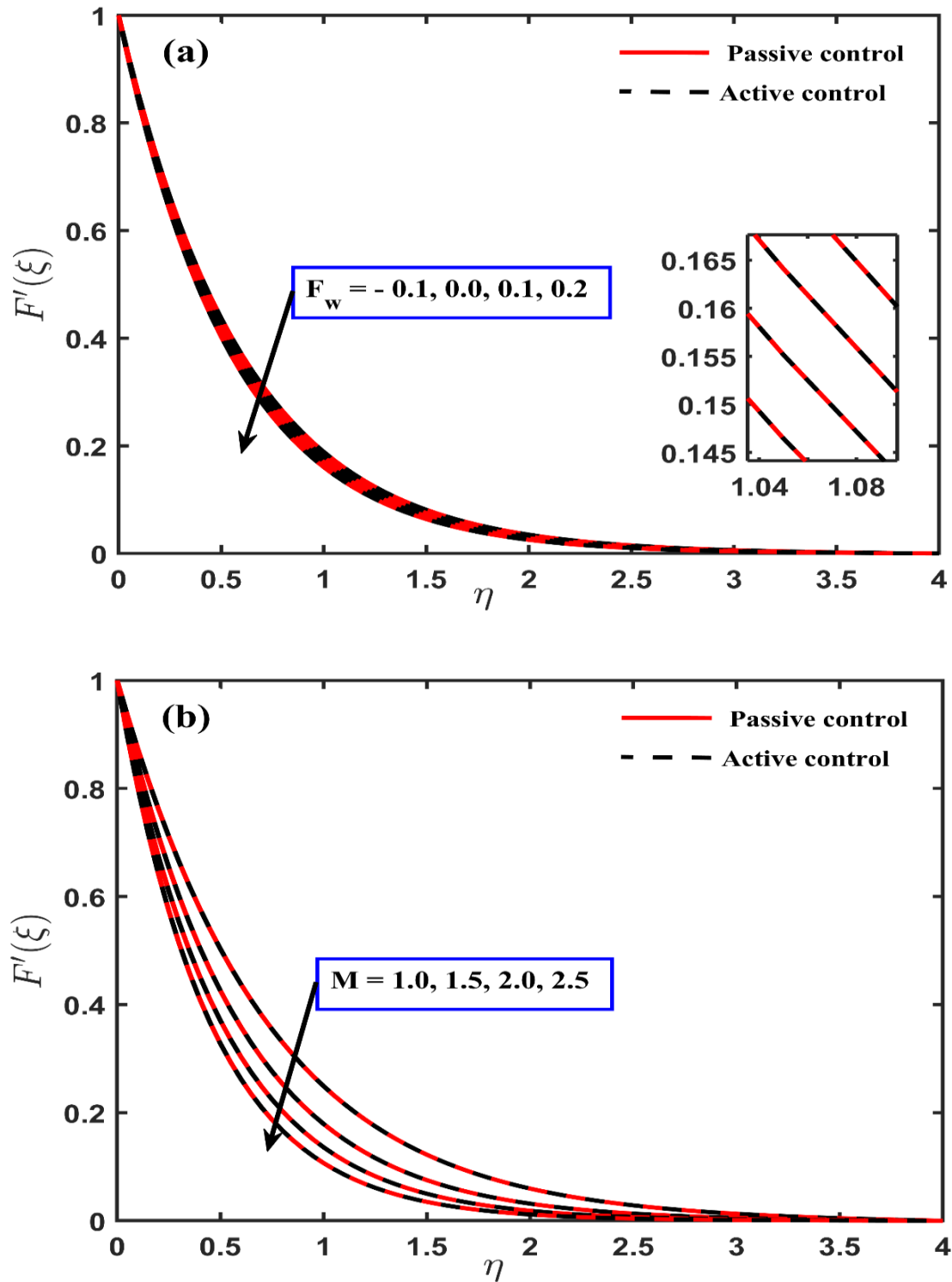


Figure 4.3.1 (a-b) Velocity at various  $F_w$  and  $M$  values under active and passive control

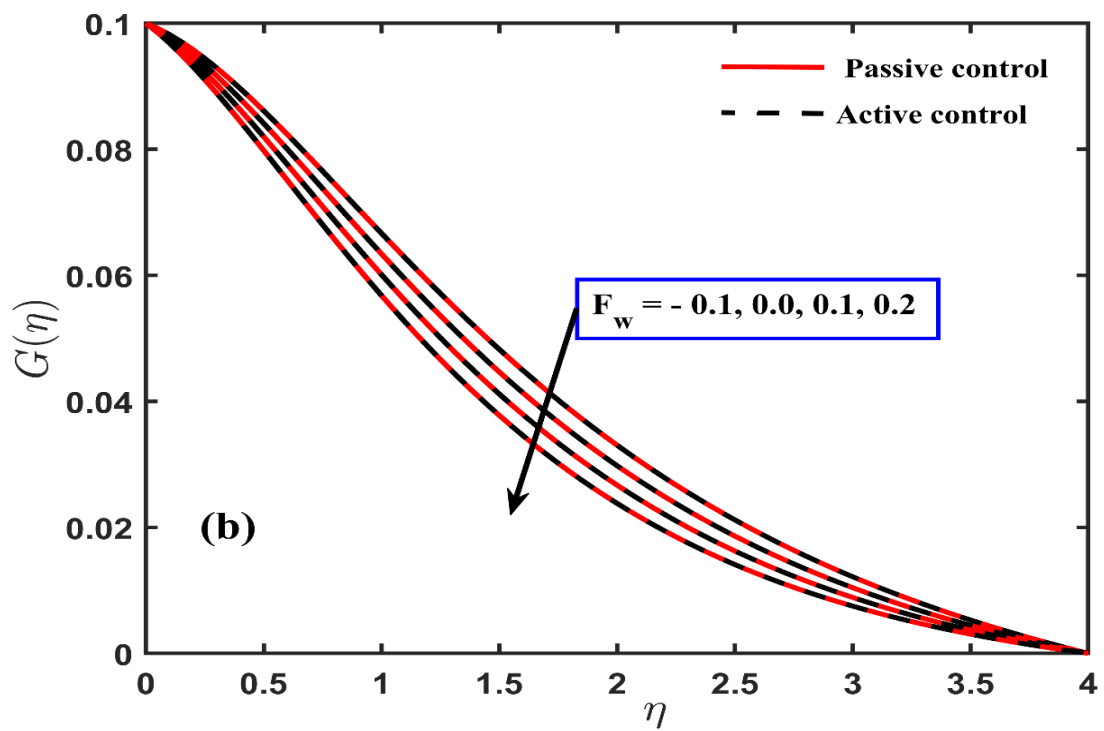
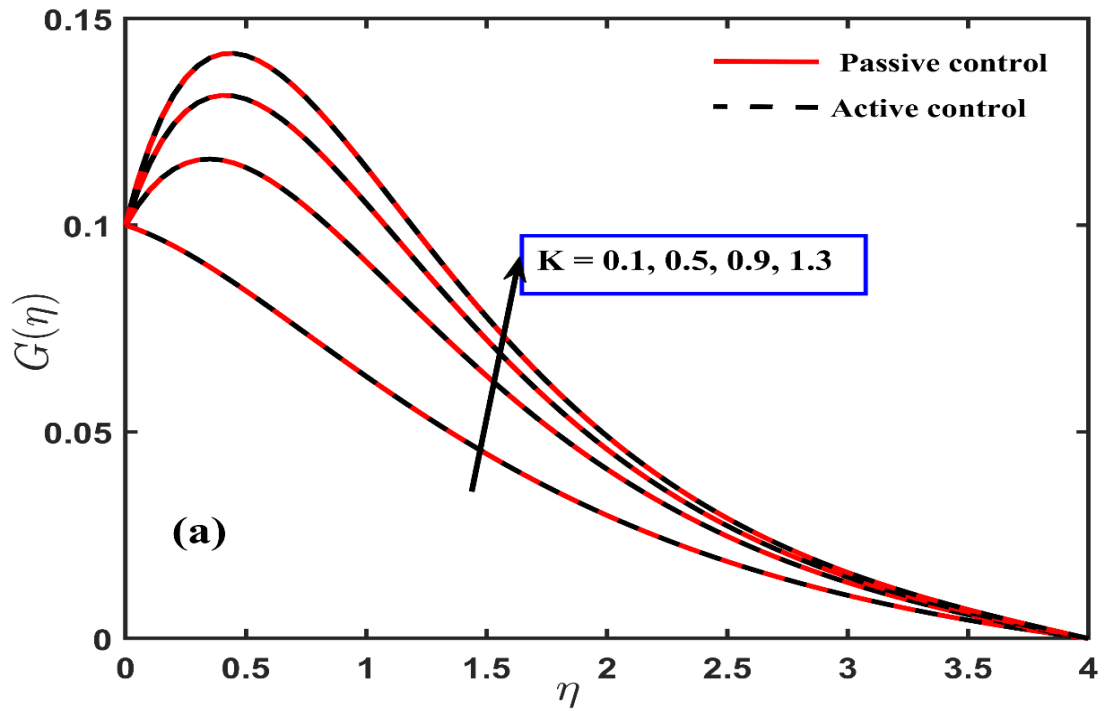


Figure 4.3.2 (a-b) Variation in  $G(\eta)$  with different values of  $K$  and  $F_w$  for both scenarios of active and passive control

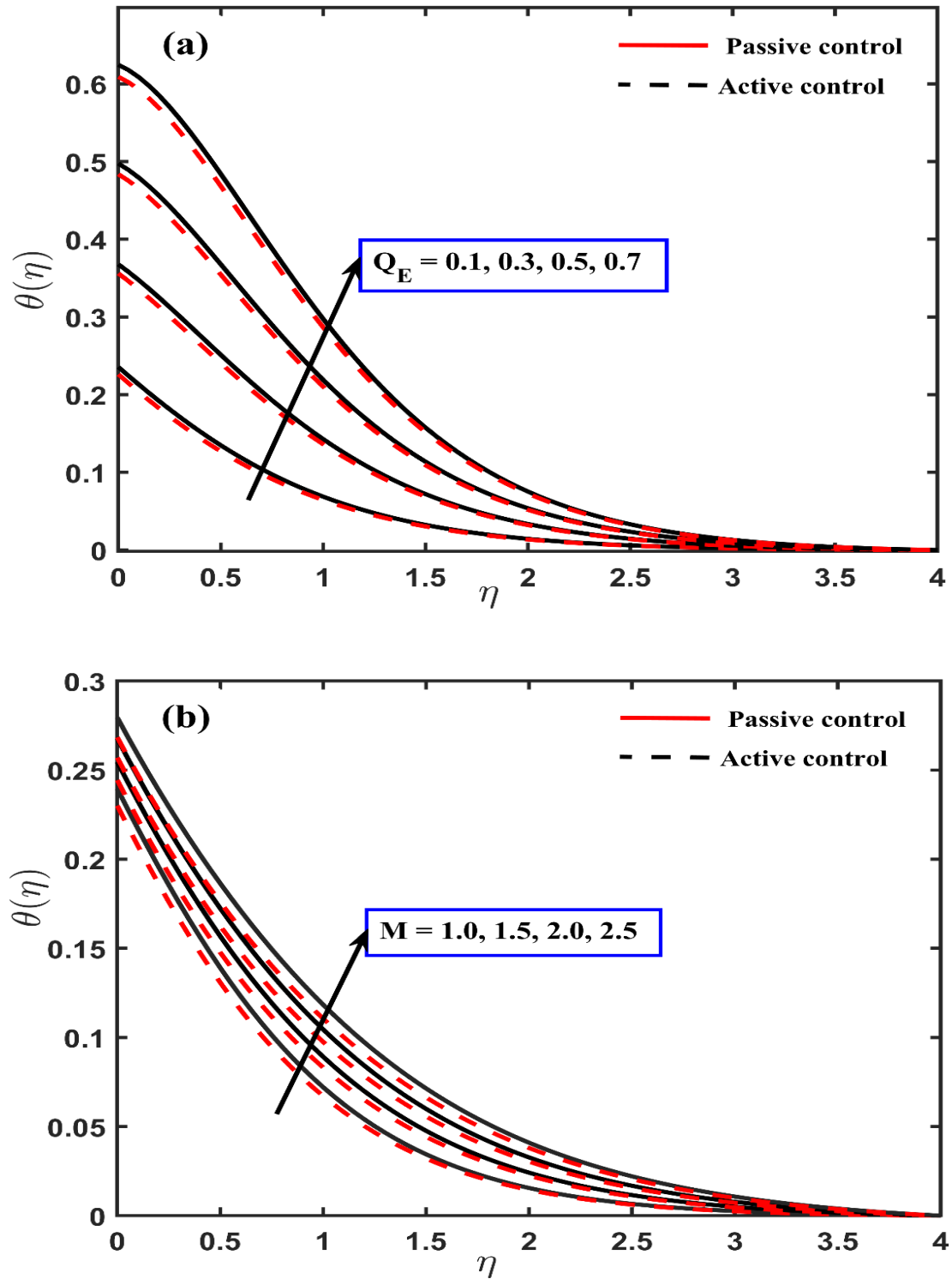


Figure 4.3.3 (a-b) Fluctuation in  $\theta(\eta)$  with different values of  $Q_E$  and  $M$  for active and passive control cases

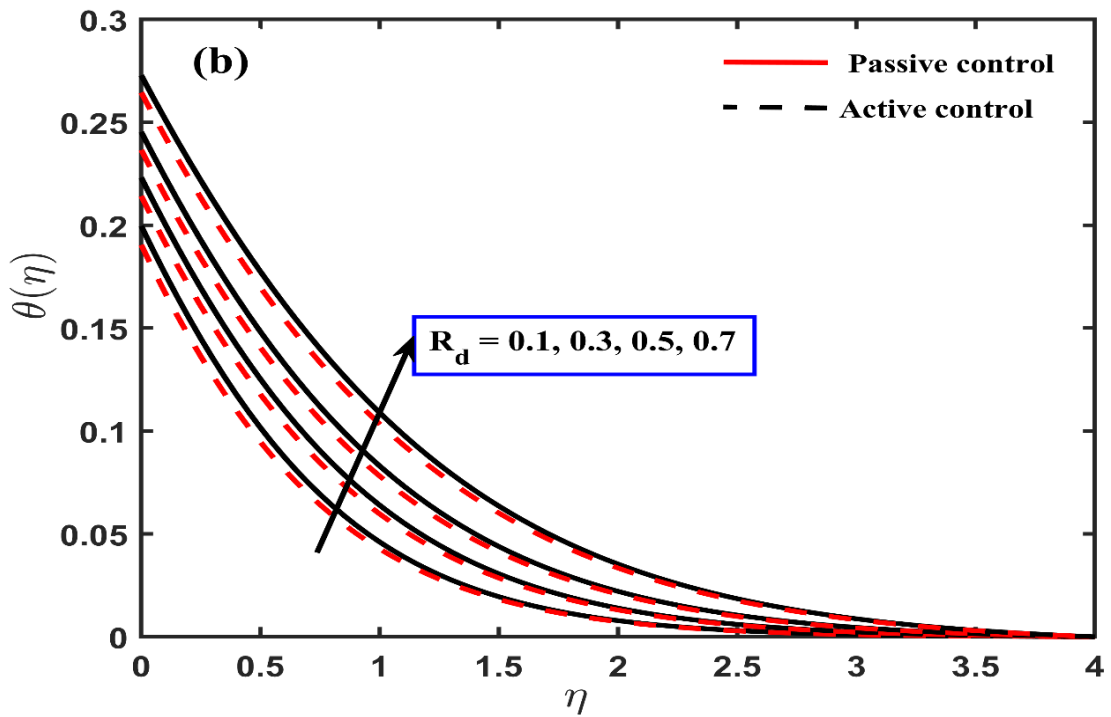
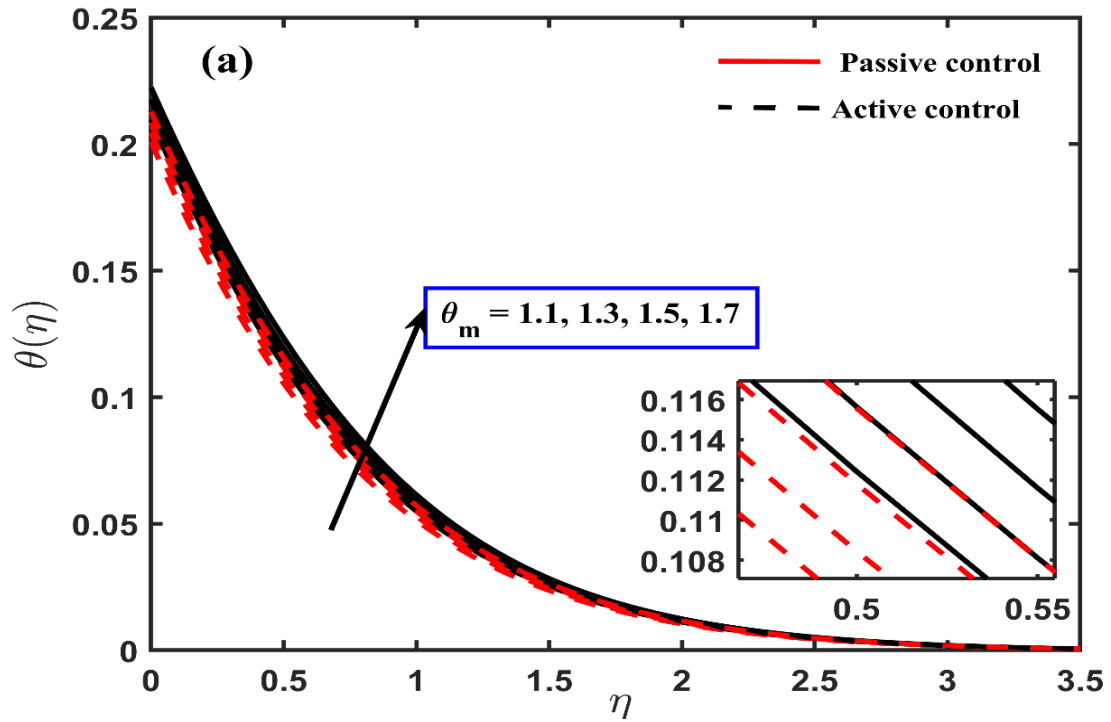


Figure 4.3.4 (a-b) Variation in  $\theta(\eta)$  at significantly different values of  $\theta_m$  and  $R_d$  for active and passive control cases

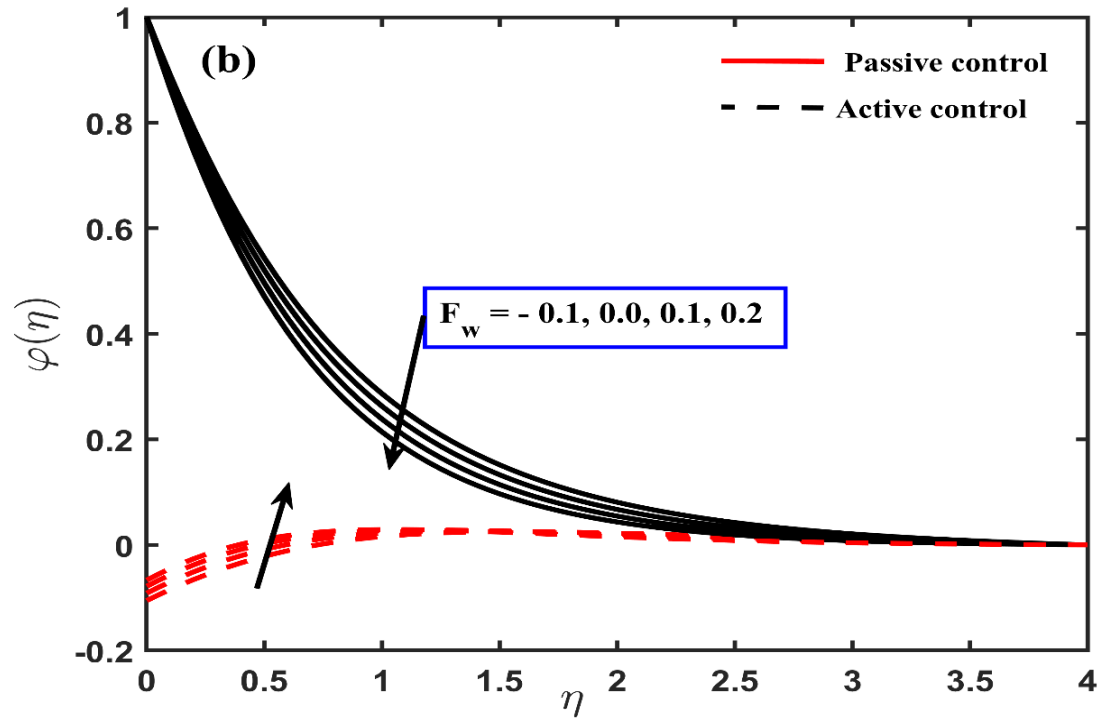
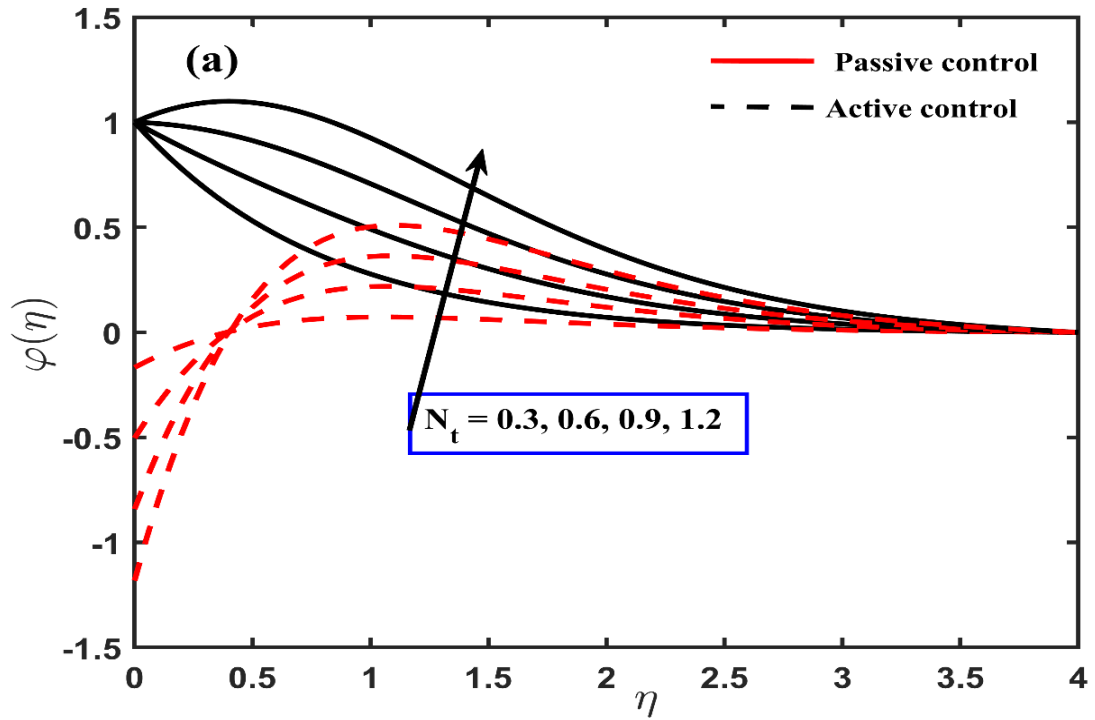


Figure 4.3.5 (a-b) Fluctuation in  $\phi(\eta)$  at different values of  $N_t$  and  $F_w$  in the presence of active and passive control

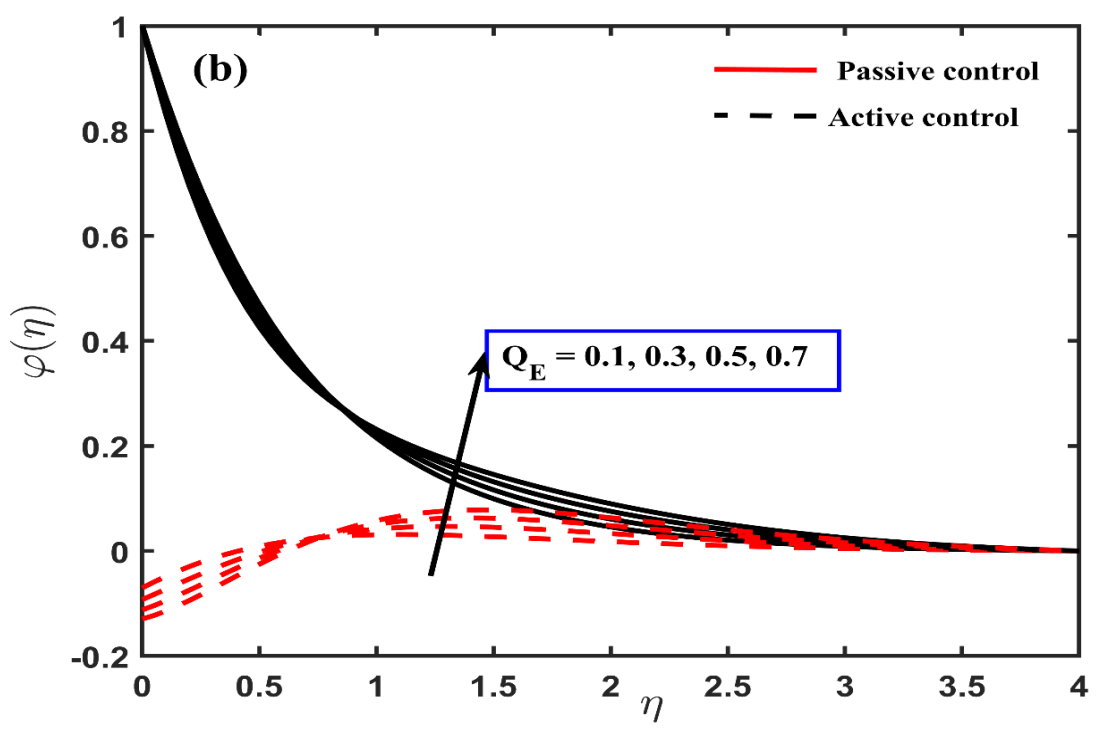
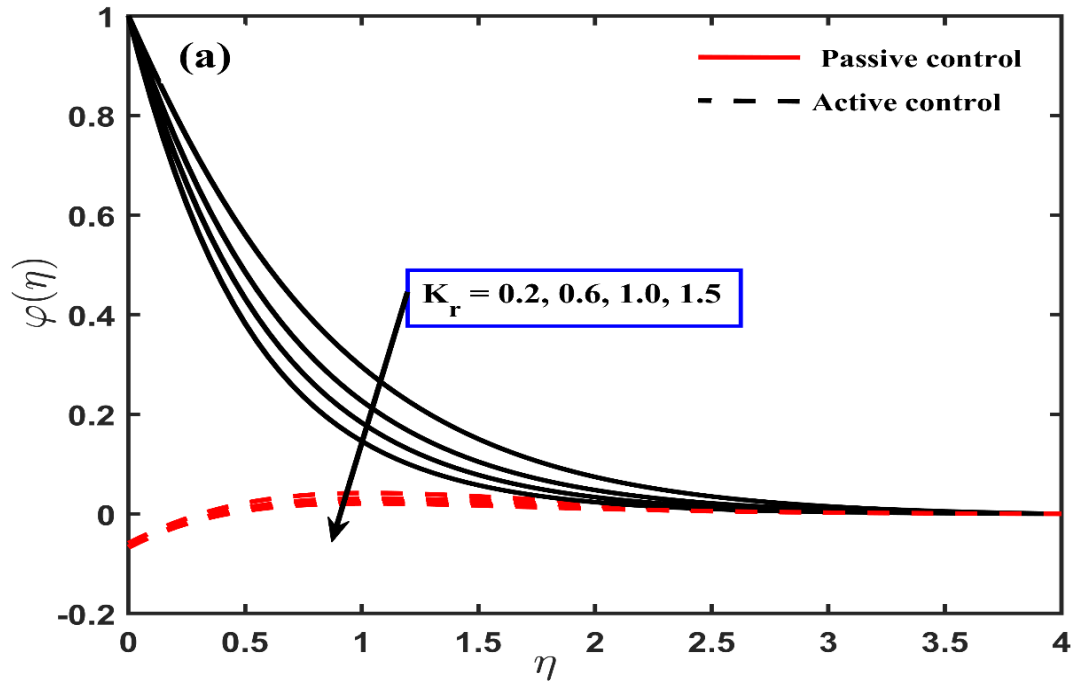


Figure 4.3.6 (a-b) Fluctuation in concentration profile for different values of  $K_r$  and  $Q_E$  for active and passive control cases.

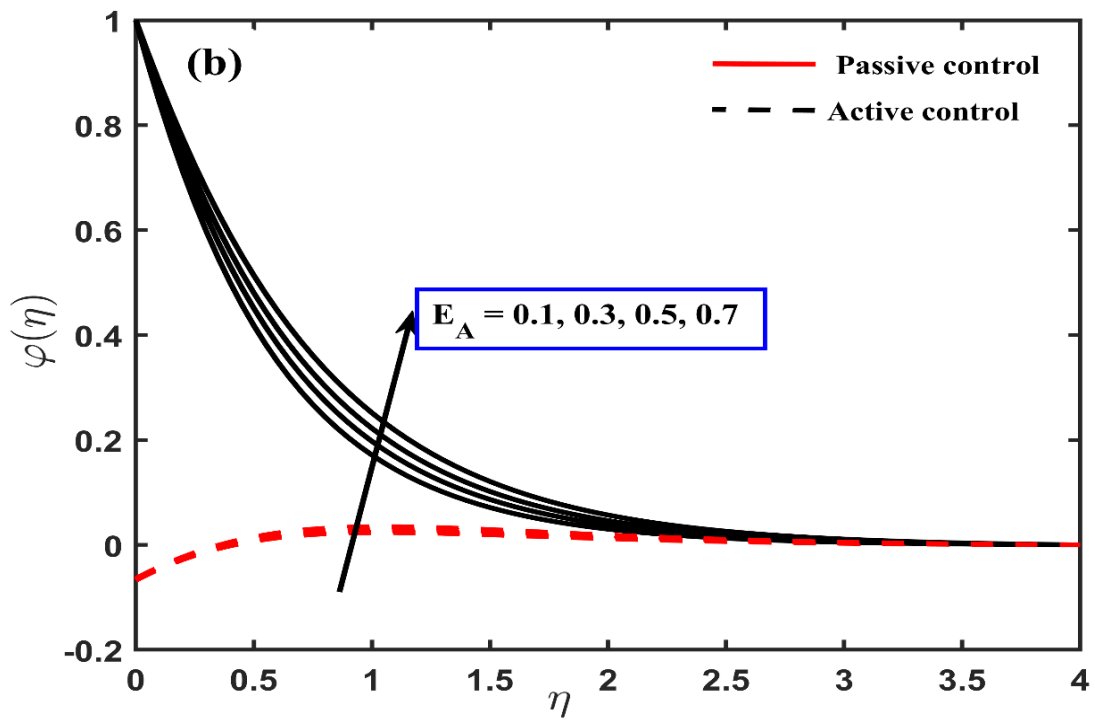
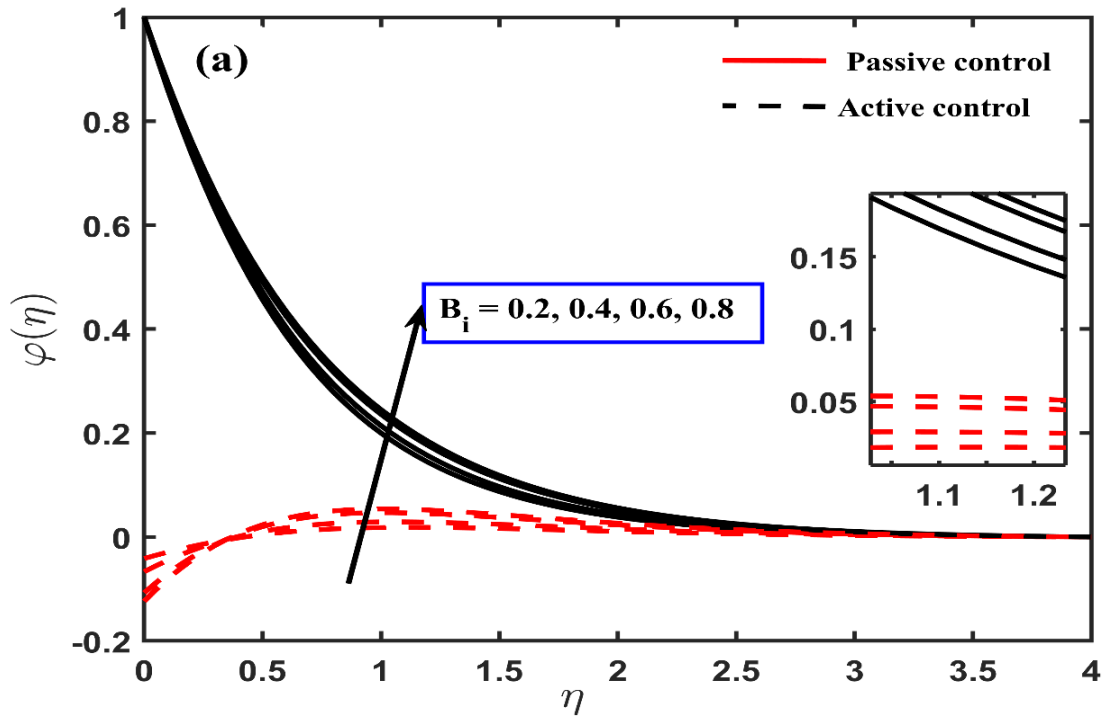
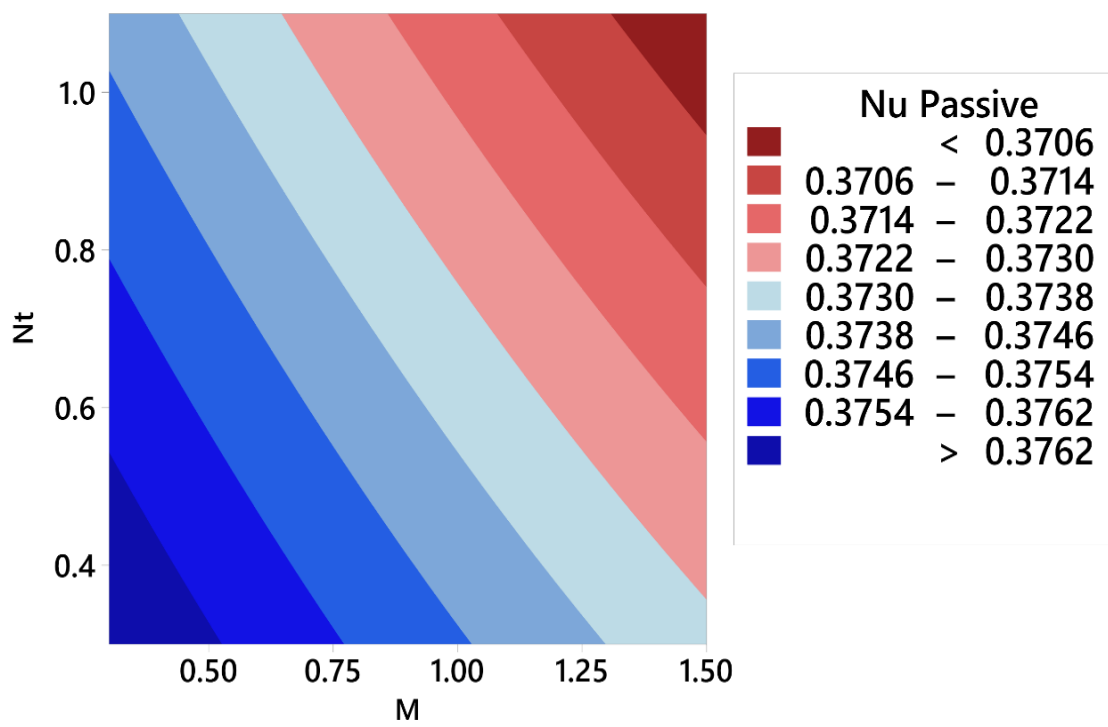
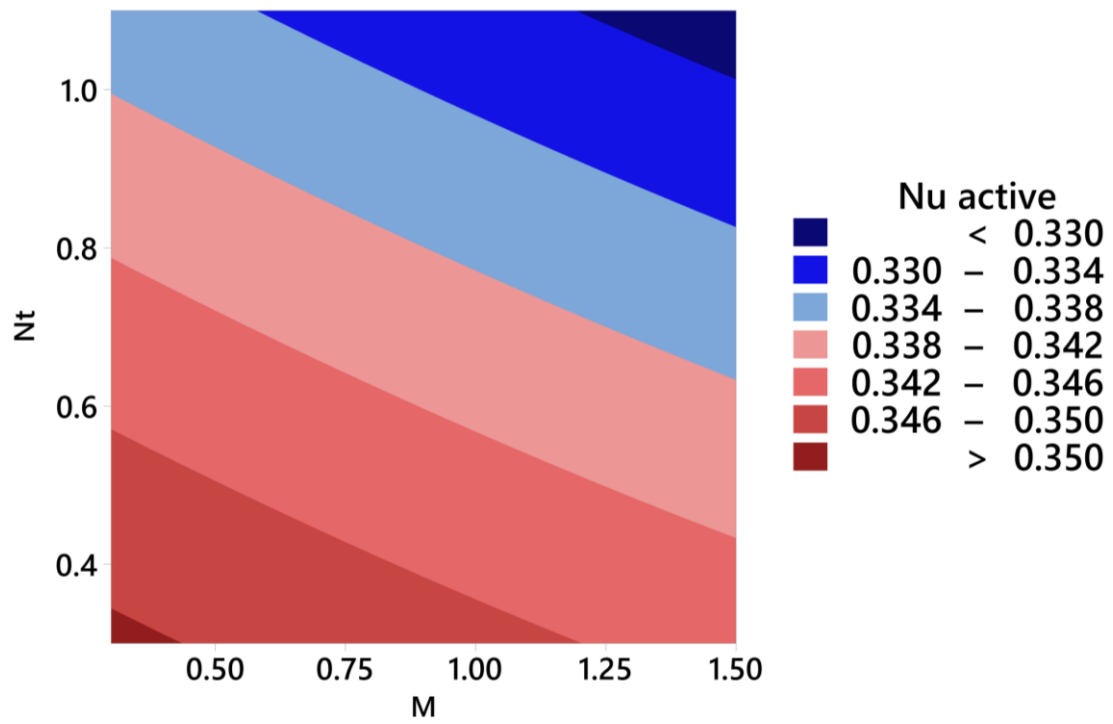


Figure 4.3.7 (a-b) Variation in  $\varphi(\eta)$  at significantly different values of  $Bi$  and  $E_A$  for active and passive control cases



**Figure 4.3.8** Contour idiographic of  $Nu_x$  in relation to magnetic field and thermophoretic diffusion

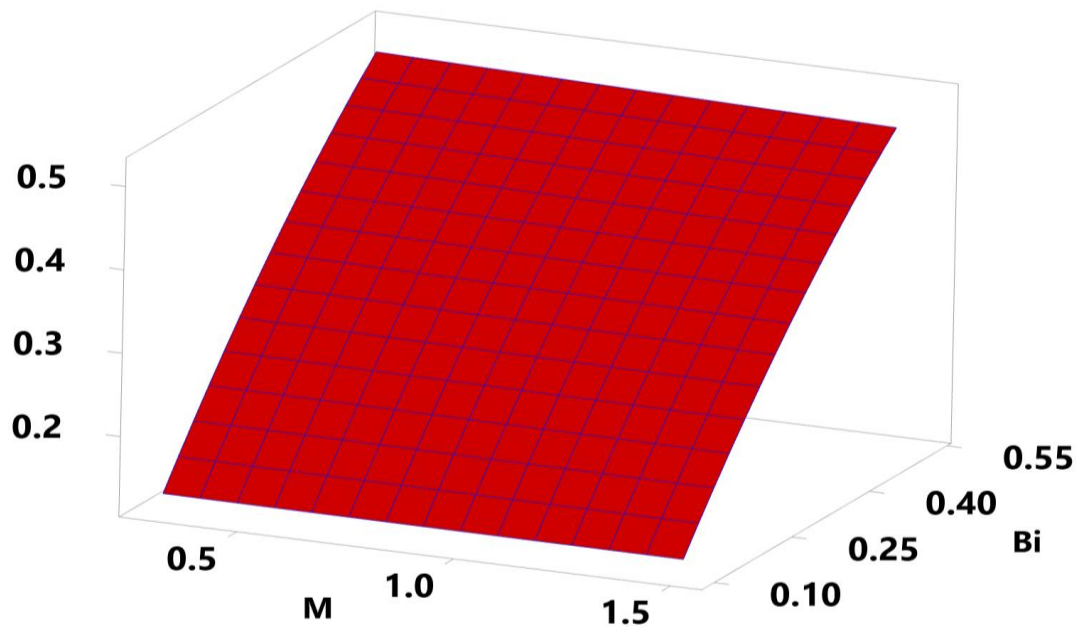
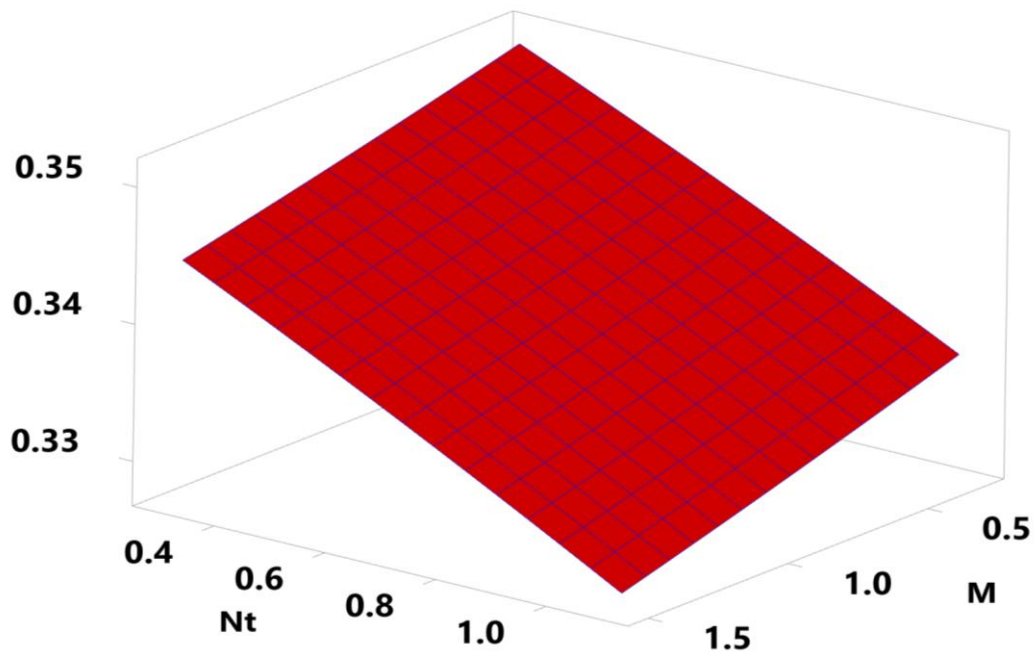


Figure 4.3.9 Surface idiographic of  $Nu_x$  in relation to magnetic field, Biot number and thermophoretic diffusion

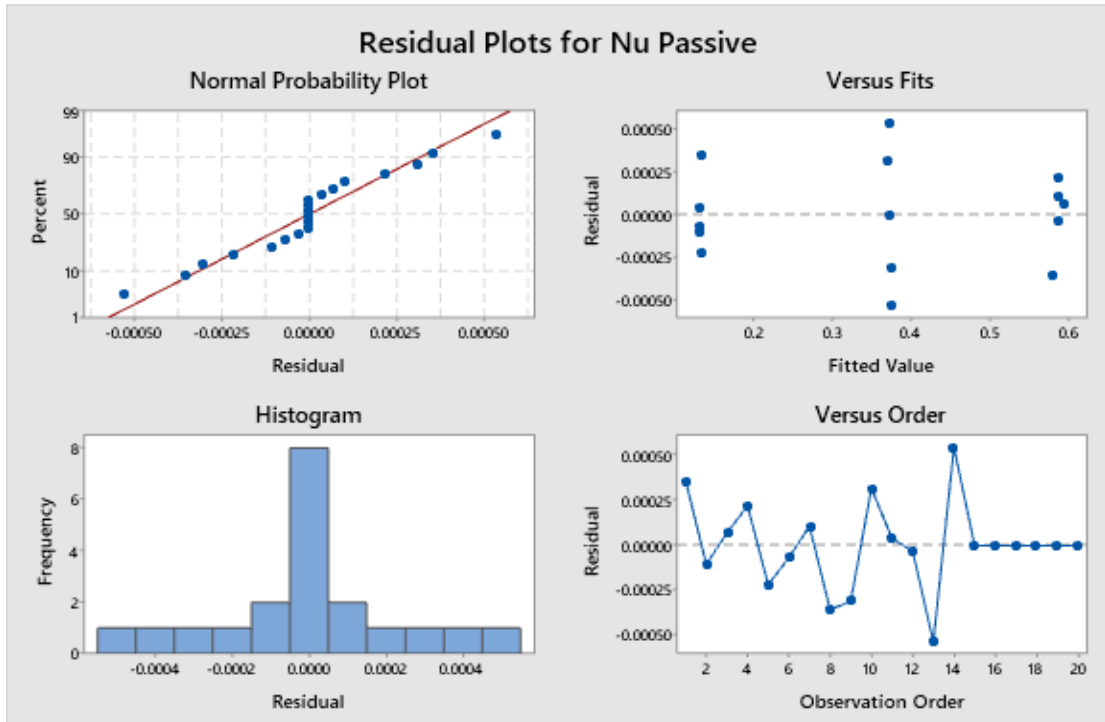


Figure 4.3.10 Plots of residuals for distorting stream

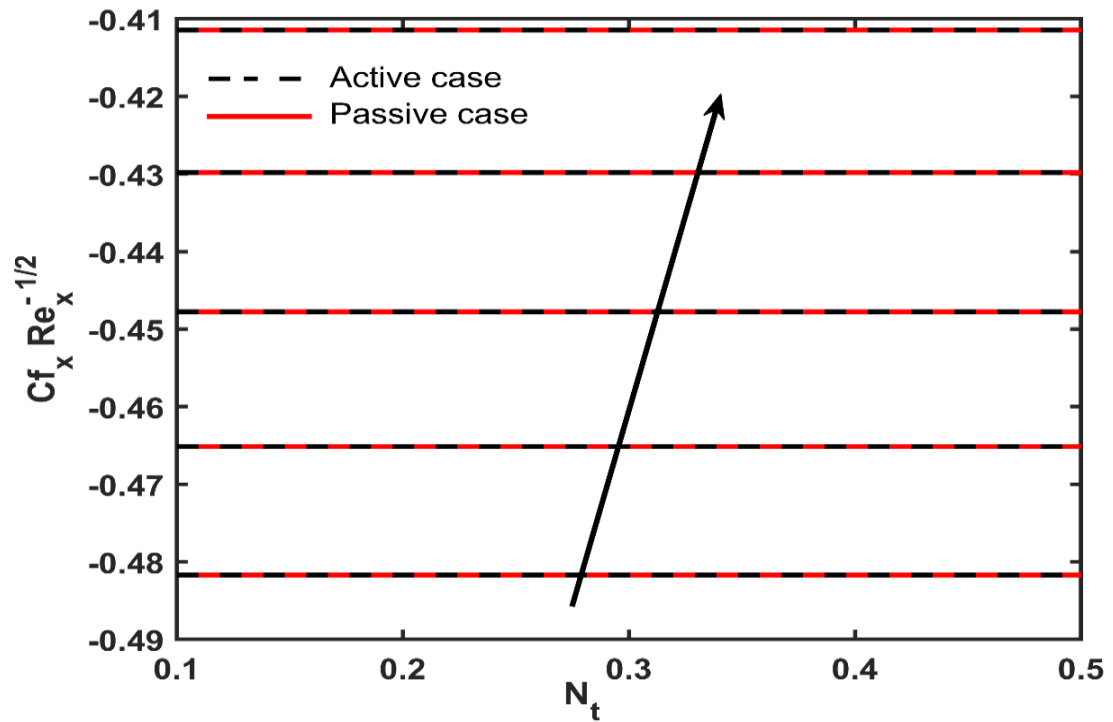


Figure 4.3.11 Fluctuation of skin friction along with  $N_t$  for active and passive control cases.

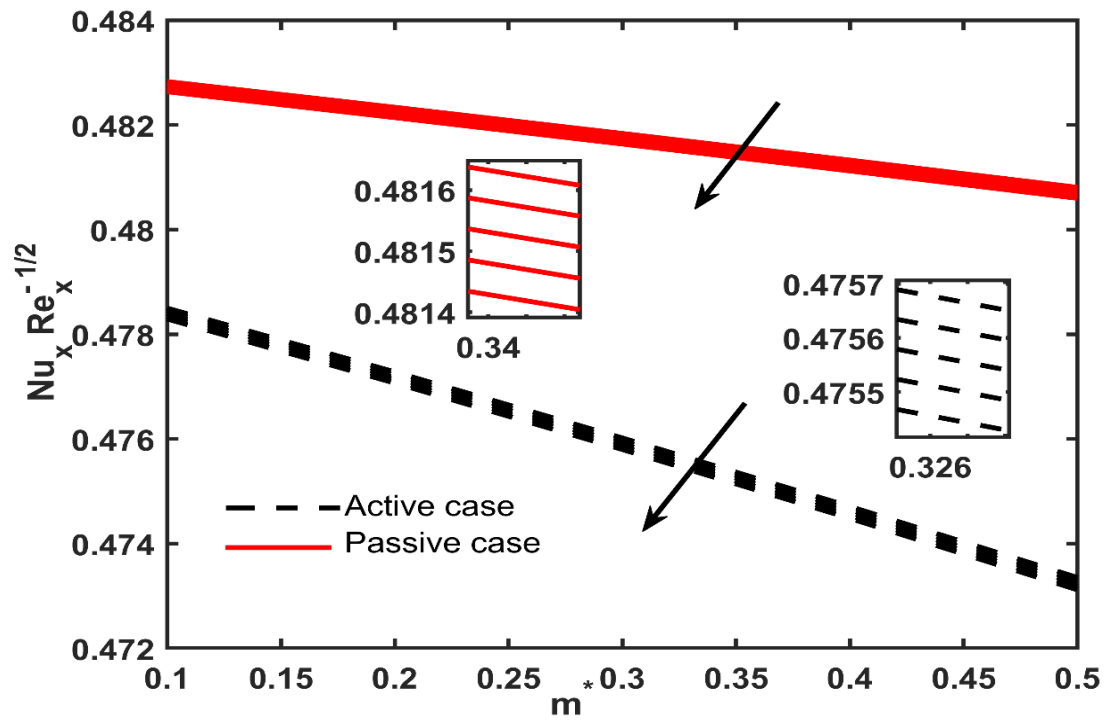
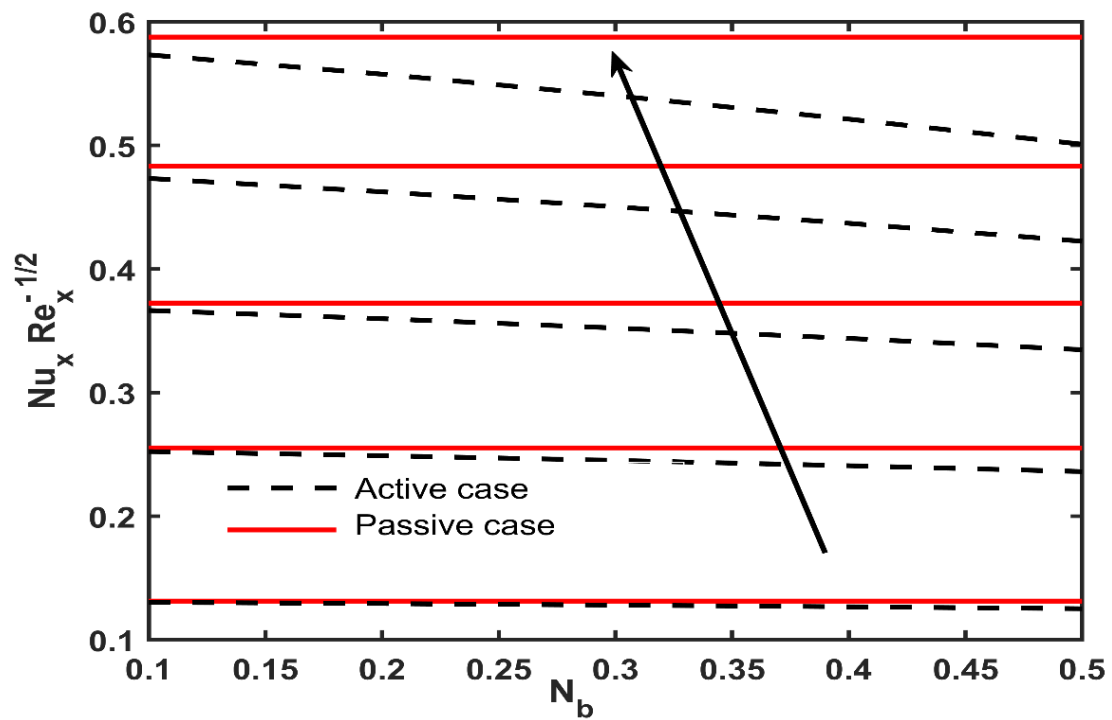


Figure 4.3.12 Fluctuation of Nusselt number along with  $m^*$  for active and passive control cases.



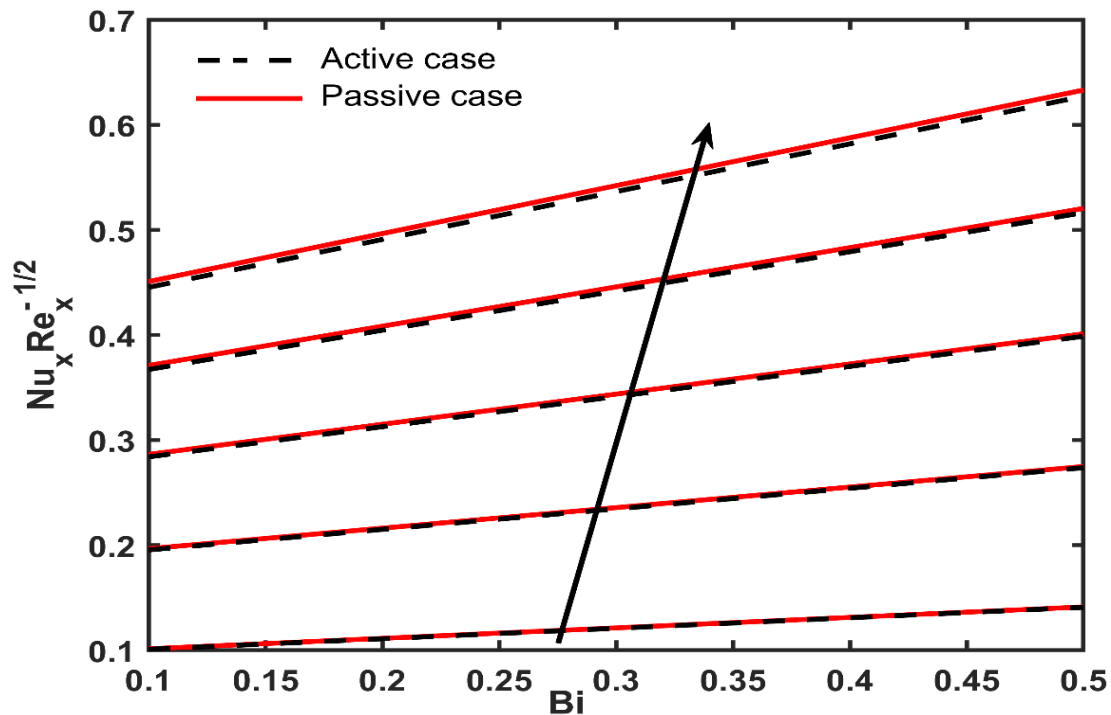


Figure 4.3.13 (a-b) Fluctuation of Nusselt number along with parameters  $N_b$  and  $Bi$  in the presence of active and passive control

#### 4.4 Sensitivity analysis of thermally convective hybrid nanofluid flow over the stretching cylinder with the impact of heat flux model

Several variables have an impact on the momentum profile  $f_1(\xi)$ , thermal distribution  $\theta(\xi)$ , nanoparticle concentration profile  $\Phi(\xi)$ , motile concentration profile  $\zeta_1(\xi)$  with local drag coefficient  $\left\{ \frac{Nu_x}{\sqrt{Re_x}} \right\}$ ,  $\left\{ \frac{Sh_x}{\sqrt{Re_x}} \right\}$ ,  $\left\{ \frac{Nn_x}{\sqrt{Re_x}} \right\}$  as clarified using graphs and tables.

The impact of the mixed convection parameter ( $\lambda$ ) on the velocity profile is shown in figure (4.4.1 (a)). The velocity profile was enhanced with ( $\lambda$ ). Physically the ratio of inertial to buoyant forces is the mixed convection parameter, an increase in ( $\lambda$ ) correlates to increased thermal buoyancy forces, which improves velocity profiles. Figure (4.4.1 (b)) reveals the impact of ( $\Gamma$ ) curvature parameter on the velocity profile. The velocity profile was lowered as one got closer to the stretching surface and increased as one got further away from it. This is physically justified as higher curvature values reduce the cylinder's radius, which further reduces the cylinder's contact area with the fluid, resulting in reduced resistance from the surface and an increase in fluid velocity. Figure (4.4.2 (c)) displays the impact of the magnetic field on the velocity profile. It can be seen from the given diagram that the dimensionless velocity falls as the magnetic parameter increases. The Lorentz force is induced by a transverse magnetic field in an electrically conducting liquid, which slows the fluid's flow within the boundary layer area. The figure (4.4.2 (d)) depicts the dropping impact of the velocity profile with the Prandtl number ( $Pr$ ). The higher the ( $Pr$ ), the more viscous the fluid will be, reducing shear stress and therefore retarding the nanofluid's flow. In

figure (4.4.3 (a)), the influence of ( $\Gamma$ ) curvature on temperature profiles is illustrated. The thermal barrier layer became thicker as ( $\Gamma$ ) became higher.

The temperature profile decreased as one got closer to the stretching surface, but it began to increase as one got further away because it slowed down heat transport and raised the temperature profile. Figure (4.4.3 (b)), describe the influence of Prandtl number ( $Pr$ ) on nanoparticle temperature. The Prandtl number is a non-dimension quantity, defined as the ratio of two quantities' momentum and thermal diffusivity. Thermal diffusivity diminished when  $Pr$  was raised, which further resulted in a drop-in boundary layer thickness.

Figure (4.4.4 (a)), explain the impact of the ( $\Gamma$ ) curvature parameter on the concentration profile. The profile was revealed to degrade near the stretching cylinder but improved as someone proceeds far from the cylinder. By raising the value of the curvature parameter, the concentration layer's thickness was improved. An illustration of the impact of the chemical reaction parameter  $C_h$  on concentration profile can be seen in figure (4.4.4 (b)). A decrease in concentration profile was observed with increased chemical reaction parameter. In the case of higher  $C_h$  values, the reaction rate, and molecular diffusivity increased, which resulted in a declination in nanoparticle concentration profiles.

Figure (4.4.5 (a)), depicts the effect of the curvature parameter on motile concentration. The value of motile concentration increased with the curvature parameter. Figure (4.4.5 (b)), shows the relationship between motile concentration and the chemical reaction parameter  $C_h$ , illustrating that as  $Ch$  upsurged, the motile concentration decreased.

The impact of  $M, \lambda, Bi, \Gamma, Sr$  on the Nusselt number, skin friction, and Sherwood number is shown in Table 4.10. The curvature parameter, Biot number, and  $\lambda$  increased the local Nusselt number and skin friction. Sherwood number raised with  $\gamma$  but decreased with  $Sr, M$  and their graphical effects are displayed in three-dimensional figures 4.4.6 – 4.4.8

The ANOVA table (Table 4.13) explains the efficiency of the estimated model. A parameter is said to be significant if the corresponding p-value is less than 0.05 and the corresponding F-value is greater than 1 Areekara *et al.* (2022). It was observed that the interactive term  $M * \phi_2$  and the quadratic terms in  $M$  and  $\phi_2$  was not significant. Hence, these terms were removed from the model. The coefficient of determination ( $R^2$ ) for the model was found to be 99.98% which boosts the model accuracy.

The reliability of the estimated model was further adjudged using the residual versus fitted plot given in figure (4.4.11). Further, a maximum error of 0.010 was observed from the fitted versus residual plot which also contributed to the accuracy of the model. The simultaneous effect of two independent variables on the response variable is illustrated in figure (4.4.9) (contour plots) and figure (4.4.10) (surface plots) respectively, by fixing the third parameter at the mid-level. From figure (4.4.9-4.4.10) it can be perceived that the heat transport is highest for smaller values of  $M$  and larger values of  $Bi$  and  $\phi_2$ .

The sensitivity of  $Nu_x Re_x^{-1/2}$ , keeping  $A$  in the medium level, has been tabulated in Table 4.14. It was noted that  $Bi$  and  $\phi_2$  exhibit positive sensitivity towards  $Nu_x Re_x^{-1/2}$  and  $M$  exhibits negative sensitivity towards  $Nu_x Re_x^{-1/2}$ . Furthermore, these results were in harmony with the RSM results.

Figure (4.4.12) visualizes the sensitivity of  $Nu_x Re_x^{-1/2}$  utilizing bar charts. It was observed that the heat transfer rate was most sensitive to the changes in  $Bi$  and least sensitive to the changes in  $M$ .

**Table 4.9: The variation of Nusselt number for various values of  $\lambda$  and remaining parameters are held fixed**

$\lambda$	<i>Merkin (1977)</i>	<i>Nazarr et al. (2004)</i>	<i>Zahar et al. (2020)</i>	<i>Present result</i>
-1.75	0.4199	0.4205	0.4198	0.419767
-1.5	0.4576	0.4601	0.4573	0.457333
-1.0	0.5067	0.5080	0.5067	0.506625
-0.5	0.5420	0.5430	0.5421	0.542022
0.0	0.5705	0.5710	0.5705	0.570428
0.5	0.5943	0.5949	0.5945	0.594496
0.88	0.6096	0.6112	0.6108	0.610725
0.89	0.6110	0.6116	0.6112	0.611132
1.0	0.6158	0.6160	0.6154	0.615551
2.0	0.6497	0.6518	0.6515	0.651456
5.0	0.7315	0.7320	0.7315	0.731476

**Table 4.10: The variation of Nusselt number, skin friction coefficient and Sherwood number for different values  $M, \lambda, \Gamma, Bi, Sr$ .**

$M$	$\lambda$	$\Gamma$	$Bi$	$Sr$	$Nu_x Re_x^{-1/2}$	$\frac{1}{2} C_f x^{-1/2}$	$Sh_x Re_x^{-1/2}$
0.1	0.5	0.1	0.5	0.2	0.661814	3.128358	0.363801
0.5	—	—	—	—	0.656615	2.965984	0.358355
0.9	—	—	—	—	0.651463	2.817433	0.353220
0.1	0.2	0.1	0.5	0.2	0.661265	3.091323	0.363559
—	0.4	—	—	—	0.661632	3.116042	0.363721
—	0.7	—	—	—	0.662176	3.152907	0.363962
0.1	0.5	0.1	0.5	0.2	0.661814	3.128358	0.363801
—	—	0.3	—	—	0.683794	3.325885	0.469100
—	—	0.7	—	—	0.717946	3.696868	0.669088
0.1	0.5	0.1	0.1	0.2	0.182665	3.083654	0.393819
—	—	—	0.5	—	0.661814	3.128358	0.363801
—	—	—	0.9	—	0.934641	3.153607	0.346675
0.1	0.5	0.1	0.5	0.4	0.661814	3.128358	0.321828
—	—	—	—	0.6	0.661814	3.128358	0.279854
—	—	—	—	0.8	0.661814	3.128358	0.237880

**Table 4.11: Effective parameter levels**

Parameter	Symbol	Levels		
		-1 (Low)	0 (Medium)	1 (High)
$Bi$	$A$	0.1	0.5	0.9
$M$	$B$	0.1	0.5	0.9
$\phi_2$	$C$	0.01	0.05	0.09

**Table 4.12: Experimental design with response**

Run	Coded Values			Actual Values			Response
	$A$	$B$	$C$	$Bi$	$M$	$\phi_2$	$Nu_x Re_x^{-1/2}$
1	-1	-1	-1	0.1	0.1	0.01	0.1633707
2	1	-1	-1	0.9	0.1	0.01	0.8509387
3	-1	1	-1	0.1	0.9	0.01	0.1626006
4	1	1	-1	0.9	0.9	0.01	0.830892
5	-1	-1	1	0.1	0.1	0.09	0.2034739
6	1	-1	1	0.9	0.1	0.09	1.0220304
7	-1	1	1	0.1	0.9	0.09	0.2026201
8	1	1	1	0.9	0.9	0.09	1.0012361
9	-1	0	0	0.1	0.5	0.05	0.1822619
10	1	0	0	0.9	0.5	0.05	0.9243729
11	0	-1	0	0.5	0.1	0.05	0.6618147
12	0	1	0	0.5	0.9	0.05	0.6514638
13	0	0	-1	0.5	0.5	0.01	0.5935715
14	0	0	1	0.5	0.5	0.09	0.7231788
15	0	0	0	0.5	0.5	0.05	0.656615
16	0	0	0	0.5	0.5	0.05	0.656615
17	0	0	0	0.5	0.5	0.05	0.656615
18	0	0	0	0.5	0.5	0.05	0.656615
19	0	0	0	0.5	0.5	0.05	0.656615
20	0	0	0	0.5	0.5	0.05	0.656615

**Table 4.13: Sensitivity of response  $Nu_x Re_x^{-1/2}$  when  $A = 0$**

$B$	$C$	Sensitivity		
		$\frac{\partial (Nu_x Re_x^{-1/2})}{\partial A}$	$\frac{\partial (Nu_x Re_x^{-1/2})}{\partial B}$	$\frac{\partial (Nu_x Re_x^{-1/2})}{\partial C}$
-1	-1	0.34375	-0.00528	0.05512
	0	0.37641	-0.00528	0.05512
	1	0.40907	-0.00528	0.05512
0	-1	0.33885	-0.00528	0.05512
	0	0.37151	-0.00528	0.05512
	1	0.40417	-0.00528	0.05512
1	-1	0.33395	-0.00528	0.05512
	0	0.36661	-0.00528	0.05512
	1	0.39927	-0.00528	0.05512

**Table 4.14: ANOVA table**

	Deg. of freedom	Adj. sum of squares	Adj. mean squares	Regression Coefficient	F-Value	P-Value
Model	9	1.47225	0.16358		6952.14	0.000
<i>Linear</i>	3	1.41089	0.47030		19987.16	0.000
<i>Bi</i>	1	1.38023	1.38023	1.48870	58658.57	0.000
<i>M</i>	1	0.00028	0.00028	0.00330	11.86	0.006
$\phi_2$	1	0.03038	0.03038	0.26100	1291.06	0.000
<i>Square</i>	3	0.05263	0.01754		745.63	0.000
<i>Bi * Bi</i>	1	0.02944	0.02944	-0.64660	1251.09	0.000
<i>M * M</i>	1	0.00000	0.00000	-0.00090	<b>0.00</b>	<b>0.962</b>
$\phi_2 * \phi_2$	1	0.00001	0.00001	1.00000	<b>0.30</b>	<b>0.598</b>
<i>2-Way Interaction</i>	3	0.00873	0.00291		123.64	0.000
<i>Bi * M</i>	1	0.00019	0.00019	-0.03060	8.17	0.017
<i>Bi * <math>\phi_2</math></i>	1	0.00854	0.00854	2.04200	362.75	0.000
<i>M * <math>\phi_2</math></i>	1	0.00000	0.00000	-0.00600	<b>0.00</b>	<b>0.953</b>
<i>Constant</i>				0.01382		
Error	10	0.00024	0.00002			
Lack-of-Fit	5	0.00024	0.00005		*	*
Pure Error	5	0.00000	0.00000			
Total	19	1.47248				
$R^2 = 99.98\%$			Adjusted $R^2 = 99.97\%$			

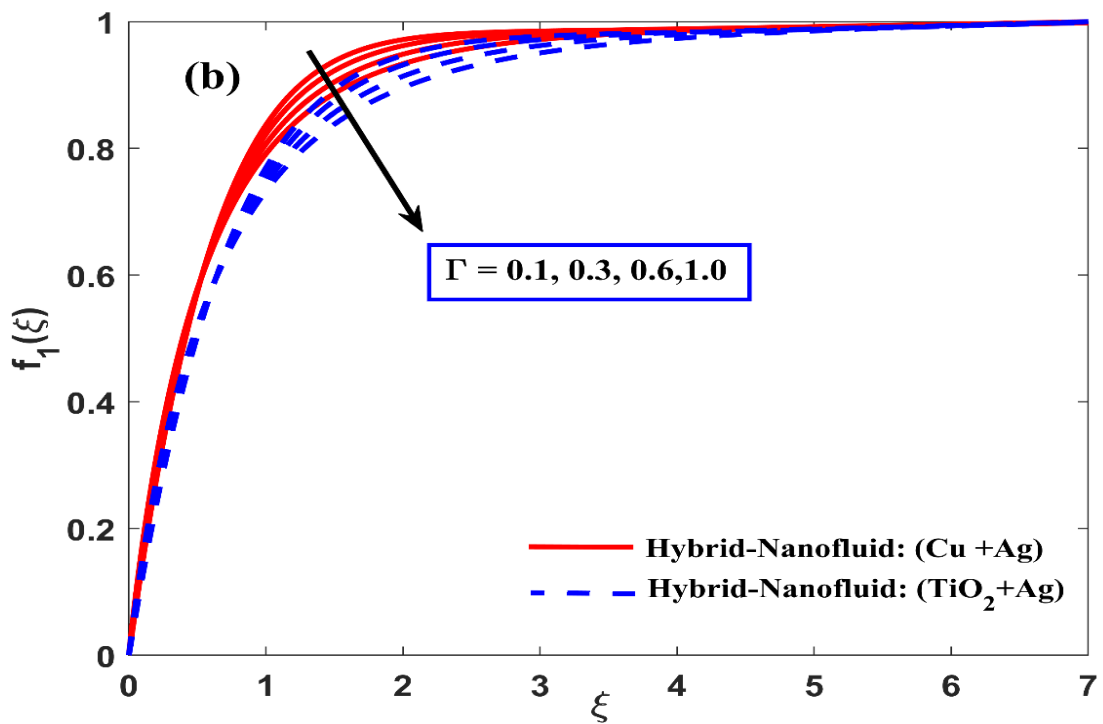
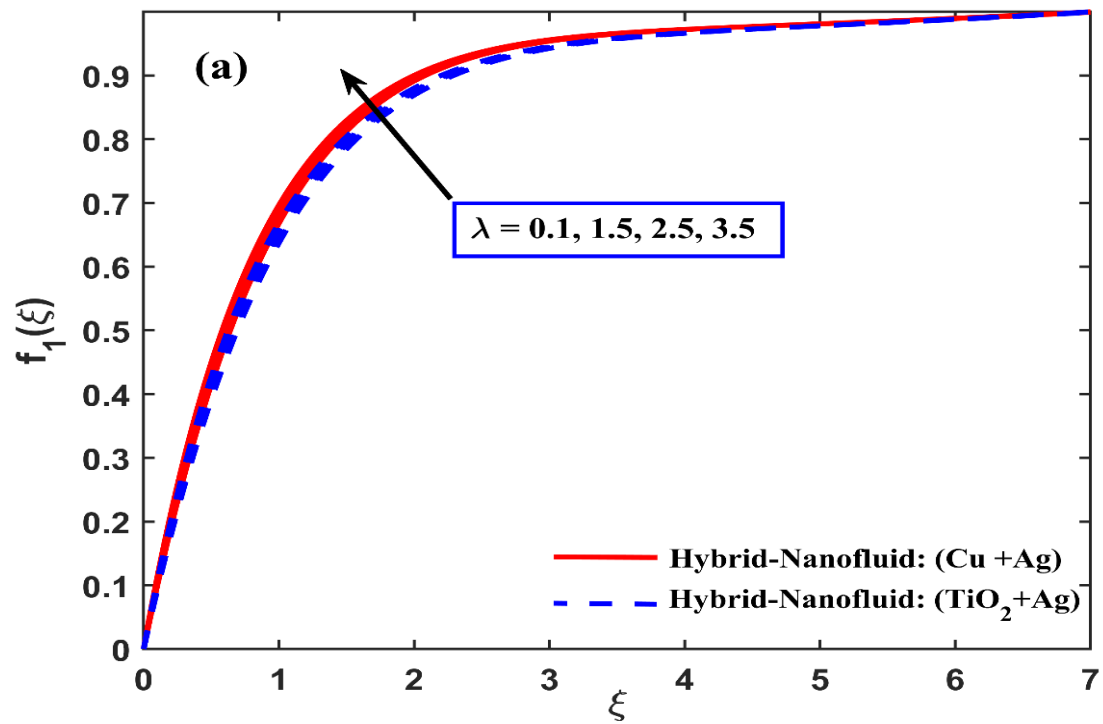


Figure 4.4.1 (a-b) Velocity profile fluctuation against  $\xi$  for numerous values of  $\lambda$ , and  $\Gamma$ .

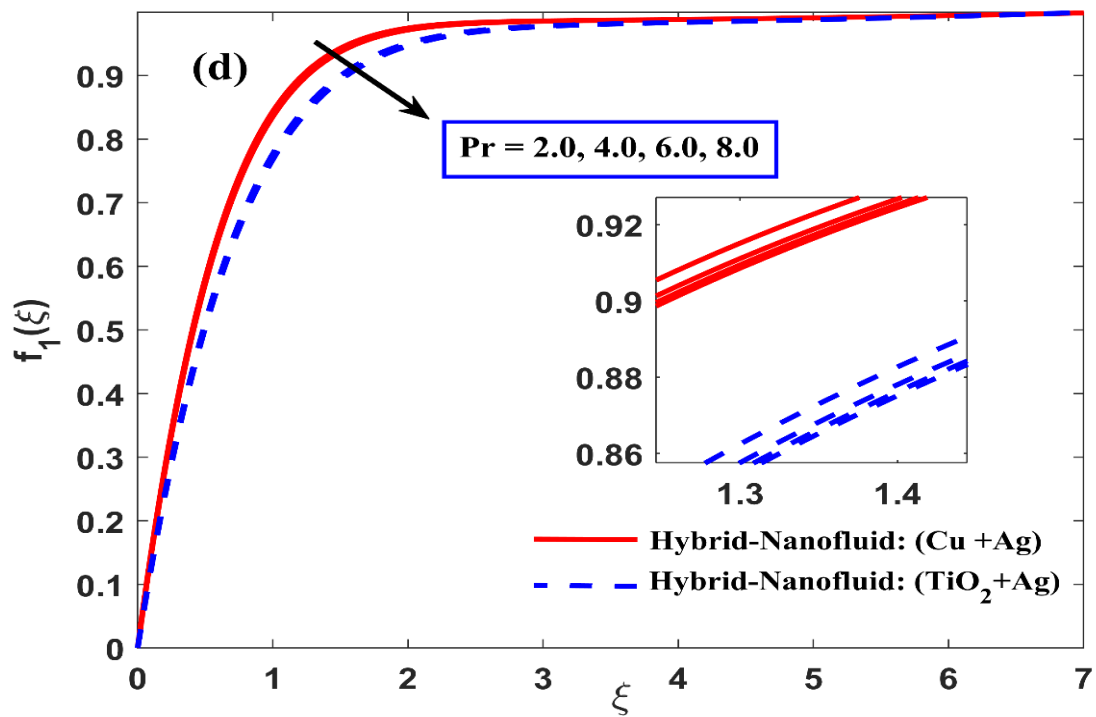
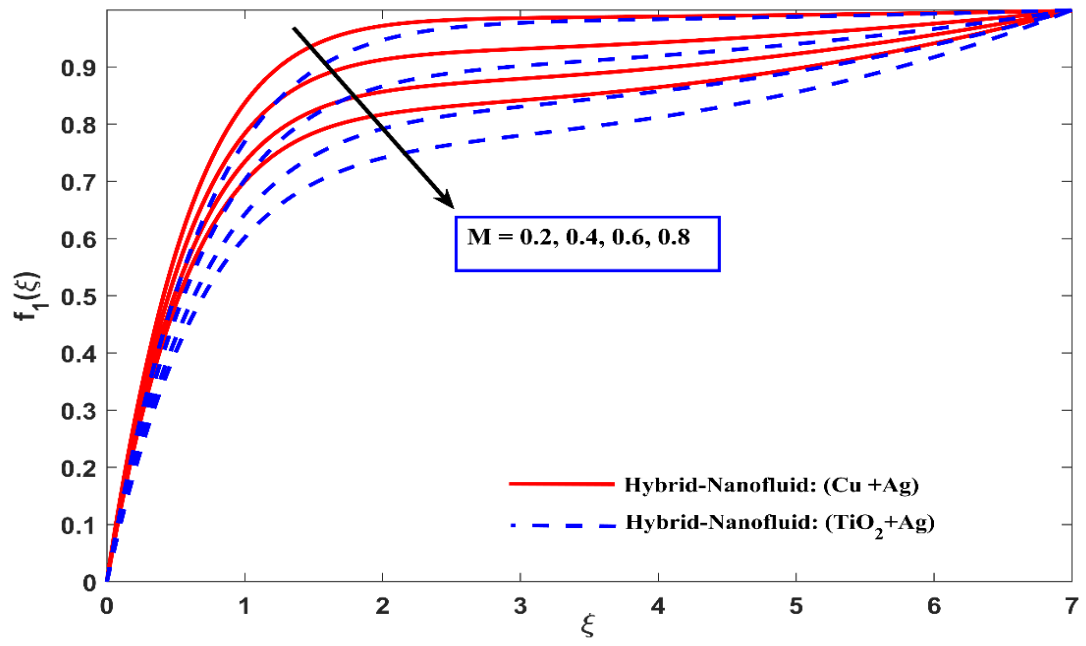


Figure 4.4.2 (c-d) Velocity profile fluctuation for numerous values of  $M$  and  $Pr$

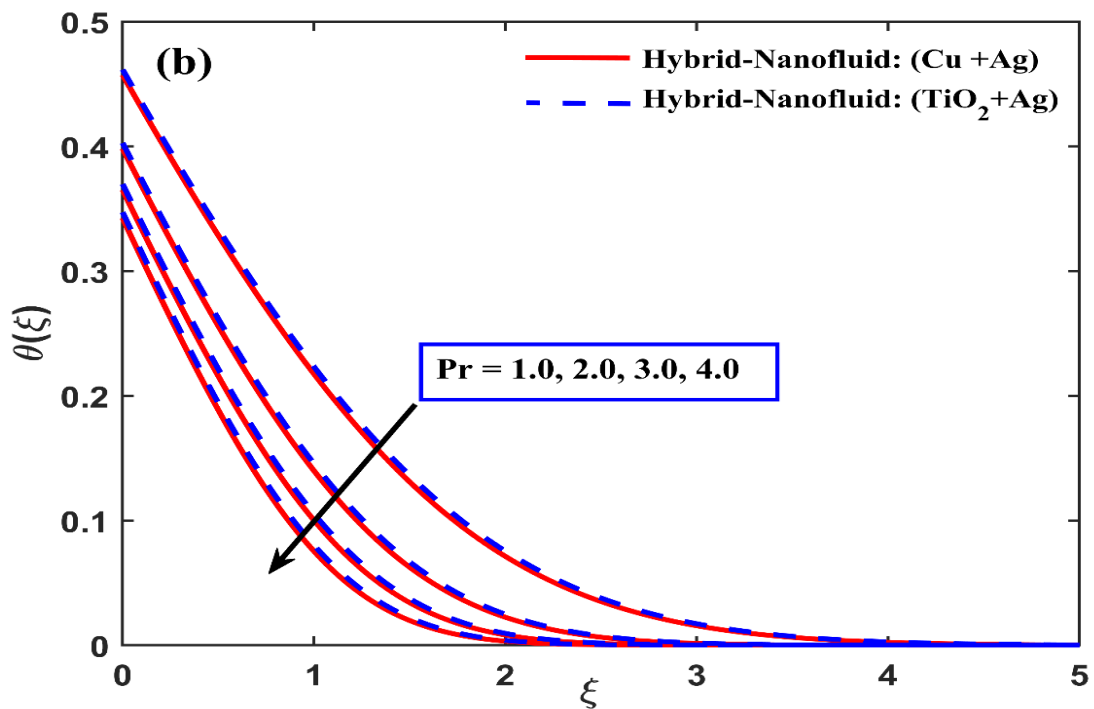
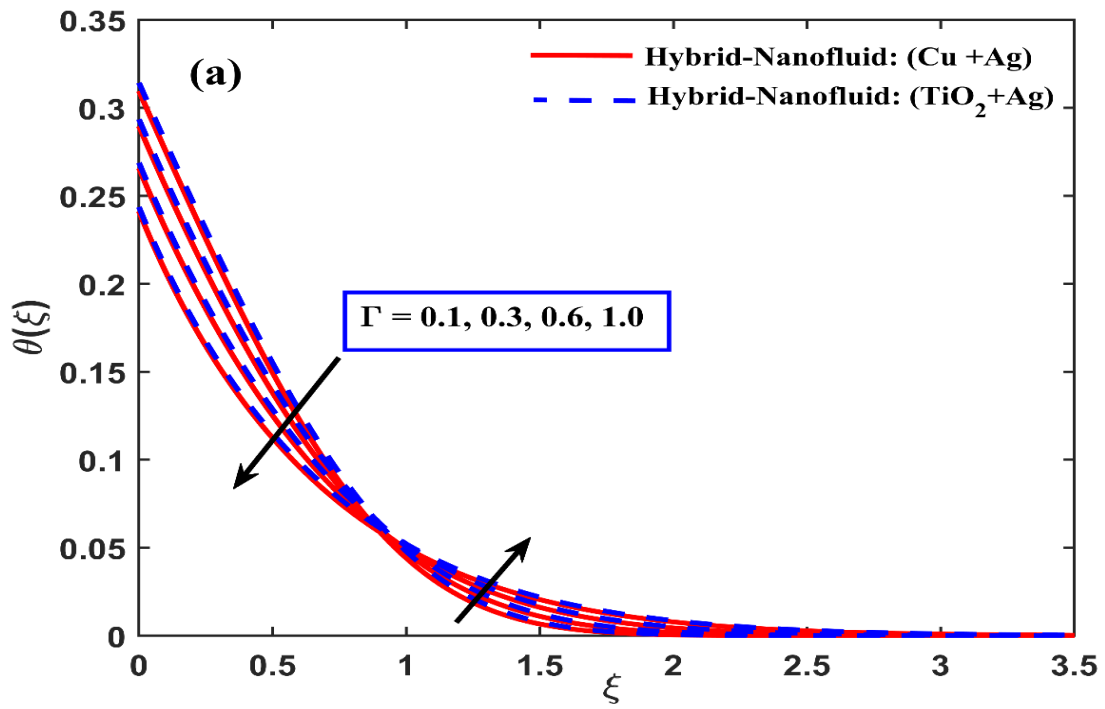


Figure 4.4.3 (a-b) Temperature distribution fluctuation against  $\xi$  for  $\Gamma$  and  $Pr$

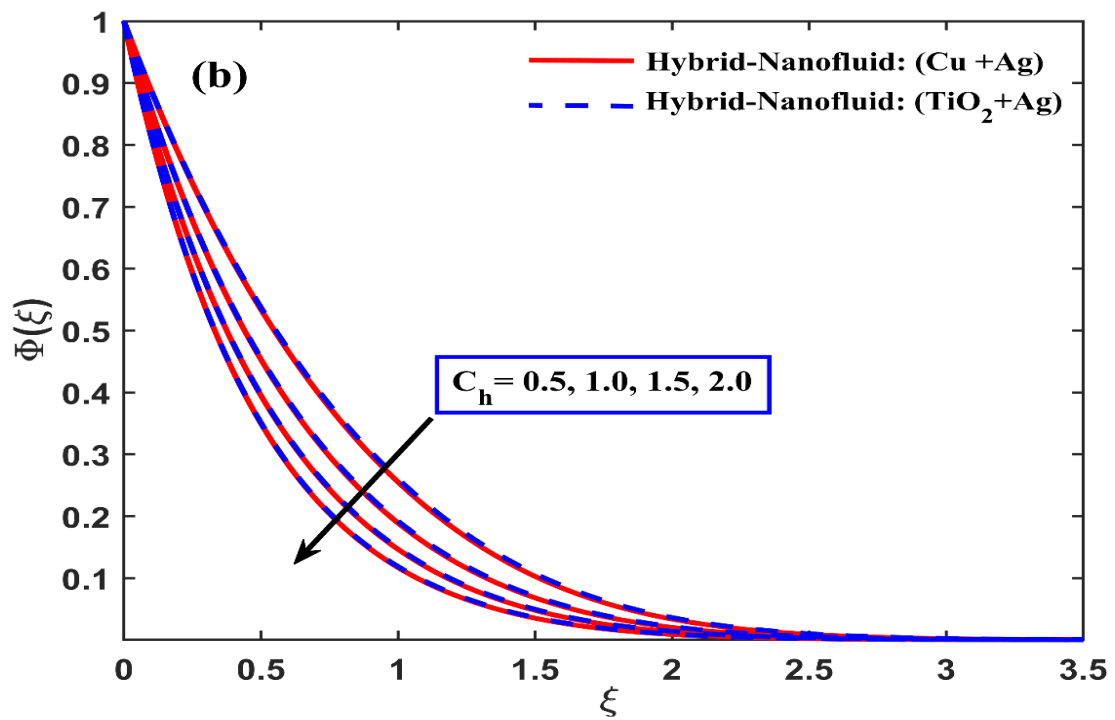
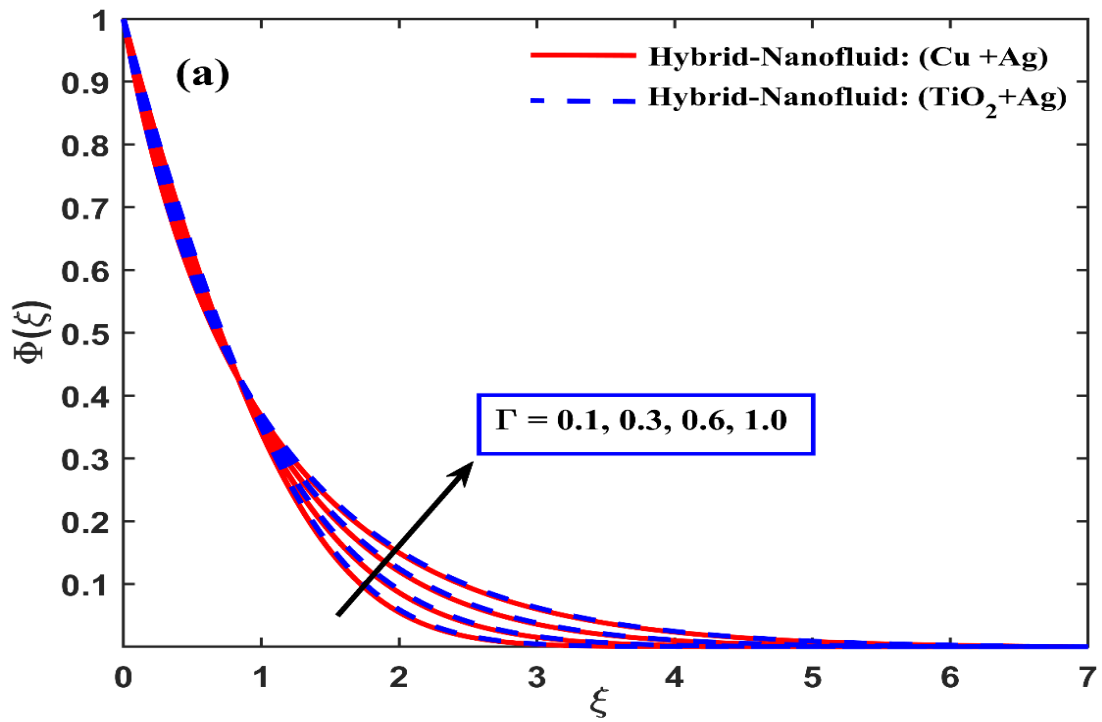


Figure 4.4.4 (a-b) Concentration profile fluctuation against  $\xi$  for values of  $\Gamma$  and  $C_h$

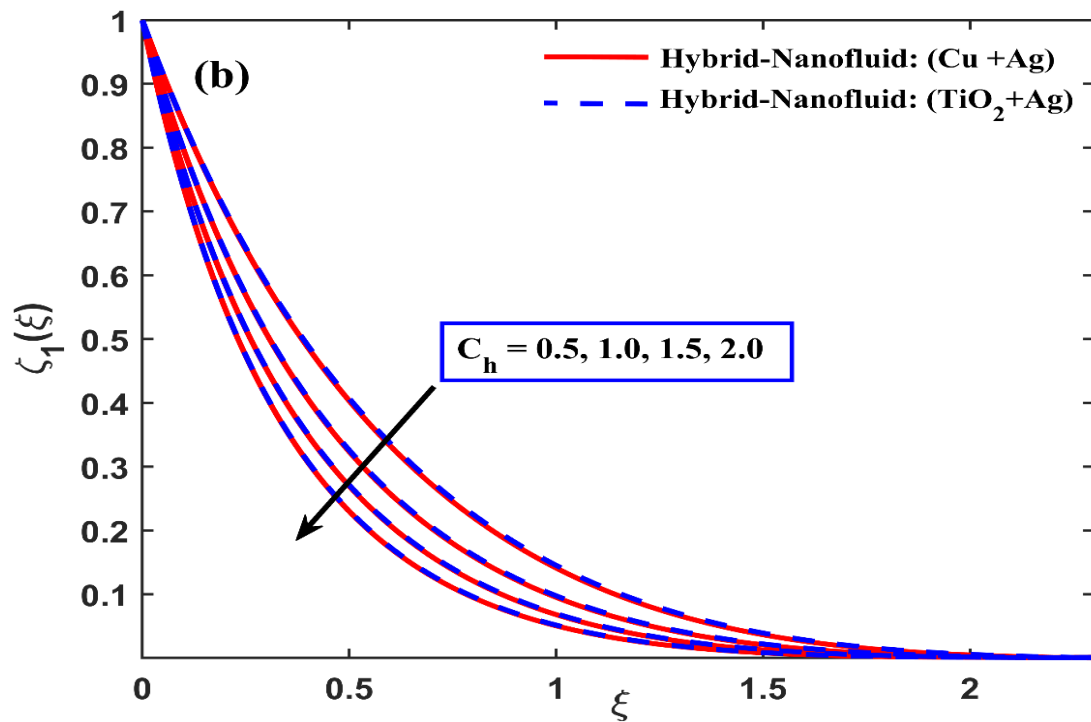
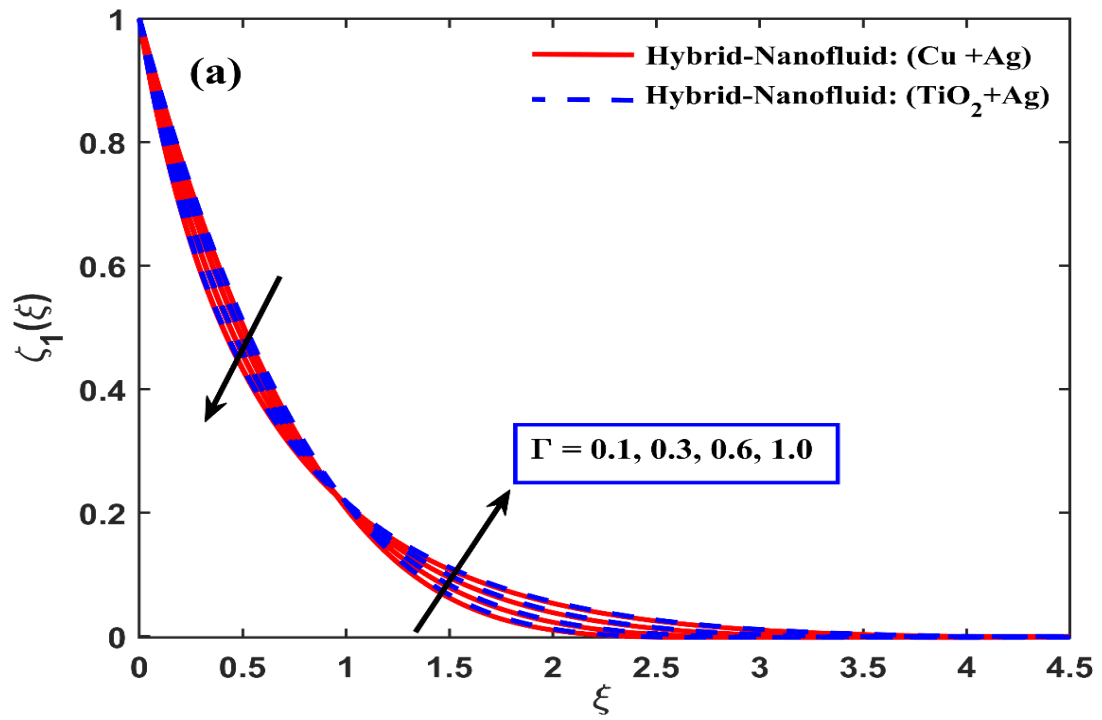


Figure 4.4.5 (a-b) Motile concentration profile fluctuation against  $\xi$  for  $\Gamma$  and  $C_h$

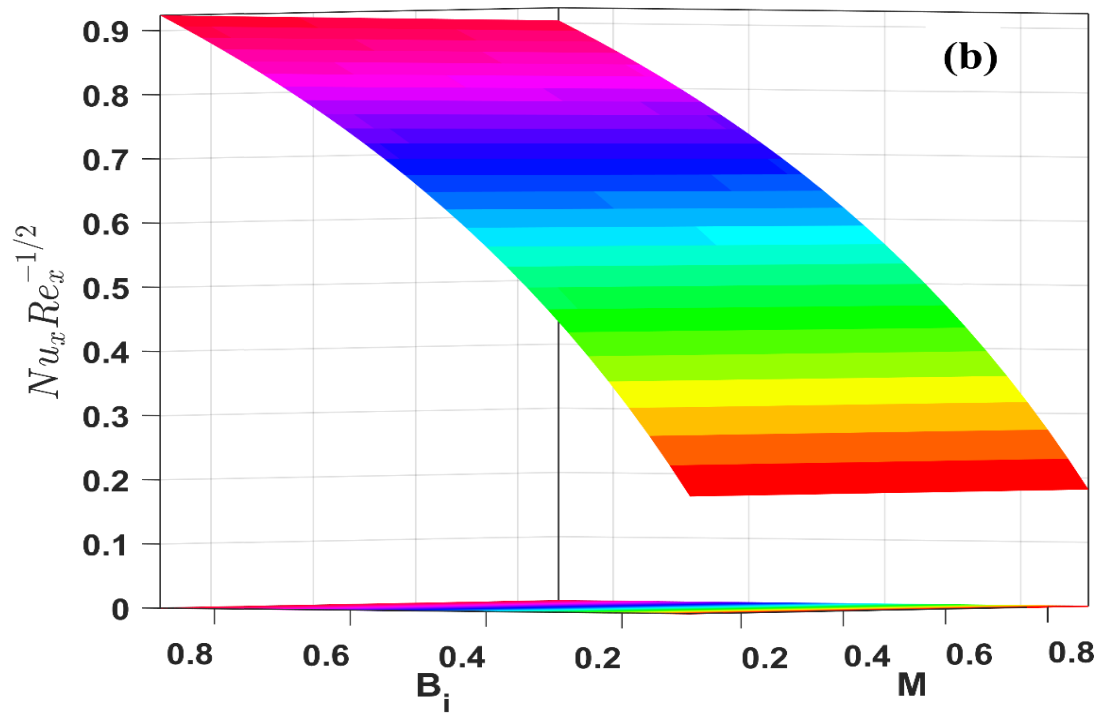
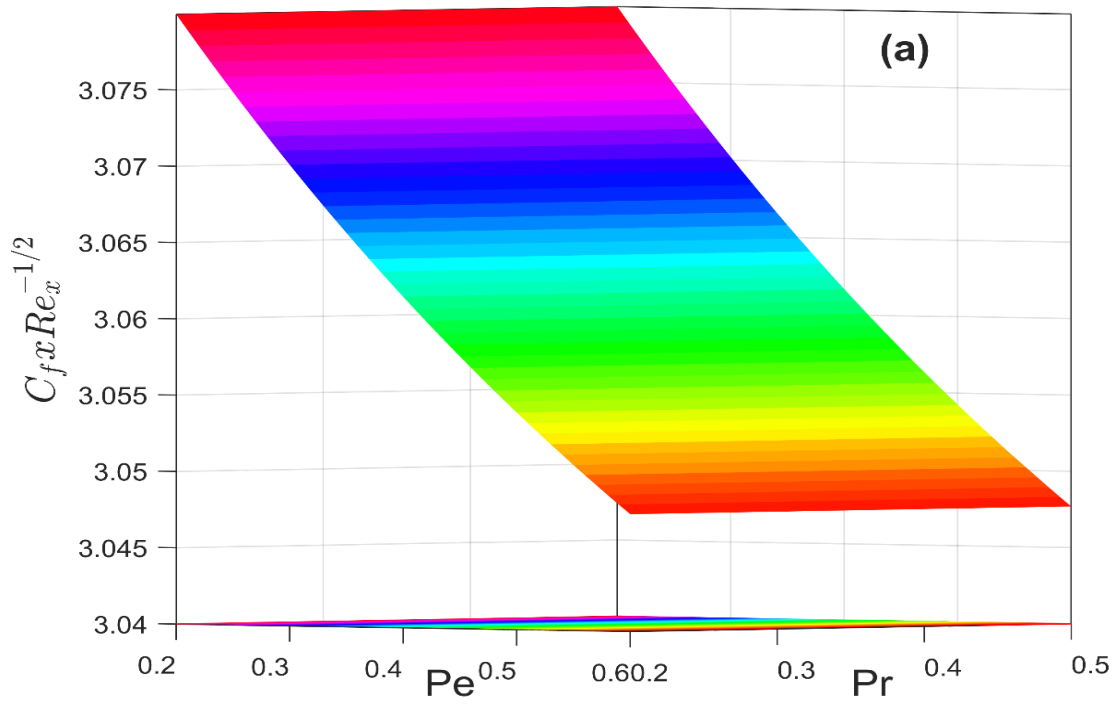


Figure 4.4.6 (a-b) Variation in skin friction against  $Pe, Pr, M, Bi$

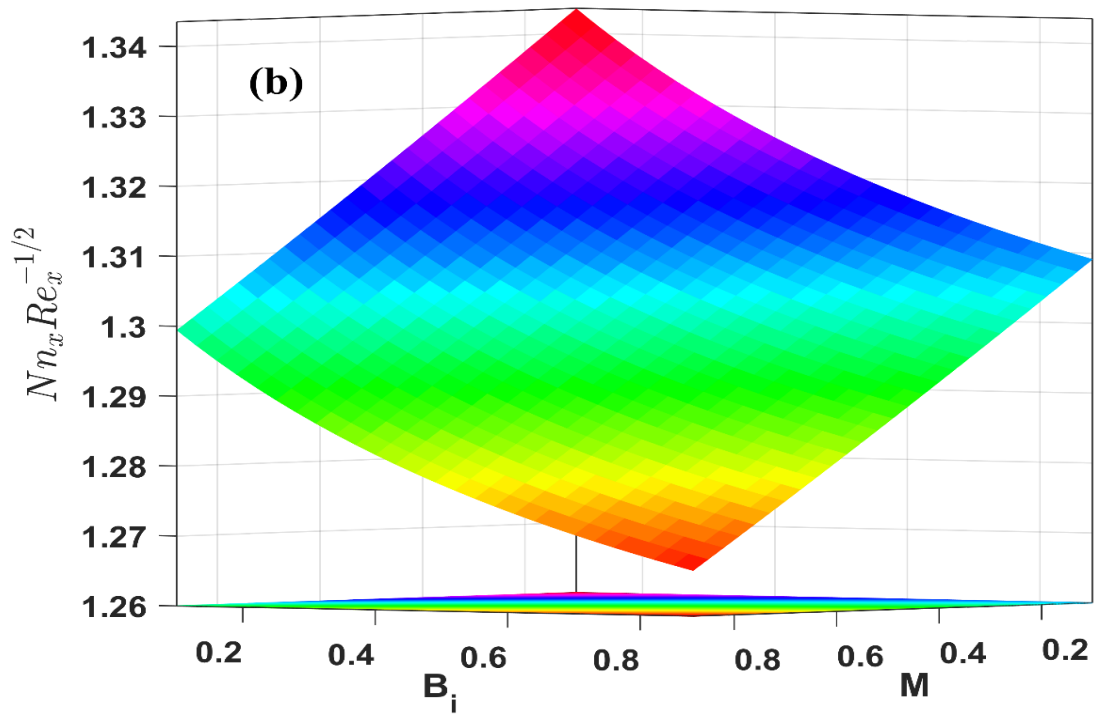
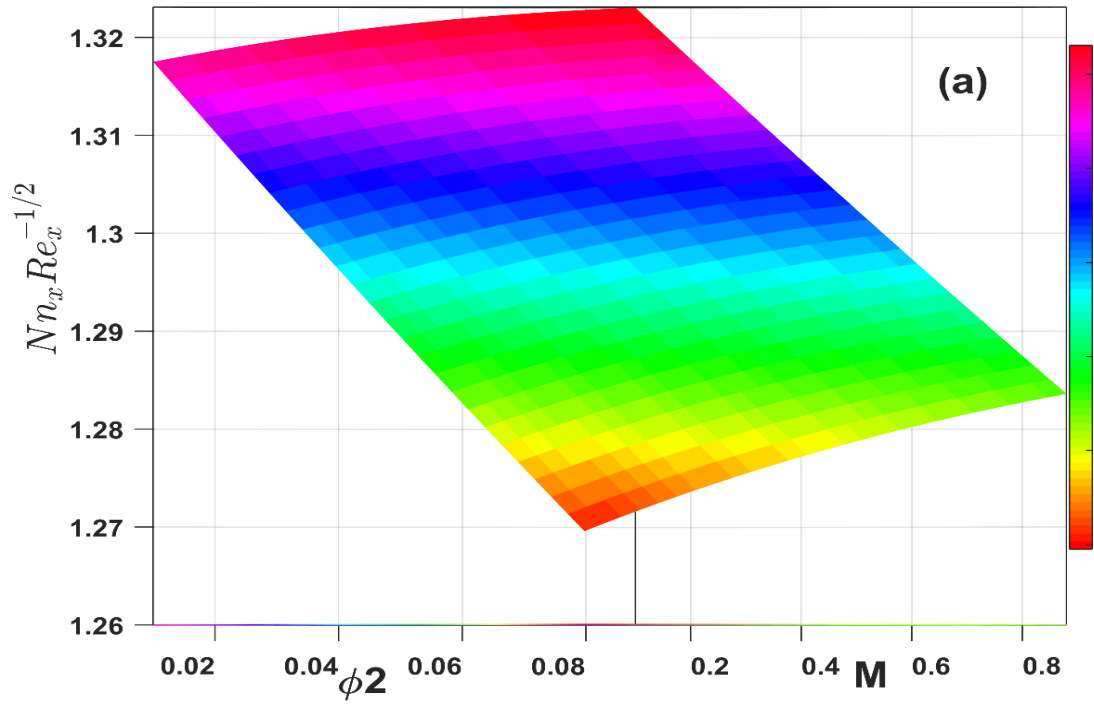


Figure 4.4.7 (a-b) Variation in Nusselt number against  $\phi_2, M, Bi$

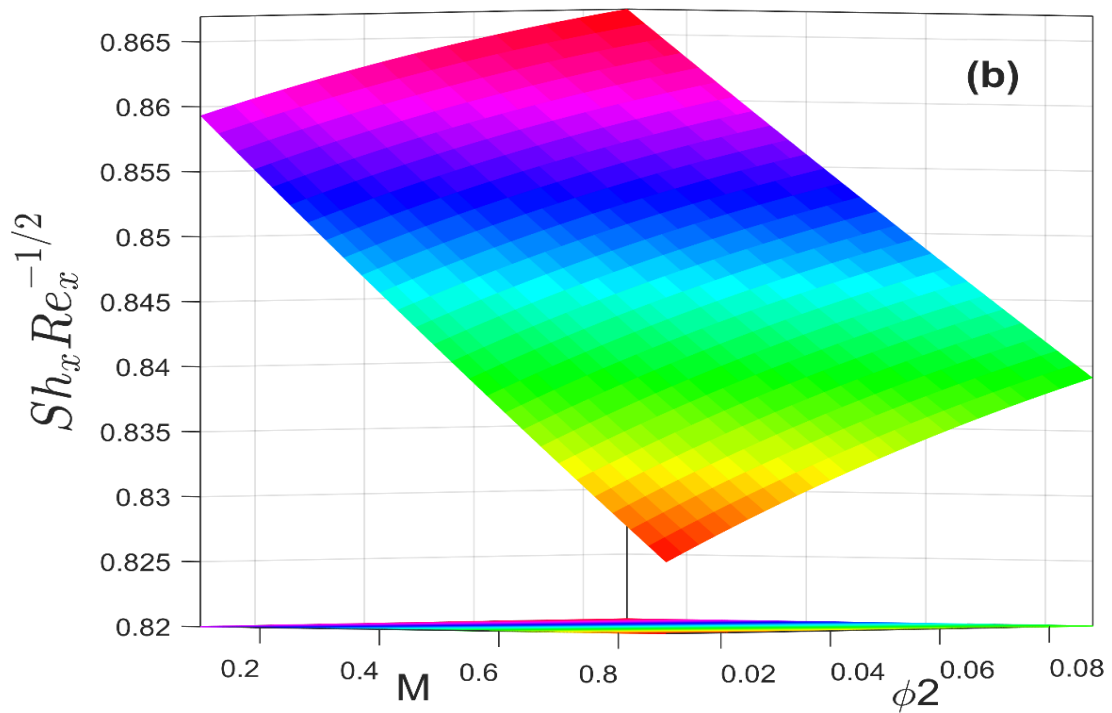
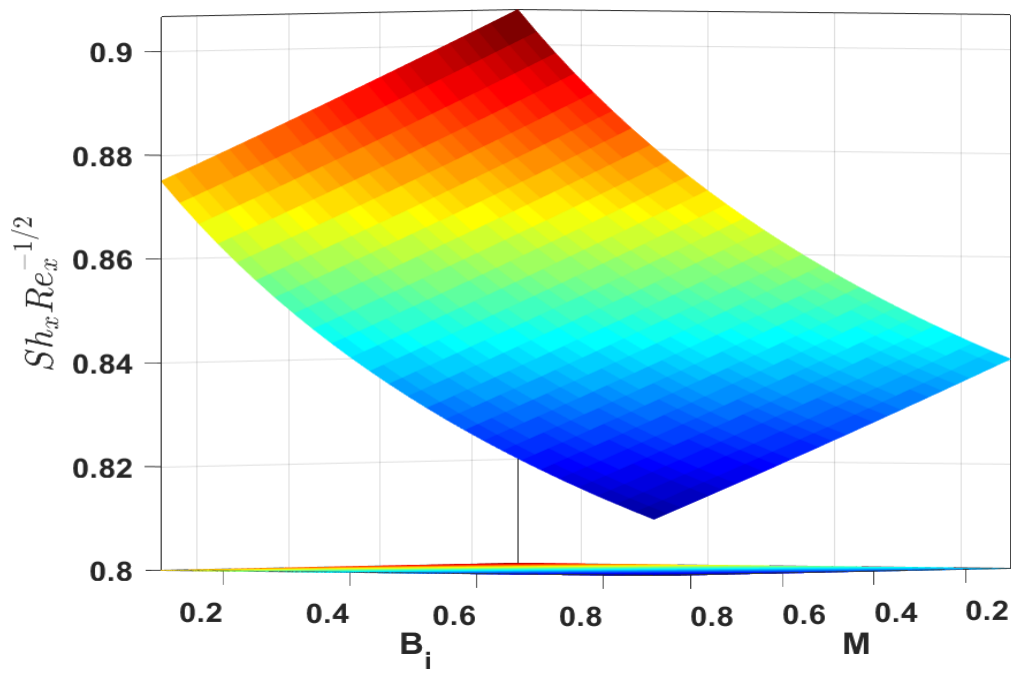


Figure 4.4.8 (a-b) Variation in Sherwood number against  $Bi, M, \phi_2$

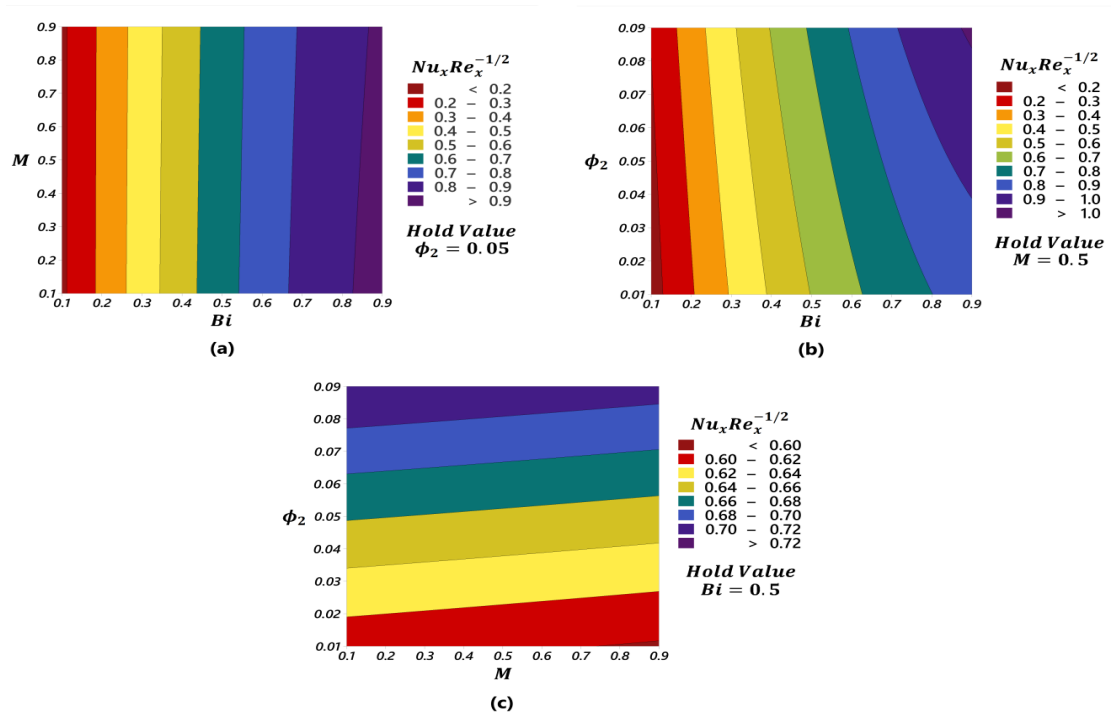


Figure 4.4.9 Contour plots for  $Nu_x Re_x^{-1/2}$

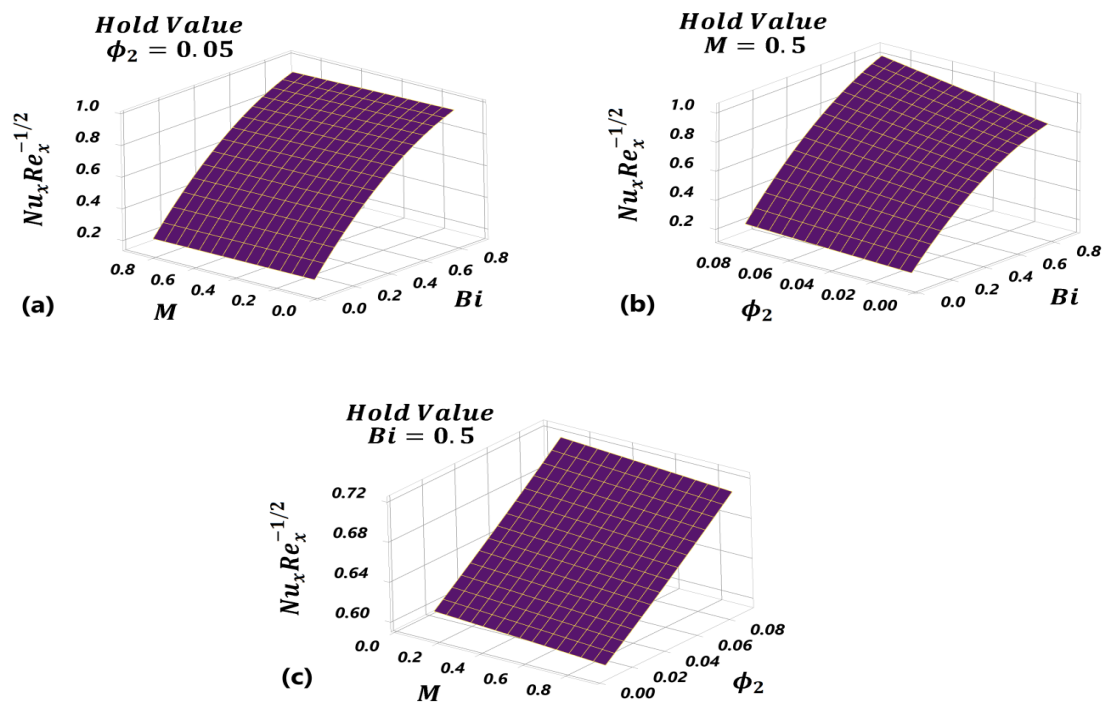


Figure 4.4.10 Surface plots for  $Nu_x Re_x^{-1/2}$

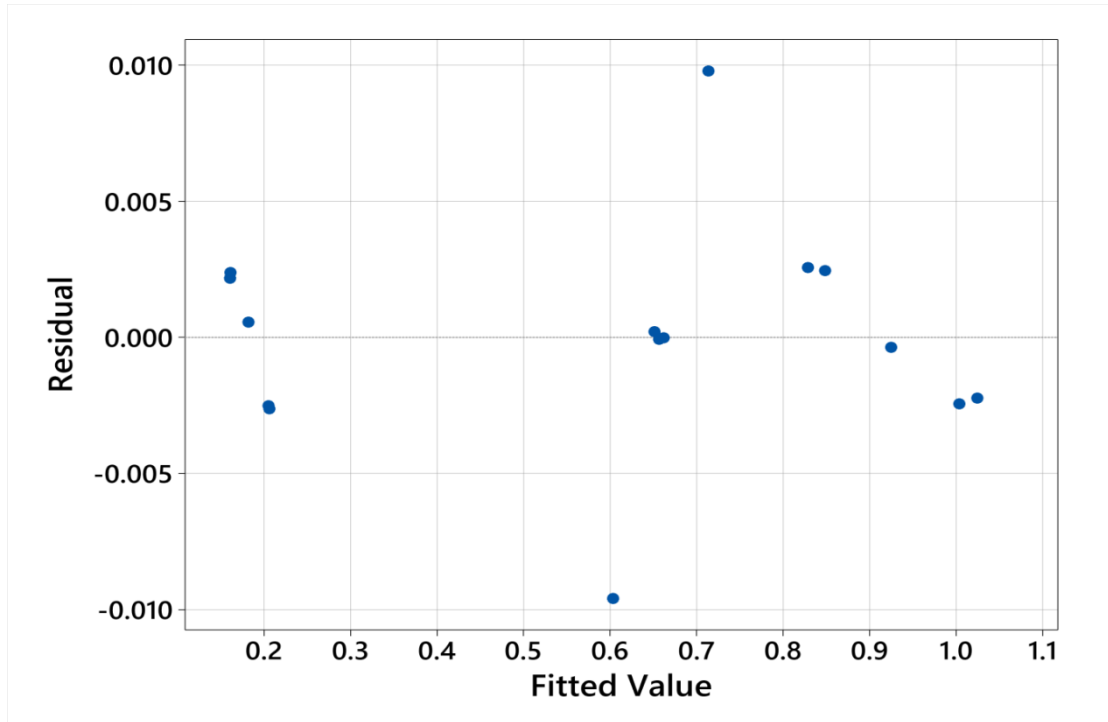


Figure 4.4.11 Residual versus Fitted value of  $Nu_x Re_x^{-1/2}$

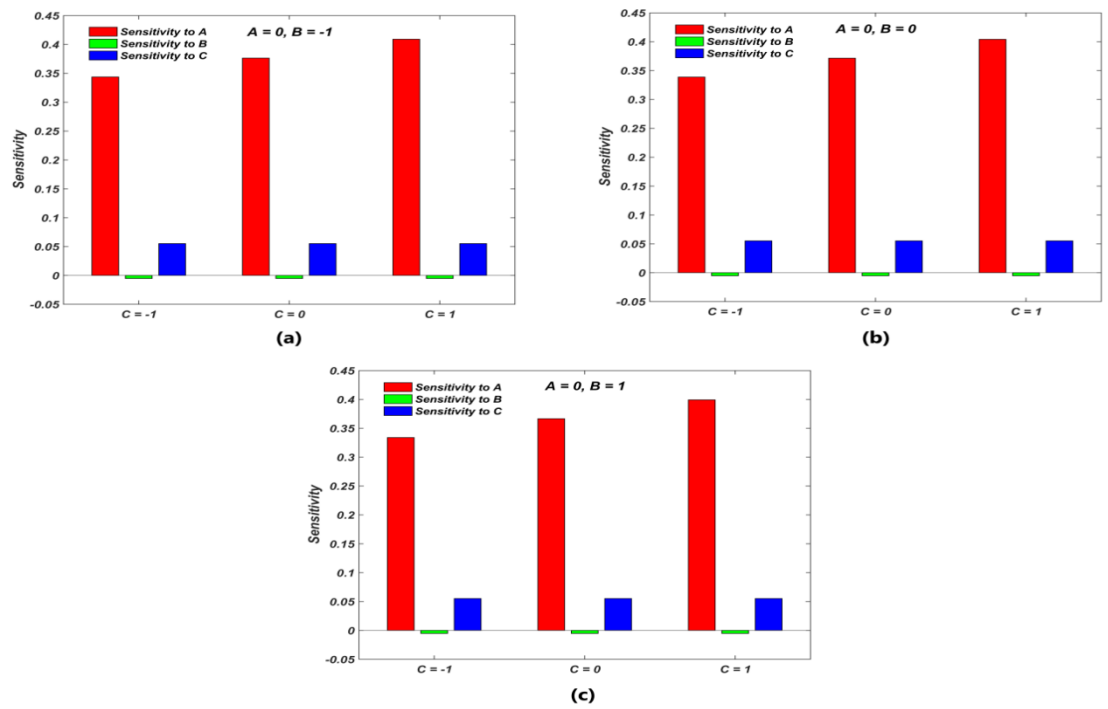


Figure 4.4.12 Bar charts depicting the sensitivity of  $Nu$

#### 4.5 Chemically reactive species effect on MHD Carreau nanofluid flow over the stretching cylinder with the impact of multiple slip and motile microorganisms

Several variables have an impact on momentum profile  $f'(\zeta)$ , thermal distribution  $\theta(\zeta)$ , nanoparticle concentration profile  $\varphi(\xi)$ , motile concentration profile  $\chi(\zeta)$  with  $\{Nu_x Re^{-\frac{1}{2}x}\}$ ,  $\{\frac{1}{2}Cf_x Re^{-\frac{1}{2}x}\}$  and Sherwood number  $\{Sh_x Re^{-\frac{1}{2}x}\}$  are clarified using graphs and tables for dilatant and pseudo-plastic fluids.

The impact of the magnetic parameter  $M$  with the simultaneous effect of velocity slip  $\lambda_1$  on the velocity profile for shearing thinning ( $n < 1$ ) and shear thickening ( $n > 1$ ) situations is shown in figures (4.5.1 (a-b)). The diagram shows that the dimensionless velocity declined as the magnetic parameter increased in both cases. Because the presence of a transverse magnetic field in an electrically conducting liquid causes the Lorentz force by slowing the flow of the fluid inside the boundary layer region. Furthermore, the slip parameter describes the interaction between a fluid and a rigid body. When  $\lambda_1$  enhanced, it creates a large gap between the solid and the fluid, thus reducing the fluid's motion. Hence the velocity profile decreased with the velocity slip parameter.

Figures (4.5.2 (a-b)) describe the fluctuation of velocity  $f'(\zeta)$  with local Weissenberg number values for both dilatant and pseudo plastic fluids with the simultaneous effect of velocity slip. For  $n < 1$ , it was observed that for arise local Weissenberg number values, the fluid velocity dropped but increased in the shear thickening case. Since, Weissenberg number increases fluid thickness, which reduces velocity, because it measures the fluid's relaxation time in relation to a particular process time.

Figures (4.5.3 (a-b)) depict the effect of magnetic parameter  $M$  on the temperature profile in the presence of thermal slip  $\lambda_2$  at the boundary for both shearing thinning ( $n < 1$ ) and shear thickening ( $n > 1$ ) scenarios. The transverse magnetic field reduces the fluid's velocity and greatly slows down the rate of transmission. Thus, the thermal boundary layer thickness becomes thicker for both situations. The susceptibility of the fluid flow within the boundary layer is also decreased by raising the thermal slip parameter  $\lambda_2$  which minimizes the quantity of heat produced and thus shrinking the thermal boundary layer.

Figures (4.5.4 (a-b)) describe the influence of Prandtl number  $Pr$  with the simultaneous effect of thermal slip  $\lambda_2$  on Carreau fluid temperature profile for situations of shearing thinning ( $n < 1$ ) and shear thickening ( $n > 1$ ). The Prandtl number is a non-dimension quantity, defined as the ratio of two quantities' momentum and thermal diffusivity. Thermal diffusivity diminishes when  $Pr$  rises, which further gives a drop-in boundary layer thickness and temperature in both cases.

An illustration of the impact of the chemical reaction parameter  $Ch$  and the effect of concentration slip  $\lambda_3$  The concentration profile for dilatant and pseudo plastic fluids can be

seen in figures (4.5.5 (a-b)). A decrease in concentration profile was observed with increased chemical reaction parameter values. In the case of high  $Ch$  values, the reaction rate, and molecular diffusivity increase, which results in a decline in nano-particle concentration profiles. A decrease in concentration profile can be observed with increased chemical reaction parameter values for  $n < 1$  and  $n > 1$ . Moreover, because of the negative nanoparticle concentration gradient at the sheet, the nanoparticle concentration layer lowers as the nanoparticle concentration slip parameter increases.

Figures (4.5.6 (a-b)) illustrate the impact of the bio convection Lewis number  $Lb$  on the density field of gyrotactic motile microorganisms with the simultaneous effect of microorganism slip parameter  $\lambda_4$  in both shearing thinning ( $n < 1$ ) and shear thickening ( $n > 1$ ) instances. For both cases, the fluid's motility was decreased when the bio-convection Lewis number was raised. Digestion behaviour is typically caused by motile particles that move continuously through the fluid while the heat transfer rate is being executed. The diffusion of microorganisms from the cylinder surface to the nanofluid's main body is delayed due to coupling with the microorganism density gradient. This delay prevents microorganisms from moving from the cylinder surface to the free stream and manifests as a reduction in the thickness of the microorganism species boundary layer with  $\lambda_4$ .

Figures (4.5.7 (a-b)) explore the impact of  $W_e$  on skin friction and thermal slip  $\lambda_2$  on Nusselt number for both the scenarios of shearing thinning ( $n < 1$ ) and shear thickening ( $n > 1$ ). The skin friction increased, but the Nusselt number decreased with the effect of respective parameters.

In figures (4.5.8 (a-b)), the simultaneous effect of  $Pe$  and  $\lambda_3$  parameters on  $\{Nn_x Re^{-\frac{1}{2}x}\}$ , is shown by the surface plot. The  $\{Nn_x Re^{-\frac{1}{2}x}\}$  was intensified when the values of parameters were decreased, similarly the impact of  $\lambda_3$  and  $M$  on  $\{Sh_x Re^{-\frac{1}{2}x}\}$  was described for shear thickening ( $n > 1$ ) case. The numerical results obtained using `bvp5c` are contrasted with those obtained using `bvp5c` and `RKF45`, shown in Tables 4.15 and 4.16.

Table (4.17-4.18) shows Nusselt number  $\{Nu_x Re^{-\frac{1}{2}x}\}$ , skin friction coefficient  $\{\frac{1}{2}Cf_x Re^{-\frac{1}{2}x}\}$  and Sherwood number  $\{Sh_x Re^{-\frac{1}{2}x}\}$  for different values of  $M, \Gamma, W_e, \lambda_1$  for scenarios of shearing thinning ( $n < 1$ ) and shear thickening ( $n > 1$ ). The local Nusselt number decreased with  $M$  and  $\lambda_1$  but increased with curvature parameter for ( $n < 1$ ) and ( $n > 1$ ). The skin friction and Nusselt number have shown dual nature with  $W_e$  as both decreased for ( $n < 1$ ) whereas they increased for ( $n > 1$ ). The Sherwood number declined with  $M$  for dilatant fluid and pseudo plastic fluid.

**Table 4.15: Comparison of  $-f''(0)$  for various values of  $n, W_e, \Gamma$  and remaining parameters are held constant**

$n$	$W_e$	$\Gamma$	BVP5C Sabu <i>et al.</i> (2021)	RKF45 Sabu <i>et al.</i> (2021)	RK4 Sabu <i>et al.</i> (2021)	Present result
<b>0.5</b>	1	0.2	0.989702	0.989709	0.989709	0.989701
	2	0.4	0.901331	0.901343	0.901343	0.901342
	3	0.6	0.830948	0.830972	0.830972	0.830949
<b>1.5</b>	1	0.2	1.145708	1.145708	1.145708	1.145704
	2	0.4	1.367061	1.367061	1.367061	1.367058
	3	0.6	1.611585	1.611585	1.611585	1.611580

**Table 4.16: Comparison of  $-\theta'(0)$  for various values of  $P_r$  and remaining parameters are held zero**

$P_r$	Khan and Pop (2010)	Sabu <i>et al.</i> (2021)	Present Result
0.7	0.4539	0.453932	0.453933
2	0.9113	0.911359	0.911359
7	1.8954	1.895428	1.895422
20	3.3539	3.354174	3.354172

**Table 4.17: The variation of the Nusselt number  $\{Nu_x Re^{-\frac{1}{2}x}\}$ , skin friction coefficient  $\{Cf_x Re^{-\frac{1}{2}x}\}$  and Sherwood number  $\{Sh_x Re^{-\frac{1}{2}x}\}$  for different values of  $M, \Gamma, W_e, \lambda_1$  ( $n < 1$ ).**

$n$	$M$	$\Gamma$	$W_e$	$\lambda_1$	$Cf_x Re^{-\frac{1}{2}x}$	$Nu_x Re^{-\frac{1}{2}x}$	$Sh_x Re^{-\frac{1}{2}x}$
0.5	0.5	-	-	-	1.038195	0.845774	-0.244909
-	1.5	-	-	-	0.875339	1.006156	-0.135125
-	2.5	-	-	-	0.619765	1.119215	0.051506
-	-	0.1	-	-	0.952643	0.921192	-0.275204
-	-	0.4	-	-	0.964925	0.960081	-0.040858
-	-	0.7	-	-	0.977579	0.996118	0.157372
-	-	-	2	-	0.964925	0.960081	-0.040858
-	-	-	3	-	0.917302	0.872254	-0.006914
-	-	-	4	-	0.870742	0.808093	0.026700
-	-	-	-	0.2	0.964925	0.960081	-0.040858
-	-	-	-	0.4	0.845168	0.816136	0.047052
-	-	-	-	0.6	0.718793	0.707215	0.140396

**Table 4.18:** The variation of the Nusselt number  $\{Nu_x Re^{-\frac{1}{2}x}\}$ , skin friction coefficient  $\{Cf_x Re^{-\frac{1}{2}x}\}$  and Sherwood number  $\{Sh_x Re^{-\frac{1}{2}x}\}$  for different values of  $M, \Gamma, W_e, \lambda_1$  ( $n > 1$ ).

$n$	$M$	$\Gamma$	$W_e$	$\lambda_1$	$Cf_x Re^{-\frac{1}{2}x}$	$Nu_x Re^{-\frac{1}{2}x}$	$Sh_x Re^{-\frac{1}{2}x}$
1.5	0.5	-	-	-	1.088769	1.082961	-0.275481
-	1.5	-	-	-	0.982632	1.342749	-0.208953
-	2.5	-	-	-	0.879563	1.531233	-0.138016
-	-	0.1	-	-	1.028744	1.187827	-0.323431
-	-	0.4	-	-	1.042463	1.295725	-0.093998
-	-	0.7	-	-	1.052298	1.392372	0.104310
-	-	-	2	-	1.042463	1.295725	-0.093998
-	-	-	3	-	1.047745	1.357226	-0.096997
-	-	-	4	-	1.050866	1.406824	-0.098531
-	-	-	-	0.2	1.042463	1.295725	-0.093998
-	-	-	-	0.4	0.888681	0.987318	0.016635
-	-	-	-	0.6	0.745529	0.804817	0.121383

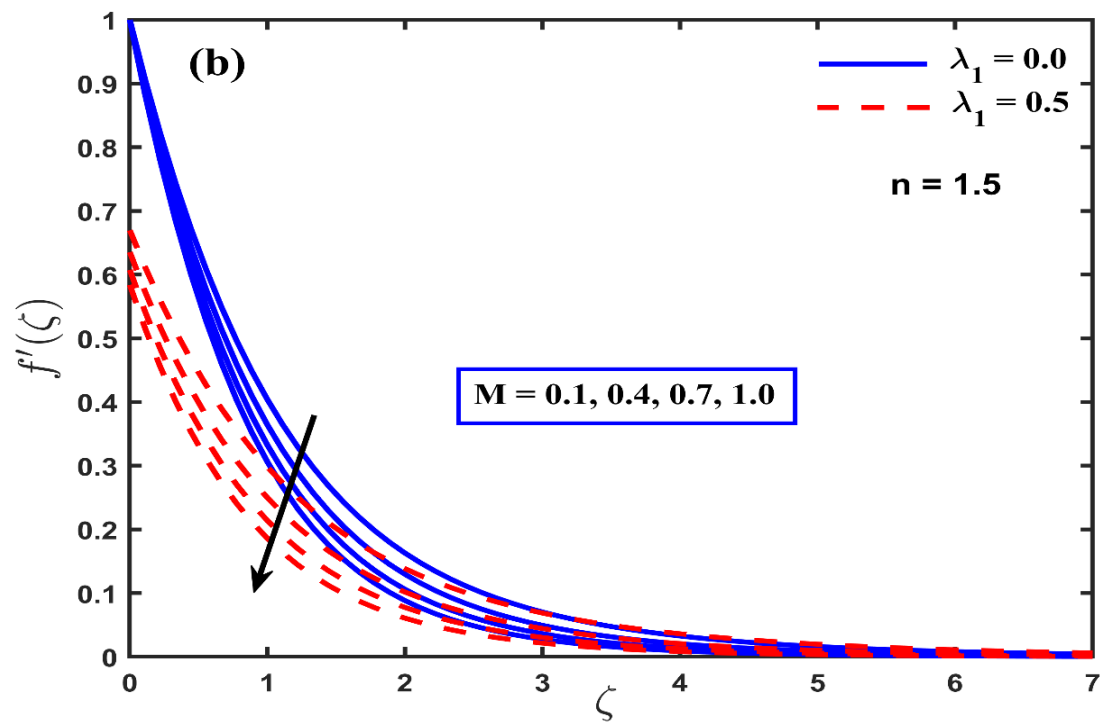
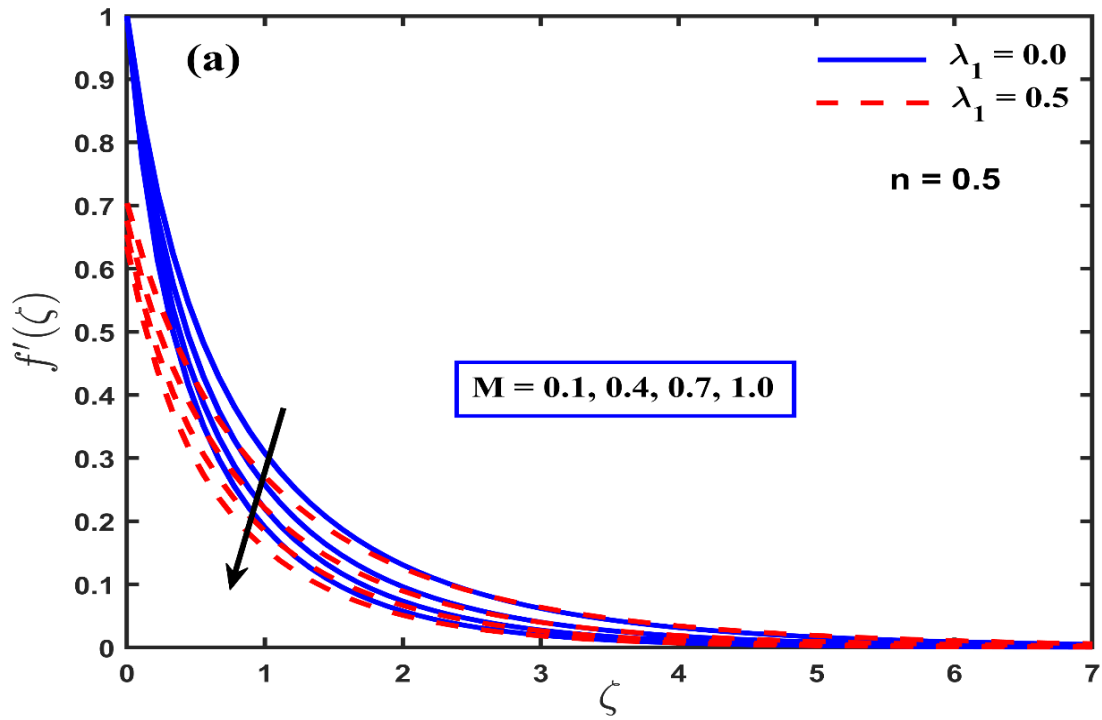


Figure 4.5.1 (a-b) Variation in velocity profile with simultaneous effect of  $M$  and  $\lambda_1$  for both shearing thinning and shear thickening occurrence

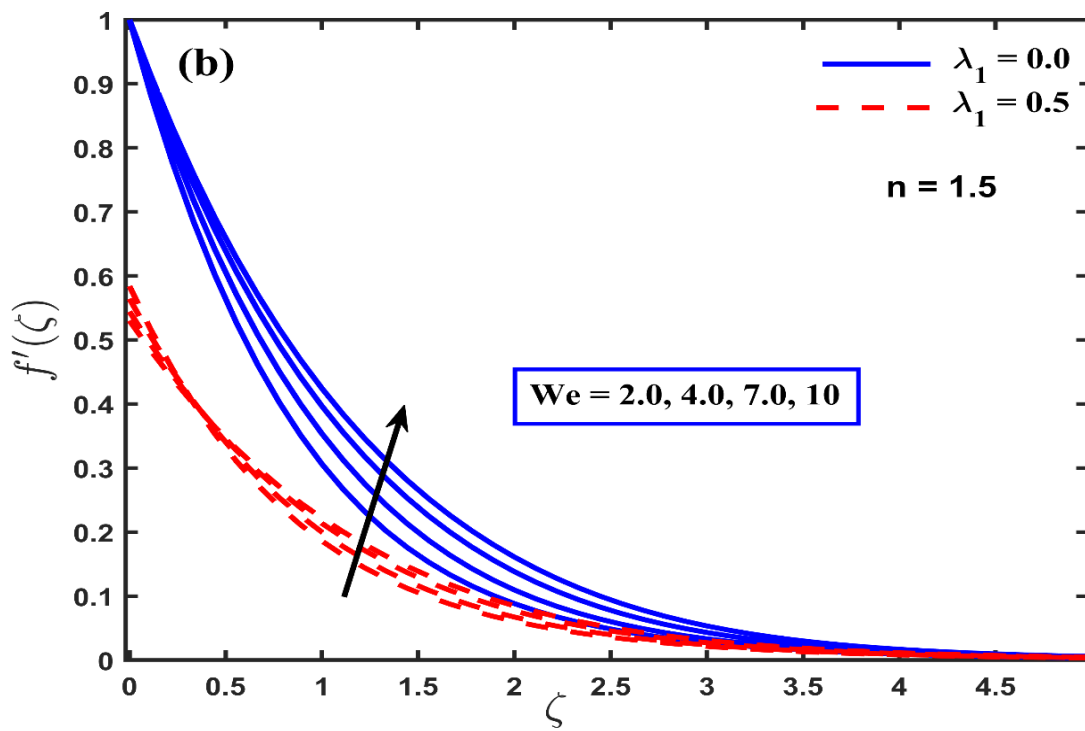
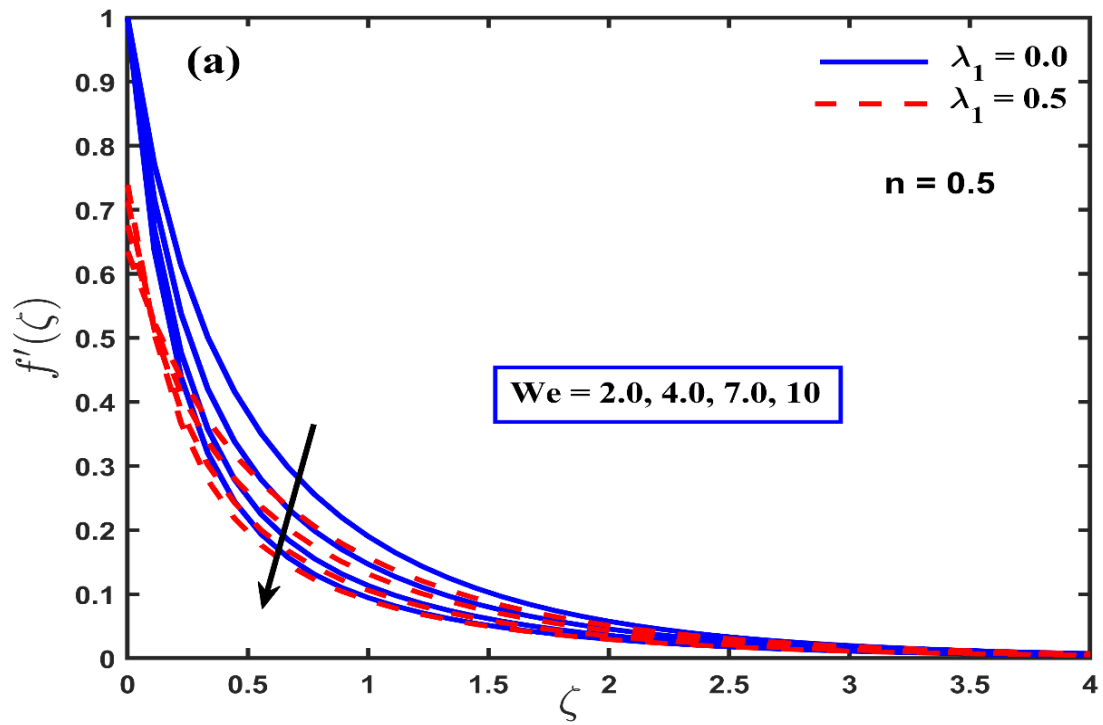


Figure 4.5.2 (a-b) Simultaneous effect of  $We$  and  $\lambda_1$  for both  $n < 1$  and  $n > 1$  on velocity profile

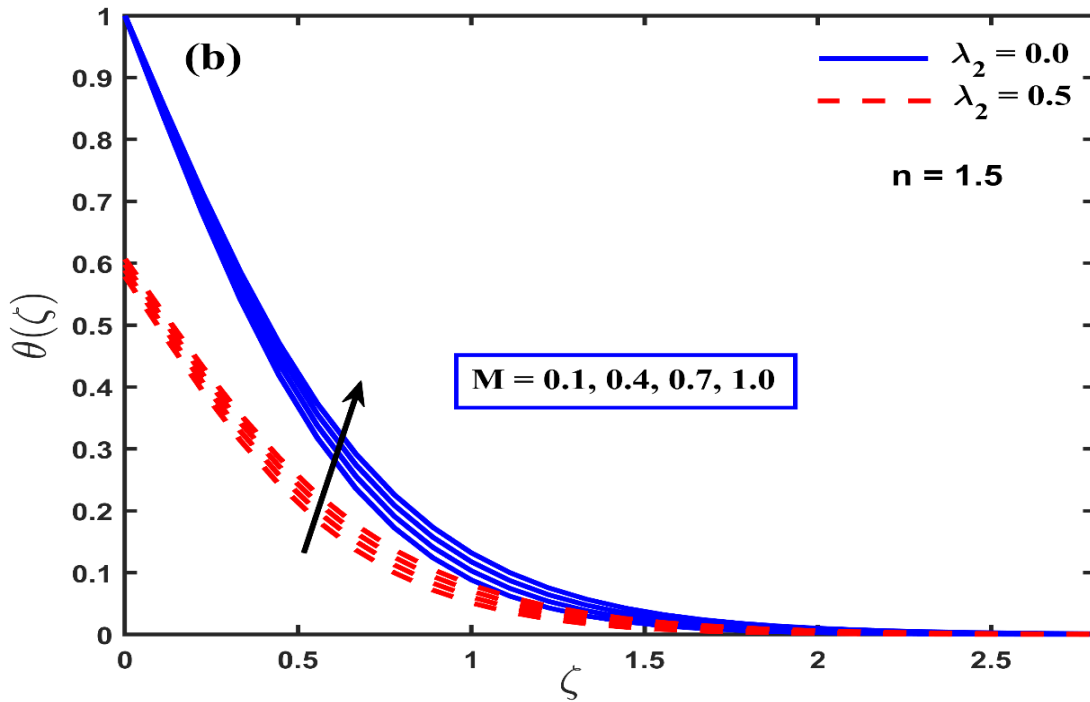
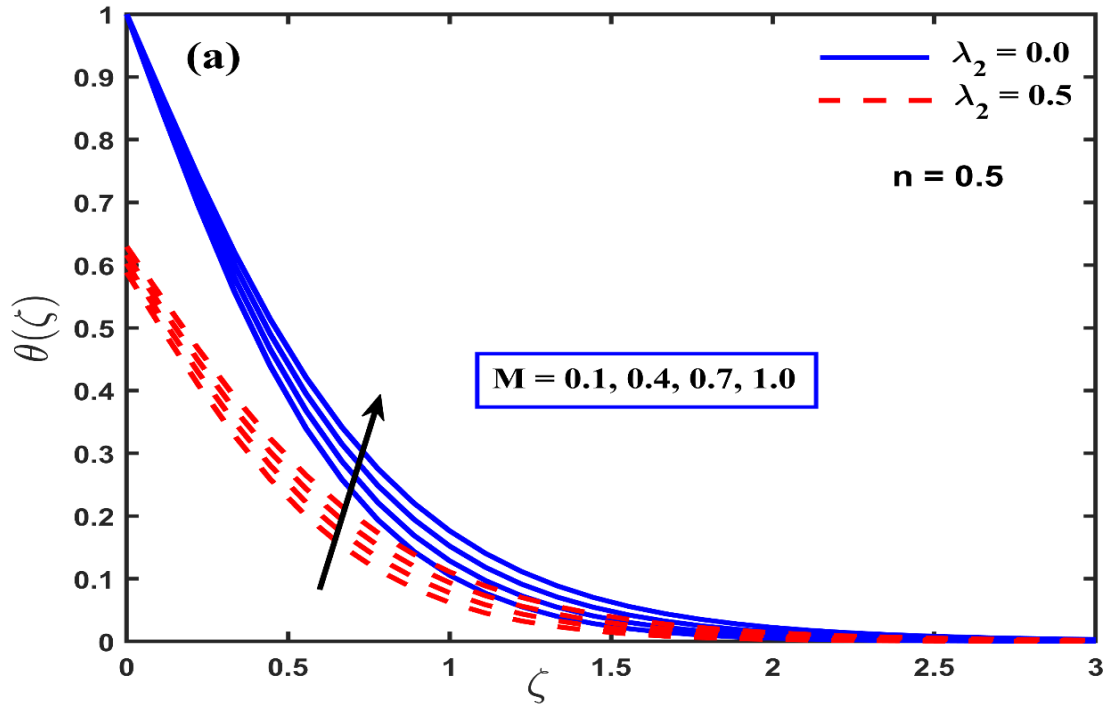


Figure 4.5.3 (a-b) Temperature distribution fluctuation with simultaneous effect of  $M$  and  $\lambda_2$  for both the shearing thinning and shear thickening instances

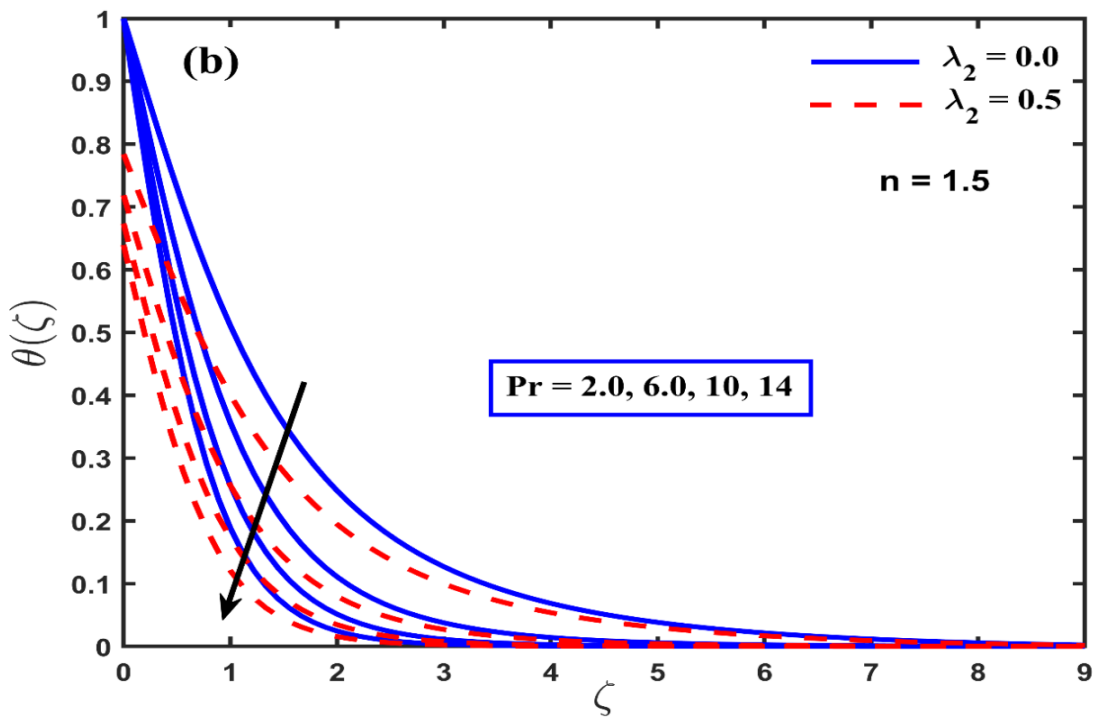
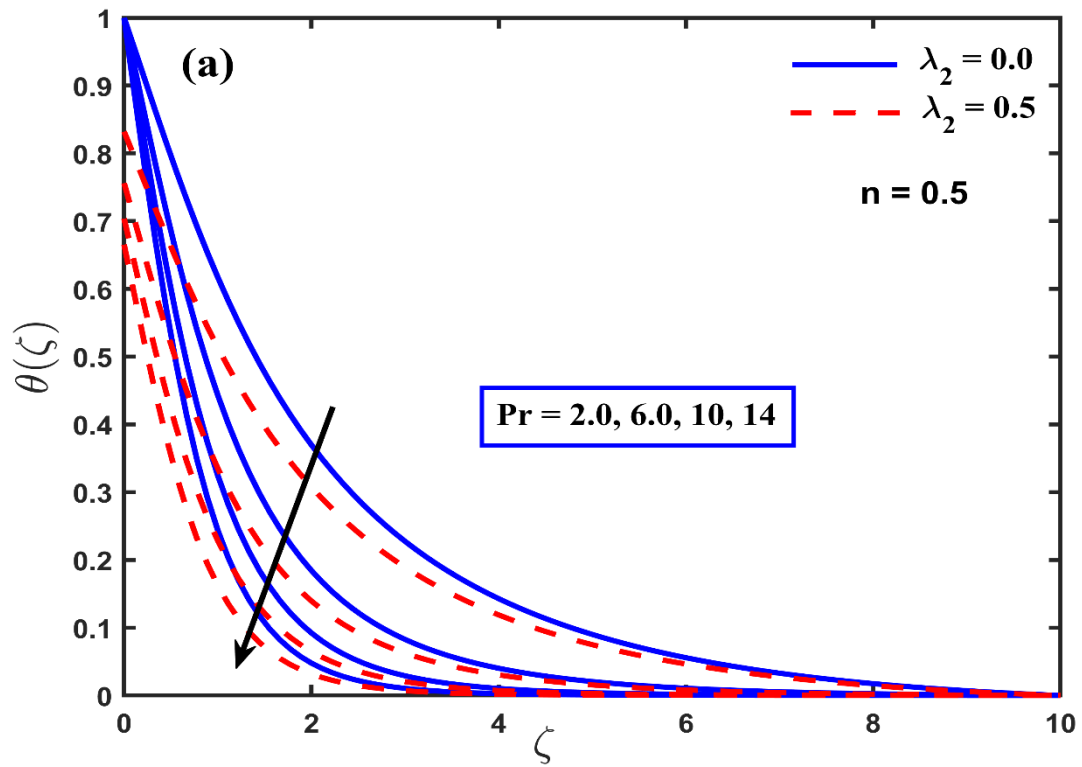


Figure 4.5.4 (a-b) Temperature distribution variation with simultaneous effect of  $Pr$  and  $\lambda_2$  for both shearing thinning and shear thickening situations

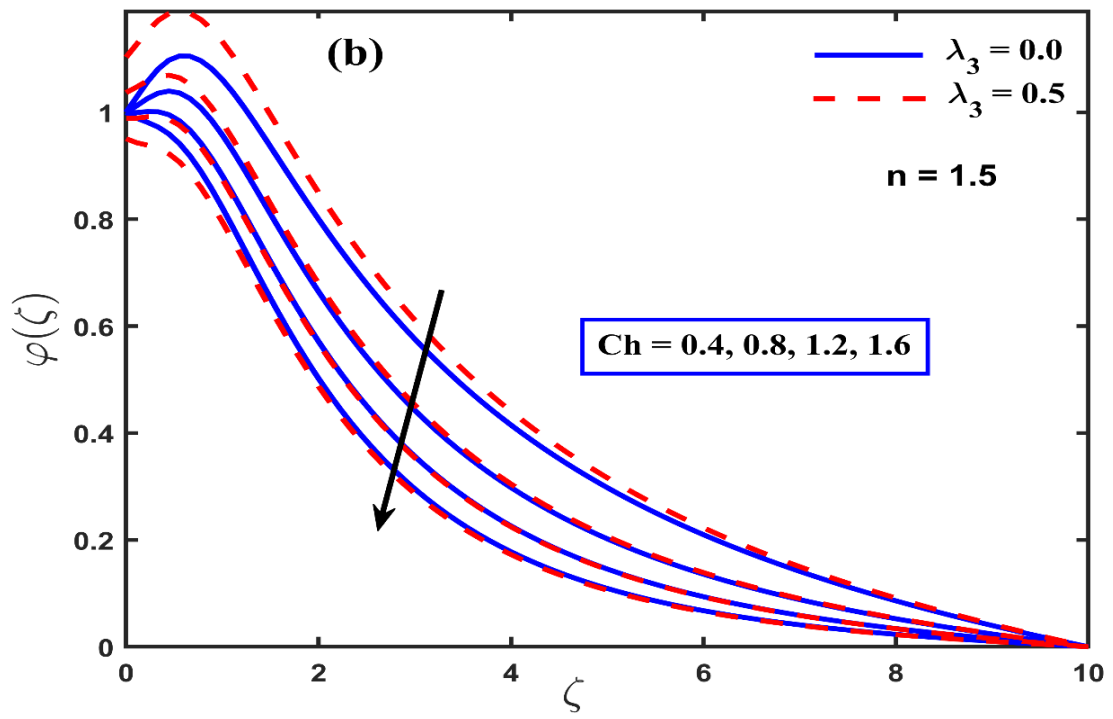
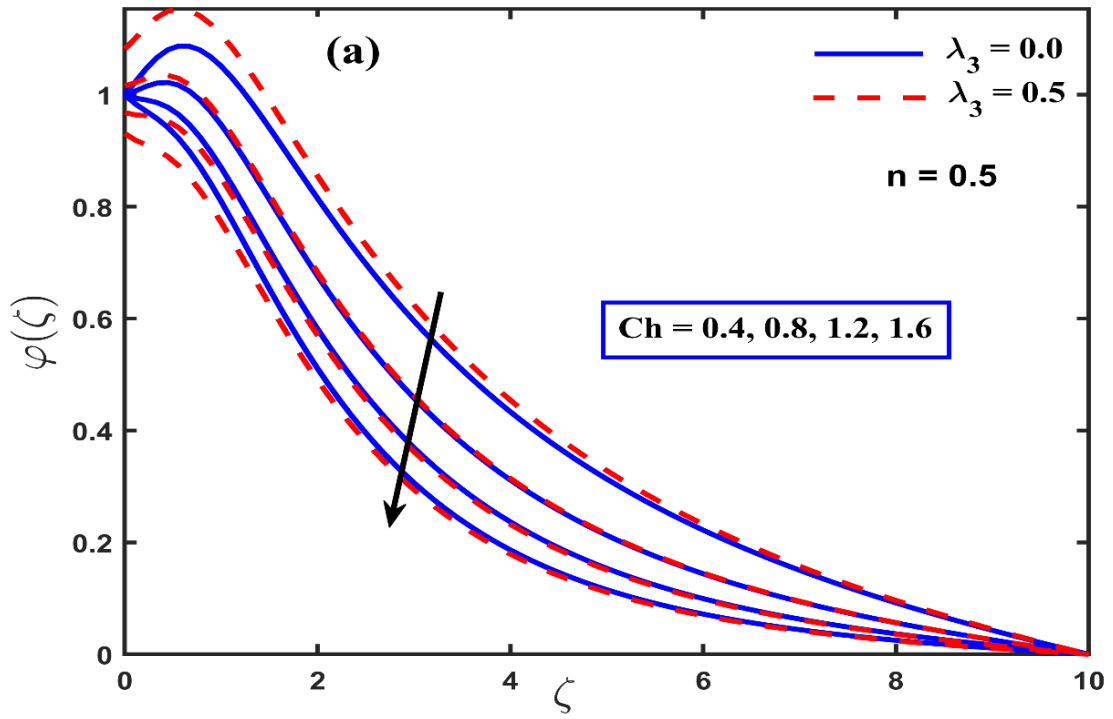


Figure 4.5.5 (a-b) Concentration profile fluctuation against simultaneous effect of  $Ch$  and  $\lambda_3$  for both shearing thinning and the shear thickening cases.

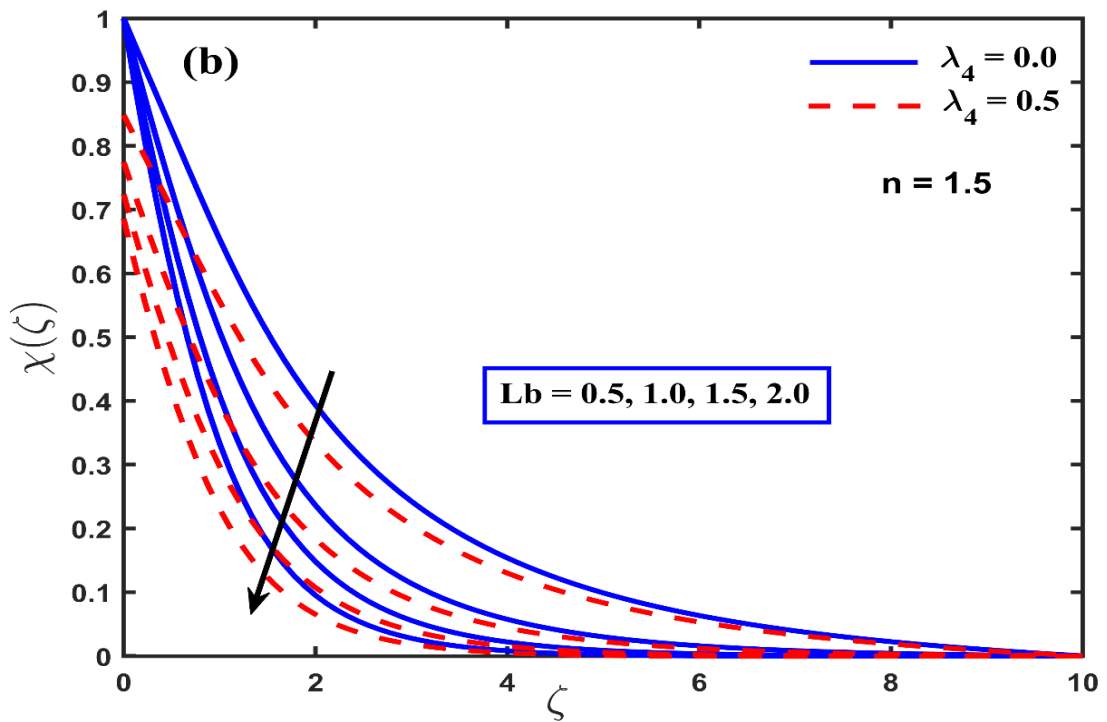
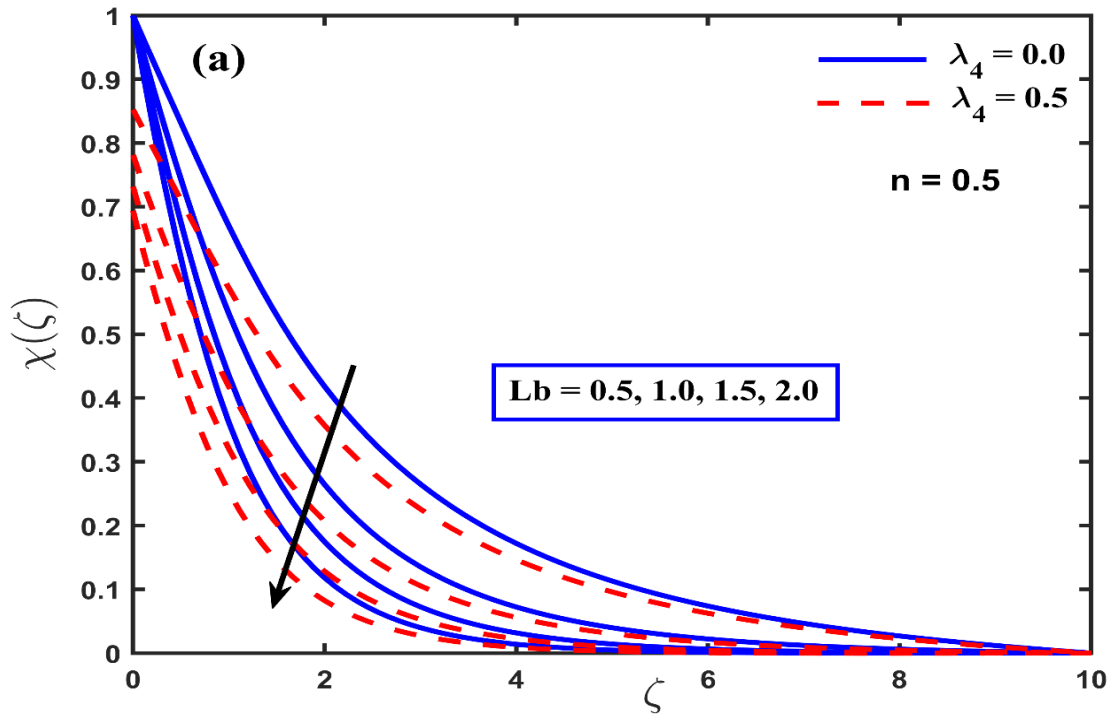


Figure 4.5.6 (a-b) Motile Concentration profile fluctuation with simultaneous effect of  $Lb$  and  $\lambda_4$  for both the shearing thinning and shear thickening situations

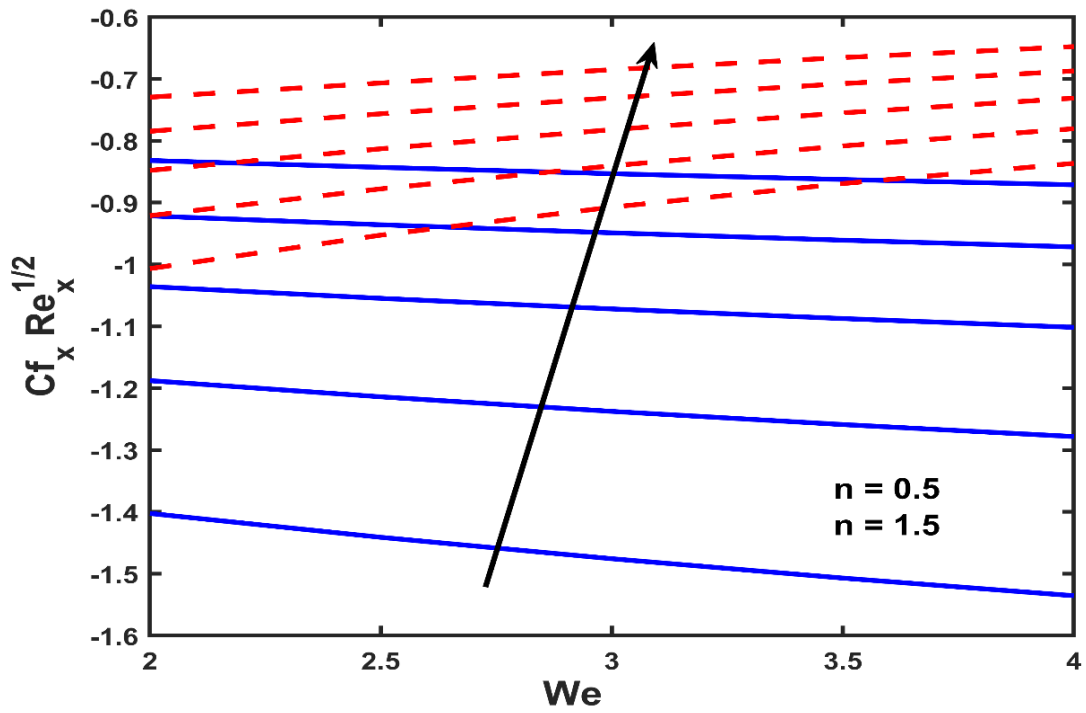
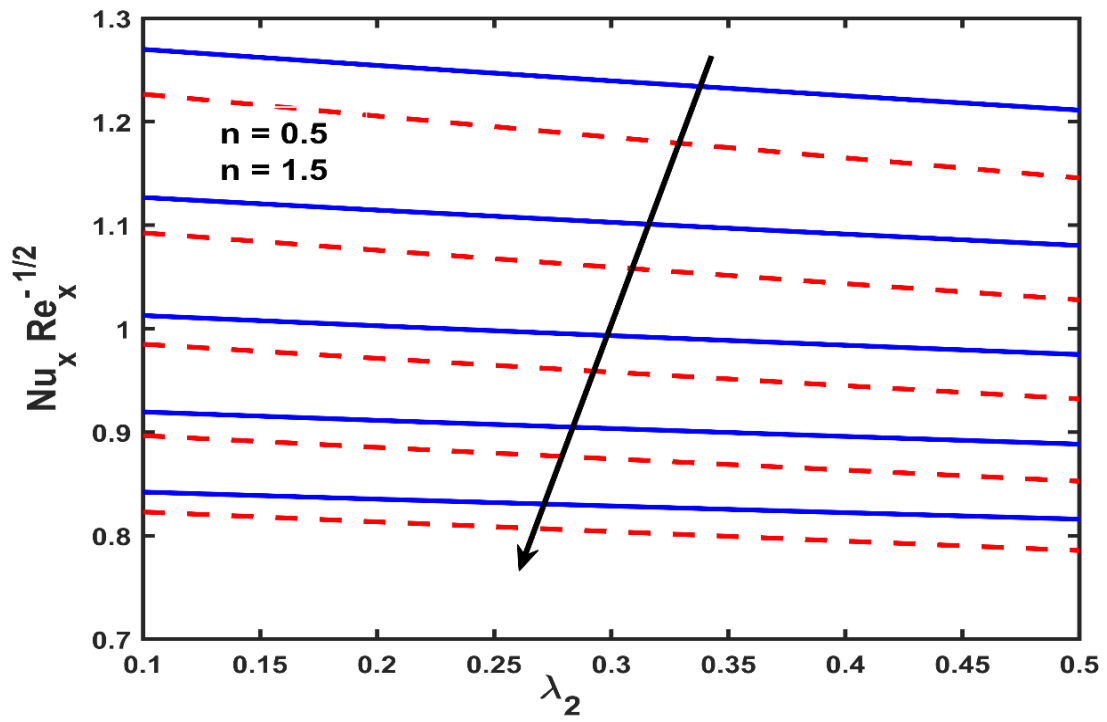


Figure 4.5.7 (a-b) Variation in  $Nu_x$ , and  $Cf_x$  for different values of  $We$  and  $\lambda_2$  for both dilatant and pseudo plastic fluids

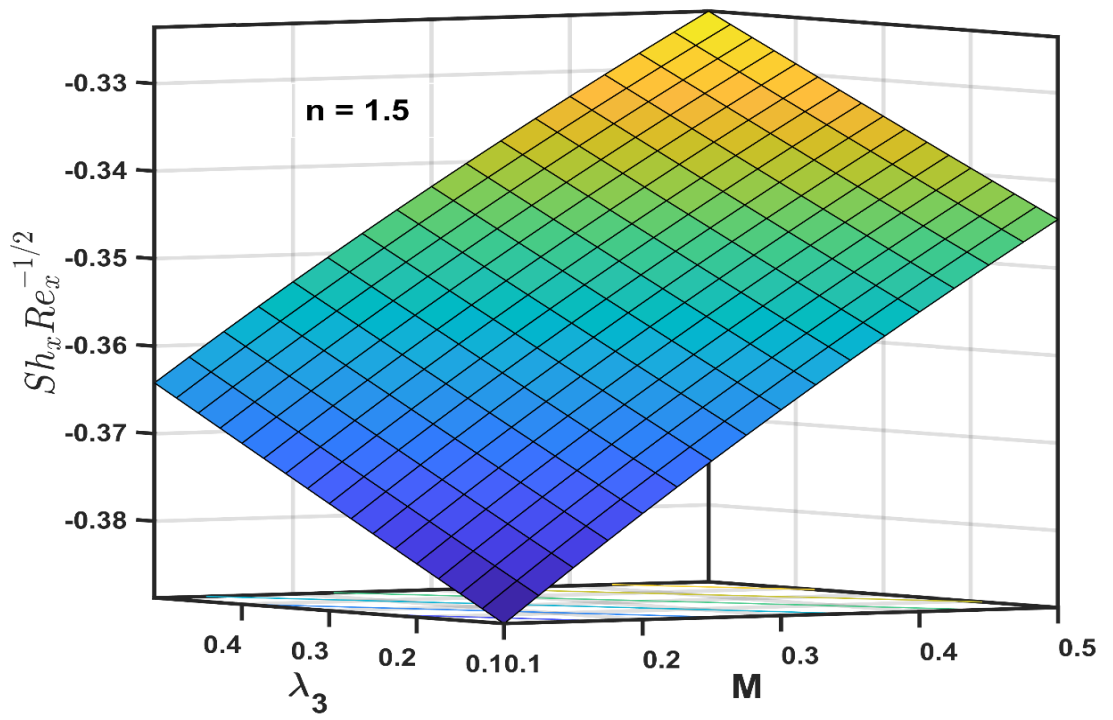
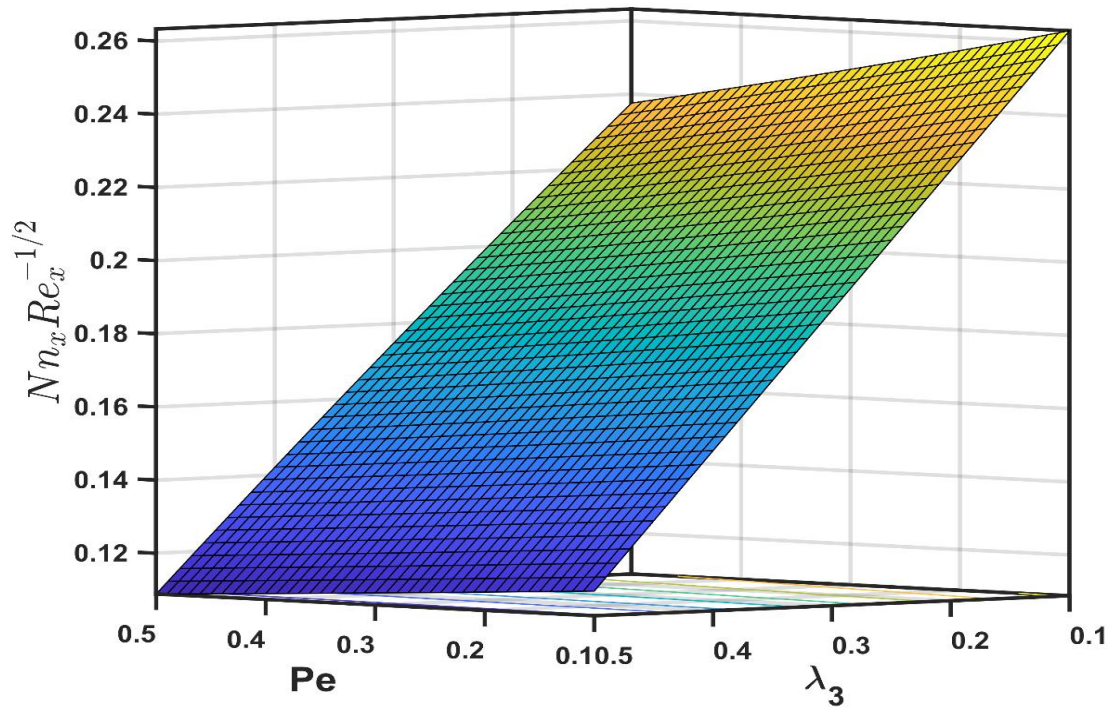


Figure 4.5.8 (a-b) Variation in  $\{Nn_x Re_x^{-\frac{1}{2}x}\}$ , and  $\{Sh_x Re_x^{-\frac{1}{2}x}\}$ , for different values of  $Pe, M$  and  $\lambda_3$  for dilatant fluid and pseudo plastic fluid.

#### 4.6 To compare the effects of heat transfer through copper nanofluid with convective boundary effect via heated Riga plate

The impact of several important parameters on velocity profile, concentration, and thermal profiles are demonstrated in figures (4.6.1-4.6.14) with  $M = 0.01$ , Prandtl number  $Pr = 150.45$ , thermophoretic variable  $N_T = 0.1$ , Biot number  $Bi = 0.1$ , Schmidt number  $= 0.4$ , Brownian motion parameter  $N_B = 0.3$ , Eckert number  $Ec = 0.3$ , Hartmann number  $M_1 = 0.1$ , thermal conductivity parameter  $= 0.3$ , and  $Rd = 0.5$  is the radiation parameter.

Figure (4.6.1) shows the simultaneous effect of the modified Hartmann number  $M_1$  and  $M$  as shown on the velocity distribution. The velocity profile declined with an increase in  $M$ . The relative boundary layer extent and velocity distribution were magnified as  $M_1$  was increased. Higher estimates of  $M_1$  are related to the strength of the external electric field that is stronger than usual, leading to the production of wall parallel Lorentz force. The velocity distribution then gets better.

The thermal buoyancy parameter  $\lambda_1$  is showing its effect in Figure (4.6.2). For the higher values of  $\lambda_1$  the velocity profile was increased. This concludes that the behavior of nanofluid flow increases across the vertical surface due to the prevailing strength of gravity.

Figures (4.6.3-4.6.4) depict the relationship of the magnetic parameter with the concentration and temperature distribution, respectively. As the magnetic parameter's values rise, the thermal boundary layer and concentration layer become thicker. The Lorentz drag, which acts as an opposing force, helps to increase the frictional heating between the fluid layers, which results in the release of energy in the form of heat. As a result, the thermal boundary layer thickens. Figure (4.6.5) illustrates the rise in fluid temperature as the Eckert number  $Ec$  and modified Hartmann number  $M_1$  were increased. The existence of the Eckert number in nanofluid enhances the intensity of thermal energy production, resulting in better temperature distributions and hence thicker thermal layers.

Figure (4.6.6) illustrates that the temperature distribution broadened as the thermal radiation parameter  $Rd$  increased. Figure (4.6.7) depicts the influence of the Brownian motion parameter  $N_B$  on the temperature field with the simultaneous effect of  $M_1$ . It is the disordered movement of suspended particles in a fluid produced by collisions which increase as the system's internal energy increases hence, the thermal field grows due to greater values of  $N_B$ . Figure (4.6.8) explains the behavior of  $N_b$  with the concentration profiles. As Brownian motion parameter magnitude grows, the stride during which nanoparticles move in a random path subject to various velocities increases. As a result, higher  $N_b$  results in decreased concentration profiles and vice versa.

Figures (4.6.9) and (4.6.10) present the effect of thermophoretic parameter  $N_T$  on the temperature and concentration fields. Both the profiles were enhanced due to the higher

thermophoretic variable. Physically, the thermophoretic parameter boosts the convection process in the current flow analysis, causing material elements to migrate from a heated to a cold surface. Kinetic energy is generated when particles are transferred from one surface to another, and the temperature field rises as a result.

The impact of Schmidt number  $Sc$  and  $\lambda_3$  on the concentration field and thermal layer is depicted in figures (4.6.11-4.6.12) respectively. The temperature profile decreased with  $\lambda_3$ , whereas the opposite behavior was seen in the case of the concentration profile with  $Sc$ . The physical significance of the Schmidt number is that the momentum diffusivity rises with  $Sc$ . It reduces the concentration profile by diluting the fluid's molecular diffusivity. Therefore, the concentration of the nanofluid dropped.

Figure (4.6.13) illustrates the observation that the thermal layer becomes a more noticeable characteristic of fluid layers with rising Biot number  $Bi$ . The change in curves of the velocity profile corresponding to various values of the buoyancy ratio parameter  $\lambda_2$  is explained in Figure (4.6.14). For larger values of buoyancy ratio parameter  $\lambda_2$ , both velocity and boundary layer thickness rise. A greater velocity profile is produced by an increase in the concentration buoyancy force caused by an increase in the buoyancy ratio parameter. The variations of important parameters for heat transmission, drag coefficient, and mass transfer are explained in Tables 4.19 and 4.20. Additionally, an increase in  $Ec$ ,  $N_B$ , and  $M$  is accompanied by a decrease in the localized Nusselt number, whereas  $Sh_x$  increased with these parameters. The  $Nu_x$  reinforced with the parameters  $Rd$ , and  $Bi$ . The drag force coefficient was reduced as  $\lambda_1$  increased. Surface plots are used to investigate the impact of effective parameters  $N_t$ ,  $N_b$ ,  $Rd$ ,  $Bi$  on  $Nu_x$  and  $Sh_x$ .

The impact of  $N_t$ ,  $Rd$ ,  $Bi$  and  $N_b$  on the Nusselt number is visualized in figures (4.6.15-4.6.16). As the surface plot is a functional relationship between a designated dependent variable ( $Nu_x$ ), and two independent variables ( $N_b$ ,  $N_b$  or  $Rd$ ,  $Bi$ ). There is an increment in the  $Nu_x$  with a rise in both  $Bi$  and  $Rd$ , whereas it decreases when we increase the value of  $N_t$  and  $N_b$  but the opposite behavior is shown with a decrease in the value of these parameters simultaneously.

The greatest value for local Nusselt is provided by the maximum value of  $Bi$  and  $Rd$ , whereas it decreases as the parameter values drop as shown in figure (4.6.16). Figure (4.6.17) analyses the Sherwood number with effective parameters  $N_t$ ,  $N_b$ . It was found that the Sherwood number declines with an increment in  $N_t$ , whereas the opposite effect is noticed for  $N_b$ . So, when both parameters worked together the  $Sh_x$  became moderate.

**Table 4.19: The variation of  $Nu_x$ , and  $Sh_x$  for  $N_t, N_b, E_c$**

$E_c$	$N_t$	$N_b$	$Nu_x Re_x^{-\frac{1}{2}}$	$Sh_x Re_x^{-\frac{1}{2}}$
0.1	0.2	0.3	0.269495	0.017084
0.3	-	-	0.247896	0.030569
0.5	-	-	0.225844	0.044336
0.2	0.2	0.3	0.258750	0.023793
-	0.3	-	0.258424	-0.026446
-	0.5	-	0.257734	-0.126245
-	0.7	-	0.256986	-0.225046
0.2	0.2	0.1	0.264615	-0.189596
-	-	0.4	0.254912	0.050892
-	-	0.6	0.244483	0.078847
-	-	0.7	0.237306	0.087354

**Table 4.20: The variation of  $Nu_x, Cf_x$  and  $Sh_x$  for  $\lambda, Rd, Bi, M$**

$M$	$\lambda$	$R_d$	$Bi$	$Nu_x Re_x^{-\frac{1}{2}}$	$\frac{-1}{2} Cf_x Re_x^{-\frac{1}{2}}$	$Sh_x Re_x^{-\frac{1}{2}}$
0	0.2	0.5	0.2	0.281470	0.979396	-0.038852
0.1	-	-	-	0.271511	1.001847	-0.034269
0.5	-	-	-	0.235195	1.083861	-0.017071
0.7	-	-	-	0.218747	1.121052	-0.009132
0.2	0.2	0.5	0.2	0.261939	1.023443	-0.029795
-	0.4	-	-	0.264232	0.810002	-0.043344
-	0.7	-	-	0.266164	0.623996	-0.056729
-	1.0	-	-	0.267249	0.510861	-0.065875
0.2	0.2	0.1	0.2	0.195584	1.023443	-0.028931
-	-	0.3	-	0.228775	1.023443	-0.029435
-	-	0.5	-	0.261939	1.023443	-0.029795
-	-	0.7	-	0.2950721	1.023443	-0.030055
0.2	0.2	0.5	0.05	0.067253	1.023443	0.089807
-	-	-	0.1	0.133310	1.023443	0.049222
-	-	-	0.3	0.386078	1.023443	-0.106043
-	-	-	0.5	0.621619	1.023443	-0.250682

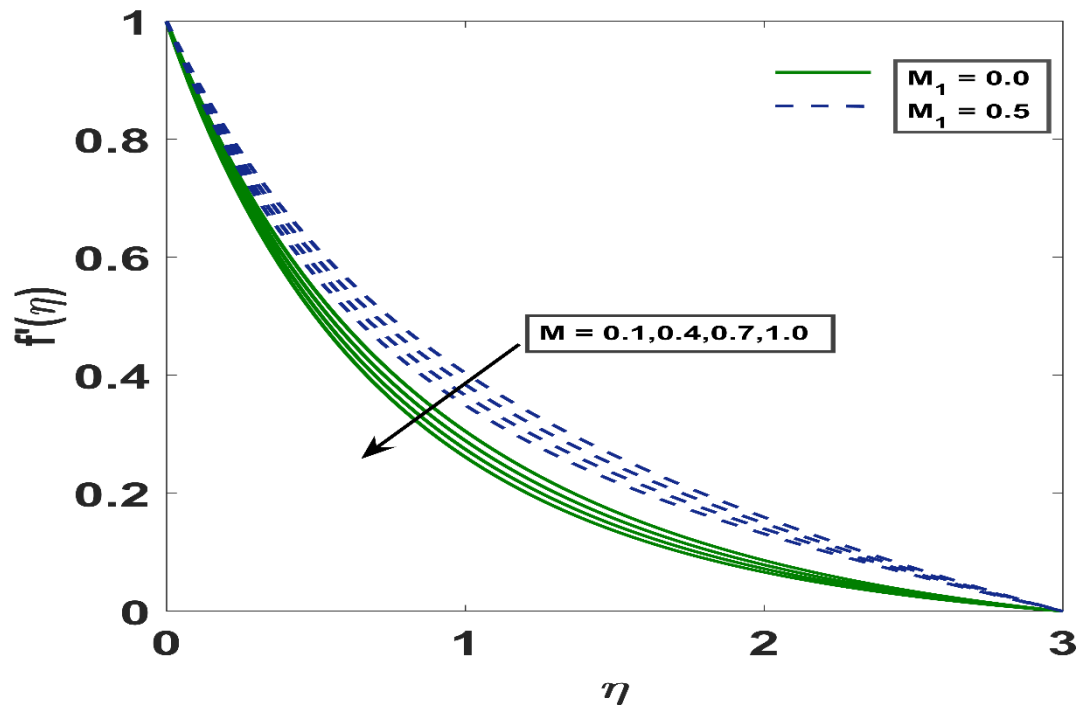


Figure 4.6.1 Velocity profiles with varying values of  $M$  with  $M_1$

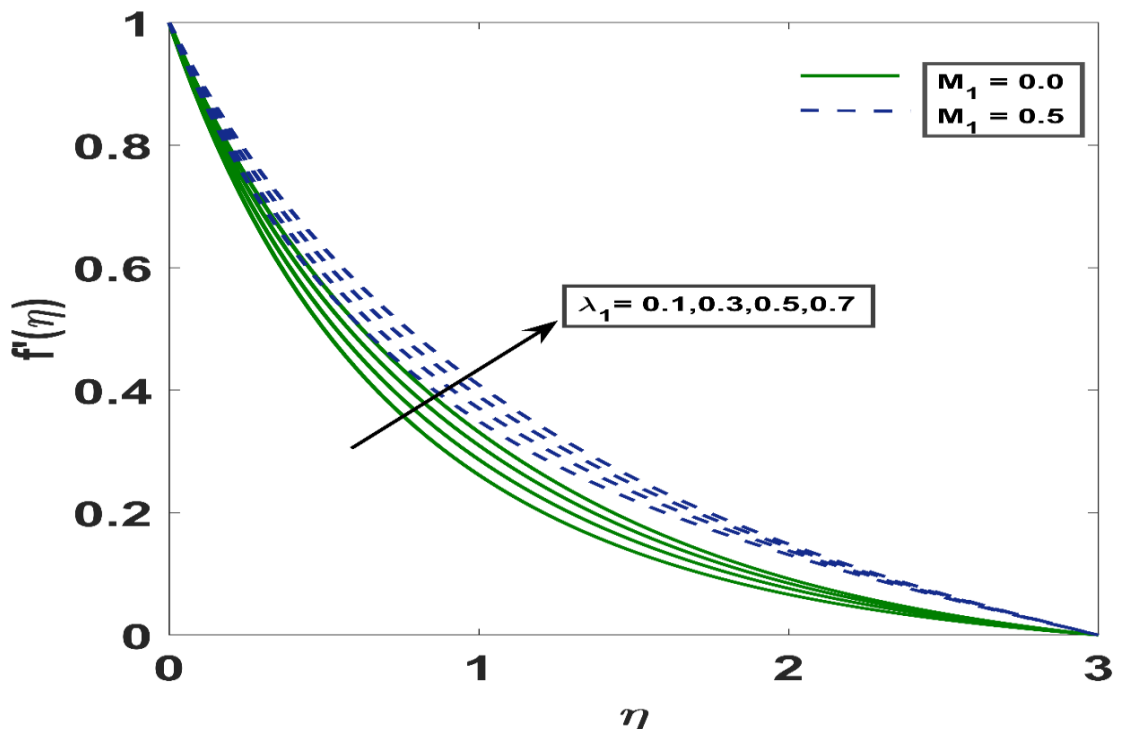


Figure 4.6.2 Velocity profiles with varying values of  $\lambda_1$  with  $M_1$

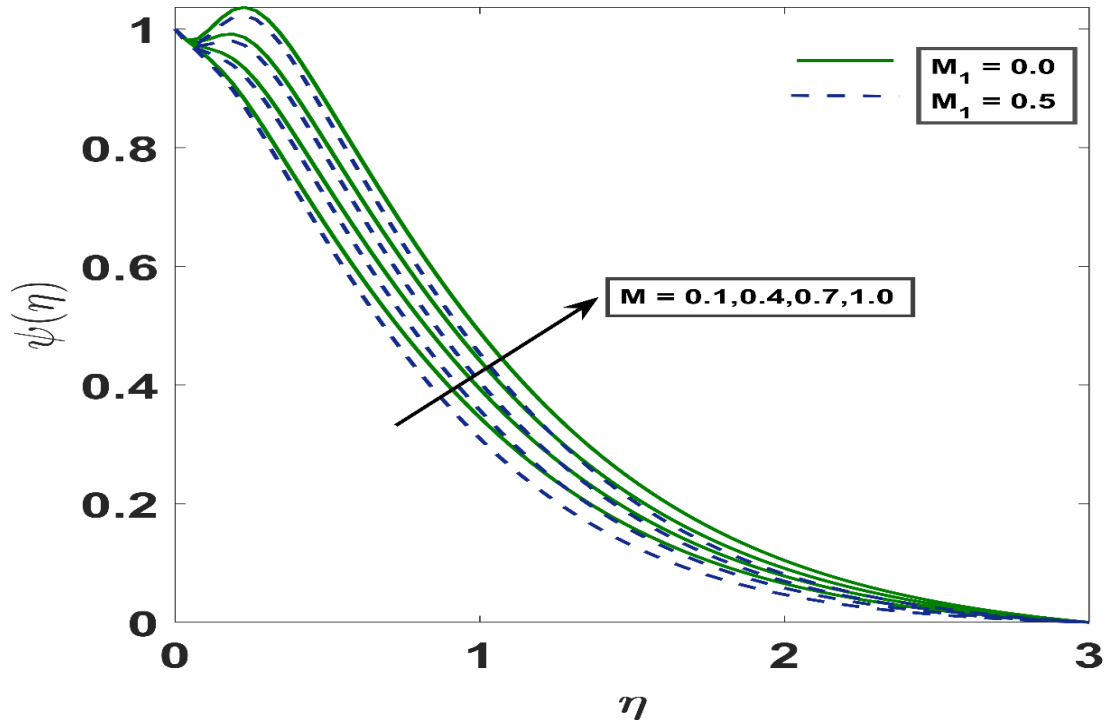


Figure 4.6.3 Variation in concentration profile with  $M_1$  at different values of  $M$

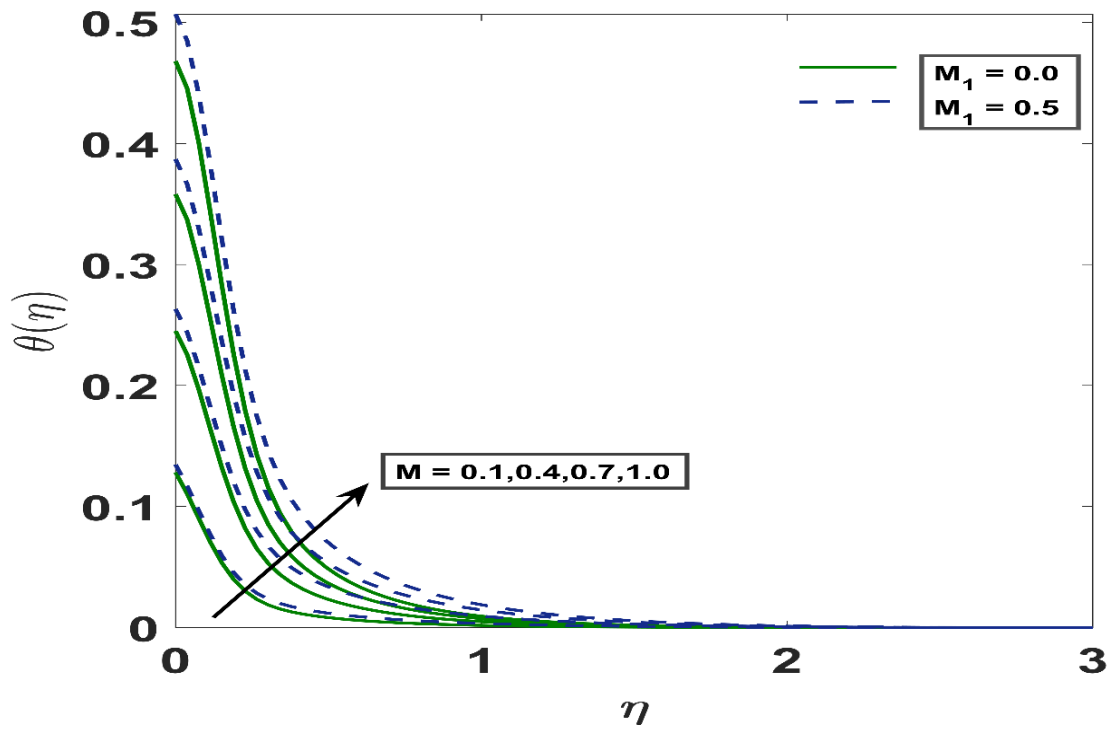


Figure 4.6.4 Variation in temperature profiles with  $M_1$  at different values of  $M$

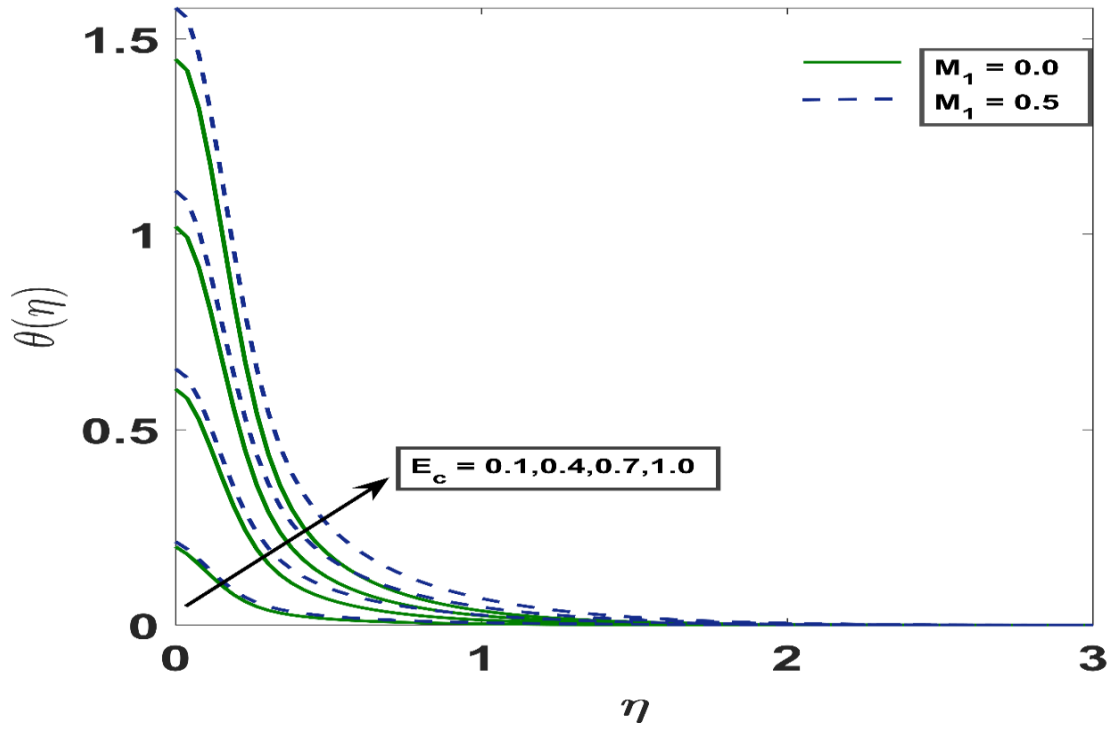


Figure 4.6.5 Variation in temperature profiles with  $M_1$  at different values of  $Ec$

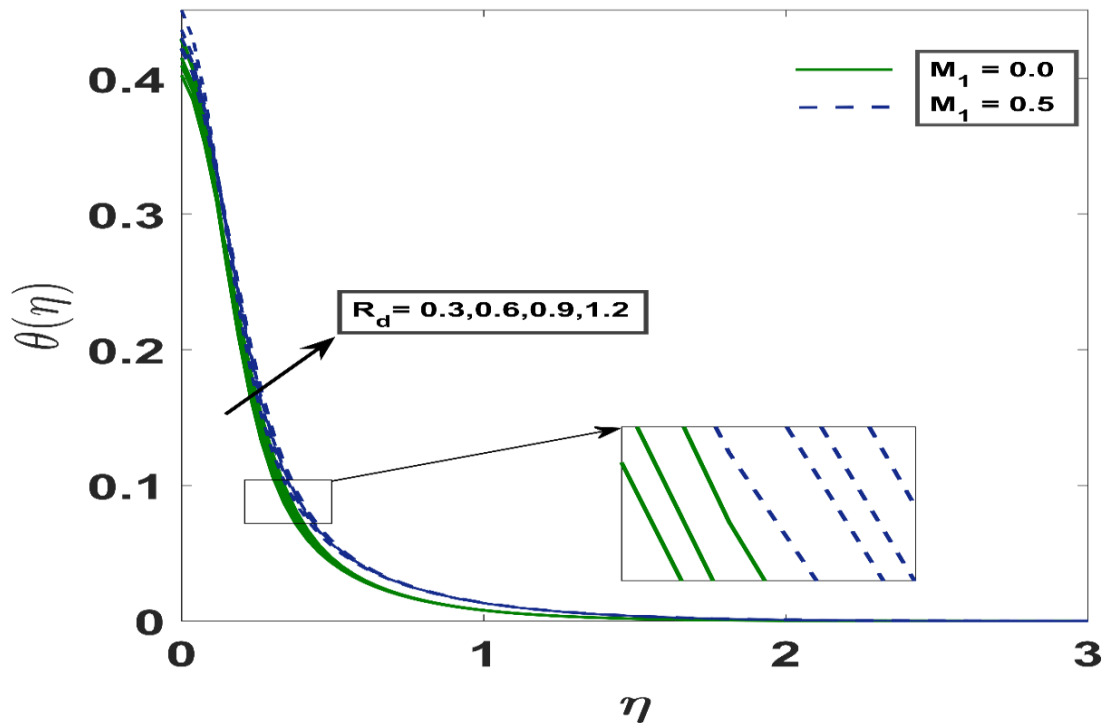


Figure 4.6.6 Variation in temperature profiles with  $M_1$  at different values of  $R_d$

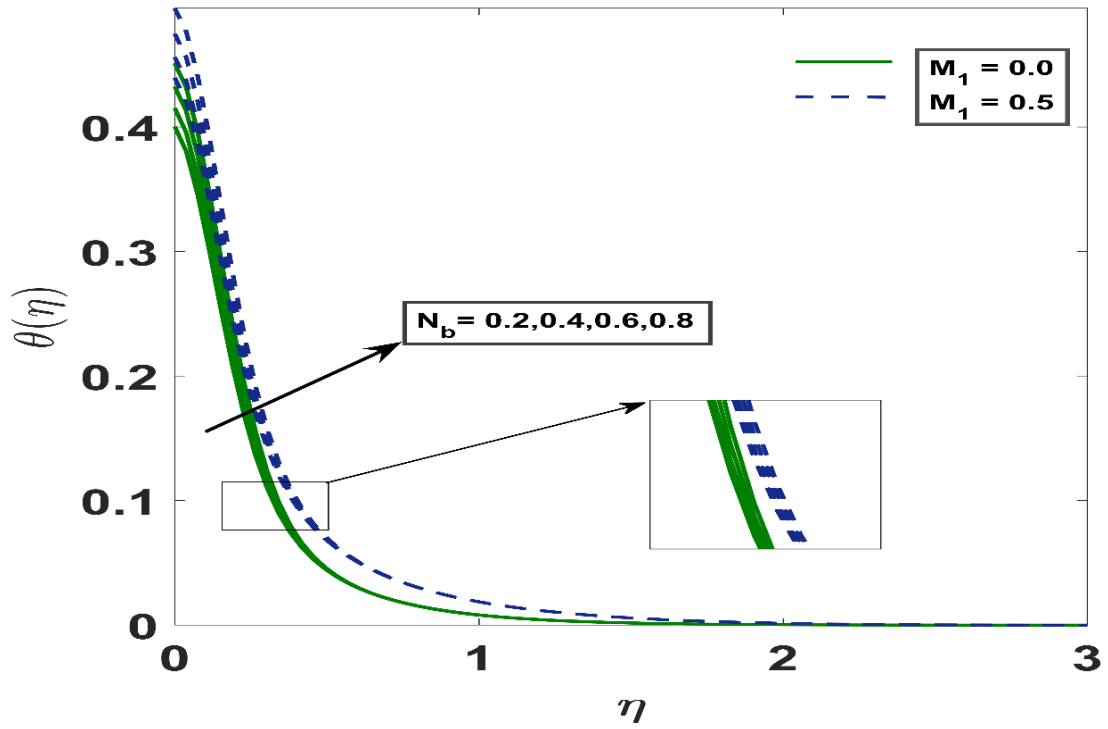


Figure 4.6.7 Variation in temperature profiles with  $M_1$  at different values of  $N_b$

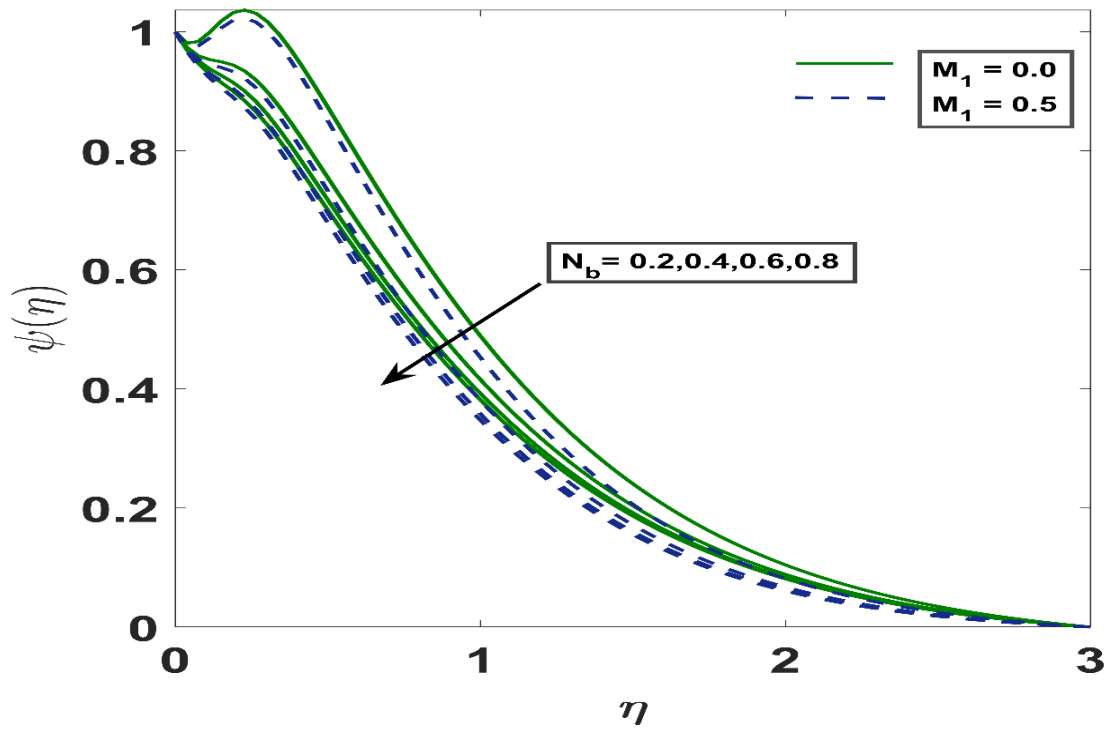


Figure 4.6.8 Variation in concentration profiles with  $M_1$  at different values of  $N_b$

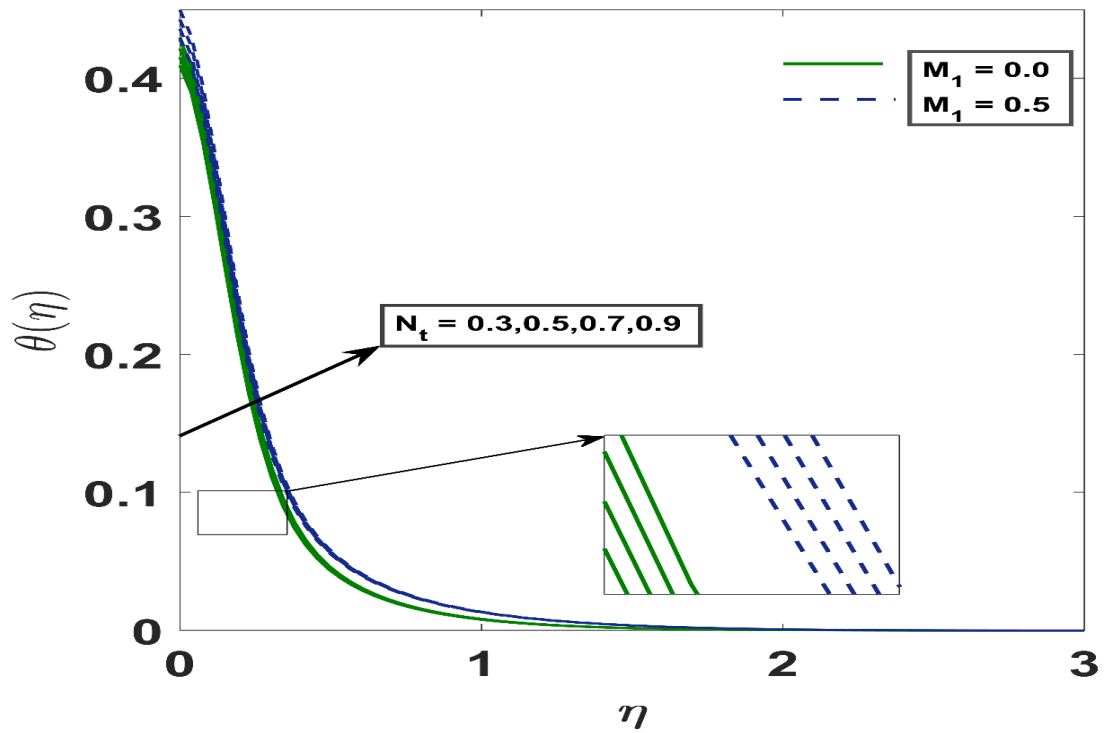


Figure 4.6.9 Variation in temperature profile with  $M_1$  at different values of  $N_t$ .

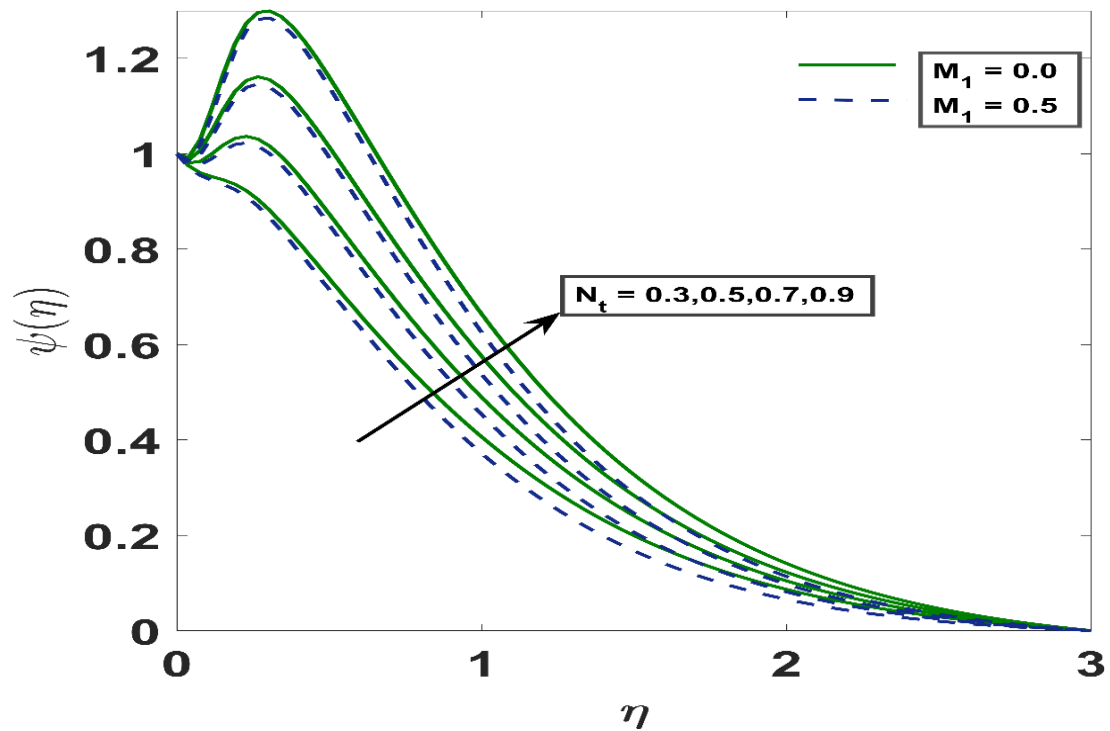


Figure 4.6.10 Variation in concentration profiles with  $M_1$  at different values of  $N_t$

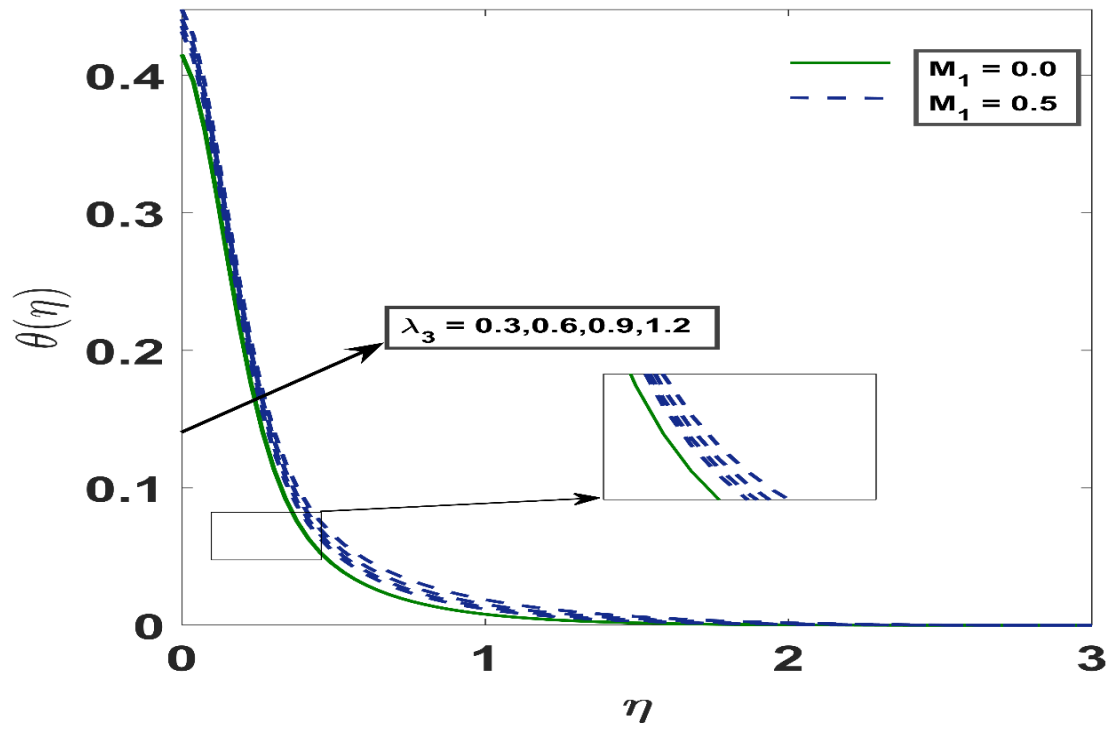


Figure 4.6.11 Fluctuation of temperature profiles along with variation of  $\lambda_3$  and  $M_1$

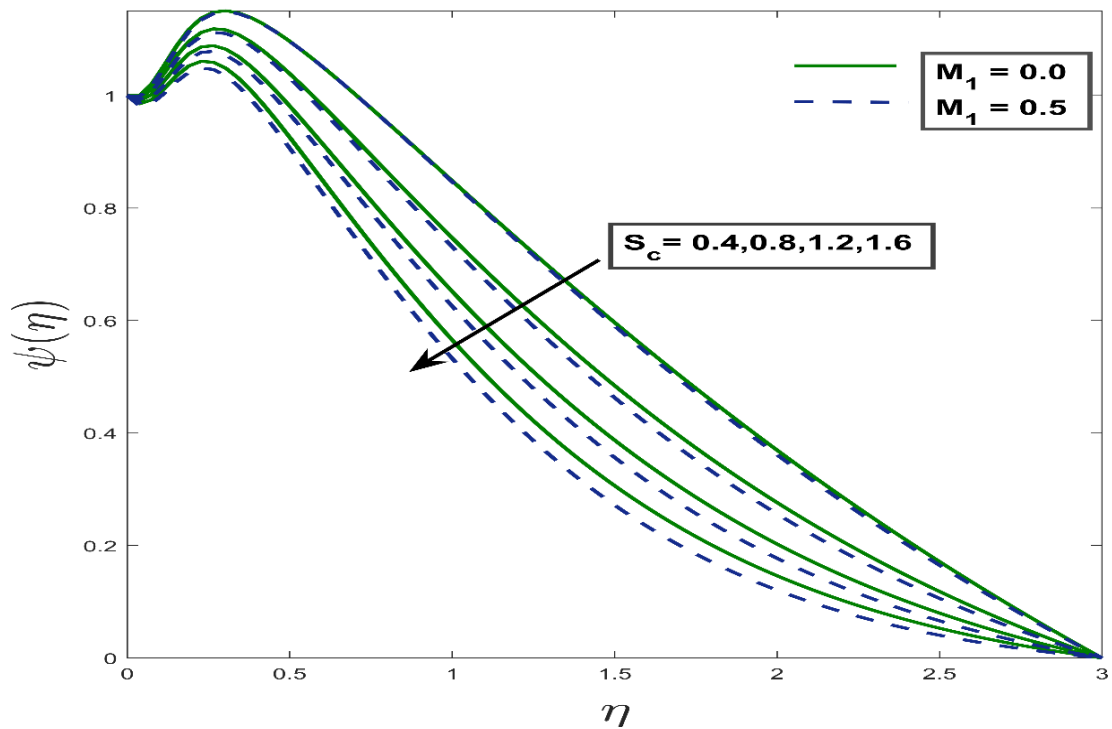


Figure 4.6.12 Fluctuation of volume fraction profiles along with variation of  $S_c$  and  $M_1$

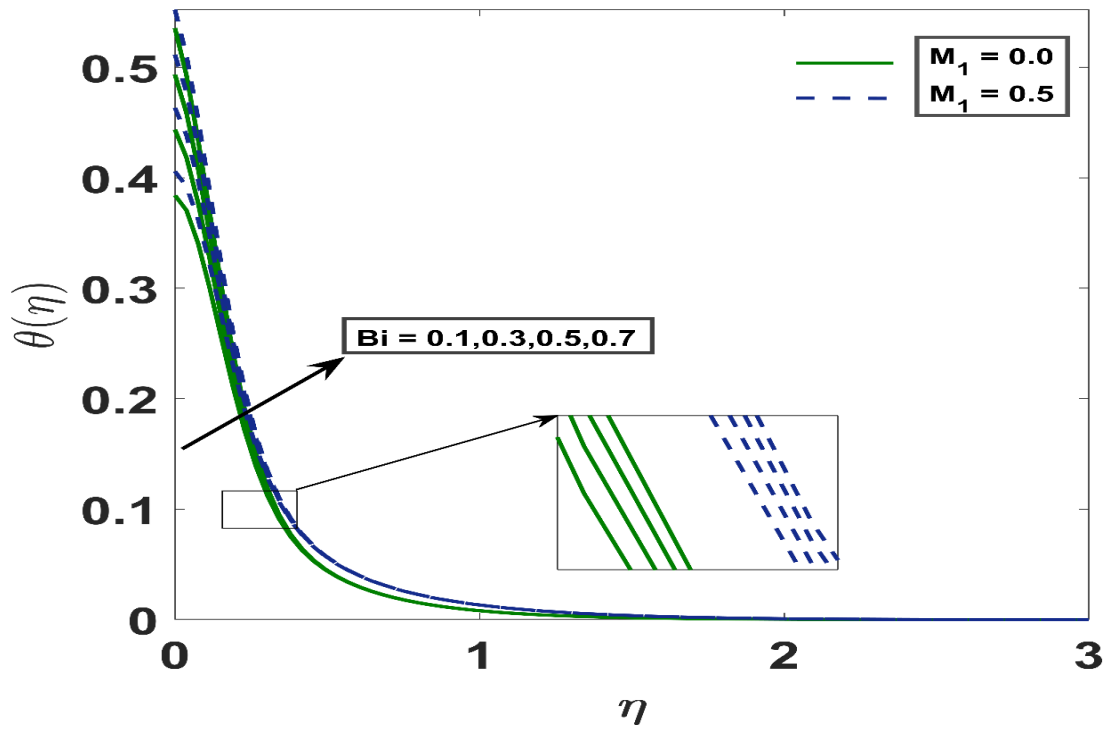


Figure 4.6.13 Fluctuation of temperature profiles along with variation of  $Bi$  and  $M_1$ .

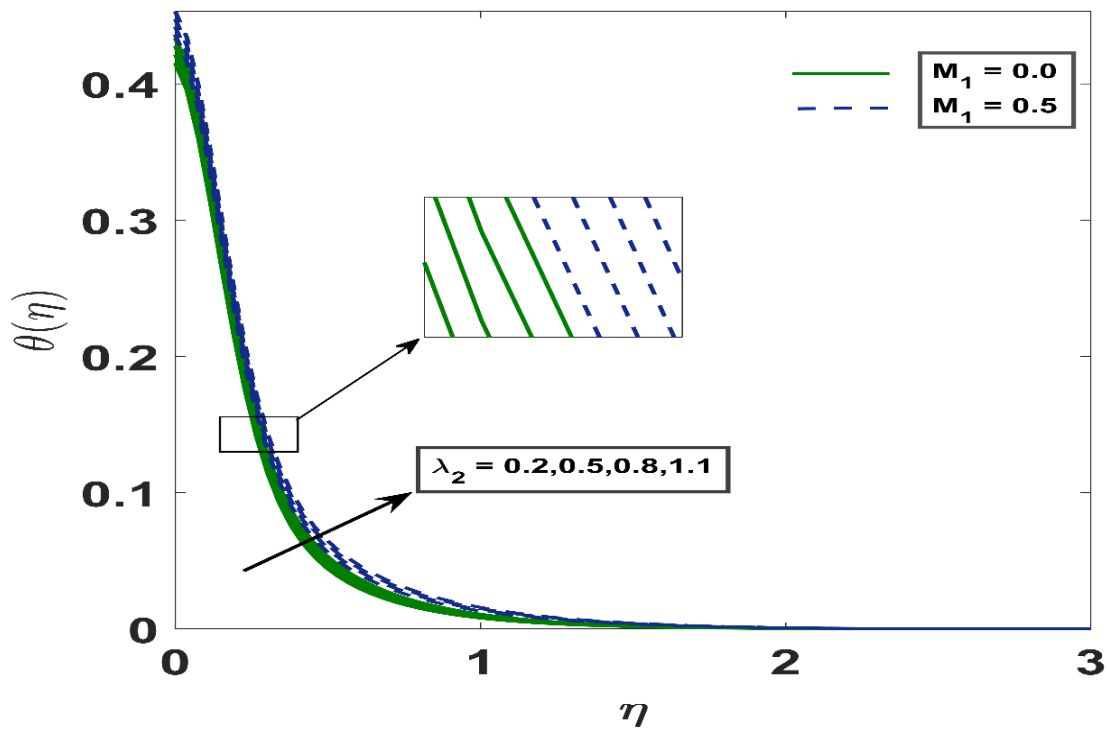


Figure 4.6.14 Fluctuation of temperature profiles along with variation of  $\lambda_2$  and  $M_1$ .

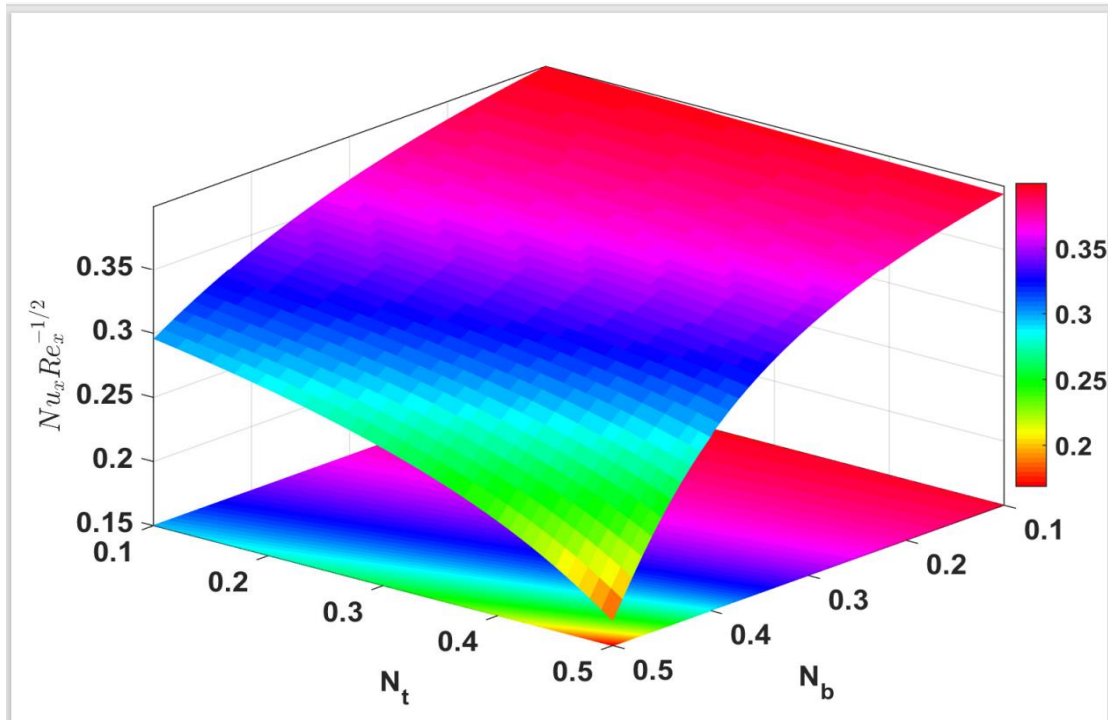


Figure 4.6.15 Fluctuation of  $Nu_x$  along with  $N_t$ ,  $N_b$

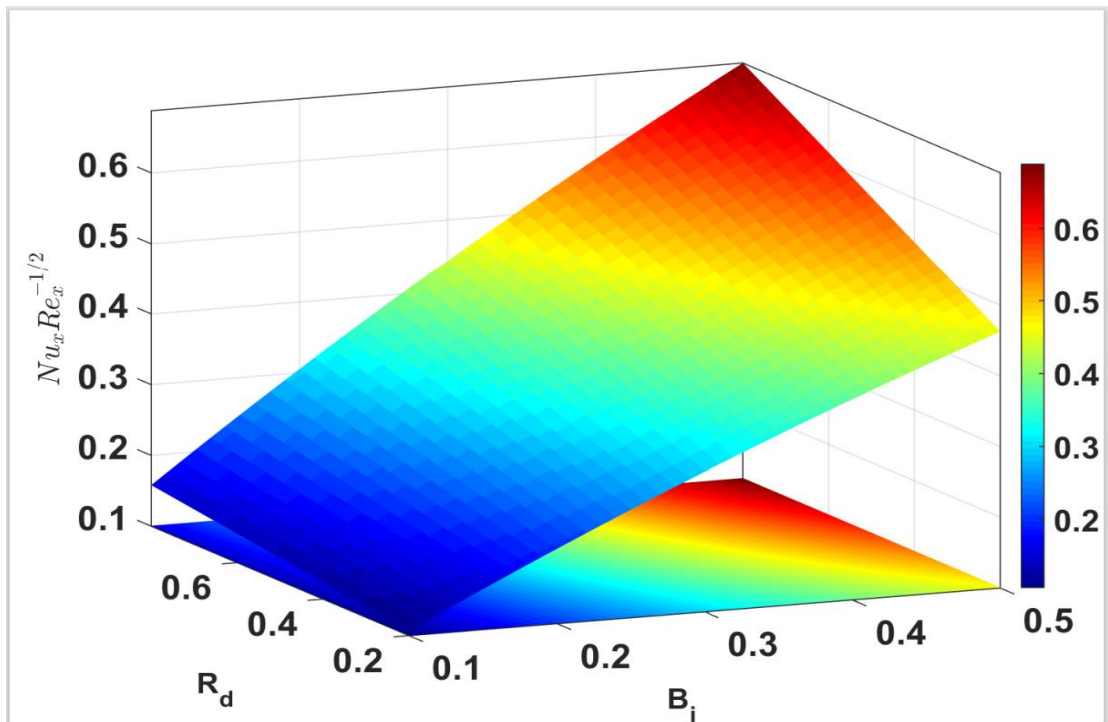
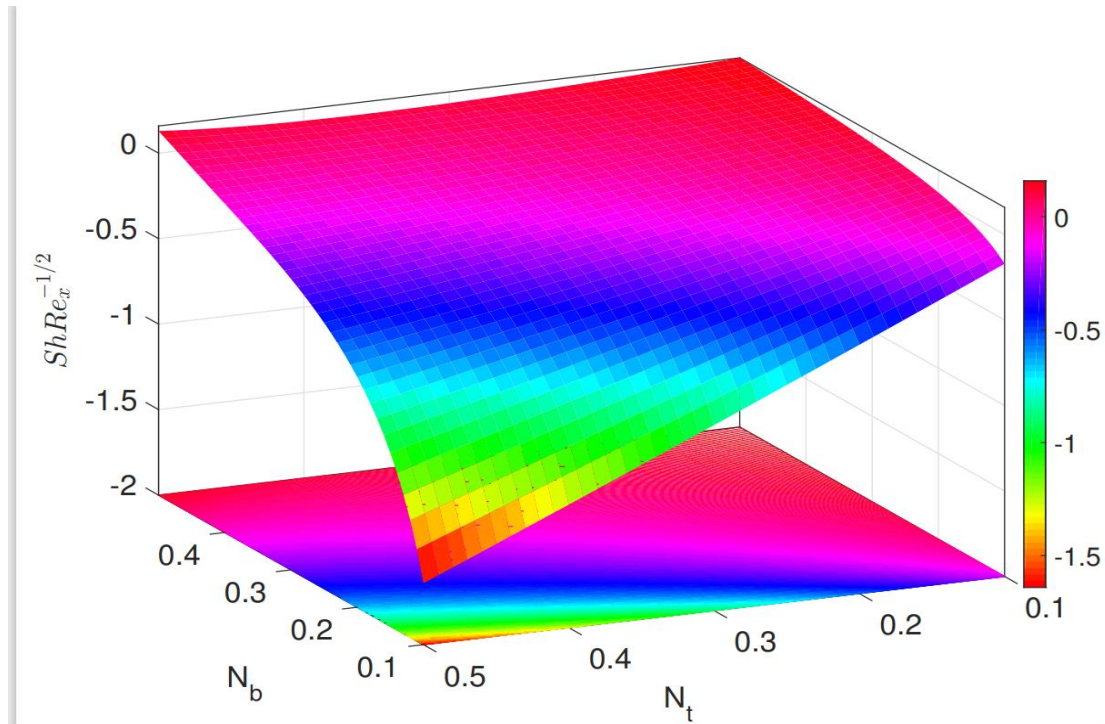


Figure 4.6.16 Fluctuation of  $Nu_x$  along with  $R_d$ ,  $B_i$



**Figure 4.6.17 Sherwood number's fluctuation with variation of  $N_t$  and  $N_b$**

#### **4.7.1 To compare the effects of heat transfer analysis of thermally convective nanofluid flow over the stretching cylinder and stretching sheet**

The stimulus of various parameters has an impact on momentum profile  $F(\xi)$ , thermal distribution  $\theta(\xi)$ , nanoparticle concentration profile  $\psi(\xi)$  which were investigated for both stretching cylinder and a flat sheet scenario, as revealed in figures 4.7.1-4.7.10. The graphical analysis was performed for flow confined by stretched cylinder ( $\Gamma = 0.5$ ) and flow due to flat plate ( $\Gamma = 0.0$ ). To accomplish this purpose, figures and tables are presented.

Figure (4.7.1) reveals magnetic field qualities on the velocity profile. From the given diagram it was made clear that the dimensionless velocity had fallen as the magnetic parameter was increased for both surfaces. The increasing change in  $F'$  was comparatively more progressive for flat plate configuration. The Lorentz force is induced by the presence of a transverse magnetic field in an electrically conducting liquid, which slows the fluid's flow within the boundary layer area.

Figures (4.7.2-4.7.3) depict the relationship between the magnetic parameter with the concentration and temperature distributions for both stretchable cylinder and sheet cases. As the magnetic parameter's values were raised, the thermal boundary layer and concentration layer became thicker. The Lorentz drag, which acts as an opposing force, helps to increase the frictional heating between the fluid layers, which results in the release of energy in the form of heat. As a result, the thermal boundary layer thickened.

The impact of the mixed convection parameter ( $\lambda$ ) on the velocity profile and temperature profile is shown in the figure (4.7.4) and figure (4.7.5). The velocity profile was enhanced with ( $\lambda$ ), whereas the thermal layer decreased for both sheet and cylinder surfaces. The increasing change in  $F'$  was comparatively more progressive for flat plate configuration. Physically the ratio of inertial to buoyant forces is the mixed convection parameter, an increase in ( $\lambda$ ) correlates to increased thermal buoyancy forces, which improve velocity profiles.

The Figure (4.7.6) depicts the dropping impact of the velocity profile with the Prandtl number ( $Pr$ ) for both stretching cylinder and a flat sheet scenario. The higher the ( $Pr$ ), the more viscous the fluid, causing the boundary layer to thicken, reducing shear stress and therefore retarding the nanofluid's flow. Hence, velocity profile decreased.

Figure (4.7.7), describes the influence of Prandtl number ( $Pr$ ) on nanoparticle temperature. Again, results were prepared by stretched cylinder ( $\Gamma = 0.5$ ) and flow due to flat plate ( $\Gamma = 0.0$ ). The Prandtl number is a non-dimension quantity, defined as the ratio of two quantities' momentum and thermal diffusivity. Thermal diffusivity diminishes when  $Pr$  rises, which further causes a drop-in boundary layer thickness and temperature.

Figure (4.7.8-4.7.9), illustrates the observation that the thermal layer and concentration profile became more noticeable characteristic of fluid layers with rising Biot number  $Bi$  both stretchable cylinder and sheet cases. Both profiles showed enhancement with  $Bi$ . Convective heating occurs at the sheet more frequently and intensifies as  $Bi$  increases, increasing the temperature. The thermal influence can reach the quiescent fluid if the variation is more significant. In addition, as the fluid temperature rises, the stretched sheet's right-hand side Biot number increases, decreasing its thermal resistance so, convective heat transfer was enhanced.

A decrease in concentration profile was observed with significant increase in  $Sr$  parameter values both stretchable cylinder and sheet cases as shown in Figure (4.7.10). Table 4.21 shows the numerical validation and the comparison of the present study with previous results.

**Table 4.21 A comparison of  $-\theta(0)$  for different values of  $Pr$**

$Pr$	Khan <i>et al.</i> (2014)	Acharya <i>et al.</i> (2016)	Das <i>et al.</i> (2015)	Present result
1	0.40135	0.40145361	0.401452	0.40146012
10	0.46903	0.46931620	0.469315	0.46931623
100	0.49260	0.49252822	0.492529	0.49252820

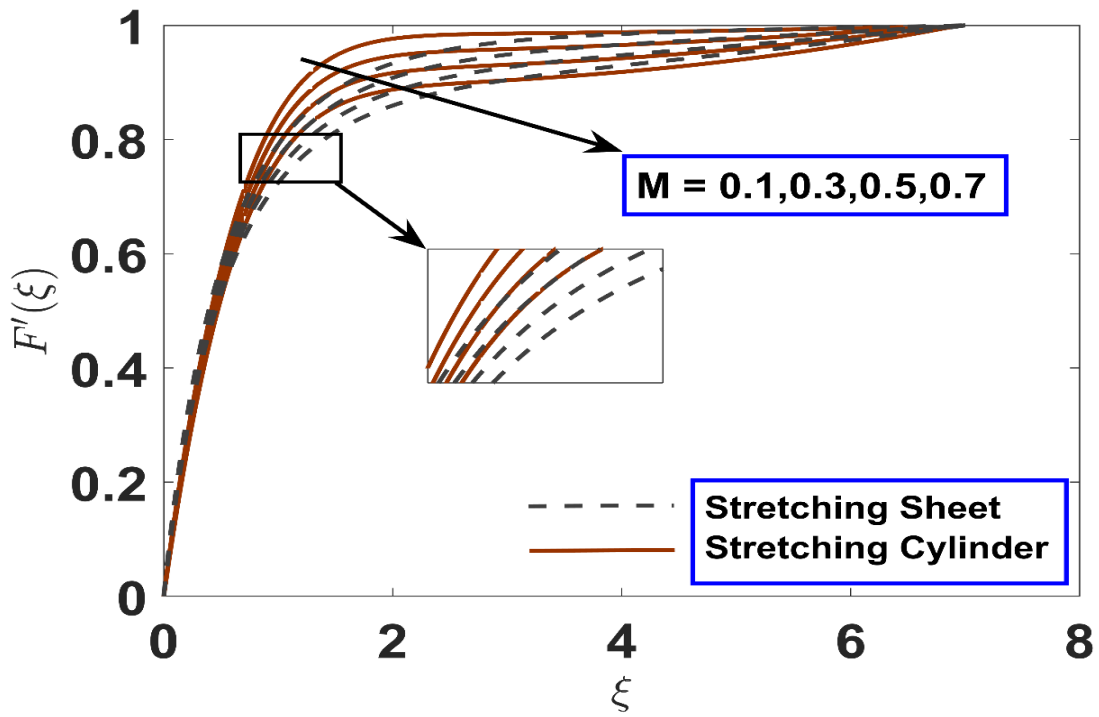


Figure 4.7.1 Fluctuation of Velocity profile along with variation of  $M$ .

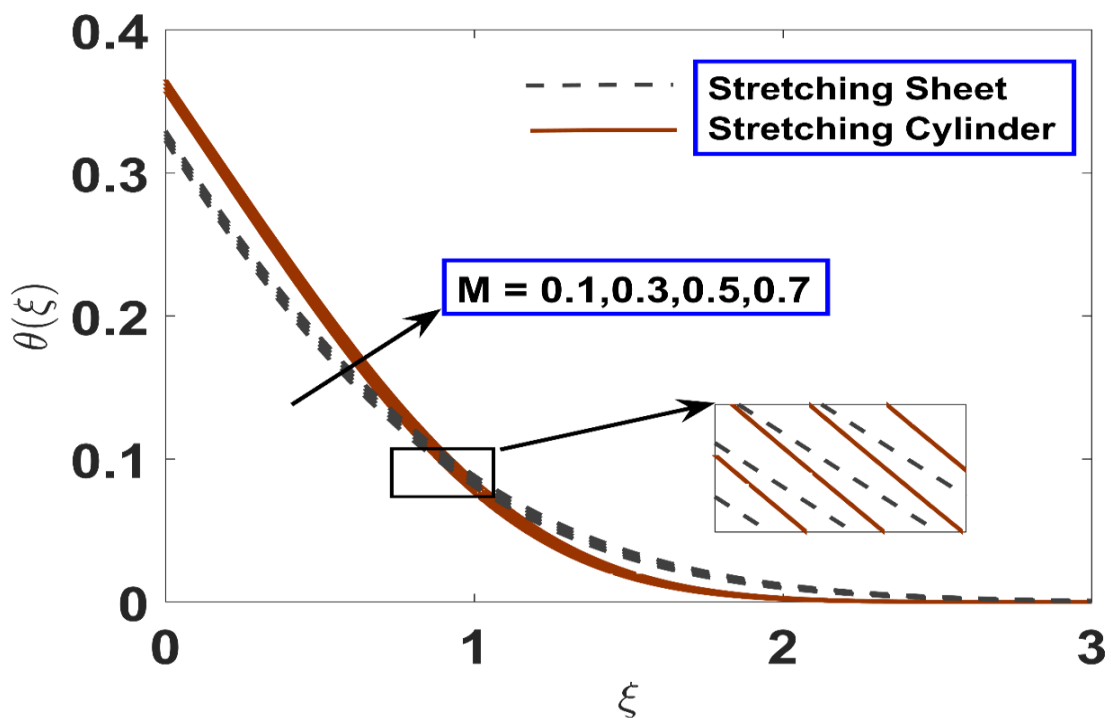


Figure 4.7.2 Fluctuation of temperature profile along with variation of  $M$ .

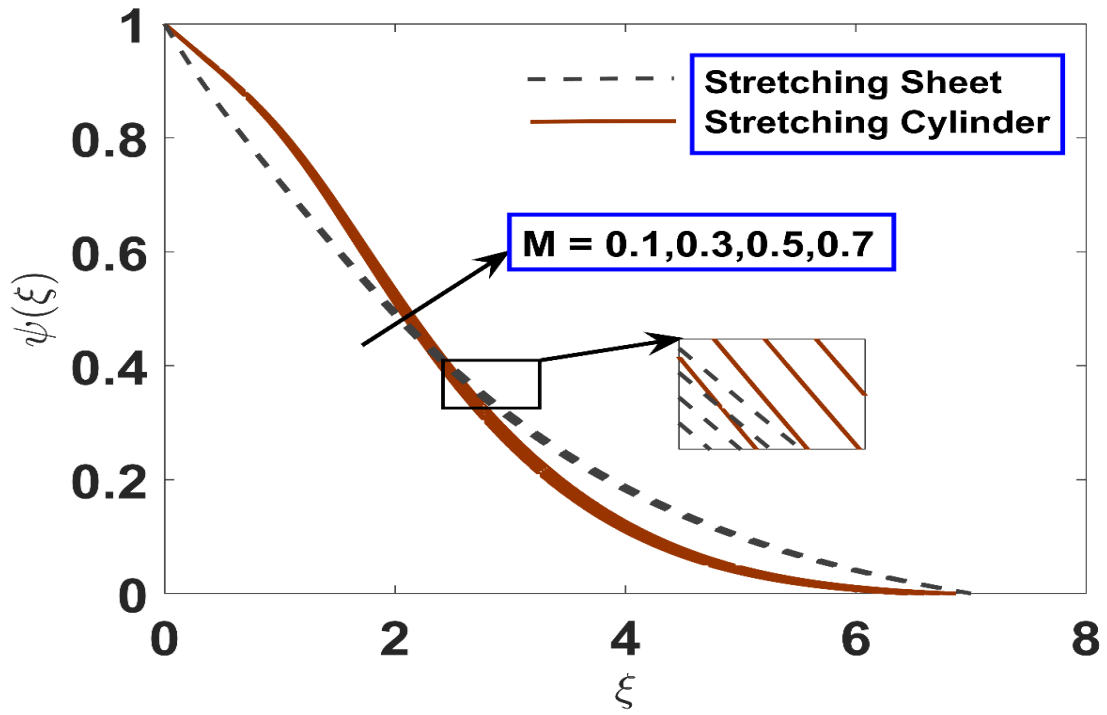


Figure 4.7.3 Fluctuation of concentration profile along with  $M$ .

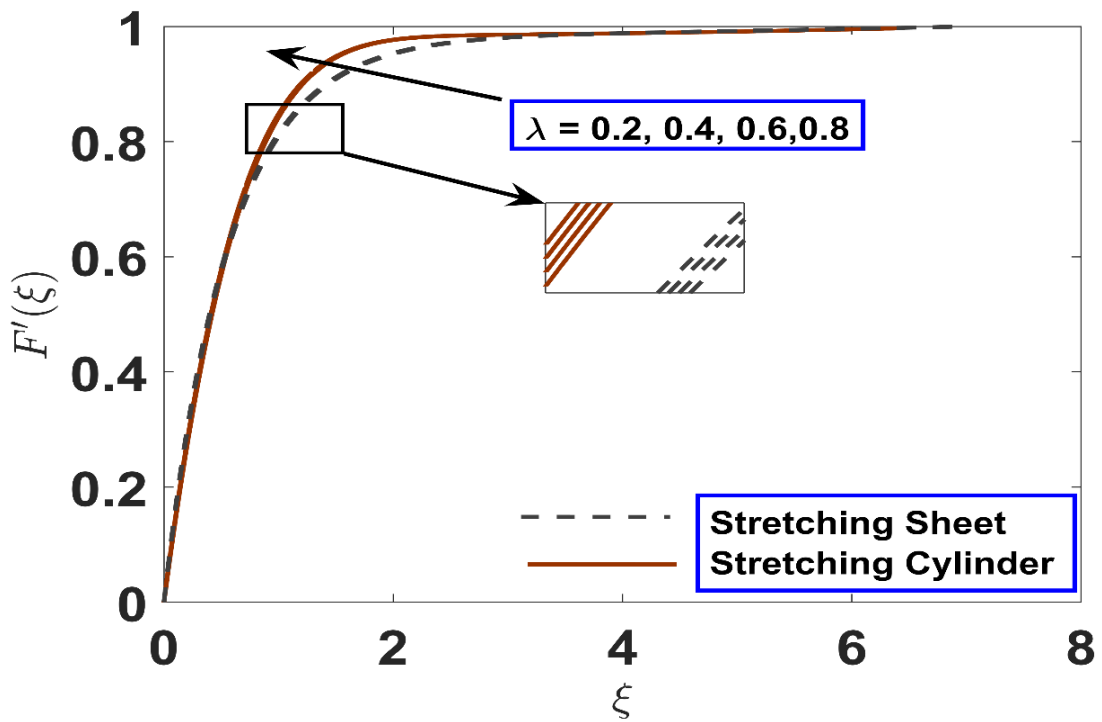


Figure 4.7.4 Fluctuation of velocity profile along with variation of  $\lambda$ .

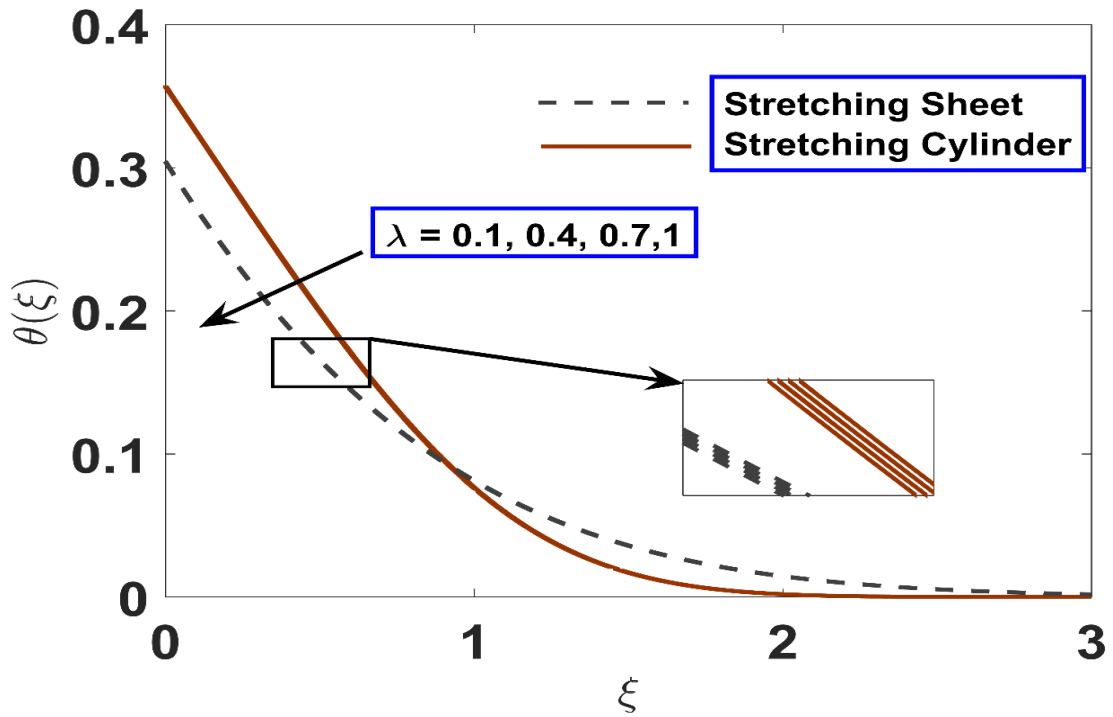


Figure 4.7.5 Fluctuation of temperature profile along with variation of  $\lambda$ .

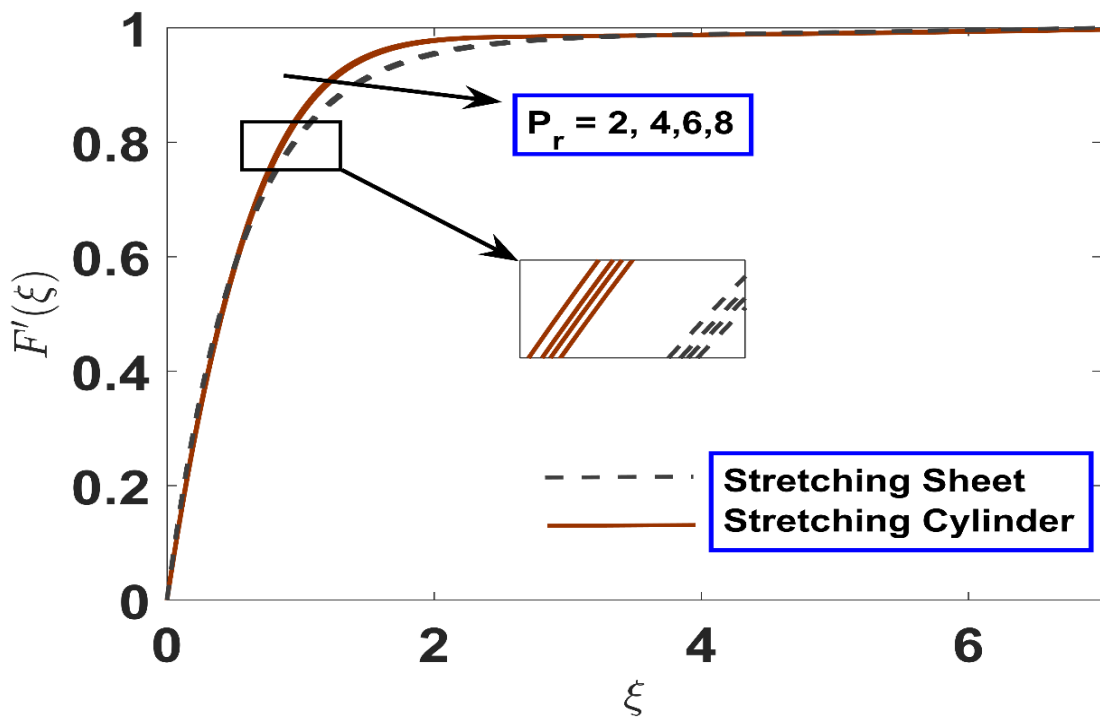


Figure 4.7.6 Variation of velocity profiles along with  $P_r$ .

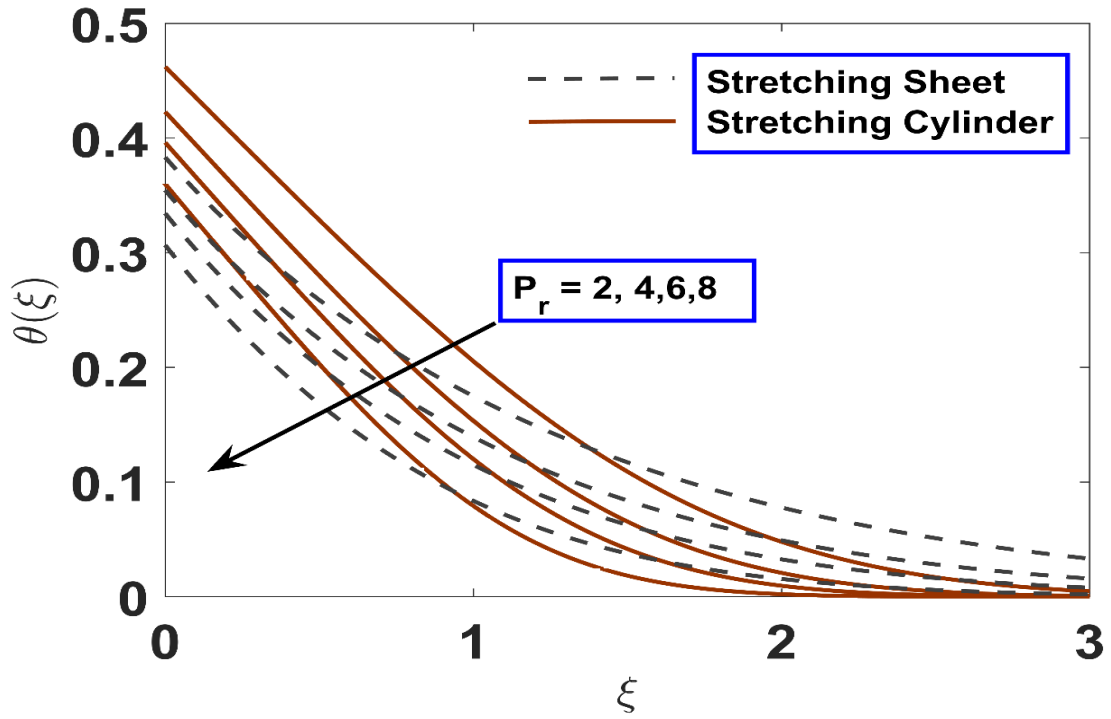


Figure 4.7.7 Variation of temperature profiles along with  $P_r$ .

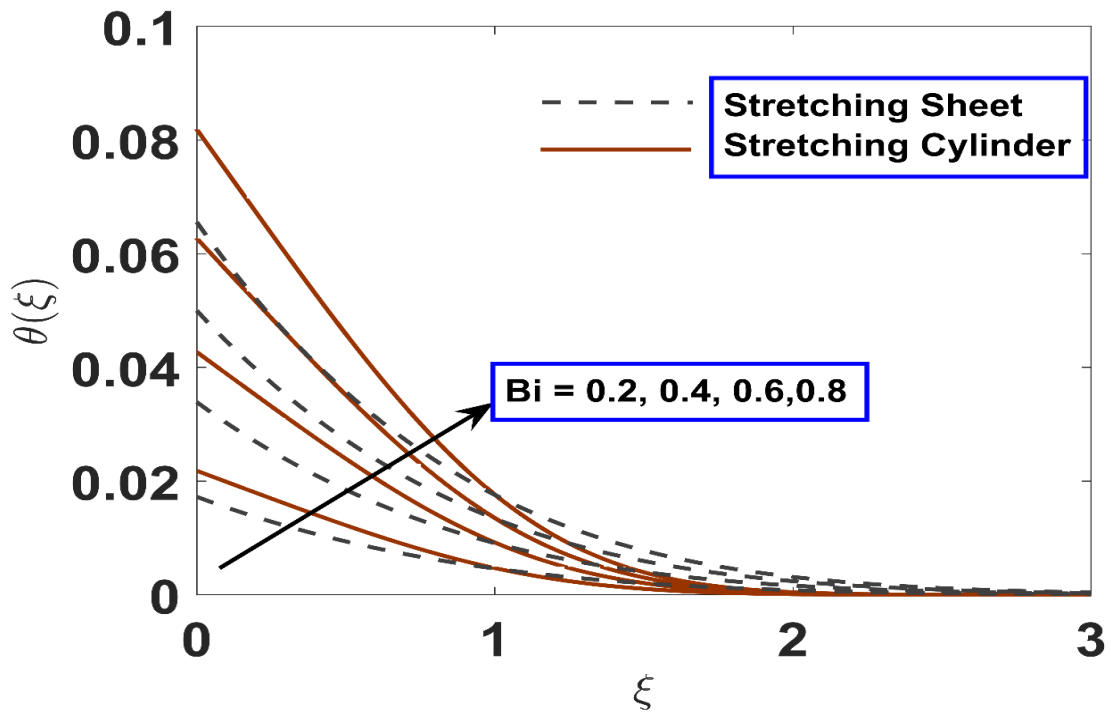


Figure 4.7.8 Temperature profiles along with variation of  $Bi$ .

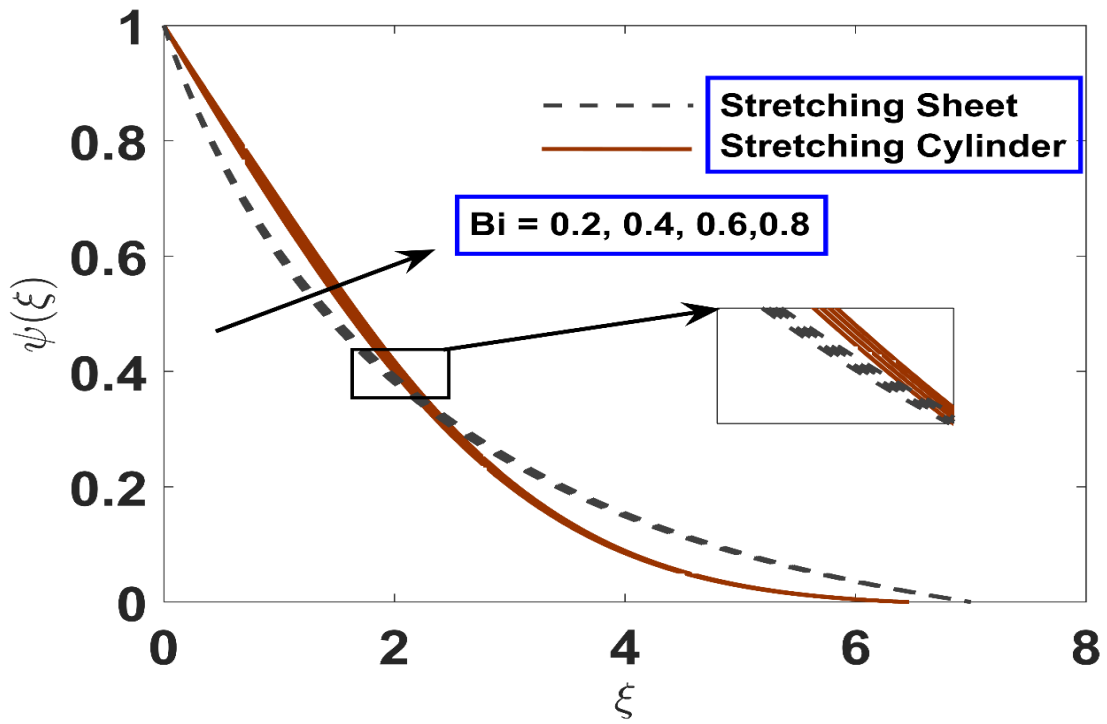


Figure 4.7.9 Concentration profiles along with variation of  $Bi$ .

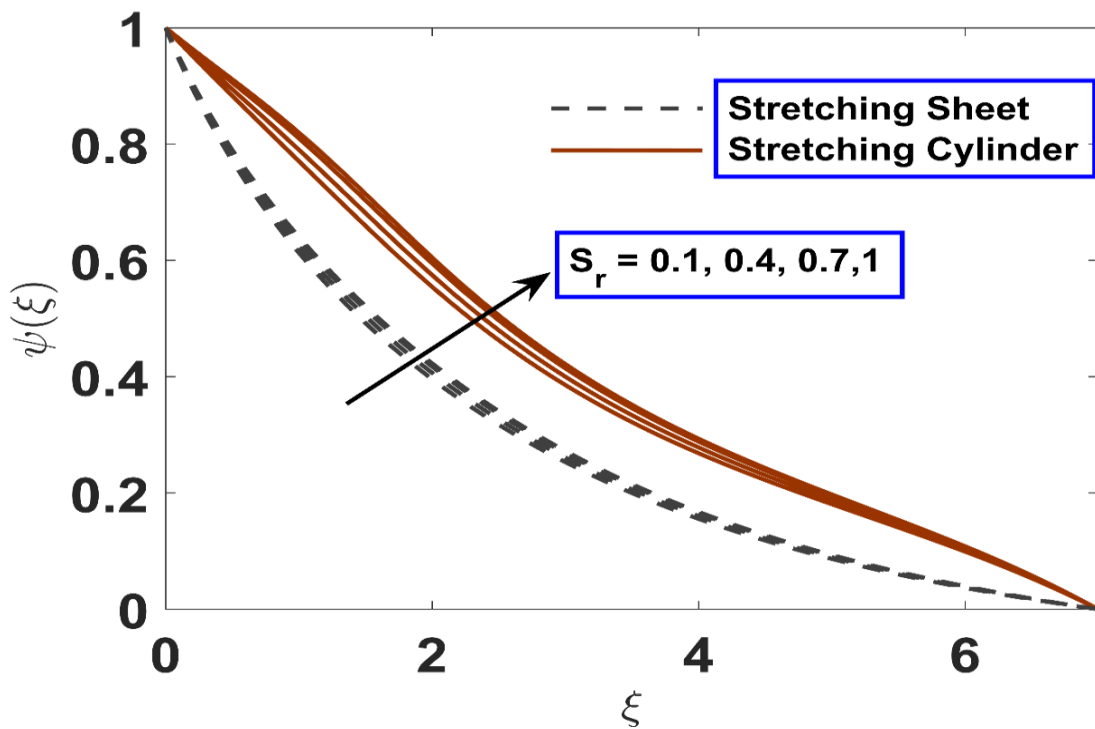


Figure 4.7.10 Fluctuation of concentration profiles along with  $S_r$ .

#### 4.8 Significance of irregular heat source and Arrhenius energy on electro magneto hydro dynamic hybrid nanofluid flow over a rotating stretchable disk with nonlinear radiation

The consequence of various influential parameters on radial velocity ( $F(\xi)$ ), azimuthal velocity ( $G(\xi)$ ), nanofluid concentration ( $\psi(\xi)$ ) and nanofluid temperature ( $\theta(\xi)$ ) profiles are illustrated through figures 4.8.1 to 4.8.19.

Figure (4.8.1) illustrates how radial velocity profile decay with increasing magnetic parameter values. Physically, magnetic parameter is connected to the Lorentz force, which is a resistive force to fluid flow. As magnetic parameter was increased, more resistive force was provided, which caused the velocity to decrease initially.

According to figure (4.8.2), velocity rises as the electric parameter increases. A drop in Lorentz force with  $E$ , which results in a reduction in the resistance to fluid motion. As a result,  $E$  increased with an increase in radial velocity profile.

Figure (4.8.3) demonstrates the impact of radial velocity behaviour for various slip parameter  $\Gamma$ . An increase in  $\Gamma$  causes the fluid flow in the radial velocity profile to slow down. So, thickness of profile decreased.

Figure (4.8.4) represents the radial velocity profiles with respect to the stretching strength parameter  $\lambda$ . It was discovered that when the radial velocity profile was increased, the stretching strength parameter value also increased. A delay in the velocity profile was observed with an increase in magnetic parameter  $M$  as shown in Figure (4.8.5). A physical increase in  $M$  increases an opposing force that slows the velocity.

Figure (4.8.6) shows that with an increase in the electric parameter  $G(\xi)$  also displayed enhancement. A decrease in opposite force with  $E$ , which less the barrier to fluid motion. Hence azimuthal velocity profile increased.

Figure (4.8.7) and Figure (4.8.8) depict the deceleration in azimuthal velocity profiles with increment in the wall slip parameter ( $\Gamma$ ) and stretching strength parameter ( $\lambda$ ) values. Physically, when  $\Gamma$  increases the rotating phenomenon's mild transmission to the surrounding fluid layers exactly causes the  $G(\xi)$  to decelerate.

Thickness of thermal boundary layer increased with an increase in magnetic parameters as shown in figure (4.8.9). Frictional heating between fluid layers is increased with opposing forces, releasing heat energy. This resulted in the thicker thermal boundary layer. Figure (4.8.10) and figure (4.8.11) describe for various values of  $E$  and  $\lambda$  that temperature profiles exhibited a declining trend. Resistance between various fluid layers diminishes as  $E$  increases because the Lorentz force decreases. Therefore, as  $E$  levels were raised, the temperature profile had fallen.

Figure (4.8.12) clarifies the effect of exponentially space-dependent heat source (ESHS)  $Q_E$  on temperature profile  $\theta(\xi)$ . Increase in  $Q_E$  values represented an improvement in the profiles of the thermal boundary layer and their corresponding thickness.

Figure (4.8.13) discusses the fluctuation of linear heat source (LHS)  $Q_T$  on temperature distribution. The profile was enhanced with an increase in  $Q_T$ . Figure (4.8.14) shows the presence of the thermal radiation parameter  $R_d$  was responsible for a rise in temperature. Thermal radiation plays a significant role in the surface heat transfer where the convection heat transfer coefficient is low because the intensity of thermal radiation results in a drop in the absorption coefficient.

Figure (4.8.15) demonstrates how changing values of the temperature ratio parameter  $\theta_m$  affect temperature. It was found that an increase in heat output improved the fluid's thermal condition, which is what caused the temperature to rise.

Figure (4.8.16) displays the positive impact of the Biot number  $Bi$  on the thermal boundary layer. Physically, stronger convection raises surface temperatures, which finally permits the thermal impact to extend deeper into the quiescent fluid.

Figure (4.8.17) depicts the relationship between the activation energy parameter  $E_A$  and the concentration profile. It demonstrated that the concentration profile raised (for the major portion of  $\xi$ ) as  $E_A$  was increased. Physically, the activation energy parameter gives atoms or molecules more energy to interact with one another, so it generated chemical process, which increased concentration profile.

The concentration profile significantly decreased (for the major portion of  $\xi$ ) as one kept increasing the chemical reaction parameter  $K_r$  as displayed in Figure (4.8.18). Positive values of  $K_r$  indicate destructive chemical reactions. The increment in  $K_r$  represents a healthier rate of consumption of species. Therefore, the concentration profile decreased.

Figure (4.8.19) describes the dual behaviour of concentration profile as  $\delta$  rises. Physically, the concentration decreases as the temperature differential between the surface of the walls and the surrounding air increases.

Table 4.22 show good agreement with other authors to present result. The impact of pertinent parameters on the drag and heat transfer rates has been analysed using Table.4.23 and 4.24. It was perceived that the heat transfer was maximum for  $R_d, \theta_m, Bi$  and minimum for  $Q_T, Q_E$ . Further, the drag rate was increased for  $M, \lambda, \phi_1, \phi_2$  and decreased for  $E, \Gamma$ .

**Table 4.22: Comparison of physical quantities when**

$$Pe = 6.2, M = E = Kr = E_A = Bi = Q_T = Q_E = \phi_1 = \phi_2 = N_t = 0$$

Physical Quantities	Turkyilmazoglu (2014)	Khan <i>et al.</i> (2018)	Sabu <i>et al.</i> (2021)	Present Study
$F'(0)$	0.51023262	0.510232	0.5102326188	0.5102294
$G'(0)$	0.61592201	0.615923	0.6159220144	0.6159199
$H'(0)$	0.88447411	0.884620	0.8844741100	0.8844846
$\theta'(0)$	0.93387794	0.933877	0.9338779396	0.9338728

**Table 4.23: The Comparison of Nusselt number for different values of  $R_d, Q_T, Q_E, \Theta_m, B_i, \phi_1, \phi_2$ , while other parameters remain fixed**

$R_d$	$Q_T$	$Q_E$	$\Theta_m$	$B_i$	$\phi_1$	$\phi_2$	$Nu_x Re_x^{-\frac{1}{2}}$
0.1	0.11	0.07	1.4	0.4	0.02	0.02	0.325237
0.4	-	-	-	-	-	-	0.449406
0.7	-	-	-	-	-	-	0.570163
-	0.01	-	-	-	-	-	0.468135
-	0.11	-	-	-	-	-	0.449406
-	0.20	-	-	-	-	-	0.423758
-	-	0.01	-	-	-	-	0.460096
-	-	0.07	-	-	-	-	0.423758
-	-	0.13	-	-	-	-	0.385478
-	-	-	1.1	-	-	-	0.341621
-	-	-	1.4	-	-	-	0.385478
-	-	-	1.7	-	-	-	0.442889
-	-	-	-	0.1	-	-	0.117929
-	-	-	-	0.4	-	-	0.385478
-	-	-	-	0.7	-	-	0.562459
-	-	-	-	-	0.01	-	0.390548
-	-	-	-	-	0.02	-	0.385478
-	-	-	-	-	0.03	-	0.380628
-	-	-	-	-	-	0.01	0.388795
-	-	-	-	-	-	0.02	0.385478
-	-	-	-	-	-	0.03	0.382301

**Table 4.24: The variation in Skin friction for different values of  $M, E, \lambda, \Gamma, \phi_1, \phi_2$  while other parameters remain fixed**

$M$	$E$	$\lambda$	$\Gamma$	$\phi_1$	$\phi_2$	$\frac{1}{2}\sqrt{Re_x}Cf_x$
0.1	0.07	0.7	0.7	0.02	0.02	0.7811364
0.7	-	-	-	-	-	0.8480928
1.3	-	-	-	-	-	0.9059089
-	0.01	-	-	-	-	0.8738257
-	0.07	-	-	-	-	0.8480928
-	0.13	-	-	-	-	0.8237208
-	-	0.4	-	-	-	0.7194813
-	-	0.7	-	-	-	0.8480928
-	-	1.0	-	-	-	1.0216125
-	-	-	0.1	-	-	1.5621920
-	-	-	0.7	-	-	0.8480928
-	-	-	1.3	-	-	0.5914095
-	-	-	-	0.01	-	0.8216624
-	-	-	-	0.02	-	0.8480928
-	-	-	-	0.03	-	0.8750334
-	-	-	-	-	0.01	0.8256133
-	-	-	-	-	0.02	0.8480928
-	-	-	-	-	0.03	0.8711992

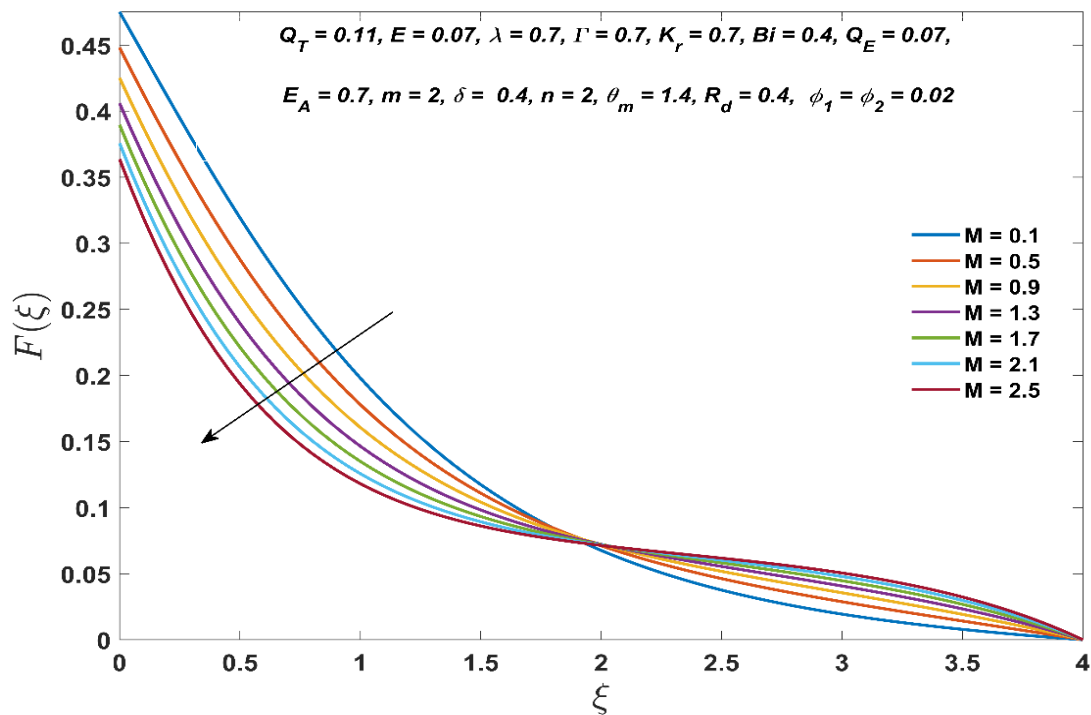


**Figure 4.8.1 Deviations in  $F(\xi)$  with  $M$**

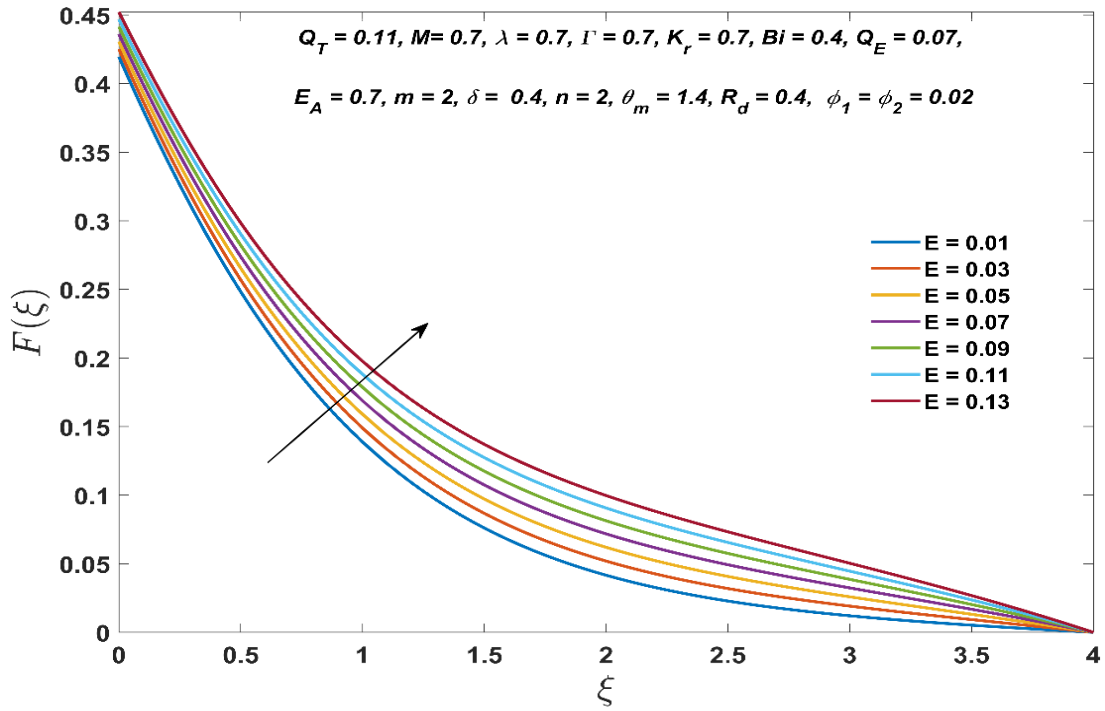


Figure 4.8.2 Deviations in  $F(\xi)$  with  $E$

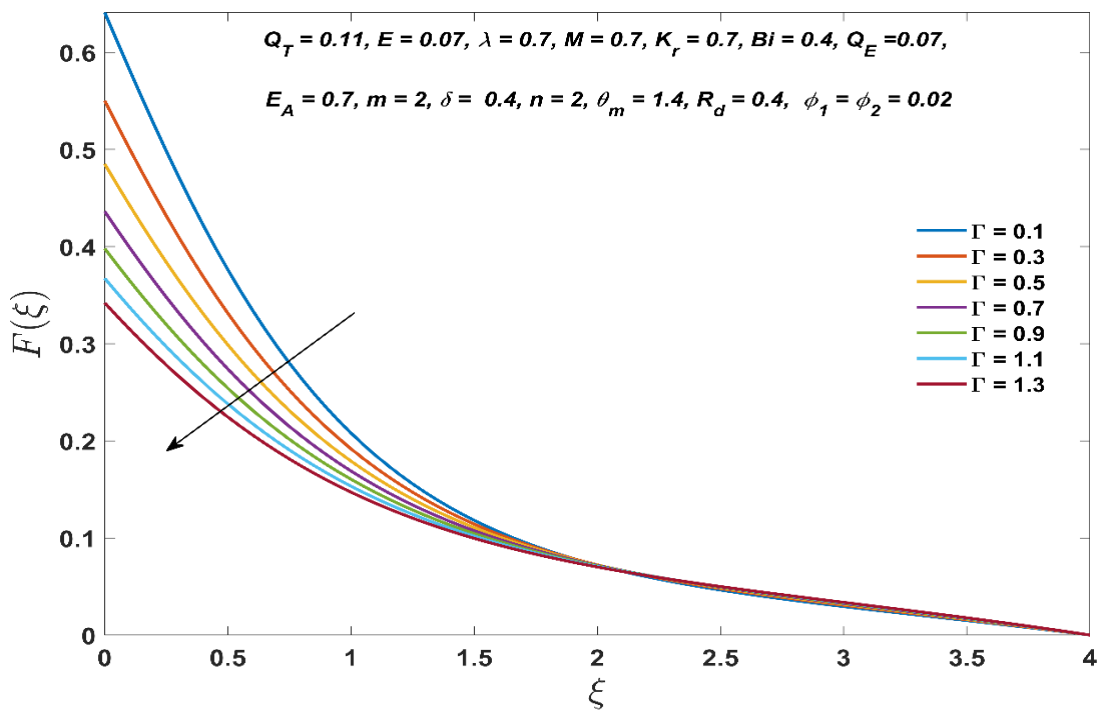


Figure 4.8.3 Deviations in  $F(\xi)$  with  $\Gamma$

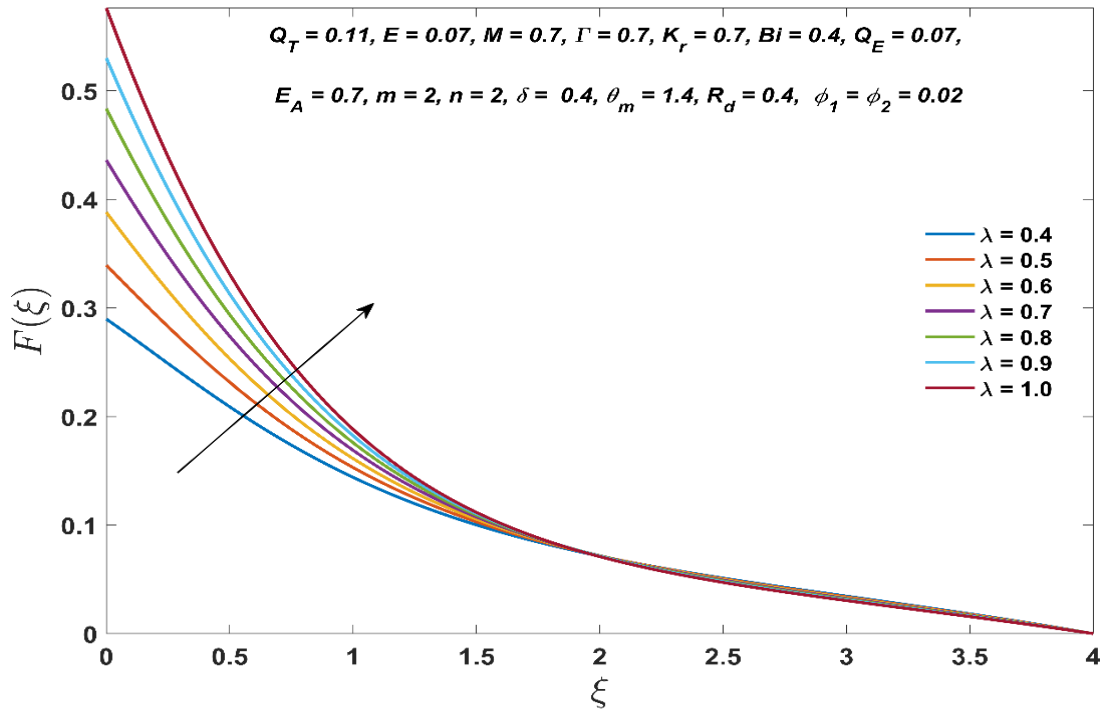


Figure 4.8.4 Deviations in  $F(\xi)$  with  $\lambda$

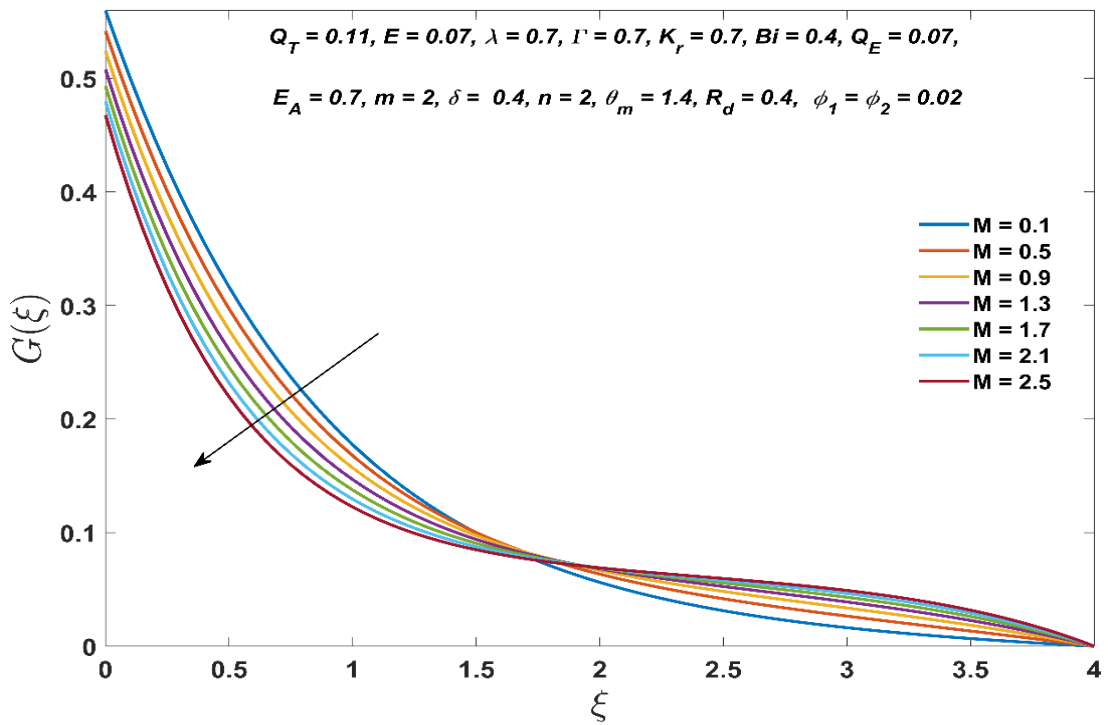


Figure 4.8.5 Deviations in  $G(\xi)$  with  $M$

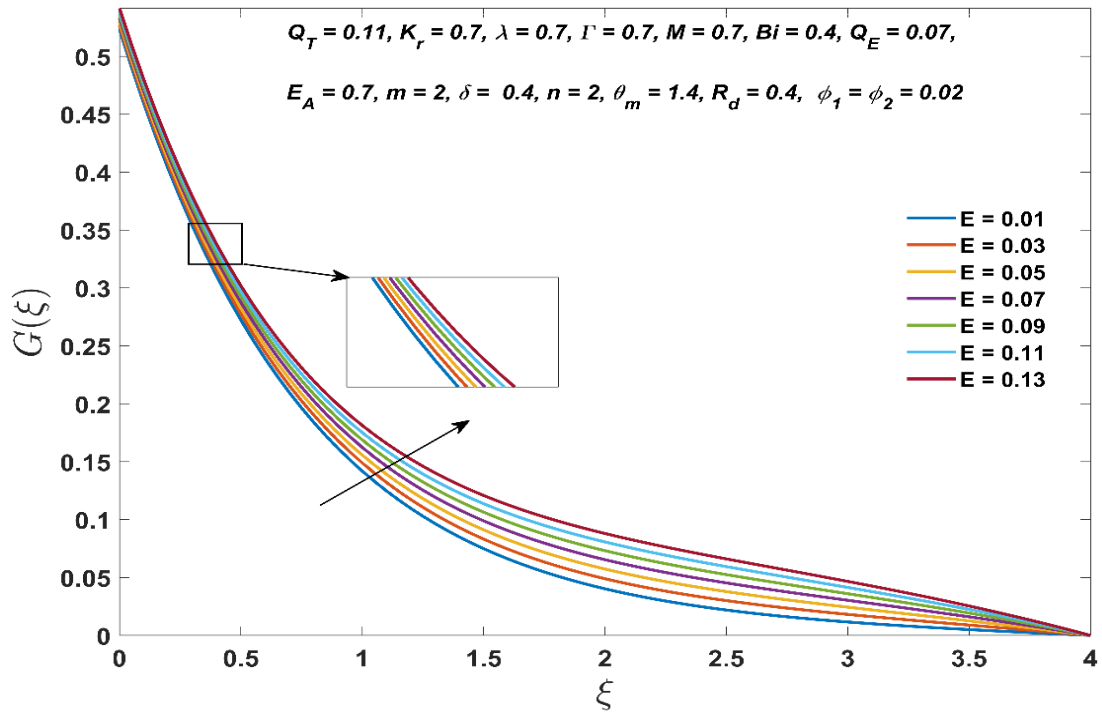


Figure 4.8.6 Deviations in  $G(\xi)$  with  $E$

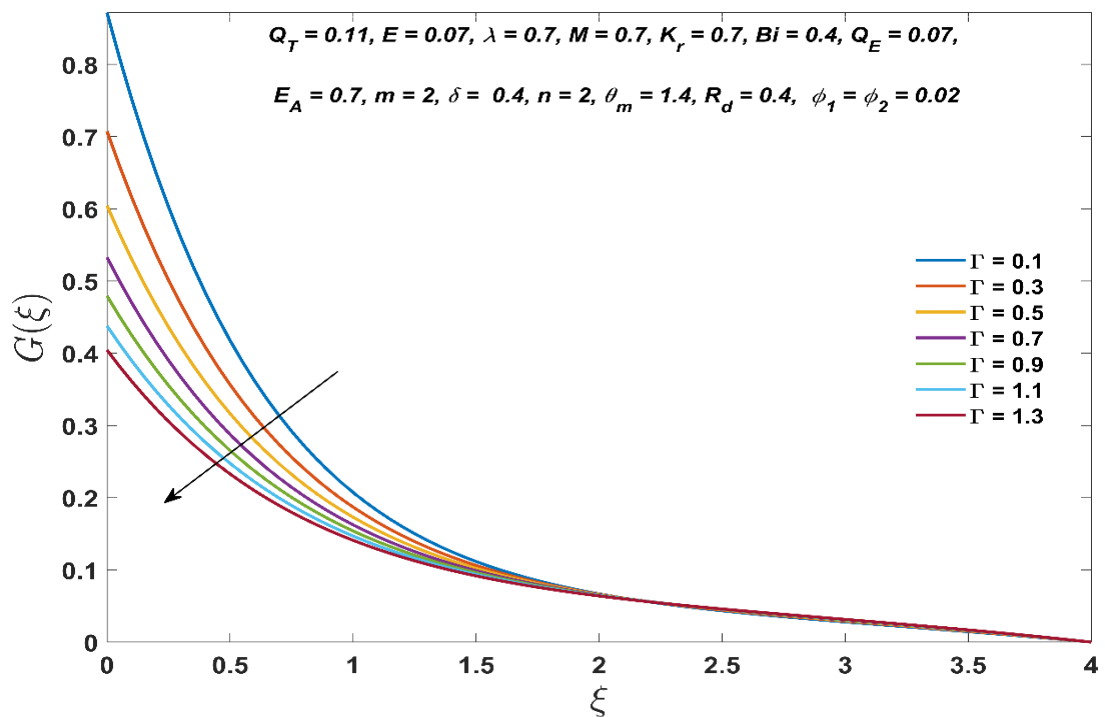


Figure 4.8.7 Deviations in  $G(\xi)$  with  $\Gamma$

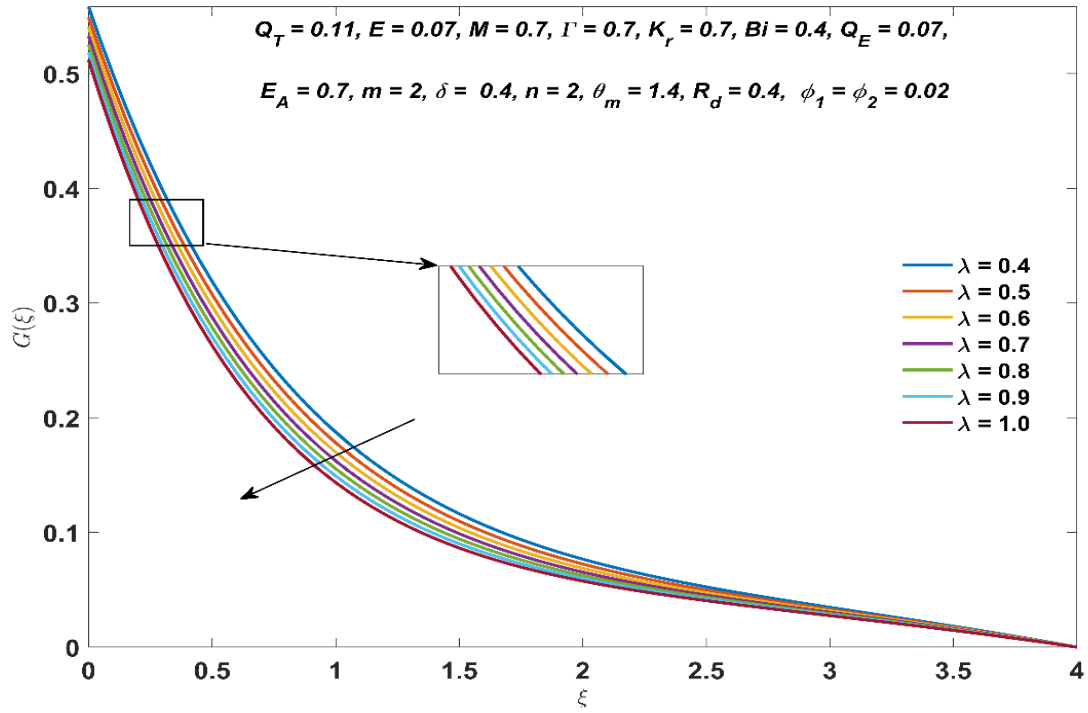


Figure 4.8.8 Deviations in  $G(\xi)$  with  $\lambda$

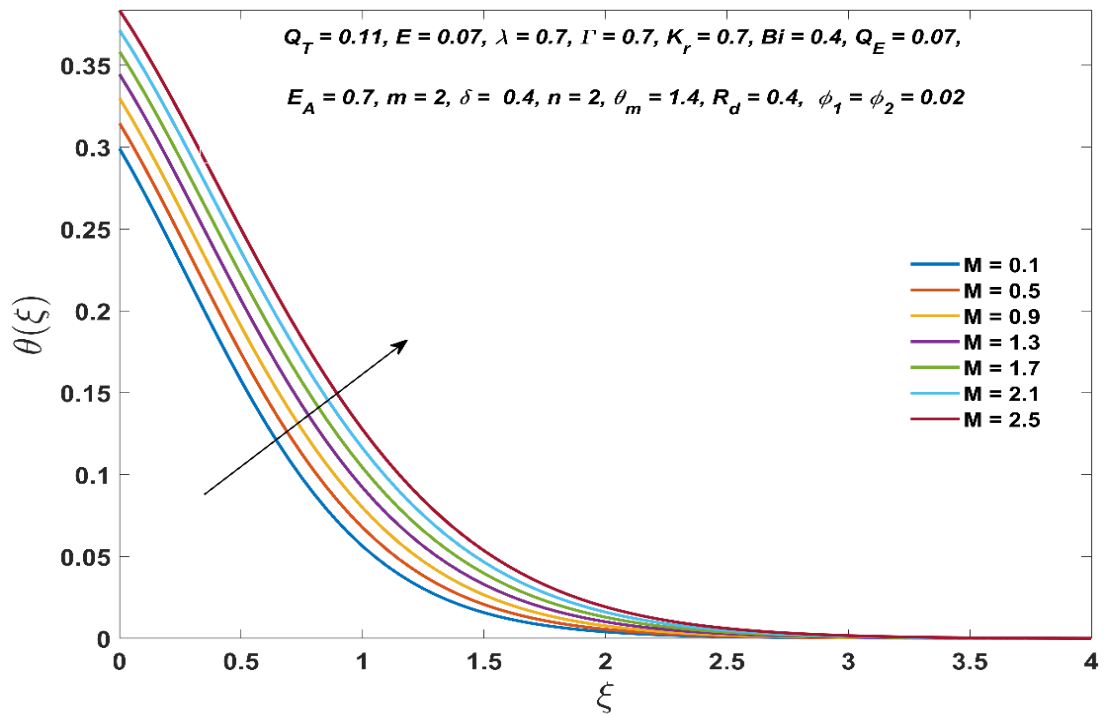


Figure 4.8.9 Deviations in  $\theta(\xi)$  with  $M$

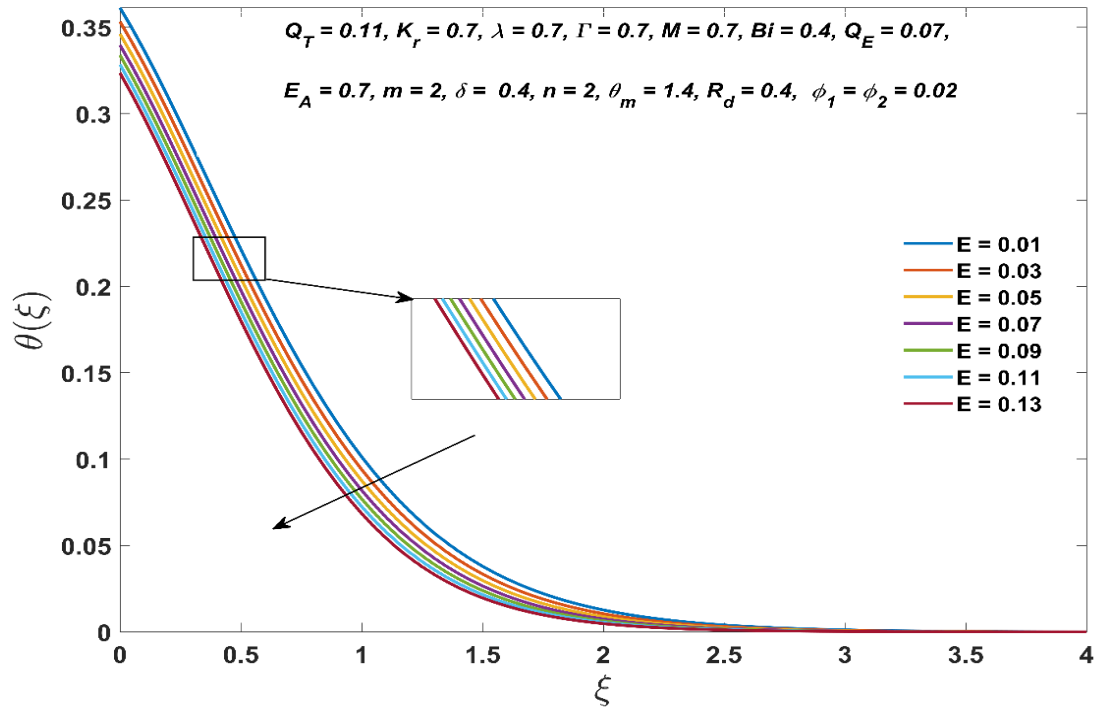


Figure 4.8.10 Deviations in  $\theta(\xi)$  with  $E$

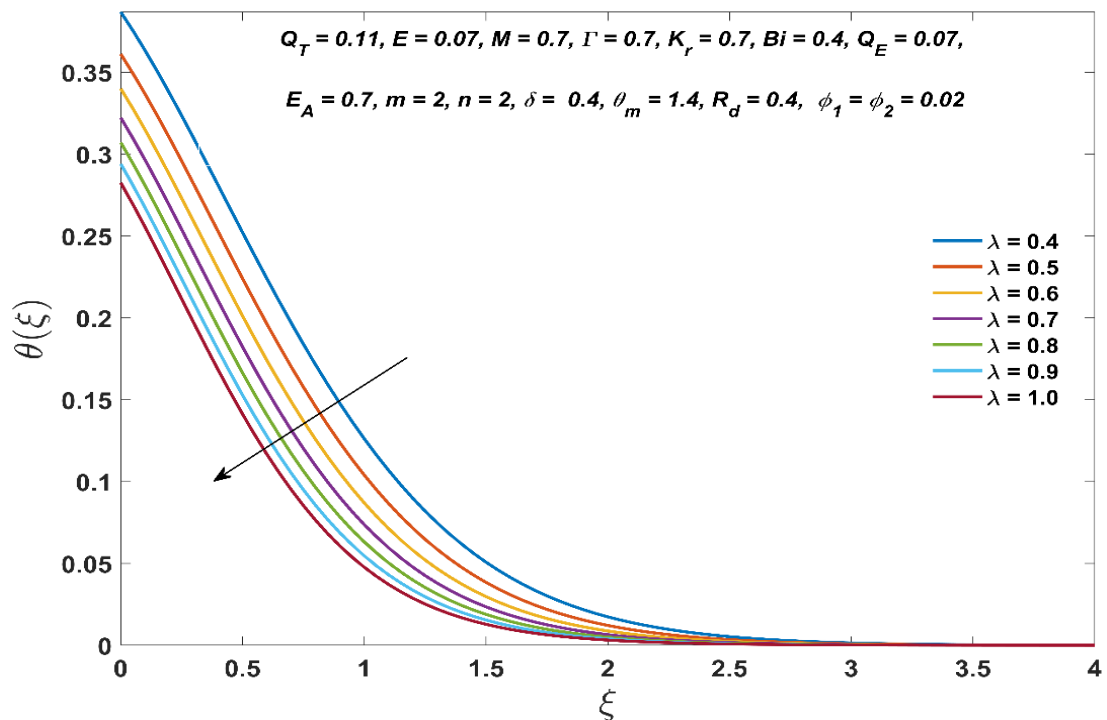


Figure 4.8.11 Deviations in  $\theta(\xi)$  with  $\lambda$

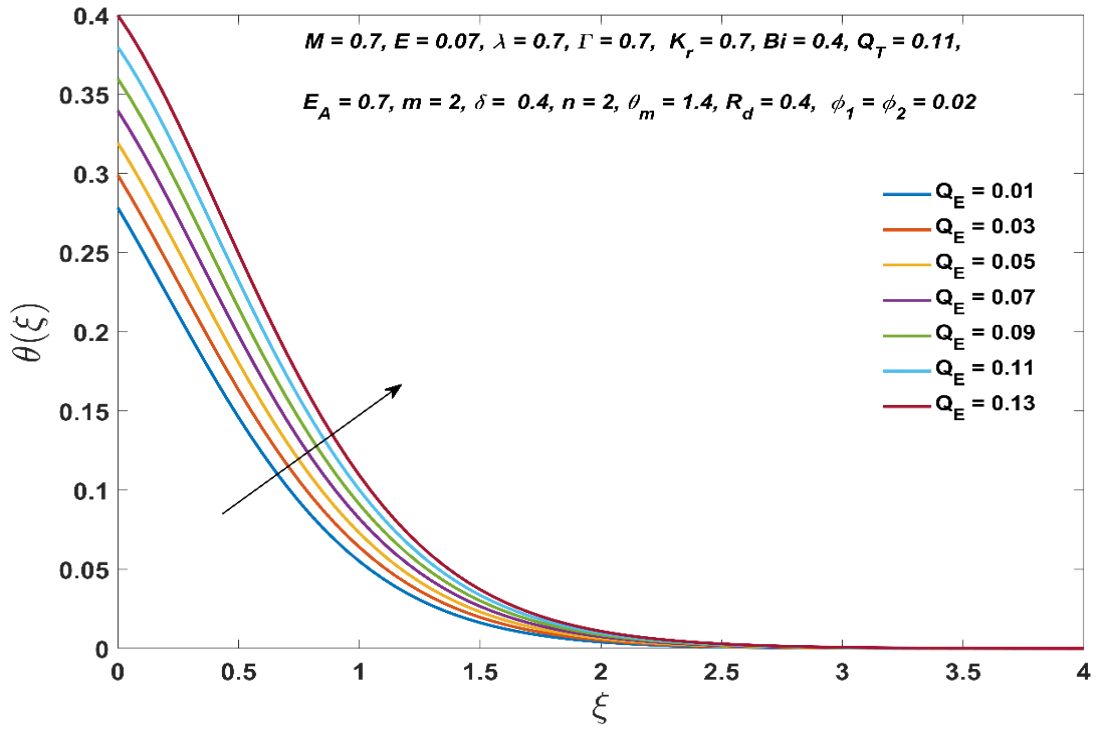


Figure 4.8.12 Deviations in  $\theta(\xi)$  with  $Q_E$

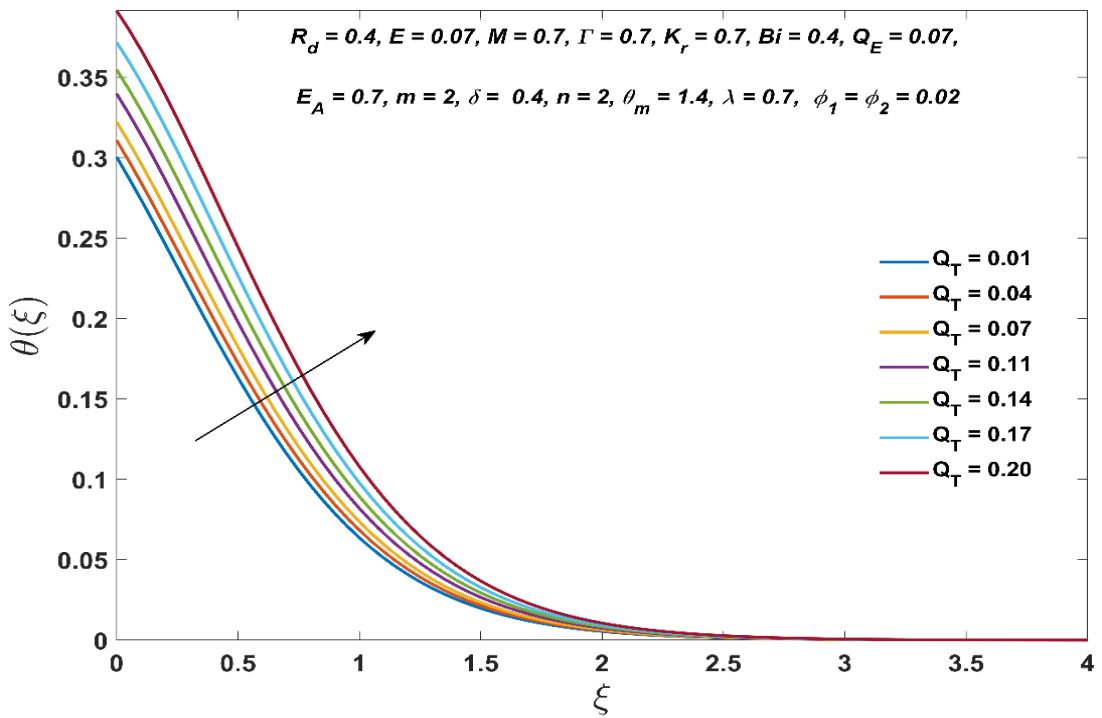


Figure 4.8.13 Deviations in  $\theta(\xi)$  with  $Q_T$

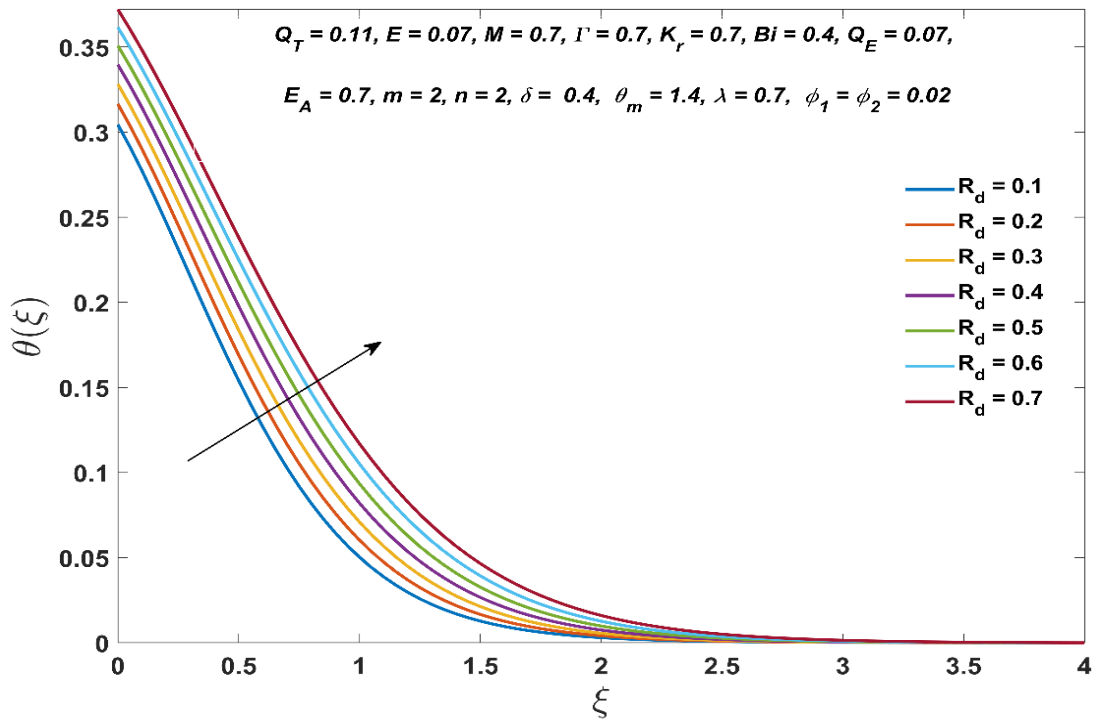


Figure 4.8.14 Deviations in  $\theta(\xi)$  with  $R_d$

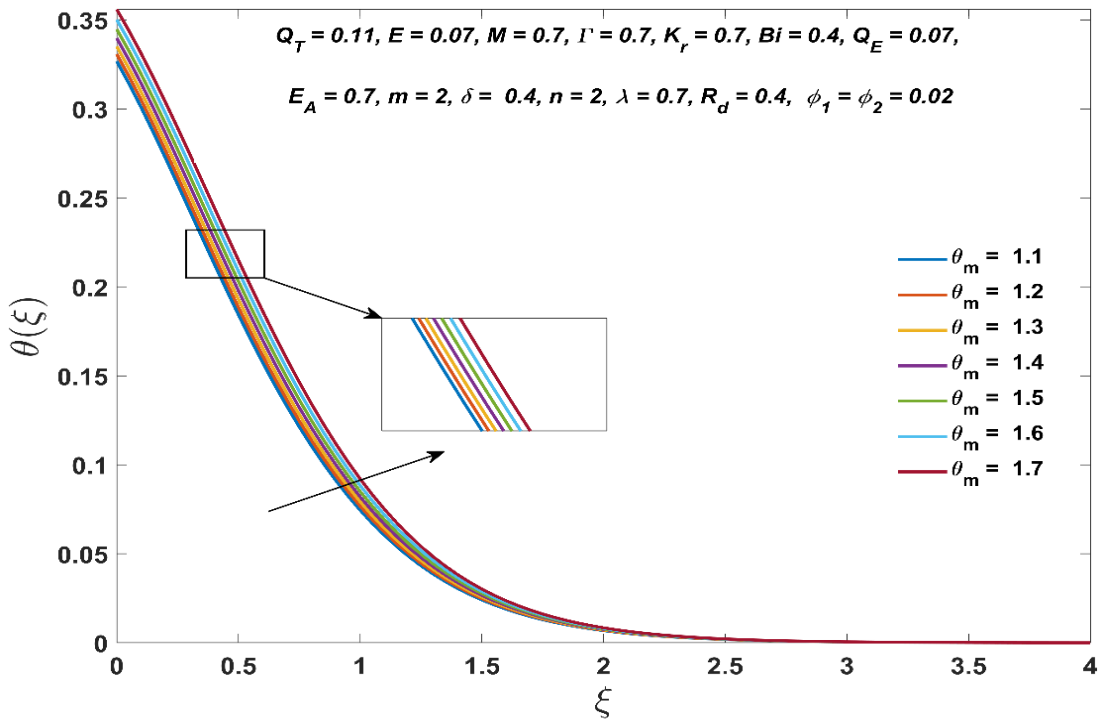


Figure 4.8.15 Deviations in  $\theta(\xi)$  with  $\theta_m$

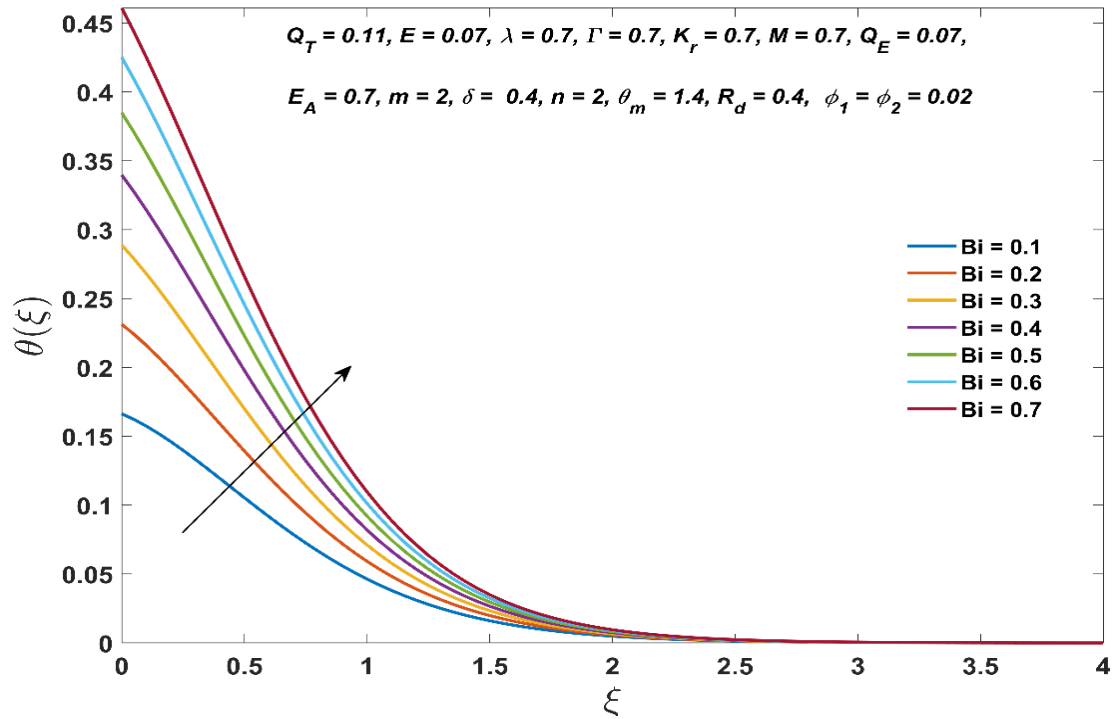


Figure 4.8.16 Deviations in  $\theta(\xi)$  with  $Bi$

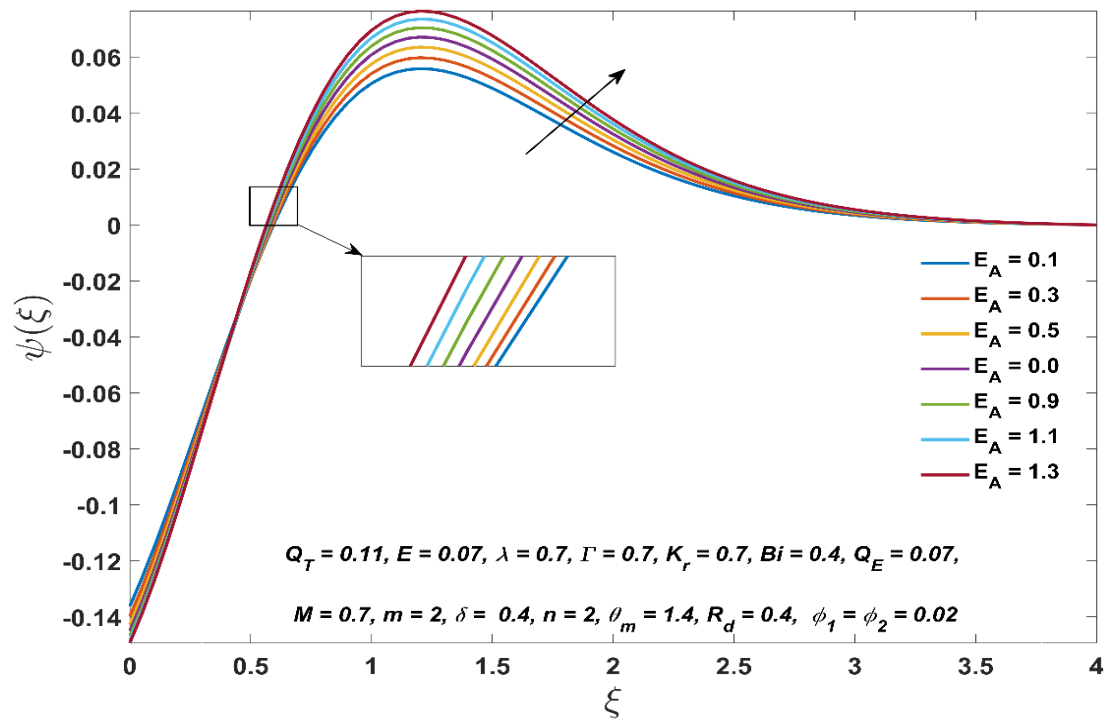


Figure 4.8.17 Deviations in  $\psi(\xi)$  with  $E_A$

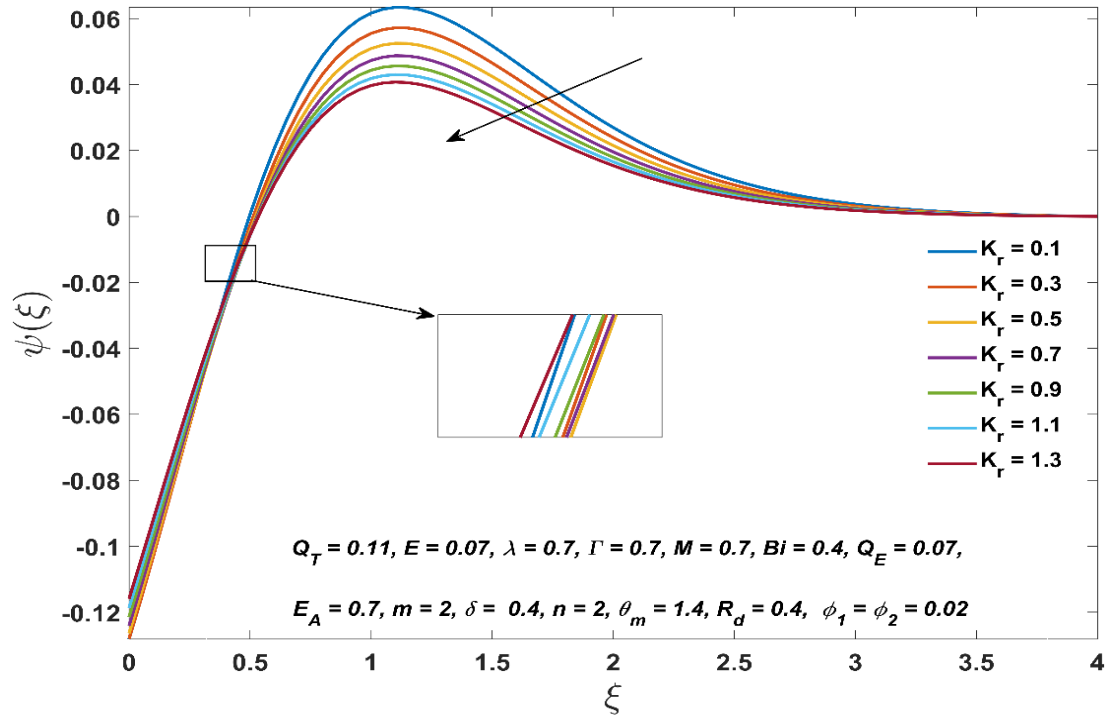


Figure 4.8.18 Deviations in  $\psi(\xi)$  with  $K_r$

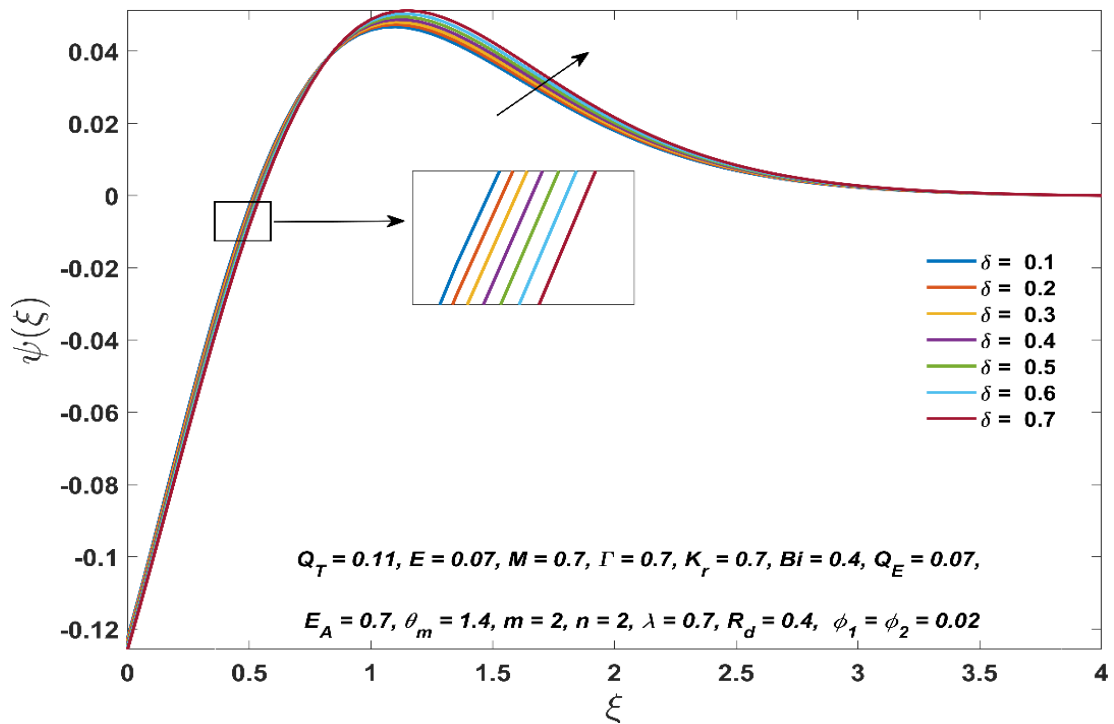


Figure 4.8.19 Deviations in  $\psi(\xi)$  with  $\delta$

## CHAPTER –V

### SUMMARY AND CONCLUSION

The present study entitled "Heat Transfer in Nanofluids Flow Over Different Conformations with Various Effects," explores the impact of various phenomena on boundary layer nanofluid flow and heat transfer over numerous solid geometries. In this study, graphical representations of velocity, temperature, and nanoparticle concentration have been discussed in relation to different factors. Furthermore, the friction factor (skin friction), Nusselt and Sherwood numbers have been calculated and analyzed. The thesis divided into five chapters. Chapter 1 presents an introduction to the problem of the current study and sets up some basic concepts. The first section explains the brief history of fluid and nanofluid. After that, some general concepts of fluid mechanics have been discussed, such as fluid classification, boundary layer theory, and equations for nanofluid flow. Furthermore, the objectives of the present study were:

- To study heat transfer in nanofluids over stretching sheet under the various effects
- To determine heat transfer in nanofluids over a stretching cylinder with various effects
- To compare the effects of heat transfer in nanofluids over conformation

The literature on fluid flow, heat and mass transfer of nanofluid was presented in Chapter-II. It includes existing literature relevant to the present work. This outline illustrates the progression of research in the field of study in the past by describing various researches conducted throughout the year. Additionally, this chapter presents literature on nanofluid applications. Chapter-III explains mathematically adapted formulae for addressing the present problems. The study contains a physical model dimension and a numerical application dimension with the depth of a numerical solution. The chapter is subdivided into nineteen major sections. 3.1-3.11 demonstrate fine details of the classification of fluids, the theory of boundary layers, and the necessary equations that control nanofluid flow and non-dimensional numbers are then described, along with some general concepts of fluid mechanics. The physical quantities of interest to engineering and physics are also discussed, incorporated methodology, including similarity transformations, Runge-Kutta numerical approaches, and shooting procedures. This chapter also discusses the mathematical software, programming tools, and graph plotting tools used. There are different models formulated with their numerical solutions from section 3.12 to section 3.19.

The results of the research study are compiled and discussed in the chapter-IV. The summary and conclusion have been presented in the chapter-V.

The salient findings of the investigations are summarized below:

- Size of the nanoparticles and the involving parameters varied the velocity and the temperature profiles which in turn increased the rate of heat transfer. The enhancement in the radius of nanoparticles decreased the skin friction factor, thermal layer, and micro-rotation. As the Biot number increased, the thermal layer became thicker.
- Micro-rotational velocity declined with suction/injection parameter but enhanced with an increase of  $K$  in the presence of active and passive controls.
- The heat transfer was maximum for larger values of thermal radiation and  $Pr$ , but opposite behavior in the case of  $Nb$  and  $Nt$  for active and passive control cases.
- Chemical reaction parameter decreased the concentration and motile concentration profiles. The heat transfer rate was least responsive to changes in the magnetic parameter and most sensitive to variations in the Biot number.
- Temperature profile, concentration profile and motile concentration profiles reduce near a stretching surface but increase as we move further away from the surface when the curvature parameter increases.
- The theoretical study associated with the Weissenberg number in the Cerreau nanofluid revealed a distinct nature in the velocity profile, skin friction, and Nusselt number.
- Biot number, thermal radiation parameter, thermal conductivity, and modified Hartmann number improved the thickness of the temperature profile over the Riga plate.
- The local Nusselt number decreased as Eckert number, magnetic field parameter, and Brownian motion parameter increased, whereas local Sherwood number enhanced with these parameters.

## CONCLUSION

This research work first proposes to modified the set of governing equations to investigate the two-dimensional magnetohydrodynamics, incompressible boundary layer flows over the multi-surfaces, like stretching sheet, cylinder. The set of transformation used to reduce the governing equations to nonlinear differential equations in dimensionless form. The numerical technique were applied on the modeled problems for the numerical solution.

The variation in velocity and the temperature profiles was the cause of increasing the size of the nanoparticles and the involving parameters that caused an increase in the rate of heat transfer. The enhancement in the radius of nanoparticles causes a decrease in the skin friction factor, thermal layer, and micro-rotation. A few researchers worked on the significance of the nanoparticle's radius, interspacing of nanoparticle with simultaneously effect of various parameter and the response surface methodology technique and the sensitivity analysis has been used to examine the effects of nanoparticle volume fraction, Biot number, and magnetic parameter on the rate of heat transfer.

Furthermore, the Weissenberg number in the Cerreau nanofluid revealed a distinct nature in the velocity profile, skin friction, and Nusselt number. The velocity was substantially higher when the stretching cylinder compared to a flat sheet. In the case of a revolving disc, the concentration profile was directly and indirectly proportional to the variations in the activation energy and chemical reaction parameters, respectively.

The results findings from this study, the constant flow of viscous, incompressible nanofluid fluid past devices like stretching sheets, stretching cylinders, Riga plates, and rotating disc have a wide range of applications in the industries.

## BIBLIOGRAPHY

---

- Abbott, D.E., and Kline, S. J. (1960). Simple Methods for Construction of Similarity Solutions of Partial Differential Equations. AFOSR TN 60-1163, Dept. of Mech. Eng. Report MD-6:41–44.
- Abo-Dahab, S., Abdelhafez, M., Mebarek-Oudina, F., and Bilal, S. (2021). Mhd casson nanofluid flow over nonlinearly heated porous medium in presence of extending surface effect with suction/injection. *Indian Journal of Physics*, **95**(12): 2703–2717.
- Acharya, N., Das, K., and Kundu, P. K. (2016). Framing the effects of solar radiation on magneto-hydrodynamics bioconvection nanofluid flow in presence of gyrotactic microorganisms. *Journal of Molecular Liquids*, **222**: 28–37.
- Ahmad, A., Asghar, S., and Afzal, S. (2016). Flow of nanofluid past a Riga plate. *Journal of Magnetism and Magnetic Materials*, **402**: 44-48.
- Ahmad, R., and Mustafa, M. (2016). Model and comparative study for rotating flow of nanofluids due to convectively heated exponentially stretching sheet. *Journal of Molecular Liquids*, **220** :635–641.
- Ahmad, R., Mustafa, M. and Turkyilmazoglu, M. (2017). Buoyancy effects on nanofluid flow past a convectively heated vertical Riga-plate: A numerical study. *International Journal of Heat and Mass Transfer*, **111**:827-835.
- Ahmad, S., Nadeem, S., Muhammad, N., and Khan, M. N. (2021). Cattaneo–christov heat flux model for stagnation point flow of micropolar nanofluid toward a nonlinear stretching surface with slip effects. *Journal of Thermal Analysis and Calorimetry*, **143**(2): 1187–1199.
- Ahmed, J., Khan, M., and Ahmad, L. (2019). Stagnation point flow of maxwell nanofluid over a permeable rotating disk with heat source/sink. *Journal of Molecular Liquids*, **287**: 110853.
- Ahmed, N., Khan, U., and Mohyud-Din, S. T. (2017). Influence of thermal radiation and viscous dissipation on squeezed flow of water between Riga plates saturated with carbon nanotubes. *Colloids and Surfaces A: Physicochemical and Engineering Aspects*, **522**: 389-398.
- Ali, L., Liu, X., Ali, B., Din, A. and Mdallal, Q. A. (2021). The function of nanoparticle’s diameter and darcy-forchheimer flow over a cylinder with effect of magnetic field and thermal radiation, *Case Studies in Thermal Engineering*, **28**:101392. (12)
- Ali, L., Liu, X., Ali, B., Mujeed, S. and Abdal, S. (2019). Finite element simulation of multi-slip effects on unsteady mhd bioconvective micropolar nanofluid flow over a sheet with solutal and thermal convective boundary conditions, *Coatings*, **9**(12): 842.
- Ali, L., Liu, X., Ali, B., Mujeed, S., Abdal, S., and Khan, S. A. (2020). Analysis of magnetic properties of nano-particles due to a magnetic dipole in micropolar fluid flow over a stretching sheet, *Coatings*, **10**(2): 170.
- Altan, T., Oh, S. I., and Gegel, G. (1983). Metal forming fundamentals and applications[J]. *American Society for Metals*, **1983**: 353.
- Areekara, S., Mackolil, J., Mahanthesh, B., Mathew, A., and Rana, P. (2022). A study on nanoliquid flow with irregular heat source and realistic boundary conditions: A modified buongiorno model for biomedical applications, *ZAMM-Journal of Applied Mathematics and Mechanics/Zeitschrift für Angewandte Mathematik und Mechanik*, **102**(3): e202100167.

- Areekara, S., Sabu, A. S., Mathew, A., and Saravanan, B. (2021). Statistical analysis on the stratification effects of bioconvective emhd nanofluid flow past a stretching sheet: Application in theranostics, *Heat Transfer*, **50**(7): 6680–6702.
- Ayub, M., Abbas, T., and Bhatti, M. (2016). Inspiration of slip effects on electromagnetohydrodynamics (emhd) nanofluid flow through a horizontal riga plate. *The European Physical Journal Plus*, **131**(6): 1–9.
- Azam, M., Khan, M., and Alshomrani, A. (2017). Unsteady radiative stagnation point flow of mhd carreau nanofluid over expanding/contracting cylinder. *International Journal of Mechanical Sciences*, **130**: 64–73.
- Aziz, A., and Khan, W. (2012). Natural convective boundary layer flow of a nanofluid past a convectively heated vertical plate. *International Journal of Thermal Sciences*, **52**:83–90.
- Aziz, A., Jamshed, W., Ali, Y. and Shams, M. (2020). Heat transfer and entropy analysis of maxwell hybrid nanofluid including effects of inclined magnetic field, joule heating and thermal radiation. *Discrete & Continuous Dynamical Systems-S*, **13**(10): 2667-2690.
- Azzam, G. E. D. A. (2002). Radiation effects on the mhd mixed free-forced convective flow past a semi-infinite moving vertical plate for high temperature differences[J]. *Physica Scripta*, **66**(1):71.
- Babu, M. J., and Sandeep, N. (2016). Three-dimensional MHD slip flow of nanofluids over a slandering stretching sheet with thermophoresis and Brownian motion effects. *Adv. Powder Tech.*, **27**: 2039-2050.
- Bilal, M., (2020). Micropolar flow of emhd nanofluid with nonlinear thermal radiation and slip effects. *Alexandria Engineering Journal*, **59**(2): 965–976.
- Bödewadt, U. T., Die D.G., and Angew, Z. (1940). *Math Mech*, **20**:241–252.
- Brewster, M. Q. (1992). Thermal radiative transfer and properties, *John Wiley & Sons*.
- Brinkman, H. C. (1951). Heat effects in capillary flow I. *Applied Scientific Research*, **2**(1):120.
- Brinkman, H. C. (1952). The viscosity of concentrated suspensions and solutions. *The Journal of Chemical Physics*, **20**(4): 571-571.
- Choi, S. U. and Eastman, J. A., (1995). Enhancing thermal conductivity of fluids with nanoparticles, Tech. rep., Argonne National Lab. (ANL), Argonne, IL (United States). No. ANL/MSD/CP-84938; CONF-951135-29).
- Crane L. J. (1970). Flow past a stretching plate[J]. *Zeitschrift für Angewandte Mathematik und Physik ZAMP*. 1970, **21**(4): 645–647.
- Das, K., Duari, P. R., and Kundu, P. K. (2015). Nanofluid bioconvection in presence of gyrotactic microorganisms and chemical reaction in a porous medium, *Journal of Mechanical Science and Technology*, **29**(11): 4841–4849.
- Datti, P., Prasad, K., Abel, M. S., and Joshi, A. (2004). Mhd visco-elastic fluid flow over a non-isothermal stretching sheet. *International Journal of Engineering Science*, **42**(8-9): 935–946
- Dawar, A., Islam, S., and Shah, Z. (2022). A comparative analysis of the performance of magnetised copper–copper oxide/water and copper–copper oxide/kerosene oil hybrid nanofluids flowing through an extending surface with velocity slips and thermal convective conditions. *International Journal of Ambient Energy*, **43**(1):1–19.

- Dawar, A., Wakif, A., Saeed, A., Shah, Z., Muhammad, T., and Kumam, P. (2022). Significance of Lorentz forces on Jeffrey nanofluid flows over a convectively heated flat surface featured by multiple velocity slips and dual stretching constraint: a homotopy analysis approach. *Journal of Computational Design and Engineering*, **9**(2): 564–582.
- El-Aziz, M. (2009). Viscous dissipation effect on mixed convection flow of a micropolar fluid over an exponentially stretching sheet. *Canadian Journal of Physics*, **87**(4): 359–368.
- Elbashbeshy, E. (2001). Heat transfer over an exponentially stretching continuous surface with suction. *Archives of Mechanics*, **53**(6): 643–651.
- Elsaid, E. M., Abdel-wahed, M.S, (2021) Impact of hybrid nanofluid coolant on the boundary layer behavior over a moving cylinder: *Numerical case study, Case Studies in Thermal Engineering* **25**:100951.
- Fisher E. G. (1976). Extrusion of plastics [M]: *Published for the Plastics and Rubber Institute [by] Wiley*.
- Gailitis, A. (1961). On a possibility to reduce the hydrodynamical resistance of a plate in an electrolyte. *Appl. Magneto-hydrodyn*, **12**: 143-146.
- Garnett, J. M. (1904). Xii. colours in metal glasses and in metallic films, *Philosophical Transactions of the Royal Society of London. Series A, Containing Papers of a Mathematical or Physical Character* **203**: 385–420
- Ghadikolaei, S.S., Yassari, S.S, Sadeghi, M. H., Hosseinzadeh, K., and Ganji, D.D., (2017) Investigation on thermophysical properties of hybrid nanofluid transport dependent on shape factor in MHD stagnation point flow, *Powder Technol* **322**:428–438
- Gökhan F., S., (2011). Effect of the Guess function & continuation method on the run time of MATLAB BVP Solvers. In: *Ionescu CM (ed) MATLAB. Intech Open*. **1**
- Gosukonda, S., Gorti, V. S., Baluguri, S. B., and Sakam, S. R. (2015). Particle spacing and chemical reaction effects on convective heat transfer through a nano-fluid in cylindrical annulus, *Procedia Engineering*, **127**: 263–270.
- Graham, A. L. (1981). On the viscosity of suspensions of solid spheres. *Applied Scientific Research*, **37** (3): 275–286.
- Gupta, P., and Gupta, A. (1977). Heat and mass transfer on a stretching sheet with suction or blowing[J]. *The Canadian Journal of Chemical Engineering*, **55**(6): 744–746.
- Hale N, Moore D., R., (2008) A sixth-order extension to the MATLAB package bvp4c of J. Kierzenka and L. Shampine. Report no 08/04A, Oxford University Computing Laboratory Numerical Analysis Group
- Halim, N., Sivasankaran, S., and Noor, N., M., (2017). Active and passive controls of the williamson stagnation nanofluid flow over a stretching/shrinking surface. *Neural Computing and Applications*, **28**(1): 1023–1033.
- Hamad, M. A. A., Pop, I., Ismail and M., A., I. (2011). Magnetic field effects on free convection flow of a nanofluid past a vertical semi-infinite flat plate. *Nonlinear Analysis: Real World Applications*, **12**: 1338–1346.
- Hansen, A., G. (1964). Similarity analyses of boundary value problems in engineering. Prentice-Hall.
- Hayat, T., Abbas, T., Ayub, M., Farooq, M., and Alsaedi, A. (2016). Flow of nanofluid due to convectively heated Riga plate with variable thickness. *Journal of Molecular Liquids*, **222**: 854-862.

- Hayat, T., Aziz, A., Muhammad, T., and Alsaedi, A. (2019). Active and passive controls of 3d nanofluid flow by a convectively heated nonlinear stretching surface. *Physica Scripta*, **94**(8): 085704
- Hayat, T., Khan, M., Imtiaz, M., and Alsaedi, A. (2017). Squeezing flow past a Riga plate with chemical reaction and convective conditions. *Journal of Molecular Liquids*, **225**: 569-576.
- Hayat, T., Muhammad, T., Shehzad, S. A., and Alsaedi, A. (2017). On magnetohydrodynamic flow of nanofluid due to a rotating disk with slip effect: A numerical study. *Comput. Methods Appl. Mech. Eng.*, **315**: 467-477.
- Hayat, T., Qayyum, S., Imtiaz, M. and Alsaedi, A. (2017). Radiative flow due to a stretchable rotating disk with variable thickness. *Results Phys.*, **7**: 156-165.
- Hayat, T., Qayyum, S., Shehzad, S. A., and Alsaedi, A. (2017). Simultaneous effects of heat generation/absorption and thermal radiation in magnetohydrodynamics (MHD) flow of Maxwell nanofluid towards a stretched surface. *Results Phys.*, **7**: 562-573.
- Hayat, T., Rashid, M., Imtiaz, M., and Alsaedi, A. (2015). Magnetohydrodynamic (MHD) flow of Cu water nanofluid due to a rotating disk with partial slip. *AIP Adv.*, **5**: 067169.
- Hayat, T., Rashid, M., Imtiaz, M., and Alsaedi, A. (2017). Mhd effects on a thermo-solutal stratified nanofluid flow on an exponentially radiating stretching sheet. *Journal of Applied Mechanics and Technical Physics*, **58**(2): 214– 223.
- Hussain, A., Malik, M., Salahuddin, T., Rubab, A., and Khan, M. (2017). Effects of viscous dissipation on mhd tangent hyperbolic fluid over a nonlinear stretching sheet with convective boundary conditions. *Results in physics*, **7**: 3502–3509.
- Imtiaz, M., Hayat, T., Alsaedi, A., and Asghar, S. (2017). Slip flow by a variable thickness rotating disk subject to magnetohydrodynamics. *Results Phys.*, **7**: 503-309
- Islam, S., Khan, A., Kumam, P., Alrabaiah, H., Shah, Z., Khan, W., Zubair, M., and Jawad, M. (2020). Radiative mixed convection flow of maxwell nanofluid over a stretching cylinder with joule heating and heat source/sink effects. *Scientific Reports*, **10**(1):1–18.
- Jagadha, S., Hari Shing Naik, S., Durgaprasad, P., Naresh Kumar, A., and Naikoti, K. (2021). Radiative newtonian carreau nanofluid through stretching cylinder considering the first-order chemical reaction. *International Journal of Ambient Energy*, 1–9.
- Kalaivanan, R., Ganesh, N. V., and Al-Mdallal, Q. M. (2020). An investigation on arrhenius activation energy of second grade nanofluid flow with active and passive control of nanomaterials. *Case Studies in Thermal Engineering*, **22**:100774.
- Kambhatla, P. K., Ojjela, O., and Das, S. K. (2016). Viscoelastic model of ethylene glycol with temperature-dependent thermophysical properties. *Journal of Thermal Analysis and Calorimetry*, **135**(2):1257–1268.
- Kandasamy, R., Muhaimin, I., and Mohammad, R. (2016). Single walled carbon nanotubes on mhd unsteady flow over a porous wedge with thermal radiation with variable stream conditions. *Alexandria Engineering Journal*, **55**(1):275–285.
- Khan, J. A., Mustafa, M., Hayat, T. and Alsaedi, A. (2018). A revised model to study the mhd nanofluid flow and heat transfer due to rotating disk: numerical solutions. *Neural Computing and Applications*, **30**(3): 957–964.

- Khan, M. I., Hayat, T., Khan, M. I., and Alsaedi, A. (2018). Activation energy impact in nonlinear radiative stagnation point flow of cross nanofluid. *International Communications in Heat and Mass Transfer*, **91**: 216–224.
- Khan, M. L., Tamor, M., Hayat, T. and Alsaedi (2017). MHD boundary layer thermal slip flow by nonlinearly stretching cylinder with suction/blowing and radiation. *Results in physics*, **7**: 1207-1211.
- Khan, N. S., Kumam, P., and Thounthong, P. (2020). Second law analysis with effects of arrhenius activation energy and binary chemical reaction on nanofluid flow. *Scientific reports*, **10**(1): 1–16.
- Khan, W., and Pop, I., (2010) Boundary-layer flow of a nanofluid past a stretching sheet, *International journal of heat and mass transfer* **53** (11-12) 2477–2483
- Khan, W., Makinde, O., and Khan, Z. (2014). Mhd boundary layer flow of a nanofluid containing gyrotactic microorganisms past a vertical plate with navier slip. *International journal of heat and mass transfer*, **74**: 285–291.
- Khan, Z., Hussain, S., and Hammouch, Z. (2016). Flow and heat transfer analysis of water and ethylene glycol-based cu nanoparticles between two parallel disks with suction/injection effects. *Journal of Molecular Liquids*, **221**: 298–304.
- Kierzenka J, and Shampine L. F., (2001) A BVP solver based on residual control and the MATLAB PSE. *ACM TOMS* **27**(3):299–316
- Kierzenka, J. and Shampine, L. F. (2008). A bvp solver that controls residual and error. *Journal of Numerical Analysis, Industrial and Applied Mathematics*, **3**(1-2): 27–41.
- Kiusalaas, J. (2005). Numerical methods in engineering with MATLAB R. *Cambridge university press, London*.
- Kumar, R., and Singh, S. (2021). Computational analysis of emhd flow of nanofluid over a rotating disk with convective boundary conditions: Buongiorno’s model. *In: Advances in Fluid and Thermal Engineering, Springer*, 231–247.
- Mahanthesh, B., Gireesha, B., and Gorla, R. S. R. (2016). Nonlinear radiative heat transfer in mhd three-dimensional flow of water based nanofluid over a non-linearly stretching sheet with convective boundary condition. *Journal of the Nigerian Mathematical Society*, **35**(1): 178–198.
- Mallawi, F., and Ullah, M. Z. (2021). Conductivity and energy change in carreau nanofluid flow along with magnetic dipole and darcy-forchheimer relation. *Alexandria Engineering Journal*, **60**(4): 3565–3575.
- Mathew, A., Areekara, S., and Sabu, A. (2021). Sensitivity analysis on radiative heat transfer of hydromagnetic carreau nanoliquid flow over an elongating cylinder using bulirsch-stoer algorithm. *Thermal Science and Engineering Progress*, **25**: 101038.
- Maxwell, J. C. (1873). A treatise on electricity and magnetism. *Clarendon press, The university of Cambridge London*, **1**.
- Mishra, A., and Panday, A., K., (2018). Viscous-ohmic and heat generative/absorptive on MHD flow against a stretching cylinder in the regions of suction and injection. *Nanoscience and Techonology: An International Journal*, **9**(2):99-115.
- Mustafa, M. (2017). MHD nanofluid flow over a rotating disk with partial slip effects: Buongiorno model. *Int J Heat Mass Transf.*, **108**:1910–1916.

- Nandi, S., Kumbhakar, B., and Sarkar, S., (2022) Mhd stagnation point flow of  $fe_3o_4/cu/ag-ch_3oh$  nanofluid along a convectively heated stretching sheet with partial slip and activation energy: Numerical and statistical approach, *International Communications in Heat and Mass Transfer* **130**:105791.
- Nazar, R., Amin, N., and Pop, I., (2004) Mixed convection boundary-layer flow from a horizontal circular cylinder in micropolar fluids: case of constant wall temperature, *International Journal of Numerical Methods for Heat & Fluid Flow*. **31**(2):1-17
- Panday, A. K. and Kumar, M. (2017). Natural convection and thermal radiation influence on nanofluid flow over a stretching cylinder in a porous medium with viscous dissipation. *Alexandria Engineering Journal*, **6**(1): 55-62.
- Pantokratoras, A. (2011). The Blasius and Sakiadis flow along a Riga plate. *Progress in Computational Fluid Dynamics, an International Journal*, **11**(5): 329-333.
- Pordanjani, A. H., Vahedi, S. M., Aghakhani, S., Afrand, M., Öztop, H. F., and Abu-Hamdeh, N. (2019). Effect of magnetic field on mixed convection and entropy generation of hybrid nanofluid in an inclined enclosure: sensitivity analysis and optimization. *The European Physical Journal Plus*, **134**(8): 1–20.
- Raju, C. S. K., Sandeep, N. and Malvandi, A. (2016). Free convective heat transfer of MHD Cu kerosene nanofluid over a cone with temperature dependent viscosity. *Acta Astronautica*, **129**: 419-428.
- Ramzan, M., Dawar, A., Saeed, A., Kumam, P., Watthayu, W., and Kumam, W. (2021). Heat transfer analysis of the mixed convective flow of magnetohydrodynamic hybrid nanofluid past a stretching sheet with velocity and thermal slip conditions. *Plos one*, **16**(12): e0260854
- Ramzan, M., Farooq, M., Hayat, T., and Chung, J. D. (2016). Radiative and joule heating effects in the mhd flow of a micropolar fluid with partial slip and convective boundary condition. *Journal of Molecular Liquids*, **221**: 394–400.
- Rashid, U., Liang, H., Ahmad, H., Abbas, M., Iqbal, A., and Hamed, Y. (2021). Study of (ag and tio<sub>2</sub>)/water nanoparticles shape effect on heat transfer and hybrid nanofluid flow toward stretching shrinking horizontal cylinder. *Results in Physics*, **21**: 103812
- Rashidi, M. M., Kavyani, N., and Abelman, S. (2014). Investigation of entropy generation in MHD and slip flow over a rotating porous disk with variable properties. *Int. J. Heat Mass Transf.*, **70**: 892-217.
- Rashidi, M.M., Abelman, S., and Mehr, N.F. (2013). Entropy generation in steady MHD flow due to a rotating porous disk in a nanofluid. *Int. Heat Mass Transf.*, **62**: 515-525.
- Reddy, M. G., Kumar, N., Prasannakumara, B., Rudraswamy, N., and Kumar K. G. (2021). Magnetohydrodynamic flow and heat transfer of a hybrid nanofluid over a rotating disk by considering arrhenius energy. *Communications in Theoretical Physics*, **73**(4): 045002.
- Rosseland, S. (1931). *Astrophysik und atom-theoretische Grundlagen* (SpringerVerlag, Berlin), 41–44.
- Sabu, A., Mackolil, J., Mahanthesh, B., and Mathew, A. (2021). Nanoparticle aggregation kinematics on the quadratic convective magnetohydrodynamic flow of nanomaterial past an inclined flat plate with sensitivity analysis. *Proceedings of the Institution of Mechanical Engineers, Part E: Journal of Process Mechanical Engineering*, **236**(3):1056-1066
- Sabu, A., S., Areekara, S., and Mathew, A., (2021) Effects of multi slip and distinct heat source on mhd carreau nanofluid flow past an elongating cylinder using the statistical method, *Heat Transfer* **50** (6):5652–5673.

- Sabu, A., Wakif, A., Areekara, S., Mathew, A., and Shah, N. A. (2021). Significance of nanoparticles' shape and thermohydrodynamic slip constraints on mhd alumina-water nanoliquid flows over a rotating heated disk: The passive control approach. *International Communications in Heat and Mass Transfer*, **129**:105711.
- Sajid, M., and Hayat, T., (2008) Influence of thermal radiation on the boundary layer flow due to an exponentially stretching sheet, *International Communications in Heat and Mass Transfer* **35** (3):347–356.
- Salahuddin, T., Hussain, A., Malik, M., Awais, M., and Khan, M. (2017). Carreau nanofluid impinging over a stretching cylinder with generalized slip effects: using finite difference scheme. *Results in physics*, **7**: 3090–3099.
- Schlichting, H. (1979). *Boundary Layer Theory*. McGraw-Hill. New York.
- Shampine L. F, Gladwell I., and Thompson S. (2003). *Solving ODEs with MATLAB*. Cambridge University Press, New York.
- Shojaei, A., Amiri, A. J., Ardahaie, S. S., Hosseinzadeh, K., and Ganji, D. (2019). Hydrothermal analysis of nonnewtonian second grade fluid flow on radiative stretching cylinder with solet and dufour effects. *Case Studies in Thermal Engineering*, **13**:100384.
- Sulochana, C. and Sandeep, N. (2016). Stagnation point flow and heat transfer behavior of cu–water nanofluid towards horizontal and exponentially stretching/shrinking cylinders. *Applied Nanoscience*, **6**(3): 451–459.
- Tiwari, R. K., and Das, M. K. (2007). Heat transfer augmentation in a two-sided lid-driven differentially heated square cavity utilizing nanofluids, *International Journal of heat and Mass transfer*, **50**(9-10): 2002–2018.
- Turkyilmazoglu, M. (2012). MHD fluid flow and heat transfer due to a stretching rotating disk. *Int. J. Thermal Sci.*, **51**: 195-201.
- Turkyilmazoglu, M. (2014). Nanofluid flow and heat transfer due to a rotating disk. *Computers & Fluids*, **94**: 139– 146.
- Turkyilmazoglu, M., and Senel, P. (2013). Heat and mass transfer of the flow due to a rotating rough and porous disk. *Int J Thermal Sci*, **63**:146–158.
- Ullah, I., Ullah, R., Alqarni, M., Xia, W. F. and Muhammad, T. (2021). Combined heat source and zero mass flux features on magnetized nanofluid flow by radial disk with the applications of coriolis force and activation energy. *International Communications in Heat and Mass Transfer*, **126** :105416.
- Usman, M., Gul, T., Khan, A., Alsubie, A., and Ullah, M. Z. (2021). Electromagnetic couple stress film flow of hybrid nanofluid over an unsteady rotating disc. *International Communications in Heat and Mass Transfer*, **127**: 105562.
- Von Karma, T. and Angew, Z. (1921). Uber laminare and burbulente Reibung, *Math. Mech.* **1**: 233-252.
- Wakif, A., Chamkha, A., Thumma, T., Animasaun, I., and Sehaqui, R. (2021). Thermal radiation and surface roughness effects on the thermo-magneto-hydrodynamic stability of alumina–copper oxide hybrid nanofluids utilizing the generalized buongiorno's nanofluid model. *Journal of Thermal Analysis and Calorimetry*, **143**(2): 1201–1220.
- Waqas, H., Imran, M., and Bhatti, M. (2020). Influence of bioconvection on maxwell nanofluid flow with the swimming of motile microorganisms over a vertical rotating cylinder. *Chinese Journal of Physics*, **68**: 558–577.

- Xuan, Z., Zhai, Y., Ma, M., Li, Y. and Wang, H. (2021). Thermo-economic performance and sensitivity analysis of ternary hybrid nanofluids. *Journal of Molecular Liquids*, **323**:114889.
- Xun, S., Zhao, J., Zheng, L., Chen, X., and Zhang, X. (2016). Flow and heat transfer of Ostwald-de Waele fluid over a variable thickness rotating disk with index decreasing. *Int. J. Heat Mass Transf.*, **103**:1214-1224.
- Yin C., Zheng L., Zhang C., Zhang X., (2017) Flow and heat transfer of nanofluids over a rotating disk with uniform stretching rate in the radial direction. *Propulsion and Power Research* **6** 25–3.

## ABSTRACT

Title of Thesis	:	<b>Heat transfer in nanofluids over different conformations with various effects</b>
Name of degree holder	:	<b>Pardeep Kumar</b>
Title of degree	:	Doctor of Philosophy
Admission No	:	<b>2019BS21D</b>
Name and address of Major advisor	:	<b>Dr. Hemant Poonia</b> <b>Assistant Professor</b> Department of Mathematics and Statistics CCS Haryana Agricultural University Hisar-125004 (Haryana) India
Degree awarding University/Institute	:	CCS Haryana Agricultural University Hisar-125004 (Haryana) India
Year of award of degree	:	<b>2023</b>
Major subject	:	Mathematics
Total number of pages in thesis	:	159 + viii
Number of words in the abstract	:	255

**Keywords:** Tangent hyperbolic, Nanofluid, Micropolar fluid, Thermal radiation, Nanoparticle, Magnetohydrodynamic, Thermophoresis and Brownian motion, Convective condition, Arrhenius energy, MHD, Heat source, Carreau nanofluid, Numerical simulation, slip effect, Modified Buongiorno model, Hybrid fluid

The boundary layer flow, heat transfer flow, and mass transfer flow past a nanofluid due to different geometries have all been examined in the current study using numerical methods. The nanofluid flow saturated in different solid objects, such as stretching sheet, stretching cylinder, Riga plate, rotating disc, etc., are commonly used in many fields of engineering and manufacturing procedures.

Numerous physical phenomena are involved in the various flow conditions, including the magnetic effect, velocity slip effect, thermal slip effect, suction/injection, Brownian motion and thermophoresis effects, porosity, heat generation/absorption, thermal radiation, Arrhenius energy, chemical reaction, viscous dissipation, Joule heating, and nanoparticle volume fraction, in nanofluid flow have been discussed. To investigate the variations in velocity profiles, temperature, and concentration distributions, the influences of these parameters are plotted and discussed. Moreover, the factors of engineering interest, such as skin friction coefficient, Nusselt and Sherwood numbers are studied and discussed in details.

The system of governing non-linear partial differential equations is transformed into the system of coupled non-linear ordinary differential equations by applying an appropriate transformation. Then, the Runge-Kutta-Fehlberg method of fourth-fifth order along with shooting technique is used to solve them with the help of computing tools. Also, `bvp4c`, `bvp5c` MATLAB inbuilt solver are used. For validation of present numerical codes, the result are compared with previously published works.

Thus, an excellent correlation between the current results and the available solutions in the literature is attained. The obtained results have huge significances in different fields of applied science and different branches of engineering and applied mathematics.

**MAJOR ADVISOR**

**SIGNATURE OF STUDENT**

**HEAD OF THE DEPARTMENT**

## CURRICULUM VITAE

Name : Pardeep Kumar  
Date of birth : 10. 10.1994  
Place of birth : Hisar  
Mother's name : Smt. Bala Devi  
Father's name : Sh. Mewa Singh  
Permanent address : Village – Ghirai, PO – Ghirai,  
Dist – Hisar (Haryana) Pin code – 125033  
Mobile : +917206232008  
E-mail : [pkboora94@gmail.com](mailto:pkboora94@gmail.com), [pkboora94@hau.ac.in](mailto:pkboora94@hau.ac.in)



### Academic qualifications

Degree	University/Board	Year of passing	Percentage of marks	Subjects
Matric	Haryana Board of School Education	2009	71.6	All Subjects
Intermediate	Haryana Board of School Education	2011	82.0	Hindi, English, Maths, Physics & Chemistry
B.Sc.	Government P.G. College, Hisar	2014	78.82	Maths, Physics, Chemistry
M.Sc.	Kurukshetra University Kurukshetra	2016	73.08	Mathematics
Net-JRF	CSIR	2021	AIR (80)	Mathematics

**Co-curricular activities** : -

**Medals/Honours received** : -

### List of Publications:

1. Kumar, P., Poonia, H., Ali, L., Areekara, S., (2022). The numerical simulation of nanoparticle size and thermal radiation with the magnetic field effect based on tangent hyperbolic nanofluid flow, *Case Studies in Thermal Engineering* **37** 102247.
2. Kumar, P., Poonia, H., (2022). Slip Effect on Magnetohydrodynamic Boundary Layer Flow of Nanofluid over an Stretching Sheet with Thermal Radiation and Thermal Convective Boundary Condition, *Current Journal of Applied Science and Technology* **41**(46), 33-45.

### **UNDERTAKING OF COPYRIGHT**

I Pardeep Kumar, Admission No. 2019BS21D undertake that I give copyright of my thesis entitled “Heat transfer in nanofluids over different conformations with various effects” to the Chaudhary Charan Singh Haryana Agricultural University, Hisar. I also undertake that the patent, if any, arising out of the research work conducted during the programme shall be filed by me only with due permission of the competent authority of CCS HAU, Hisar.

**SIGNATURE OF THE STUDENT**